
MAGNETIC ACTUATORS AND SENSORS

John R. Brauer

Milwaukee School of Engineering

IEEE Magnetic Society, *Sponsor*



IEEE PRESS



A JOHN WILEY & SONS, INC., PUBLICATION

MAGNETIC ACTUATORS AND SENSORS

IEEE Press
445 Hoes Lane
Piscataway, NJ 08854

IEEE Press Editorial Board
Mohamed E. El-Hawary, *Editor in Chief*

M. Akay	T. G. Croda	M. S. Newman
J. B. Anderson	R.J. Herrick	F. M. B. Pereira
R. J. Baker	S. V. Kartalopoulos	C. Singh
J. E. Brewer	M. Montrose	G. Zobrist

Kenneth Moore, *Director of IEEE Book and Information Services (BIS)*
Catherine Faduska, *Senior Acquisitions Editor*
Jeanne Audino, *Project Editor*

IEEE Magnetic Society, *Sponsor*
Magnetic Society Liaisons to IEEE Press,
Stanley Charap
John T. Scott

Technical Reviewers
Mark A. Juds, Eaton Corporation
John T. Scott, American Institute of Physics (Retired)

MAGNETIC ACTUATORS AND SENSORS

John R. Brauer

Milwaukee School of Engineering

IEEE Magnetic Society, *Sponsor*



IEEE PRESS



A JOHN WILEY & SONS, INC., PUBLICATION

Copyright © 2006 by the Institute of Electrical and Electronics Engineers, Inc. All rights reserved.

Published by John Wiley & Sons, Inc., Hoboken, New Jersey.
Published simultaneously in Canada.

No part of this publication may be reproduced, stored in a retrieval system, or transmitted in any form or by any means, electronic, mechanical, photocopying, recording, scanning, or otherwise, except as permitted under Section 107 or 108 of the 1976 United States Copyright Act, without either the prior written permission of the Publisher, or authorization through payment of the appropriate per-copy fee to the Copyright Clearance Center, Inc., 222 Rosewood Drive, Danvers, MA 01923, (978) 750-8400, fax (978) 750-4470, or on the web at www.copyright.com. Requests to the Publisher for permission should be addressed to the Permissions Department, John Wiley & Sons, Inc., 111 River Street, Hoboken, NJ 07030, (201) 748-6011, fax (201) 748-6008, or online at <http://www.wiley.com/go/permission>.

Limit of Liability/Disclaimer of Warranty: While the publisher and author have used their best efforts in preparing this book, they make no representations or warranties with respect to the accuracy or completeness of the contents of this book and specifically disclaim any implied warranties of merchantability or fitness for a particular purpose. No warranty may be created or extended by sales representatives or written sales materials. The advice and strategies contained herein may not be suitable for your situation. You should consult with a professional where appropriate. Neither the publisher nor author shall be liable for any loss of profit or any other commercial damages, including but not limited to special, incidental, consequential, or other damages.

For general information on our other products and services or for technical support, please contact our Customer Care Department within the United States at (800) 762-2974, outside the United States at (317) 572-3993 or fax (317) 572-4002.

Wiley also publishes its books in a variety of electronic formats. Some content that appears in print may not be available in electronic format. For information about Wiley products, visit our web site at www.wiley.com.

Library of Congress Cataloging-in-Publication Data is available.

ISBN-13 978-0-471-73169-6
ISBN-10 0-471-73169-2

Printed in the United States of America.

10 9 8 7 6 5 4 3 2 1

Contents

Preface	xi
PART I MAGNETICS	1
1. Introduction	3
1.1 Overview of Magnetic Actuators	3
1.2 Overview of Magnetic Sensors	4
1.3 Actuators and Sensors in Motion Control Systems	5
References	6
2. Basic Electromagnetics	7
2.1 Vectors	7
2.1.1 Gradient	7
2.1.2 Divergence	9
2.1.3 Curl	9
2.2 Ampere's Law	12
2.3 Magnetic Materials	15
2.4 Faraday's Law	18
2.5 Potentials	22
2.6 Maxwell's Equations	24
Problems	26
References	28
3. Reluctance Method	29
3.1 Simplifying Ampere's Law	29
3.2 Applications	32
3.3 Fringing Flux	36
3.4 Complex Reluctance	36
3.5 Limitations	37
Problems	37
References	37

4. Finite-Element Method	39
4.1 Energy Conservation and Functional Minimization	39
4.2 Triangular Elements for Magnetostatics	40
4.3 Matrix Equation	42
4.4 Finite-Element Models	44
Problems	48
References	49
5. Magnetic Force	51
5.1 Magnetic Flux Line Plots	51
5.2 Magnetic Energy	56
5.3 Magnetic Force on Steel	57
5.4 Magnetic Pressure on Steel	60
5.5 Lorentz Force	62
5.6 Permanent Magnets	62
5.7 Magnetic Torque	66
Problems	67
References	67
6. Other Magnetic Performance Parameters	69
6.1 Magnetic Flux and Flux Linkage	69
6.1.1 Definition and Evaluation	69
6.1.2 Relation to Force and Other Parameters	70
6.2 Inductance	72
6.2.1 Definition and Evaluation	72
6.2.2 Relation to Force and Other Parameters	74
6.3 Capacitance	75
6.3.1 Definition	75
6.3.2 Relation to Energy and Force	76
6.4 Impedance	77
Problems	80
References	80
PART II ACTUATORS	83
7. Magnetic Actuators Operated by Direct Current	85
7.1 Solenoid Actuators	85
7.1.1 Clapper Armature	85
7.1.2 Plunger Armature	91
7.2 Voice Coil Actuators	96
7.3 Other Actuators Using Coils and Permanent Magnets	97
7.4 Proportional Actuators	98

7.5 Rotary Actuators	101
Problems	104
References	105
8. Magnetic Actuators Operated by Alternating Current	107
8.1 Skin Depth	107
8.2 Power Losses in Steel	108
8.2.1 Laminated Steel	108
8.2.2 Equivalent Circuit	109
8.2.3 Solid Steel	111
8.3 Force Pulsations	113
8.3.1 Force with Single AC Coil	113
8.3.2 Force with Added Shading Coil	114
8.4 Cuts In Steel	116
8.4.1 Special Finite-Element Formulation	117
8.4.2 Loss and Reluctance Computations	118
Problems	122
References	123
9. Magnetic Actuator Transient Operation	125
9.1 Basic Timeline	125
9.2 Size, Force, and Acceleration	125
9.3 Linear Magnetic Diffusion Times	128
9.3.1 Steel Slab Turnon and Turnoff	128
9.3.2 Steel Cylinder	131
9.4 Nonlinear Magnetic Diffusion Time	132
9.4.1 Simple Equation for Steel Slab with “Step” $B-H$	132
9.4.2 Transient Finite-Element Computations for Steel Slabs	132
9.4.3 Simple Equation for Steel Cylinder with “Step” $B-H$	135
9.4.4 Transient Finite-Element Computations for Steel Cylinders	136
Problems	138
References	142
PART III SENSORS	143
10. Hall Effect and Magnetoresistive Sensors	145
10.1 Simple Hall Voltage Equation	145
10.2 Hall Effect Conductivity Tensor	146
10.3 Finite-Element Computation of Hall Fields	149
10.3.1 Unsymmetric Matrix Equation	149
10.3.2 2D Results	150
10.3.3 3D Results	156

10.4	Toothed Wheel Hall Sensors for Position	157
10.5	Magnetoresistance	159
10.5.1	Classical Magnetoresistance	159
10.5.2	Giant Magnetoresistance	160
10.5.3	Newest Forms of Magnetoresistance	160
10.6	Magnetoresistive Heads for Hard-Disk Drives	161
	Problems	162
	References	162
11.	Other Magnetic Sensors	165
11.1	Speed Sensors Based on Faraday's Law	165
11.2	Inductive Recording Heads	167
11.3	Proximity Sensors Using Impedance	169
11.3.1	Stationary Eddy Current Sensors	170
11.3.2	Moving Eddy Current Sensors	173
11.4	Linear Variable Differential Transformers	174
11.5	Magnetostrictive Sensors	177
11.6	Flux Gate Sensors	179
11.7	Magnetometers and Motes	181
	Problems	186
	References	186
PART IV	SYSTEMS	189
12.	Coil Design and Temperature Calculations	191
12.1	Wire Size Determination for DC Currents	191
12.2	Coil Time Constant and Impedance	194
12.3	Skin Effects and Proximity Effects for AC Currents	195
12.4	Finite-Element Computations of Temperatures	199
12.4.1	Thermal Conduction	199
12.4.2	Thermal Convection and Thermal Radiation	201
12.4.3	AC Magnetic Device Cooled by Conduction, Convection, and Radiation	202
	Problems	206
	References	206
13.	Electromagnetic Compatibility	209
13.1	Signal-to-Noise Ratio	209
13.2	Shields and Apertures	210
13.3	Test Chambers	215
13.3.1	TEM Transmission Lines	215

13.3.2	TEM Cells	217
13.3.3	Triplate Cells	217
	Problems	220
	References	220
14.	Electromechanical Finite Elements	223
14.1	Electromagnetic Finite-Element Matrix Equation	223
14.2	0D and 1D Finite Elements for Coupling Electric Circuits	225
14.3	Structural Finite-Element Matrix Equation	228
14.4	Force and Motion Computation by Timestepping	232
14.5	Typical Electromechanical Applications	234
14.5.1	DC Solenoid with Slowly Rising Input Current	234
14.5.2	DC Solenoid with Step Input Voltage	235
14.5.3	AC Clapper Solenoid Motion and Stress	238
14.5.4	Transformers with Switches or Sensors	242
	Problems	242
	References	244
15.	Electromechanical Analysis Using Systems Models	247
15.1	Electric Circuit Models of Magnetic Devices	247
15.1.1	Electric Circuit Software Including SPICE	247
15.1.2	Simple LR Circuits	247
15.1.3	Tables of Nonlinear Flux Linkage and Force	249
15.1.4	Analogies for Rigid Armature Motion	250
15.1.5	Maxwell SPICE Model of Bessho Actuator	251
15.1.6	Simplorer Model of Bessho Actuator	252
15.2	VHDL-AMS/Simplorer Models	254
15.2.1	VHDL-AMS Standard IEEE Language	254
15.2.2	Model of Solenoid Actuator	254
15.3	MATLAB/Simulink Models	258
15.3.1	Software	258
15.3.2	MATLAB Model of Voice Coil Actuator	259
15.4	Including Eddy Current Diffusion Using a Resistor	264
15.4.1	Resistor for Planar Devices	264
15.4.2	Resistor for Axisymmetric Devices	265
	Problems	268
	References	268
16.	Coupled Electrohydraulic Analysis Using Systems Models	271
16.1	Comparing Hydraulics and Magnetics	271
16.2	Hydraulic Basics and Electrical Analogies	272

x CONTENTS

16.3	Modeling Hydraulic Circuits in SPICE	274
16.4	Electrohydraulic Models in SPICE and Simpler	277
16.5	Hydraulic Valves and Cylinders in Systems Models	283
16.5.1	Valves and Cylinders	283
16.5.2	Use in SPICE Systems Models	286
16.6	Magnetic Diffusion Resistor in Electrohydraulic Models	292
	Problems	296
	References	297
Appendix: Symbols, Dimensions, and Units		299
Index		301

Preface

This book is written for practicing engineers and engineering students involved with the design or application of magnetic actuators and sensors. The reader should have completed at least one basic course in electrical engineering and/or mechanical engineering. This book is suitable for engineering college juniors, seniors, and graduate students.

IEEE societies whose members will be interested in this book include the Magnetics Society, Computer Society, Power Engineering Society, Industry Applications Society, and Control System Society. Readers of the *IEEE/ASME Transactions on Mechatronics*, sponsored by the IEEE Industrial Electronics Society, may also want to read this book. Many SAE (Society of Automotive Engineers) members might also be very interested in this book because the magnetic devices discussed here are commonly used in automobiles and aircraft.

This book is a suitable text for upper-level engineering undergraduates or graduate students in courses with titles such as “Actuators and Sensors” or “Mechatronics.” It can also serve as a supplementary text for courses such as “Electromagnetic Fields,” “Electromechanical Energy Conversion,” or “Feedback Control Systems.” It is also appropriate as a reference book for “Senior Projects” in electrical and mechanical engineering. Its basic material has been used in a 16-hour seminar for industry that I have taught many times at Milwaukee School of Engineering. More than twice as many class hours, however, will be required to thoroughly cover the contents of this book.

The chapters on magnetic actuators are intended to replace a venerable book by Herbert C. Roters, *Electromagnetic Devices*, published by John Wiley & Sons in 1941. Over the decades since 1941, many technological revolutions have occurred. Perhaps the most wide-ranging revolution has been the rise of the modern computer. The computer not only uses magnetic actuators and sensors in its disk drives and external interfaces but also enables new ways of analyzing and designing magnetic devices. Hence this book includes the latest computer-aided engineering methods from the most recently published technical papers. The latest software tools are used, especially the electromagnetic finite-element software package Maxwell SV, which is available to students at no charge from Ansoft Corporation, for which I am a part-time consultant. Other software tools used include SPICE, MATLAB, and Simplorer. Simplorer SV, the student version, is also available to students free of charge from Ansoft Corporation. If desired, the reader can work the computational

examples and problems with other available software packages, which should yield similar results. To download Maxwell SV and Simplorer SV along with their example files, please visit the web site for this book:

ftp://ftp.wiley.com/public/sci_tech_med/magnetic_actuators/

This book is divided into four parts, each containing several chapters. Part 1, on *magnetics*, begins with an introductory chapter defining magnetic actuators and sensors and why they are important. The second chapter is a review of basic electromagnetics, needed because magnetic fields are the key to understanding magnetic actuators and sensors. Chapter 3 is on the reluctance method, a way to approximately calculate magnetic fields by hand. Chapter 4 covers the finite-element method, which calculates magnetic fields very accurately via the computer. Magnetic force is a required output of magnetic actuators and is discussed in Chapter 5, and other magnetic performance parameters are the subject of Chapter 6.

Part 2 is on *actuators*. Chapter 7 discusses DC (direct-current) actuators, while Chapter 8 deals with AC (alternating-current) actuators. The last chapter devoted strictly to magnetic actuators is Chapter 9, on their transient operation.

Part 3 of the book is on *sensors*. Chapter 10 describes in detail the Hall effect and magnetoresistance, and applies these principles to sensing position. Chapter 11 covers many other types of magnetic sensors. However, types of sensors involving quantum effects are not included, because quantum theory is beyond the scope of this book.

Part 4 of the book, on *systems*, covers many systems aspects common to both magnetic actuators and sensors. Chapter 12 presents coil design and temperature calculations. Electromagnetic compatibility issues common to sensors and actuators are discussed in Chapter 13. Electromechanical performance is analyzed in Chapter 14 using coupled finite elements, while Chapter 15 uses electromechanical systems software. Finally, Chapter 16 shows the advantages of electrohydraulic systems that incorporate magnetic actuators and/or sensors.

Many examples are presented throughout the book because my teaching experience has shown that they are vital to learning. The examples that are numbered are simple enough to be fully described, solved, and repeated by the reader. In addition, problems at the ends of the chapters enable the reader to progress beyond the solved examples.

I would like to thank the many engineers whom I have known for making this book possible. Starting with my father, Robert C. Brauer, P.E., it has been my great pleasure to work with you for many decades. I thank my wife, Susan McCord Brauer, for her encouragement and advice on writing. Thanks also go to the reviewers of this book for their many excellent suggestions. All of you have taught me many things. This book is my attempt to summarize some of what I've learned and to pass it on.

JOHN R. BRAUER

jbrauer@ieee.org
Fish Creek, Wisconsin

PART I

MAGNETICS

Introduction

Magnetic actuators and sensors use magnetic fields to produce and sense motion. Magnetic actuators allow an electrical signal to move small or large objects. To obtain an electrical signal that senses the motion, magnetic sensors are often used.

Since computers have inputs and outputs that are electrical signals, magnetic actuators and sensors are ideal for computer control of motion. Hence magnetic actuators and sensors are increasing in popularity. Motion control that was in the past accomplished by manual command is now increasingly carried out by computers with magnetic sensors as their input interface and magnetic actuators as their output interface.

Both magnetic actuators and magnetic sensors are energy conversion devices. Both involve the energy stored in static, transient, or low-frequency magnetic fields. Devices that use electric fields or high-frequency electromagnetic fields are not considered to be magnetic devices and thus are not discussed in this book.

1.1 OVERVIEW OF MAGNETIC ACTUATORS

Figure 1.1 is a block diagram of a magnetic actuator. Input electrical energy in the form of voltage and current is converted to magnetic energy. The magnetic energy creates a magnetic force, which produces mechanical motion over a limited range. Thus magnetic actuators convert input electrical energy into output mechanical energy. As mentioned in the figure caption, the blocks are often nonlinear, as will be discussed later in this book.

Typical magnetic actuators include

- Electrohydraulic valves in airplanes, tractors, robots, automobiles, and other mobile or stationary equipment
- Fuel injectors in engines of automobiles, trucks, and locomotives
- Biomedical prosthesis devices for artificial hearts, limbs, ears, and other organs
- Head positioners for computer disk drives
- Loudspeakers

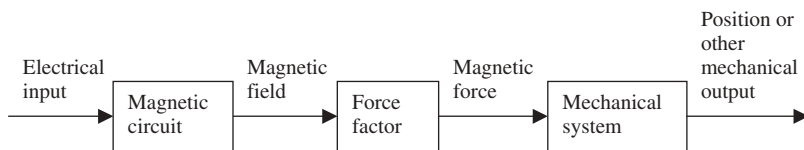


Figure 1.1 Block diagram of a magnetic actuator. The blocks are not necessarily linear. Both the magnetic circuit block and the force factor block are often nonlinear. The force factor block often produces a force proportional to the square of the magnetic field.

- Contactors, circuit breakers, and relays to control electric motors and other equipment
- Switchgear and relays for electric power transmission and distribution

Since magnetic actuators produce motion over a limited range, other electro-mechanical energy converters with wide ranges of motion are not discussed in this book. Thus electric motors that produce multiple 360° rotations are not covered here. However, “step motors,” which produce only a few degrees of rotary motion, are classified as magnetic actuators and are included in this book.

1.2 OVERVIEW OF MAGNETIC SENSORS

A magnetic sensor has the block diagram shown in Fig. 1.2. Compared to a magnetic actuator, the energy flow is different, and the amount of energy is often much smaller. The main input is now a mechanical parameter such as position or velocity, although electrical and/or magnetic input energy is usually needed as well. Input energy is converted to magnetic field energy. The output of a magnetic sensor is an electrical signal. In many cases the signal is a voltage with very little current, and thus the output electrical energy is often very small.

Magnetic devices that output large amounts of electrical energy are not normally classified as sensors. Hence typical generators and alternators are not discussed in this book.

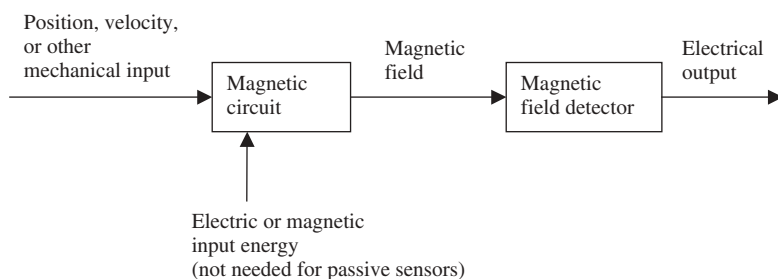


Figure 1.2 Block diagram of a magnetic sensor. The blocks are not necessarily linear.

Typical magnetic sensors include

- Proximity sensors to determine presence and location of conducting objects for factory automation, bomb or weapon detection, and petroleum exploration
- Microphones that sense air motion (sound waves)
- Linear variable-differential transformers to determine object position
- Velocity sensors for antilock brakes and stability control in automobiles
- Hall effect position or velocity sensors

Design of magnetic actuators and sensors involves analysis of their magnetic fields. The actuator or sensor should have geometry and materials that utilize magnetic fields to produce maximum output for minimum size and cost.

1.3 ACTUATORS AND SENSORS IN MOTION CONTROL SYSTEMS

Motion control systems can use nonmagnetic actuators and/or nonmagnetic sensors. For example, electric field devices called *piezoelectrics* are sometimes used as sensors instead of magnetic sensors. Other nonmagnetic sensors include Global Positioning System (GPS) sensors that use high-frequency electromagnetic fields, radio frequency identification (RFID) tags, and optical sensors such as television cameras. Nonmagnetic actuators and nonmagnetic sensors are not discussed in this book.

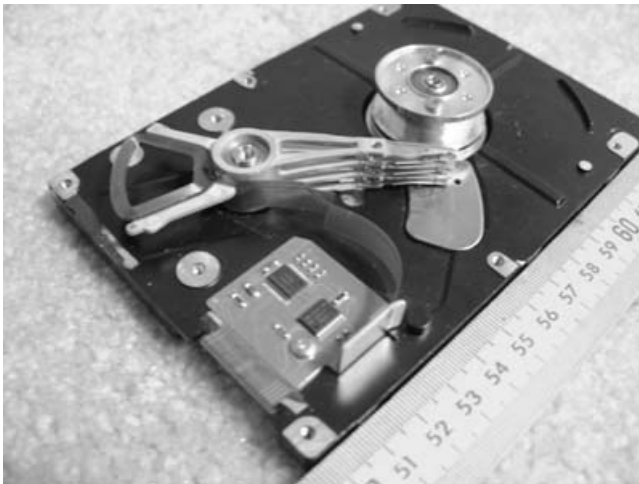


Figure 1.3 Typical computer disk drive head assembly. The actuator coil is the rounded triangle in the upper left. The four heads are all moved inward and outward toward the spindle hub by the force and torque on the actuator coil. Portions of the actuator and all magnetic disks are removed to allow the coil and heads to be seen.

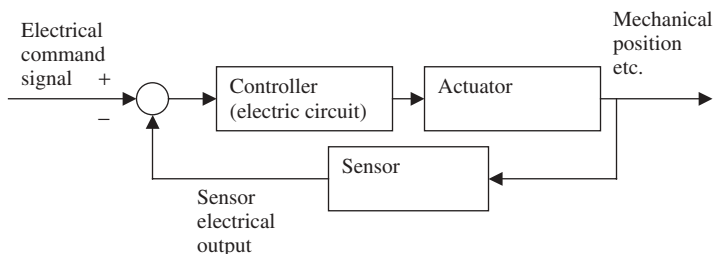


Figure 1.4 Basic feedback control system that may use both a magnetic actuator and a magnetic sensor.

An example of a motion control system that uses both a magnetic actuator and a magnetic sensor is the computer disk drive head assembly shown in Fig. 1.3. The head assembly is a magnetic sensor that senses (“reads”) not only the computer data magnetically recorded on the hard disk but also the position (track) on the disk. To position the heads at various radii on the disk, a magnetic actuator called a *voice coil actuator* is used.

Often the best way to control motion is to use a feedback control system. Such systems often involve the combination of electronics and mechanics, called *mechatronics*. The system block diagram shown in Fig. 1.4 contains both an actuator and a sensor. The sensor may be a magnetic sensor measuring position or velocity. The actuator may be a magnetic device producing a magnetic force. It is found that accurate control requires an accurate sensor. Control systems books widely used by electrical and mechanical engineers describe how to analyze and design such control systems [1–4]. The system design requires mathematical models of both actuators and sensors, which will be discussed throughout this book.

REFERENCES

1. R. C. Dorf and R. H. Bishop, *Modern Control Systems*, 9th ed., Prentice-Hall, Upper Saddle River, NJ, 2001.
2. J. Dorsey, *Continuous and Discrete Control Systems*, McGraw-Hill, New York, 2002.
3. C. L. Phillips and R. D. Harbor, *Feedback Control Systems*, 4th ed., Prentice-Hall, Upper Saddle River, NJ, 2000.
4. J. H. Lumkes, Jr., *Control Strategies for Dynamic Systems*, Marcel Dekker, New York, 2002.

Basic Electromagnetics

Study of magnetic fields provides an explanation of how magnetic actuators and sensors work. Hence this chapter presents the basic principles of *electromagnetics*, a subject that includes magnetic fields.

In reviewing electromagnetic theory, this chapter also introduces various parameters and their symbols. The symbols and notations used in this chapter will be used throughout the book, and most are also listed in the Appendix along with their units.

2.1 VECTORS

Magnetic fields are vectors, and thus it is useful to review mathematical operations involving vectors. A *vector* is defined here as a parameter having both magnitude and direction. Thus it differs from a *scalar*, which has only magnitude (and no direction). In this book, vectors are indicated by bold type, and scalars are indicated by italic nonbold type.

To define *direction*, rectangular coordinates are often used. Also called *Cartesian coordinates*, the position and direction are specified in terms of x , y , and z . This book denotes the three rectangular direction unit vectors as \mathbf{u}_x , \mathbf{u}_y , and \mathbf{u}_z ; they all have magnitude equal to one.

Common to several vector operations is the “del” operator (also termed “nabla”). It is denoted by an upside-down (inverted) delta symbol, and in rectangular coordinates is given by

$$\nabla = \frac{\partial}{\partial x} \mathbf{u}_x + \frac{\partial}{\partial y} \mathbf{u}_y + \frac{\partial}{\partial z} \mathbf{u}_z \quad (2.1)$$

2.1.1 Gradient

A basic vector operation is *gradient*, also called “grad” for short. It involves the del operator operating on a scalar (value), for example, temperature T . In rectangular coordinates the gradient of T is expressed as:

$$\nabla T = \frac{\partial T}{\partial x} \mathbf{u}_x + \frac{\partial T}{\partial y} \mathbf{u}_y + \frac{\partial T}{\partial z} \mathbf{u}_z \quad (2.2)$$

An example of temperature gradient is shown in Fig. 2.1. A block of ice is placed to the left of $x = 0$, for position x values less than zero. At $x = 1$ m (meter), a wall of room temperature 20°C is located. Assuming the temperature varies linearly from $x = 0$ to $x = 1$ m, then

$$T = 20x \quad (2.3)$$

To find the temperature gradient, substitute (2.3) into (2.2), obtaining:

$$\nabla T = 20\mathbf{u}_x^\circ\text{C/m} \quad (2.4)$$

The direction of the gradient is the direction of maximum rate of change of the scalar (here temperature). The magnitude of the gradient equals the maximum rate of change per unit length. Since this book uses the SI (Système International) or metric system of units, all gradients presented here are per meter.

Two other vector operations involve multiplication with the del operator. Another word for multiplication is *product*, and there are two types of vector products.

Example 2.1 Gradient Calculations Find the gradient of the following temperature distribution at locations $(x,y,z) = (1,2,3)$ and $(4,-2,5)$:

$$T = 5x + 8y^2 + 3z \quad (\text{E2.1.1})$$

Solution: You must be careful in taking the partial derivatives in the gradient equation (2.2), and you must first find the expression for the gradient before evaluating it at any location. Thus the first step is to find the gradient expression:

$$\nabla T = \frac{\partial(5x + 8y^2 + 3z)}{\partial x}\mathbf{u}_x + \frac{\partial(5x + 8y^2 + 3z)}{\partial y}\mathbf{u}_y + \frac{\partial(5x + 8y^2 + 3z)}{\partial z}\mathbf{u}_z \quad (\text{E2.1.2})$$

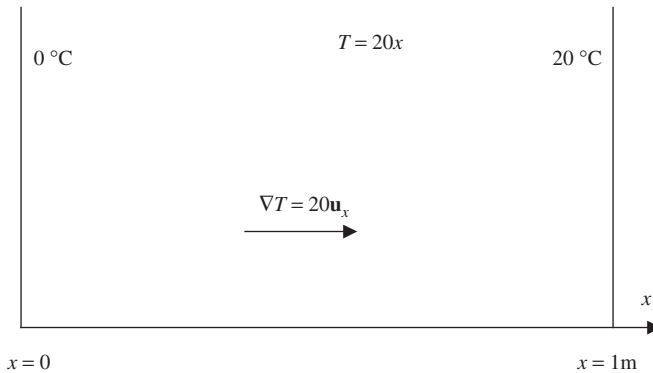


Figure 2.1 Temperature distribution and gradient versus position x .

The partial derivative of y with respect to x is zero, and so are all other partial derivatives of unlike variables, and thus we obtain

$$\nabla T = \frac{\partial(5x)}{\partial x} \mathbf{u}_x + \frac{\partial(8y^2)}{\partial y} \mathbf{u}_y + \frac{\partial(3z)}{\partial z} \mathbf{u}_z \quad (\text{E2.1.3})$$

Carrying out the derivatives gives

$$\nabla T = 5\mathbf{u}_x + 16y\mathbf{u}_y + 3\mathbf{u}_z \quad (\text{E2.1.4})$$

Finally, the gradient can be evaluated at the two specified locations:

$$\nabla T(1,2,3) = 5\mathbf{u}_x + 16(2)\mathbf{u}_y + 3\mathbf{u}_z = 5\mathbf{u}_x + 32\mathbf{u}_y + 3\mathbf{u}_z \quad (\text{E2.1.5})$$

$$\nabla T(4,-2,5) = 5\mathbf{u}_x + 16(-2)\mathbf{u}_y + 3\mathbf{u}_z = 5\mathbf{u}_x - 32\mathbf{u}_y + 3\mathbf{u}_z \quad (\text{E2.1.6})$$

Recall that the gradient must always be a vector.

2.1.2 Divergence

The *scalar product* or *dot product* obtains a scalar and is denoted by a “dot” symbol. Applying it to the del operator and a typical vector, here called \mathbf{J} , obtains “del dot \mathbf{J} ,” called the *divergence* of the vector:

$$\nabla \cdot \mathbf{J} = \frac{\partial J_x}{\partial x} + \frac{\partial J_y}{\partial y} + \frac{\partial J_z}{\partial z} \quad (2.5)$$

The divergence of a vector is its net outflow per unit volume, which is a scalar. In some cases, the divergence is zero, that is, the vector is *divergenceless*. For example, if \mathbf{J} is current density (to be defined later), then Kirchhoff’s law that total current at a point is zero ($\sum I = 0$) can be expressed as a divergenceless \mathbf{J} :

$$\nabla \cdot \mathbf{J} = 0 \quad (2.6)$$

Figure 2.2 shows typical fields with and without divergence.

2.1.3 Curl

The other type of vector product obtains a vector and is called the *vector product* or *cross product*. It is expressed using a cross or \times sign. If it is the product of the del operator and a typical vector, here called \mathbf{A} , one obtains a vector “del cross \mathbf{A} ,” called the *curl* of a vector. It can be expressed as a 3×3 determinant:

$$\nabla \times \mathbf{A} = \begin{vmatrix} \frac{\partial}{\partial x} & \frac{\partial}{\partial y} & \frac{\partial}{\partial z} \\ A_x & A_y & A_z \\ \mathbf{u}_x & \mathbf{u}_y & \mathbf{u}_z \end{vmatrix} \quad (2.7)$$

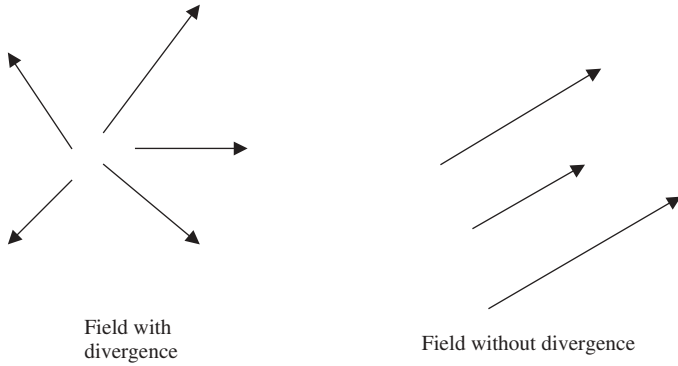


Figure 2.2 Field with and without divergence.

A 3×3 determinant is evaluated by the “basket-weave” method. Row 1 column 1 (the (1,1) or top left entry) is multiplied by row 2, column 2 and then by row 3, column 3, resulting in one of six terms of the cross product. The next term is found by multiplying the (1,2) entry by the (2,3) entry and the (3,1) entry. The next term multiplies the (1,3), (2,1), and (3,2) entries. The next three terms must be subtracted, and consist of (3,1) times (2,2) times (1,3), then (3,2) times (2,3) times (1,1), and finally (3,3) times (2,1) times (1,2). Thus (2.7) can be rewritten as follows:

$$\nabla \times \mathbf{A} = \left(\frac{\partial A_z}{\partial y} - \frac{\partial A_y}{\partial z} \right) \mathbf{u}_x + \left(\frac{\partial A_x}{\partial z} - \frac{\partial A_z}{\partial x} \right) \mathbf{u}_y + \left(\frac{\partial A_y}{\partial x} - \frac{\partial A_x}{\partial y} \right) \mathbf{u}_z \quad (2.8)$$

Besides the rectangular (x, y, z) coordinates analyzed above, engineers often use cylindrical coordinates or spherical coordinates. In cylindrical and spherical coordinates there are differences in the gradient, divergence, and curl equations.

In general, curl is analogous to a wheel that rotates, and thus curl is sometimes called *rot*. Figure 2.3 shows a water wheel and its curl. The wheel has paddles and is rotated by a stream of water. The stream may either be a river (mill stream) or may be a diversion channel inside a dam. Note that the wheel has curl (rotation) about its z axis because its velocities vary with position. Plots of the x and y components of velocity \mathbf{v} are shown as functions of y and x , respectively. The partial derivatives of (2.8) produce a z component of curl. The partial of velocity component v_y with respect to x gives a positive contribution, and the negative partial of v_x with respect to y also gives a positive contribution, resulting in a curl of \mathbf{v} with a large positive z component. Thus the curl is directed along the axis of rotation.

Figure 2.2 also indicates a relation between curl and the integral all around the circular path on the surface of the wheel. The velocity follows the outer circular path. The integral is called the *circulation*. In the next section, Stokes’ law will mathematically define the relation between circulation and curl.

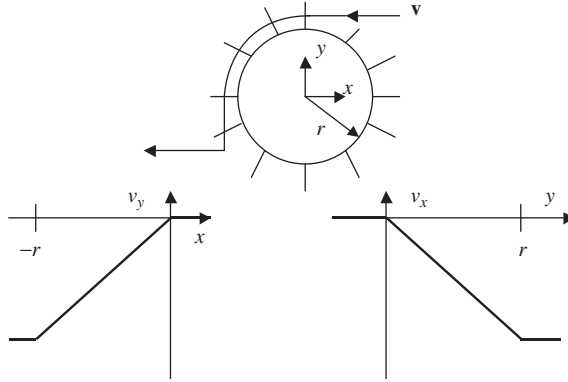


Figure 2.3 A rotating wheel is analogous to curl.

Example 2.2 Divergence and Curl of Vector Find the divergence and curl at location $(3, 2, -1)$ of the vector:

$$\mathbf{A} = [8x^4 + 6(y^2 - 2)]\mathbf{u}_x + [9x + 10y + 11z]\mathbf{u}_y + [4x]\mathbf{u}_z \quad (\text{E2.2.1})$$

Solution: You must first find the expressions for divergence and curl, and then evaluate them at the desired location.

In finding the divergence using (2.5), only partial derivatives of *like variables* (such as x with respect to x) are involved. Thus we obtain

$$\nabla \cdot \mathbf{A} = \frac{\partial A_x}{\partial x} + \frac{\partial A_y}{\partial y} + \frac{\partial A_z}{\partial z} = \frac{\partial [8x^4 + 6(y^2 - 2)]}{\partial x} + \frac{\partial [9x + 10y + 11z]}{\partial y} + \frac{\partial [4x]}{\partial z} \quad (\text{E2.2.2})$$

Again, the partial (derivative) with respect to x treats y and z as constants, the partial with respect to y treats x and z as constants, and the partial with respect to z treats x and y as constants. Thus we obtain for the divergence expression

$$\nabla \cdot \mathbf{A} = \frac{\partial [8x^4]}{\partial x} + \frac{\partial [10y]}{\partial y} + \frac{\partial [0]}{\partial z} = 32x^3 + 10 \quad (\text{E2.2.3})$$

which, evaluated at $(3, 2, -1)$, gives 874. Recall that the divergence is always a scalar.

In finding the curl using (2.8), only partial derivatives of *unlike variables* (such as y with respect to x) are involved. Thus from (2.8) we obtain

$$\begin{aligned} \nabla \times \mathbf{A} = & \left(\frac{\partial [4x]}{\partial y} - \frac{\partial [9x + 10y + 11z]}{\partial z} \right) \mathbf{u}_x + \left(\frac{\partial [8x^4 + 6y^2 - 12]}{\partial z} - \frac{\partial [4x]}{\partial x} \right) \mathbf{u}_y \\ & + \left(\frac{\partial [9x + 10y + 11z]}{\partial x} - \frac{\partial [8x^4 + 6y^2 - 12]}{\partial y} \right) \mathbf{u}_z \end{aligned} \quad (\text{E2.2.4})$$

Again, since partials of unlike variables are zero, a simplified equation is obtained

$$\nabla \times \mathbf{A} = \left(\frac{\partial[0]}{\partial y} - \frac{\partial[11z]}{\partial z} \right) \mathbf{u}_x + \left(\frac{\partial[0]}{\partial z} - \frac{\partial[4x]}{\partial x} \right) \mathbf{u}_y + \left(\frac{\partial[9x]}{\partial x} - \frac{\partial[6y^2]}{\partial y} \right) \mathbf{u}_z \quad (\text{E2.2.5})$$

which yields the curl expression:

$$\nabla \times \mathbf{A} = (-11)\mathbf{u}_x + (-4)\mathbf{u}_y + (9 - 12y)\mathbf{u}_z \quad (\text{E2.2.6})$$

Substituting the point (3,2,-1) yields the final answer:

$$\nabla \times \mathbf{A} = (-11)\mathbf{u}_x + (-4)\mathbf{u}_y + (-15)\mathbf{u}_z \quad (\text{E2.2.7})$$

2.2 AMPERE'S LAW

With the background in vector operations presented above, the fundamental source of magnetic fields can now be presented. The origin of magnetic fields is expressed by Ampere's law, named after André-Marie Ampere of France.

Ampere's law at any point in space states that the curl of static magnetic field intensity \mathbf{H} equals current density \mathbf{J}

$$\nabla \times \mathbf{H} = \mathbf{J} \quad (2.9)$$

where \mathbf{H} is magnetic field intensity in amperes per meter, and current density \mathbf{J} is in amperes per square meter. These units are SI, and will be used throughout this book as listed in the Appendix.

In air, related to \mathbf{H} is magnetic flux density \mathbf{B} by

$$\mathbf{B} = \mu_0 \mathbf{H} \quad (2.10)$$

where \mathbf{B} is magnetic flux density in teslas and μ_0 is the permeability of free space (vacuum) or air. The unit tesla has the symbol T and is named after renowned American inventor Nikola Tesla. One tesla (1 T) equals one weber per square meter (Wb/m^2). The value $\mu_0 = 12.57 \times 10^{-7}$ henrys per meter ($12.57 \text{ E} - 7 \text{ H/m}$). Thus in air, vector \mathbf{B} equals vector \mathbf{H} multiplied by a very small number. Often in this book and other books, \mathbf{B} is simply called the *magnetic field*. A *field* in this context is any quantity that can vary over space, and \mathbf{B} is a vector field.

Because the curl of \mathbf{H} equals \mathbf{J} , \mathbf{H} "circles" around an axis consisting of current much as the wheel circles around its axis in Fig. 2.3. Another way to express Ampere's Law of (2.9) is to integrate it over a surface \mathbf{S} to obtain

$$\int (\nabla \times \mathbf{H}) \cdot d\mathbf{S} = \int \mathbf{J} \cdot d\mathbf{S} \quad (2.11)$$

The units of both sides of this equation are amperes. The surface \mathbf{S} is a vector with direction normal (perpendicular) and magnitude equal to the surface area.

There is a purely mathematical vector identity that can be used to replace the surface integral of the curl in the left side of (2.11). As mentioned at the end of the preceding section, Stokes' law replaces the surface integral by a *closed* path (or line) integral, giving the most common expression for Ampere's law in integral form:

$$\oint \mathbf{H} \cdot d\mathbf{l} = \int \mathbf{J} \cdot d\mathbf{S} = NI \quad (2.12)$$

where \mathbf{l} is the vector pathlength in meters, and the path being closed is indicated by the circle on the integral sign. Note that the total current, the surface integral of current density, can also be written as the product of current I times the number of conductors N carrying that current. To create large \mathbf{H} and \mathbf{B} with reasonably small current I values, often a coil winding with many conductors (or turns) N is used in magnetic devices.

While \mathbf{B} is magnetic flux density, its integral over any surface \mathbf{S} is called *magnetic flux*. Flux is the Latin word for the English word *flow*, and magnetic flux flows around much like other fluids such as water. Since the SI units of \mathbf{B} are teslas or webers per square meter, magnetic flux has units of webers. Using ϕ for flux, the surface integral can be written as

$$\phi = \int \mathbf{B} \cdot d\mathbf{S} \quad (2.13)$$

An important property of magnetic flux is that if \mathbf{S} is a *closed* surface, such as a spherical surface or any surface that completely encloses a volume, then the total magnetic flux through the closed surface is zero. A closed surface integral is indicated by a circle on the integral sign, and thus flux through a closed surface obeys the following formula:

$$\phi_c = \oint \mathbf{B} \cdot d\mathbf{S} = 0 \quad (2.14)$$

Since divergence has been previously defined as the net output flux per unit volume, the zero flux of (2.14) applied to a tiny volume and its closed surface means that

$$\nabla \cdot \mathbf{B} = 0 \quad (2.15)$$

Thus magnetic flux density is always divergenceless. Since the total magnetic flux through any closed surface is zero, magnetic flux flows in a manner similar to that for an incompressible fluid. In air, since $\mathbf{B} = \mu_0 \mathbf{H}$, both \mathbf{B} and \mathbf{H} must both “circle around” the “axis” of a current-carrying wire.

Example 2.3 Ampere's Law at a Point and along a Closed Path Apply Ampere's law to two situations:

- (a) Given the magnetic field intensity expression in space (in amperes per meter),

$$\mathbf{H} = [8x^4 + 6(y^2 - 2)]\mathbf{u}_x + [9x + 10y + 11z]\mathbf{u}_y + [4x]\mathbf{u}_z \quad (\text{E2.3.1})$$

Find the expression for current density \mathbf{J} at location (2,4,6).

- (b) Given a region of four conductors, each carrying current $I = 5$ A outward. As shown in Fig. E2.3.1, two closed paths are defined, \mathbf{l}_1 and \mathbf{l}_2 . Find the integral of \mathbf{H} along each of the closed paths.

Solution

- (a) The current density \mathbf{J} at any point is the curl of \mathbf{H} at that point. The \mathbf{H} expression (E2.3.1) is recognized as identical to (E2.2.1) for \mathbf{A} , for which the curl has already been found. Thus

$$\mathbf{J} = \nabla \times \mathbf{H} = (-11)\mathbf{u}_x + (-4)\mathbf{u}_y + (9 - 12y)\mathbf{u}_z \quad (\text{E2.3.2})$$

which, evaluated at (2,4,6), gives

$$\mathbf{J} = (-11)\mathbf{u}_x + (-4)\mathbf{u}_y + (-39)\mathbf{u}_z \quad (\text{E2.3.3})$$

in amperes per square meter.

- (b) Both the number of conductors and their individual currents are known. Their product $NI = 20$ A, since the number N is dimensionless. Since both closed paths enclose all conductors, the integral of \mathbf{H} along each of the closed paths equals 20 A.

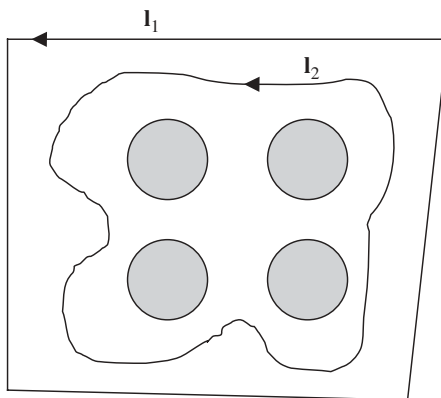


Figure E2.3.1 Two closed paths adjacent to a current-carrying region.

2.3 MAGNETIC MATERIALS

The main magnetic property that can vary among materials is permeability. The permeability of free space (vacuum), μ_0 , is also applicable in air. Also, many other materials, including copper and aluminum, have free space permeability μ_0 .

The general symbol for permeability is μ , and materials with permeability other than μ_0 are often expressed in terms of relative permeability μ_r , defined using

$$\mu = \mu_r \mu_0 \quad (2.16)$$

where we recall that $\mu_0 = 12.57\text{E-}7$ H/m. Several materials have $\mu_r \gg 1$ and thus are much more permeable than air. *Permeability* is another word common to both magnetism and fluid flow. Highly fluid-permeable earth, such as sand, conducts water flow much better than does low-fluid-permeable rock. Thus magnetic flux, like fluids, prefers to flow in materials of high permeability.

Magnetic materials with high relative permeability μ_r are said to be magnetically *soft*. The most common soft magnetic materials are *ferromagnetics*, including iron (Fe or ferrous material), nickel (Ni), and cobalt (Co). Besides these three pure elements, alloys containing these elements are usually also ferromagnetic with high permeability. The most common ferromagnetic alloys are steels, which contain both iron and carbon. The relative permeability of typical steel is often on the order of 2000. Steel is often used as the main inner or *core* material of magnetic devices.

The reason for the high permeability of certain materials is that they contain many *magnetic domains*. Each domain has \mathbf{B} in a particular direction created by its atomic electron spins. As \mathbf{H} is applied and increased, more domains rotate and/or expand in the direction of \mathbf{H} . Each domain is of size as large as $0.1 \text{ mm} = 100 \text{ }\mu\text{m}$ (micrometers) [1]. Since permeability is a macroscopic or average number over all domains, it applies only for materials with at least one dimension approximately $100 \text{ }\mu\text{m}$. The macroscopic concept of permeability therefore does not apply for material samples of nanometer dimensions in all three directions. Often nanotechnology relies instead on microscopic effects such as those of quantum mechanics, which is not covered in this book.

As an example of the effect of permeability on magnetic field \mathbf{B} , Fig. 2.4 shows the application of Ampere's law to a single circular wire carrying current I . Ampere's law and material permeability are used here to find \mathbf{B} at any location of radius $r > r_w$, the wire radius. First, Ampere's law over the closed path of radius r completely enclosing the current I gives

$$\oint \mathbf{H} \cdot d\mathbf{l} = 2\pi r H = I \quad (2.17)$$

Note that the closed-path integral can be replaced by the pathlength $2\pi r$ times a scalar constant H , the magnitude of the magnetic field intensity, because symmetry requires the field to be independent of angular position, that is, to be a constant magnitude at any given radius. The direction of \mathbf{H} must circle around the current as

shown in Fig. 2.4. Such a peripheral direction is usually called a *circumferential polar direction* \mathbf{u}_ϕ . The direction follows the *right-hand rule*: For your right-hand thumb pointing in the direction of the current, the direction of \mathbf{H} circles around in the direction of the right-hand fingers. Then, solving (2.17) gives the magnitude:

$$H = \frac{I}{2\pi r} \quad (2.18)$$

Finally, the magnetic flux density \mathbf{B} is found by multiplying \mathbf{H} by permeability μ of the material surrounding the wire. If the material is air, then the flux density magnitude is

$$B = \mu_0 H = \mu_0 I / (2\pi r) \quad (2.19)$$

Note that the magnetic field is inversely proportional to radius from the current, assuming that the radius is no smaller than the wire radius.

If the material surrounding the wire is steel of relative permeability 2000, then the flux density magnitude is increased to

$$B = \mu_r \mu_0 H = 2000 \mu_0 I / (2\pi r) \quad (2.20)$$

Note that the direction of \mathbf{B} is the same as the direction of \mathbf{H} , which is true for all materials except *anisotropic* (directionally dependent) magnetic materials. Air and many ferromagnetic materials are magnetically *isotropic* with a scalar permeability. Anisotropic magnetic materials require a tensor permeability, which is not discussed in this book but has been investigated elsewhere [2,3]. Tensor material properties are also discussed in Chapter 10.

An important property of magnetic permeability, to be discussed next, is the *nonlinear B–H curve*. Such nonlinearity is exhibited by all ferromagnetic materials. Their high relative permeability, such as the 2000 assumed in (2.20), is applicable only for low values of flux density. For high values of flux density, *saturation* is said to occur. Flux no longer flows as easily, similar to a towel that becomes saturated with water and no longer picks up as much liquid. The ratio B/H gradually de-

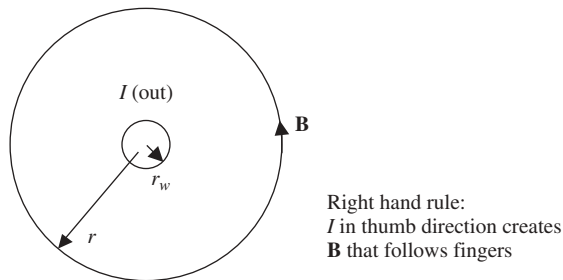


Figure 2.4 Magnetic field of a wire found using Ampere's law.

creases, and thus the permeability is no longer a constant. Figure 2.5 shows a typical nonlinear B – H curve for steel. It is customarily plotted with H along the horizontal axis. Note that in the neighborhood of 1.5 T or so, the curve has a “knee” that transitions to a much flatter slope. The *incremental permeability*, defined as the slope, gradually decreases to the permeability of free space. Usually the slope equals μ_0 at a *saturation flux density* somewhat above 2 T.

To obtain B – H curves, steel suppliers and other sources can be consulted. While their curves are often in the SI units of teslas and amperes per meter, sometimes they are expressed in CGS (centimeter–gram–second) units instead. For flux density B values given in gauss (G), multiply by $1\text{E-}4$ to obtain teslas. For field intensity H values in oersteds (Oe), multiply by 79.577 to obtain amperes per meter. Steel suppliers can provide better B – H curves (with higher permeabilities) with more expensive heat treatment such as annealing (heating followed by very slow cooling) and by adding alloy materials such as Co.

A useful approximate expression for steel B – H curves uses three constants [4]:

$$H = (k_1 e^{k_2 B^2} + k_3) \quad (2.21)$$

Values of these three constants are listed in Table 2.1 for typical types of steel. Cast steel is cast or forged into its desired shape. Cold-rolled steel has been formed into a thin sheet in a steel rolling mill at typical room temperature. Annealed steel has been heat-treated, where annealing involves high-temperature heating often in low-oxygen atmospheres, followed by slow cooling. The annealing temperature, length of time, atmosphere, cooling process, and other details all can significantly affect the B – H curve. The B – H relation also may actually be a set of multiple curves depending on history of applied H ; such *hard magnetic* materials will be discussed in the Chapter 5. Mechanical hardness also tends to follow the magnetic hardness (or softness) of materials. However, hard magnetic materials often are brittle, not nearly as mechanically strong as steel.

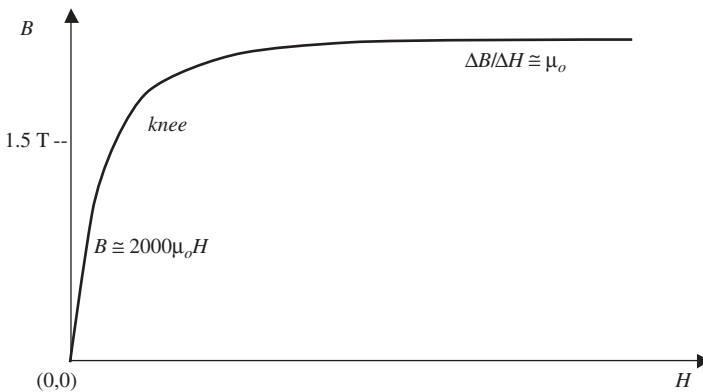


Figure 2.5 Typical nonlinear magnetization curve of steel.

TABLE 2.1 Constants for B – H Curves of Three Typical Types of Steel

	k_1	k_2	k_3
Cast	49.4	1.46	520.6
Cold-rolled	3.8	2.17	396.3
Annealed	2.6	2.72	154.4

Another important property of magnetic materials is their electrical conductivity. Air has zero electrical conductivity (except in special cases such as lightning), but ferromagnetic materials usually have high electrical conductivities. To see why electrical conductivity is important, Faraday’s law must be presented.

Example 2.4 Magnetic Flux Density in Various Materials Surrounding a Wire

- (a) A copper wire of radius 1 mm is placed at location (1,0,0) meters, carrying a current of 100 kA (kiloamperes) in the $+z$ direction. Find the vector \mathbf{B} at location (3,0,0) for the wire embedded in the following materials that extend infinitely far in all three directions: (1) air, (2) steel with constant relative permeability = 2500, and (3) steel with a B – H curve with the following (B,H) values: (0,0), (1.5,1000), (1.8, 7958), . . .
- (b) Repeat this sequence assuming that the current direction is reversed to the $-z$ direction.

Solution

- (a) The radius from (1,0,0) to (3,0,0) is 2 m. From the right-hand rule, the direction of \mathbf{B} is in the $+y$ direction. From (2.20), the magnitude is

$$B = \mu_r \mu_0 I / (2\pi r) = \mu_r (12.57\text{E-}7)(100\text{E}3) / (4\pi) = \mu_r (1\text{E-}3) \quad (\text{E2.4.1})$$

- (1) Thus for air, $\mathbf{B} = 1\text{E-}3$ tesla \mathbf{u}_y
(2) For steel with relative permeability = 2500, $\mathbf{B} = 2.5$ T \mathbf{u}_y
(3) For steel with the nonlinear B – H curve

$$H = I / (2\pi r) = 1\text{E}5 / (4\pi) = 7958 \text{ A/m} \quad (\text{E2.4.2})$$

From the (B,H) curve, the corresponding flux density $\mathbf{B} = 1.8$ tesla \mathbf{u}_y

- (b) When the current direction is reversed in the three cases above, the right-hand rule shows that the direction of \mathbf{B} changes to $-\mathbf{u}_y$.

2.4 FARADAY’S LAW

Following Ampere’s law in importance for magnetic devices is Faraday’s law. It was discovered by Michael Faraday of England. While Ampere’s law deals primarily with current, Faraday’s law deals primarily with voltage.

Faraday's law at any point in space equates the negative partial time derivative of \mathbf{B} with the curl of the electric field intensity \mathbf{E}

$$\nabla \times \mathbf{E} = -\frac{\partial \mathbf{B}}{\partial t} \quad (2.22)$$

where \mathbf{E} is in volts per meter. The line or path integral of \mathbf{E} is the negative of voltage V_1 :

$$V_1 = -\int \mathbf{E} \cdot d\mathbf{l} \quad (2.23)$$

Taking the integral of both sides of (2.22) over any unchanging surface \mathbf{S} gives

$$\int (\nabla \times \mathbf{E}) \cdot d\mathbf{S} = -\frac{\partial}{\partial t} \int \mathbf{B} \cdot d\mathbf{S} \quad (2.24)$$

As for Ampere's law in integral form, Stokes' law can be used to replace the surface integral of curl by a closed-line integral. Thus (2.23) becomes

$$\oint \mathbf{E} \cdot d\mathbf{l} = -\frac{\partial}{\partial t} \int \mathbf{B} \cdot d\mathbf{S} \quad (2.25)$$

which is Faraday's law in integral form. The electric field (intensity) is *induced* by a time varying magnetic field (flux density).

As previously mentioned, often magnetic devices have N conductors, usually arranged in coils of wire with N turns. The voltage induced in such a coil is N times that of one turn, and thus from (2.23) the coil voltage V is

$$V = -N \oint \mathbf{E} \cdot d\mathbf{l} \quad (2.26)$$

where the line integral is over the closed path of one turn. Finally, multiplying both sides of (2.25) by N and using (2.26) gives the expression for induced coil voltage:

$$V = -N \frac{\partial}{\partial t} \int \mathbf{B} \cdot d\mathbf{S} \quad (2.27)$$

Recall from (2.13) that the surface integral of flux density is flux, giving

$$V = -N \frac{\partial \phi}{\partial t} \quad (2.28)$$

This form of Faraday's law states that voltage is $(-N)$ times the time rate of change of magnetic flux. Note that the flux in a stationary coil must change with time in order for voltage to be induced.

Assuming that the number of turns does not change with time, another expression of Faraday's law is

$$V = -\frac{\partial \lambda}{\partial t} \quad (2.29)$$

where λ is *flux linkage*, which is defined by

$$\lambda = N\phi \quad (2.30)$$

If a conductor moves with a velocity \mathbf{v} through a magnetic flux density \mathbf{B} , Faraday's law shows that a *motional electric field* is induced given by

$$\mathbf{E}_{\text{motion}} = \mathbf{v} \times \mathbf{B} \quad (2.31)$$

The motionally induced voltage is found by the line integral of (2.23). Note that a motional voltage can be produced even by a constant (DC) magnetic flux density.

Since a voltage is induced by a time-varying magnetic field, current I may also flow according to Ohm's law of electric circuits

$$I = V/R \quad (2.32)$$

where R is resistance in ohms, named after Georg Ohm of Germany. Another form of Ohm's law is for fields:

$$\mathbf{J} = \sigma \mathbf{E} \quad (2.33)$$

where σ is electrical conductivity in the reciprocal of ohm-meters, also expressed as siemens per meter (S/m). The reciprocal of conductivity is resistivity ρ in ohm-meters.

If \mathbf{E} is induced by magnetic fields, then the current density \mathbf{J} is also said to be induced. Induced current densities and induced currents occur in many magnetic devices with time-varying magnetic fields. These induced currents can be either desirable or undesirable.

A prime example of desirable induced current is the current in the secondary (or output) coil of a transformer. Transformers produce secondary voltage and current from Faraday's law as long as the primary (input) coil voltage and current are time-varying. Usually the primary voltage and current are AC sinusoids, producing from Ampere's law a time-varying magnetic field and flux. The flux *links* or passes through both the primary and secondary windings. Faraday's law states that this flux induces a secondary voltage and current whose magnitudes depend on the number of secondary turns. Thus transformers produce useful induced currents. The induced currents produce their own flux (from Ampere's law), which can be shown to oppose the original primary magnetic flux according to Lenz' law, a corollary of Faraday's law.

Induced currents may also be undesirable. For example, the transformer described above with its desirable secondary induced current may also have undesirable induced currents in other parts. The transformer is customarily surrounded by a steel case to confine its magnetic fields, and steel has high electrical conductivity. Typical steel conductivities range from about $5E5$ S/m to $1.E7$ S/m. The lower values are for steels with high silicon content. Because of the high steel conductivity, the transformer housing often contains induced *eddy* currents, the name derived from their flow patterns, which somewhat resemble the eddy patterns of turbulent rivers. The housing eddy currents are of no use and consume power (the product of voltage and current). They also produce heating. Thus eddy currents are usually undesirable.

A common way to reduce eddy currents in steel (or other conductive materials) is to *lamine*. Figure 2.6 shows typical steel *laminations*, or thin sheets. Because of the thin airspaces, surface oxidation, and/or surface treatments, electric current cannot flow from one lamination to another. Instead, any eddy currents are confined to flow within each lamination. Thus steel eddy current loss, often given in watts per cubic meter, is usually greatly reduced by using laminations.

Alternatives to steel laminations are *ferrites* and *composites*. Both have much lower conductivities than does steel, on the order of 1 S/m. However, their B - H curves are poorer than those of most steels. Ferrites saturate at only about 0.4 T. Composites, made of iron powder and insulating binders, have relative permeability of only a few hundred [5].

Eddy currents and their effects will be considered in detail in Chapters 6–16.

Example 2.5 Induced Voltage and Current

- (a) A coil called the *primary coil* establishes the magnetic flux density $B = 1.1 \sin(2\pi ft) \mathbf{u}_z$ teslas. The frequency $f = 60$ Hz. A secondary coil is of thin uniform copper (conductivity $5.8E7$ S/m) wire and has resistance $R = 2 \Omega$. Assume $I = V/R$ and that the magnetic field is not changed by the secondary

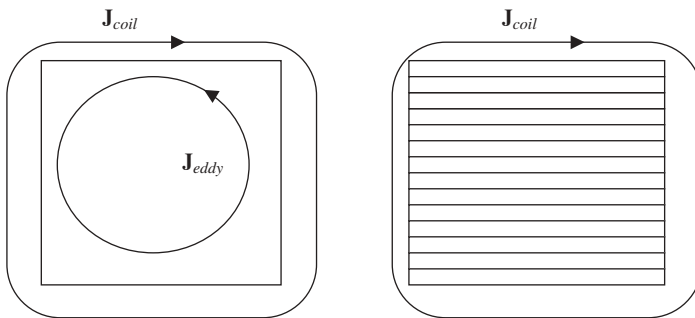


Figure 2.6 Comparison of eddy current flow patterns in conductive steel without and with laminations. Due to Lenz' law, the eddy currents tend to flow in the direction opposing the applied coil current.

current. The secondary coil is square in shape, connecting the points $(x,y,z) = (0,0,0), (0.5 \text{ m},0,0), (0.5 \text{ m},0.6 \text{ m},0), (0,0.6 \text{ m},0)$ and back to the origin, with a total of 50 turns. Find the voltage and the current induced in the secondary, including their polarities (directions). Also find both \mathbf{E} and \mathbf{J} in the wire.

(b) Repeat for frequency $f = 50 \text{ Hz}$.

Solution

(a) The coil has turns $N = 50$ and area $A = (0.5 \text{ m})(0.6 \text{ m}) = 0.3 \text{ square meters (m}^2\text{)}$. Faraday's law gives

$$\begin{aligned} V &= -NA \frac{\partial B}{\partial t} = -50(0.3) \frac{\partial}{\partial t} (1.1 \sin 377t) = -15(1.1)(377) \cos 377t \\ &= -6221 \cos(2\pi 60t) \end{aligned}$$

This negative voltage has polarity following the right-hand rule, which is counterclockwise when viewed from the $+z$ axis.

The secondary current is the voltage divided by 2Ω , or $-3111 \cos(2\pi 60t)$ amperes. The electric field is the voltage divided by the wire length; the wire length is $(50)(1 \text{ m} + 1.2 \text{ m}) = 110 \text{ m}$. Thus the electric field is $-56.55 \cos(2\pi 60t)$ volts per meter, directed around the loop in the same direction as the current. To find the current density, multiply by the conductivity $5.8\text{E}7 \text{ S/m}$, giving $3.28\text{E}9 \text{ A/m}^2$ in the same direction as the current.

(b) The lower frequency changes both frequency and amplitude of the secondary voltage and current. The voltage becomes $-5184 \cos(2\pi 50t)$ volts, and the current is $-2592 \cos(\pi 50t)$ amperes. The electric field is $-47.13 \cos(2\pi 50t)$ volts per meter, and the current density is $2.73\text{E}9 \text{ A/m}^2$. Directions and polarities do not change.

2.5 POTENTIALS

Potentials are very useful in electrical engineering. The most common example is voltage, which is a scalar, not a vector.

DC or static electric field is the negative gradient of electrostatic scalar potential, denoted here as ϕ_v

$$\mathbf{E} = -\nabla \phi_v \quad (2.34)$$

where ϕ_v has units of volts. For time-varying fields, the induced electric field of Faraday's law must also be added.

Similar to magnetic flux density, there is an electric flux density \mathbf{D} (in units of coulombs per square meter) defined by

$$\mathbf{D} = \epsilon \mathbf{E} \quad (2.35)$$

where ε is permittivity in farads per meter, a material property. Air and vacuum have $\varepsilon = \varepsilon_0 = 8.854\text{E-}12$ F/m.

Materials with permittivity other than ε_0 are often expressed in terms of relative permittivity ε_r defined using

$$\varepsilon = \varepsilon_r \varepsilon_0 \quad (2.36)$$

Another common term for relative permittivity is dielectric constant.

There is an important relation between \mathbf{D} and electric charge density

$$\nabla \cdot \mathbf{D} = \rho_v \quad (2.37)$$

where ρ_v is electric charge density per unit volume in units of coulombs per cubic meter.

The relation between electric scalar potential, electric field, and charge is illustrated in the capacitor shown in Fig. 2.7. The capacitor consists of two metal plates spaced one meter apart in air. Because they are made of high-conductivity copper or aluminum, there is essentially zero voltage drop along either plate. The lower plate at $y = 0$ is grounded, that is, set to 0 V. The upper plate at $y = 1$ is attached to a 1-V DC battery. Thus the expression for the electric scalar potential in volts in Fig. 2.7 is $\phi_v = y$ volts. Substituting into (2.34) gives

$$\mathbf{E} = -\nabla y = -\frac{\partial y}{\partial x} \mathbf{u}_x - \frac{\partial y}{\partial y} \mathbf{u}_y - \frac{\partial y}{\partial z} \mathbf{u}_z = -1 \mathbf{u}_y \text{ V/m} \quad (2.38)$$

Note that the electric field in Fig. 2.7 points from high scalar potential in volts to low scalar potential. Since \mathbf{D} is \mathbf{E} times the permittivity of air, and from (2.37) is *not* divergenceless, both \mathbf{D} and \mathbf{E} terminate on the plates, which contain electric

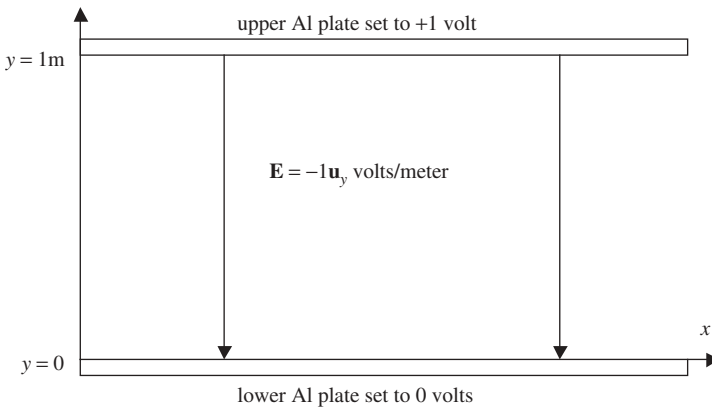


Figure 2.7 Two plates of a capacitor spaced 1 m apart and with 1 V DC applied.

charge. Unlike magnetic flux lines, which must always “circle” because of their divergencelessness, the electric flux lines of Fig. 2.7 can terminate or stop.

For magnetic fields, the potential required is a vector, not a scalar. Magnetic vector potential \mathbf{A} is defined using

$$\mathbf{B} = \nabla \times \mathbf{A} \quad (2.39)$$

Substituting into Faraday’s law at a point (2.22) gives

$$\nabla \times \mathbf{E} = -\frac{\partial}{\partial t}(\nabla \times \mathbf{A}) = -\left(\nabla \times \frac{\partial \mathbf{A}}{\partial t}\right) \quad (2.40)$$

where the \mathbf{E} is the induced electric field intensity:

$$\mathbf{E}_{\text{ind}} = -\frac{\partial \mathbf{A}}{\partial t} \quad (2.41)$$

Adding this induced electric field to the electric field due to electric scalar potential of (2.34) gives the total electric field expression:

$$\mathbf{E} = -\nabla \phi_v - \frac{\partial \mathbf{A}}{\partial t} \quad (2.42)$$

Example 2.6 Fields from Potentials Given the following potentials in a region, find its fields \mathbf{B} and \mathbf{E} :

$$\phi_v = 2x, \quad \mathbf{A} = 0.2y \sin(2\pi 60t) \mathbf{u}_z$$

Solution

$$\mathbf{B} = \nabla \times \mathbf{A} = (\nabla \times 0.2y \mathbf{u}_z) \sin(2\pi 60t) = \frac{\partial(0.2y)}{\partial y} \mathbf{u}_x (\sin 2\pi 60t) = 0.2 \sin(2\pi 60t) \mathbf{u}_x$$

$$\mathbf{E} = -\nabla \phi_v - \frac{\partial \mathbf{A}}{\partial t} = -2\mathbf{u}_x - (0.2)(2\pi 60) \cos(2\pi 60t) \mathbf{u}_z$$

2.6 MAXWELL’S EQUATIONS

James Clerk Maxwell of Scotland summarized all electromagnetics in four equations. Expressed in point form, they are:

$$\nabla \cdot \mathbf{B} = 0 \quad (2.43)$$

$$\nabla \cdot \mathbf{D} = \rho_v \quad (2.44)$$

$$\nabla \times \mathbf{E} = -\frac{\partial \mathbf{B}}{\partial t} \quad (2.45)$$

$$\nabla \times \mathbf{H} = \mathbf{J} + \frac{\partial \mathbf{D}}{\partial t} \quad (2.46)$$

These four equations need not appear in any particular order. As listed above, the first three were given earlier in this chapter: (2.43) expresses the continuity of magnetic flux, (2.44) expresses that electric flux terminates on charge, and (2.45) expresses Faraday's law. Note that the final equation, (2.46), is Ampere's law, which has been enhanced by an additional term on its right-hand side. The additional term is called *displacement current density*:

$$\mathbf{J}_{\text{disp}} = \frac{\partial \mathbf{D}}{\partial t} \quad (2.47)$$

Displacement current density and its surface integral, displacement current, only exist for time-varying fields. Examples of displacement current include current through capacitors and coupled high frequency electromagnetic fields. Coupled electromagnetic fields [6] often range in frequency from 1 MHz to over 1 GHz, and are discussed further in Chapter 13.

Maxwell's equations can also be written in integral form by integrating the preceding four differential Maxwell equations, obtaining respectively

$$\oint \mathbf{B} \cdot d\mathbf{S} = 0 \quad (2.48)$$

$$\oint \mathbf{D} \cdot d\mathbf{S} = \int \rho_v dV \quad (2.49)$$

$$\oint \mathbf{E} \cdot d\mathbf{l} = -\frac{\partial}{\partial t} \int \mathbf{B} \cdot d\mathbf{S} \quad (2.50)$$

$$\oint \mathbf{H} \cdot d\mathbf{l} = \int \left(\mathbf{J} + \frac{\partial \mathbf{D}}{\partial t} \right) \cdot d\mathbf{S} \quad (2.51)$$

This entire chapter is summarized by the preceding Maxwell equations. Now that they are known and understood, their application to real-world problems can begin in the next chapter.

Example 2.7 Displacement Current in a Capacitor The parallel-plate capacitor of Fig. E2.7.1 has the following electric field \mathbf{E} between its plates

$$\mathbf{E} = 2500 \sin(2\pi 60t) \mathbf{u}_y \text{ V/m}$$

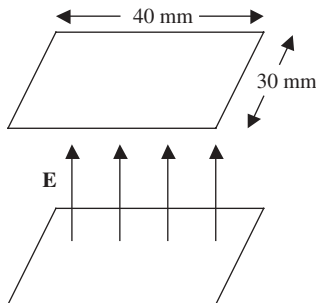


Figure E2.7.1 A capacitor made of two 30×40 -mm plates spaced by 10 mm and with a known AC electric field intensity.

where y is directed between the plates, which are separated by 50 mm of air. Each plate is of area 40×30 mm. Find the displacement current density and the total current in the capacitor.

Solution

$$\begin{aligned}\mathbf{J}_{\text{disp}} &= \frac{\partial \mathbf{D}}{\partial t} = \epsilon_0 \frac{\partial \mathbf{E}}{\partial t} = (8.854\text{E} - 12)(2\pi 60)(2500)\cos(2\pi 60t)\mathbf{u}_y \\ &= 8.34\text{E} - 6 \cos(2\pi 60t)\mathbf{u}_y\end{aligned}$$

$$I_C = \int \mathbf{J}_{\text{disp}} \cdot d\mathbf{S} = (8.34\text{E} - 6 \cos 377t)(0.04)(0.03) = 1\text{E} - 8 \cos 377t \quad (\text{E2.7.1})$$

2.8 PROBLEMS

- 2.1** A temperature distribution in Cartesian coordinates follows the equation $T(x,y,z) = 10x + 20y^3 + 30z$. Find the expression for the temperature gradient.
- 2.2** A mosquito flies in the direction of maximum rate of change of temperature, thereby seeking warm-blooded animals. If the temperature distribution obeys $T(x,y,z) = 40x + 10y^2 + 30z$ and the mosquito is sitting at location (1 m, 2 m, 3 m), find the direction it will fly.
- 2.3** Find the divergence and curl at location (1,2,-3) of the vector:

$$\mathbf{A} = [8x^4 + 6(y^2 - 2)]\mathbf{u}_x + [9x + 10y + 11z]\mathbf{u}_y + [4x]\mathbf{u}_z$$

- 2.4** Find the divergence and curl at location (2,-3,4) of the vector:

$$\mathbf{A} = [5x^4 + 6(y^3 - 2)]\mathbf{u}_x + [9x + 11y + 12z]\mathbf{u}_y + [4y]\mathbf{u}_z$$

- 2.5 Given the magnetic field intensity expression in space (in amperes per meter)

$$\mathbf{H} = [5x^4 + 6(y^3 - 2)]\mathbf{u}_x + [9x + 11y + 12z]\mathbf{u}_y + [4x]\mathbf{u}_z$$

Find the expression for current density \mathbf{J} at location (2,4,3).

- 2.6 Given a region of 20 conductors, each carrying current $I = 10$ A. As shown in Fig. E2.3.1, two closed paths are defined, \mathbf{l}_1 and \mathbf{l}_2 . Find the integral of \mathbf{H} along each closed path.
- 2.7 A copper wire of radius 2 mm is placed at location (0,3,0) m, carrying a current of 50 kiloamperes in the $+z$ direction. Find the vector \mathbf{B} at location (4,0,0) for the wire embedded in the following materials that extend infinitely far in all three directions: (a) air; (2) steel with constant relative permeability = 2500; (3) steel with a B - H curve with the following (B , H) values: (0,0), (1.5,1000), (1.55,1592), and (1.8, 7958).
- 2.8 Same as the preceding problem, except the current direction is reversed to the $-z$ direction.
- 2.9 A coil called the primary coil establishes the magnetic flux density $\mathbf{B} = 1.0 \sin(2\pi ft) \mathbf{u}_z$ teslas. The frequency $f = 60$ Hz. A secondary coil is of thin uniform aluminum (conductivity $3.54\text{E}7$ S/m) wire and has resistance $R = 4 \Omega$. Assume $I = V/R$ and that the magnetic field is not changed by the secondary current. The secondary coil is square in shape, connecting the points (x,y,z) = (0,0,0), (0.5 m,0,0), (0.5 m,0.6 m,0), (0,0.6 m,0) and back to the origin, with a total of 40 turns. Find the voltage and the current induced in the secondary, including their polarities (directions). Also find both \mathbf{E} and \mathbf{J} in the wire.
- 2.10 Same as preceding problem, except the frequency is changed to 400 Hz.
- 2.11 Given the following potentials in a region, find its fields \mathbf{B} and \mathbf{E} :

$$\phi_v = 4y, \quad \mathbf{A} = 0.2x \sin(2\pi 60t) \mathbf{u}_z$$

- 2.12 Given the following potentials in a region, find its fields \mathbf{B} and \mathbf{E} :

$$\phi_v = 4xy, \quad \mathbf{A} = 0.3x \sin(2\pi 50t) \mathbf{u}_z$$

- 2.13 The parallel-plate capacitor of Fig. 2.7 has the following electric field \mathbf{E} between its plates: $\mathbf{E} = 4500 \sin(2\pi 50t) \mathbf{u}_y$ V/m, where y is directed between the plates, which are separated by 5 mm of air. Each plate is of area 70×50 mm. Find the displacement current density and the total current in the capacitor.
- 2.14 The parallel-plate capacitor of Fig. 2.7 has the following electric field \mathbf{E} between its plates: $\mathbf{E} = 3500 \sin(2\pi 400t) \mathbf{u}_y$ V/m, where y is directed between the plates, which are separated by 8 mm of air. Each plate is of area 40×90 mm. Find the displacement current density and the total current in the capacitor.

REFERENCES

1. C. Kittel, *Introduction to Solid State Physics*, 3rd ed., Wiley, New York, 1967.
2. J. R. Brauer and E. Nakamoto, Finite element analysis of nonlinear anisotropic B-H curves, *Int. J. Appl. Electromagn. Mater.* **3** (1992).
3. J. R. Brauer and F. Hirtenfelder, Anisotropic materials in electromagnetic finite element analysis, *Proc. IEE Int. Conf. Computation in Electromagnetics*, London, Nov. 1991.
4. J. R. Brauer, Simple equations for the magnetization and reluctivity curves of steel, *IEEE Trans. Magn.* **11**: 81 (Jan. 1975).
5. G. L. Skibinski, B. G. Schram, J. R. Brauer, and Z. Badics, Finite element prediction of losses and temperatures of laminated and composite inductors for AC drives, *Proc. IEEE Int. Electric Machines and Drives Conf.*, June 2003.
6. M. Sadiku, *Elements of Electromagnetics*, 3rd ed., Oxford Univ. Press, New York, 2001.

Reluctance Method

The reluctance method is a way of using Ampere's law of the preceding chapter to solve for magnetic fluxes and magnetic fields. Simplifying assumptions must be made, and thus the reluctance method cannot always obtain accurate results. For very simple problems, its results are often reasonably accurate, and can be quickly obtained "on the back of an envelope." Thus it often serves as a first step in the process of designing magnetic actuators and sensors.

3.1 SIMPLIFYING AMPERE'S LAW

The reluctance method begins with Ampere's law in integral form from the preceding chapter

$$\oint \mathbf{H} \cdot d\mathbf{l} = NI \quad (3.1)$$

where ampere-turns NI are assumed given, and magnetic field intensity \mathbf{H} and magnetic flux density \mathbf{B} are to be found. The closed-line integral is replaced by a summation

$$\sum_k H_k l_k = NI \quad (3.2)$$

where the closed path consists of line segments of subscript k , each of which is in the direction of the field intensity. Thus the direction of the field and flux is assumed known. Because flux density \mathbf{B} prefers to flow through high-permeability materials, the line segments (straight or curved) are assumed to follow a path through high-permeability materials such as steel. If the steel has a gap made of air, the closed path follows the shortest part of the airgap.

To account for the permeability of the closed path of (3.2), recall that \mathbf{B} is permeability μ times \mathbf{H} , giving

$$\sum_k (B_k / \mu_k) l_k = NI \quad (3.3)$$

where μ_k is the permeability of path segment k . Next, recall from the preceding chapter that flux is the surface integral of flux density:

$$\phi = \int \mathbf{B} \cdot d\mathbf{S} \quad (3.4)$$

Assuming that each path segment has cross-sectional surface area S_k normal to the segment direction carrying B_k , each segment carries the flux:

$$\phi_k = B_k S_k \quad (3.5)$$

Substituting into (3.3) gives

$$\sum_k [(\phi_k / \mu_k S_k)] l_k = NI \quad (3.6)$$

Recall from the preceding chapter that flux is continuous (because the divergence of flux density is zero). Thus the flux through all segments of (3.6) is the same value, giving

$$\phi \sum_k [(l_k / (\mu_k S_k))] = NI \quad (3.7)$$

The term being summed is called *reluctance*, symbolized by the script letter \mathcal{R} . Thus (3.7) becomes

$$\phi \sum_k \mathcal{R}_k = NI \quad (3.8)$$

Units of reluctance must be amperes per weber; see the Appendix for alternative expression of its units.

From the preceding two equations, *reluctance* is defined as:

$$\mathcal{R} = l / (\mu S) \quad (3.9)$$

If all path reluctances are known, then (3.8) can be used to find the unknown flux:

$$\phi = (NI) / \left(\sum_k \mathcal{R}_k \right) \quad (3.10)$$

With flux known, individual flux densities can be found using (3.5) to give

$$B_k = \phi_k / S_k \quad (3.11)$$

Thus reluctances can be used in the reluctance method to solve for flux and flux density everywhere along the closed flux path. The simplest equation for the reluctance method is a simplification of (3.8)

$$\phi \mathcal{R} = NI \quad (3.12)$$

which is analogous to the familiar Ohm's law of electric circuits:

$$IR = V \quad (3.13)$$

Thus the reluctance method is also called *the magnetic circuit method*. In magnetic circuits, reluctance is analogous to resistance, and flux is analogous to current. The excitation of magnetic circuits is ampere-turns, analogous to voltage. Since voltage is sometimes called *electromotive force* (EMF), NI is sometimes called *magnetomotive force* (MMF). Also, just as any voltage drop in an electric circuit can be called an *EMF drop*, the corresponding drop in a magnetic circuit is an *MMF drop*. Table 3.1 summarizes the analogies between electric and magnetic circuits. Figure 3.1 shows the magnetic circuit parameters.

The reluctance method or magnetic circuit method is also sometimes called the *permeance method*. Permeance is defined as the reciprocal of reluctance

$$\mathcal{P} = 1/\mathcal{R} \quad (3.14)$$

and thus permeance is proportional to permeability.

The reluctance method consists of the following steps:

1. Find the closed flux path (or paths) that “circles” the given ampere-turns NI . This path is usually through high-permeability materials such as steel, but may also contain air segments, which should be as short as possible. The path direction must follow the right-hand rule, where your thumb is in the direction of NI .
2. Find the lengths and cross-sectional areas of all path segments, assuming average values of lengths and the inverses of areas. Also note the permeability of each path segment. For nonlinear materials, assume initially that their permeability is the constant value below their “knee.”
3. Find the reluctance of each path segment using (3.9).
4. Combine the reluctances and use (3.10) or (3.8) to find the flux. Reluctances in series add directly. Reluctances in parallel combine in the same way as do resistances in parallel; the combined value is the reciprocal of the sum of reciprocals.
5. Find the flux density of each path segment using (3.11).

TABLE 3.1 Analogous Parameters of Electric Circuits and Magnetic Circuits.

Parameter	Electric Circuit	Magnetic Circuit
Flow	Current I in amperes (A)	Flux ϕ in webers (Wb)
Potential	EMF in volts (V)	MMF in ampere-turns
Potential/flow	Resistance R in ohms (Ω)	Reluctance \mathcal{R} in A/Wb
Flow/potential	Conductance G in siemens (S)	Permeance \mathcal{P} in Wb/A
Flow density	Current density \mathbf{J} in A/m ²	Flux density \mathbf{B} in teslas (T)

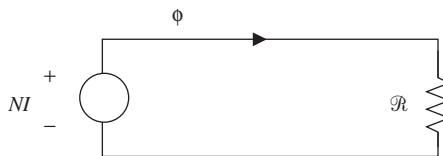


Figure 3.1 Magnetic circuit parameters.

6. If the flux density in any nonlinear material is beyond the knee, then make a new (lower) assumption of its permeability and repeat steps 3, 4, and 5 until the calculated flux densities match the assumed nonlinear permeabilities. For details and various examples consult books such as that by Roters [1].

3.2 APPLICATIONS

Example 3.1 Reluctance Method for “C” Steel Path with Airgap The first example of the reluctance method is shown in Fig. E3.1.1. A “C”-shaped piece of steel of uniform thickness 0.1 m lies in the plane of the paper. The steel is of depth 0.1 m into the page. The opening of the “C” is an air gap of length 0.1 m between the steel poles. (A magnetic *pole* is a surface where magnetic flux leaves to form a north pole or enters to form a south pole.) The object is to find magnetic flux density **B** throughout the steel and airgap produced by the 10,000 ampere-turns directed out of the page in a coil inside the “C” and returning to its left. The steel is assumed to have a relative permeability of 2000.

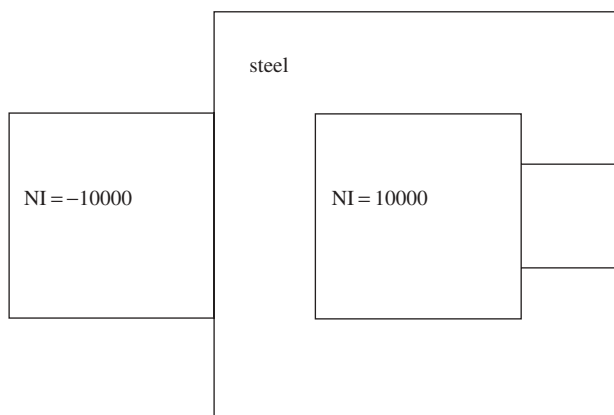


Figure E3.1.1 Steel structure with a single airgap. Each side of the steel “C” core is 0.4 m long and the steel thickness and depth are 0.1 m.

Solution: Follow the six steps at the end of Section 3.1:

1. From the right-hand rule, the flux flows counterclockwise (CCW) around the steel “C” as shown in Fig. E3.1.2. The flux path shown is in the middle of the steel and airgap, and thus is of average length. The longest flux path (not shown) follows the outer surface of the steel, while the shortest flux path follows the interface between the winding and the steel.
2. The steel segment length along the flux path is

$$\ell_{Fe} = (0.4 + 0.4 + 0.4 + 0.15 + 0.15)\text{m} = 1.5\text{ m}$$

The steel segment cross-sectional area is $(0.1\text{ m})(0.1\text{ m}) = 0.01\text{ m}^2$. (At the four corners the area is bigger, but the corners are only a small portion of the steel.) The steel relative permeability is given as 2000. The air segment length, called the airgap, is 0.1 m. The airgap cross-sectional area is $(0.1\text{ m})(0.1\text{ m}) = 0.01\text{ m}^2$. Actually, as will be discussed in the next section, because air extends beyond the steel poles, the flux can expand or “fringe” to a larger area. For now, however, fringing is ignored and hence 0.01 m^2 is assumed. The relative permeability of air (or vacuum) is 1.

3. The reluctances are

$$\mathcal{R}_{Fe} = 1.5 / [(2000)(12.57\text{E} - 7)(0.01)] = 59666 \quad (\text{E3.1.1})$$

$$\mathcal{R}_{air} = 0.1 / [(12.57\text{E} - 7)(0.01)] = 7.955\text{E}6 \quad (\text{E3.1.2})$$

4. The flux obeys the following rule:

$$\phi(59666 + 7.955\text{E}6) = 10000 \quad (\text{E3.1.3})$$

$$\phi = 12.477\text{E} - 4\text{ W} \quad (\text{E3.1.4})$$

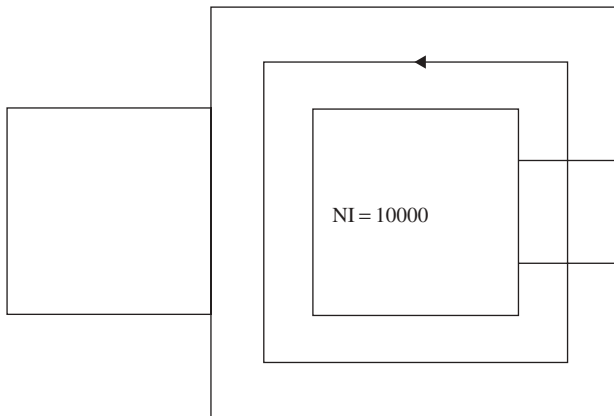


Figure E3.1.2 Flux path of Fig. E3.1.1 following the right-hand rule.

5. Since the cross-sectional area is the same, the flux density is the same everywhere:

$$B = \frac{\phi}{S} = \frac{12.477\text{E} - 4}{1\text{E} - 2} = 0.125 \text{ tesla} \quad (\text{E3.1.5})$$

6. Since this flux density is less than 1.5 T, which is the approximate knee of steel B - H curves, the values calculated above are valid. However, one must remember that all reluctance method calculations are approximate.

Example 3.2 Reluctance Method for Sensor with Variable Airgap The second example of the reluctance method is shown in Fig. E3.2.1. It shows a simplified magnetic sensor with stationary stator and movable armature. Both stator and armature are made of steel; the stator also has a coil made of copper or aluminum. The armature is shown in two positions. In the first position the armature and stator teeth are aligned. In the second position the armature teeth are moved halfway between the stator teeth, so they are as misaligned as possible.

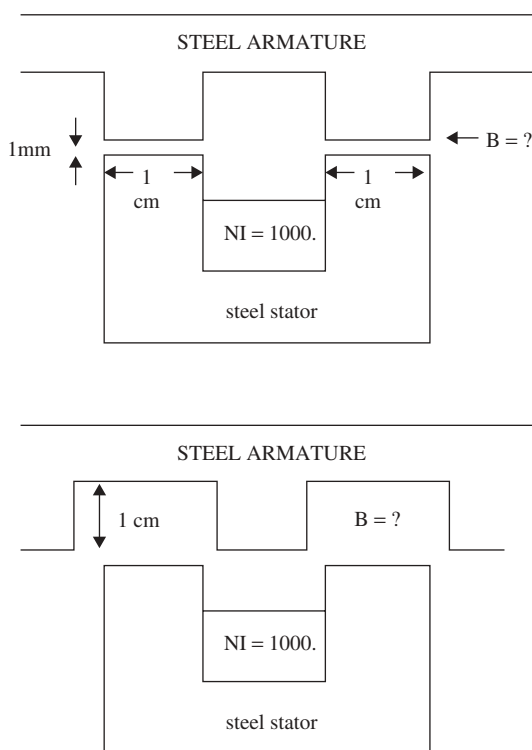


Figure E3.2.1 Portion of simple magnetic sensor.

The stator coil in Fig. E3.2.1 has 1000 ampere-turns. The stator and armature teeth are shown to have width equal to 1 cm. The airgap between stator and rotor teeth is 1 mm when these two components are aligned. In the misaligned position, the airgap is assumed to increase to 1 cm. The depth into the page of the sensor of Fig. E3.2.1 is given as 10 cm.

The steel permeability is given as infinitely high, and thus only airgap reluctances are needed. Hence dimensions of the steel are not given.

The airgap flux densities are to be found for both armature positions in Fig. E3.2.1.

Solution: Follow the six steps at the end of Section 3.1:

1. From the right-hand rule, the flux flows counterclockwise (CCW) around the steel stator “U” shape. It must cross the airgap twice, once entering the armature on its right and then leaving the armature on its left.
2. The air segment length is total air length over the entire closed path and thus equals the right airgap plus the left airgap. Hence in the aligned position the air length is 2 mm, while in the misaligned position the air length is 2 cm = 20 mm.
3. The reluctances are airgap reluctances only. For the two positions, aligned and misaligned, they are proportional to total air lengths:

$$\mathcal{R}_{\text{align}} = 0.002 / (12.57\text{E} - 7)(.01)(.10)] = 1.591\text{E}6 \quad (\text{E3.2.1})$$

$$\mathcal{R}_{\text{misalign}} = 0.02 / (12.57\text{E} - 7)(.01)(.10)] = 15.91\text{E}6 \quad (\text{E3.2.2})$$

4. The flux obeys

$$\phi_{\text{align}} = (1000 / \mathcal{R}_{\text{align}}) = 628.5\text{E} - 6 \text{ Wb} \quad (\text{E3.2.3})$$

$$\phi_{\text{misalign}} = (1000 / \mathcal{R}_{\text{misalign}}) = 62.85\text{E} - 6 \text{ Wb} \quad (\text{E3.2.4})$$

5. Assuming that the cross-sectional area for the airgap flux is always 1×10 cm, the airgap flux density is the same on both sides. For the two positions, B varies as follows:

$$B_{\text{align}} = \phi_{\text{align}} / [(0.01)(0.10)] = 1000\phi_{\text{align}} = 0.6285 \text{ T (tesla)} \quad (\text{E3.2.5})$$

$$B_{\text{misalign}} = \phi_{\text{misalign}} / [(0.01)(0.10)] = 1000\phi_{\text{misalign}} = 0.06285 \text{ T} \quad (\text{E3.2.6})$$

6. Since these flux densities are less than 1.5 T, which is the approximate knee of steel B – H curves, the assumption of infinite steel permeability might be approximately true. However, one must remember that all reluctance method calculations are approximate, especially if the steel reluctance is ignored.

3.3 FRINGING FLUX

As mentioned in solving Example 3.1, *fringing* is the expansion of flux in air. Magnetic flux paths in steel can expand outward when entering air, much like water flow paths through a hose can expand outward in air at the end of the hose or nozzle. Thus the area seen by the flux or flow increases, and fringing can cause the airgap reluctance to decrease significantly. Since, as in Examples 3.1 and 3.2, airgap reluctance is often the largest reluctance determining the flux, ignoring fringing can reduce the accuracy of the reluctance method.

In general, fringing flux can be ignored when the airgap pathlength is small compared with the airgap width. One can define a *fringing factor* as

$$K_{\text{fringe}} = \mathcal{R}_{\text{nofringe}} / \mathcal{R}_{\text{fringe}} \quad (3.15)$$

where the factor is usually greater than 1, because the reluctance with fringing is less than without fringing. For example, if a steel leg is cylindrical with diameter D and the air gap length is g , then K_{fringe} is a function of the ratio g/D that increases with the ratio. For g/D less than approximately 0.04, K_{fringe} is close to 1 and fringing can usually be ignored. For larger g/D ratios, however, fringing can cause greater than 5% changes in magnetic parameters such as reluctance and force.

Reluctances or permeances due to fringing have been derived for several common geometries. Examples include quarter- and half-cylinders and shells [1–3]. Example 5.2 will display fringing flux.

3.4 COMPLEX RELUCTANCE

The reluctance derived above is a real number and is based on Ampere's law. To include AC eddy losses produced by Faraday's law currents in conducting materials such as steel, the reluctance becomes a complex number. Complex numbers are customarily used in AC electrical engineering to account for phase shifts between AC sinusoids. Complex permeability, which produces complex permeance and complex reluctance, is often specified for semiconducting ferrites [4,5].

In general, the reluctance \mathcal{R} is the sum of ferromagnetic (Fe) and airgap reluctances:

$$\phi = NI / (\mathcal{R}_{\text{Fe}} + \mathcal{R}_{\text{gap}}) \quad (3.16)$$

The airgap reluctance is real (lossless), but the steel reluctance may be complex in order to include eddy current losses and/or other power losses [6]. Hence \mathcal{R}_{Fe} has both a real part and a positive imaginary part:

$$\mathcal{R}_{\text{Fe}} = \mathcal{R}_{\text{Re}} + j\mathcal{R}_{\text{IM}} = |\mathcal{R}_{\text{Fe}}| < \theta \quad (3.17)$$

where θ is the phase angle. Chapter 8 will discuss and apply complex reluctance to AC devices.

3.5 LIMITATIONS

The reluctance method described above has several limitations. The limitations and ways to address them are

1. Fringing flux in air is either ignored or approximated with fringing factors.
2. The pathlength of each part is often assumed to be average pathlength. A more accurate method is to use the reciprocal of the average reciprocal length, since reluctance is proportional to the reciprocal of length.
3. Since reluctance is inversely proportional to permeability, prediction of non-linear B – H effects in steel is difficult. However, B – H curves can be used in the reluctance method [1].
4. As discussed in the preceding section, losses in steel can be represented by use of complex reluctance. However, obtaining values of complex reluctance is often very difficult.
5. Most real world devices have complicated geometries with multiple flux paths that are difficult to analyze. However, magnetic circuits can be constructed with series and parallel reluctances to more accurately model such devices.
6. For many magnetic devices, however, the necessity of assuming flux paths makes the reluctance method inaccurate. Thus the reluctance method cannot be accurately applied to many devices.

PROBLEMS

- 3.1 Redo Example 3.1 with steel relative permeability equal to 100.
- 3.2 Change both tooth width and airgap in Fig. E3.2.1 of Example 3.2. The tooth width on both sides is reduced to 8 mm. The airgap is 2 mm in the aligned position and 11 mm in the misaligned position.
- 3.3 Apply Ampere's law directly to Example 3.2 to obtain flux density in both airgaps for both positions. Ampere's law can be applied directly because H and B are the same on both left and right sides because of their exact symmetry, and the steel is assumed to have zero reluctance.
- 3.4 Apply Ampere's law directly to Problem 3.2.

REFERENCES

1. H. C. Roters, *Electromagnetic Devices*, Wiley, New York, 1941.
2. E. Kallenbach, R. Eick, P. Quendt, T. Ströhla, K. Feindt, and M. Kallenbach, *Elektromagnete*, 2nd ed., B. G. Teubner Verlag/Springer, Wiesbaden, Germany, 2003 (in German).

3. M. A. Juds, *Notes on Solenoid Design*, Eaton Corporate R&D, Milwaukee, WI, July 15, 2004.
4. J. R. Brauer and F. Hirtenfelder, Anisotropic materials in electromagnetic finite element analysis, *Proc. IEE Int. Conf. Computation in Electromagnetics*, London, Nov. 1991.
5. E. P. Valstyn and T. Hadiono, The transfer function of a ferrite head, *IEEE Trans. Magn.*, **26**:2424–2426 (Sept. 1990).
6. A. Payne, W. Cain, R. Hempstead, and G. McCrea, Measuring core losses in thin film heads, *IEEE Trans. Magn.*, **32**:3518–3520 (Sept. 1996).

Finite-Element Method

Because of the limitations of the reluctance method of the preceding chapter, engineers have long sought more accurate ways to calculate magnetic fields. This chapter is devoted to the finite-element method, the most general and accurate method yet found [1–3].

Even before digital computers existed, a few scientists and engineers employed *relaxation techniques* [4] to iteratively solve governing differential equations of phenomena including heat and magnetics. For magnetic fields, for example, Ampere’s law at a point can be solved using a method commonly called the *finite-difference method*. Whether solved on a computer or not, the finite-difference method involves replacing differentials such as ∂x with differences such as Δx . Usually the geometric spacing, such as Δx and Δy in two dimensions, must be uniform everywhere, although some finite-difference software allows a nonuniform “grid” of spacing. The process of subdividing the problem region into such a gridwork is called *discretization*, and a major problem with the finite difference method is that a uniform discretization is not appropriate for many engineering devices. Most devices have regions with intricate geometry requiring fine discretization, along with regions without intricate geometry not requiring such detailed modeling.

4.1 ENERGY CONSERVATION AND FUNCTIONAL MINIMIZATION

The *finite-element method* can be derived using the basic principle of energy conservation. Assuming for now that the region analyzed has no power loss, the energy input must equal the energy stored:

$$W_{\text{in}} = W_{\text{stored}} \quad (4.1)$$

The finite-element method has been applied to structural analysis using the energies input and stored as mechanical stress, to thermal analysis using thermal energies, and to fluid dynamics using fluidic energies [1].

The finite-element equation (4.1) is applied here to magnetic field problems. Energy is stored in magnetic fields and is input using a current density \mathbf{J} . Thus expressions for the energies over the problem volume v can be substituted to obtain

$$\frac{1}{2} \int \mathbf{J} \cdot \mathbf{A} \, dv = \int \frac{B^2}{2\mu} \, dv \quad (4.2)$$

where constant permeability μ (linear B - H) is assumed for now, and integrations are taken on both sides over the problem volume. Recall from Chapter 2 that \mathbf{A} is magnetic vector potential, here unknown. Recall also that magnetic field (flux density) \mathbf{B} is the curl of \mathbf{A} :

$$\mathbf{B} = \nabla \times \mathbf{A} \quad (4.3)$$

The next step in finite-element analysis is to define an *energy functional* as the difference between stored energy and input energy [1]:

$$F = W_{\text{stored}} - W_{\text{input}} \quad (4.4)$$

For linear magnetic fields, substituting (4.2) gives the functional:

$$F = \int \left[\frac{B^2}{2\mu} - \frac{1}{2} \int \mathbf{J} \cdot \mathbf{A} \right] dv \quad (4.5)$$

The law of energy conservation requires the functional to be zero. However, rather than setting (4.5) directly to zero, the finite-element method minimizes the functional. Thus, the correct solution for unknown fields \mathbf{B} and \mathbf{A} is found by setting the partial derivative of the functional to zero:

$$\frac{\partial F}{\partial A} = 0 \quad (4.6)$$

As shown in most calculus texts, the derivative is a slope. At a minimum of a function, the slope is zero, as shown in Fig. 4.1.

Substituting the functional of (4.5) into (4.6), we obtain

$$\frac{\partial}{\partial A} \int \frac{B^2}{2\mu} \, dv = \int J \, dv \quad (4.7)$$

This equation is the basis for finite-element analysis of linear magnetostatic (DC magnetic) fields.

4.2 TRIANGULAR ELEMENTS FOR MAGNETOSTATICS

Besides the energy functional, the second main requirement of finite element analysis is to discretize (break up) the volume analyzed into small pieces called *finite elements*. The most basic finite element is the triangle.

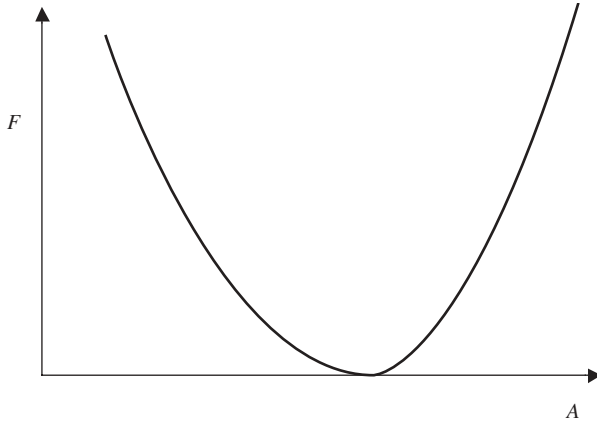


Figure 4.1 Functional F with a minimum having zero slope (derivative).

Figure 4.2 shows the simplest triangular finite element for magnetostatic fields. It lies in the xy plane, and its magnetic flux density \mathbf{B} is assumed to lie in the same plane. As in the reluctance examples of the preceding chapter, the planar \mathbf{B} is produced by a current coming out of the plane. Thus the current density \mathbf{J} is in the z direction out of the plane of the page. Since \mathbf{J} lies only in the z direction, the unknown magnetic vector potential \mathbf{A} lies only in the z direction. In many magnetic devices, especially those made of steel laminations, \mathbf{B} lies in the plane and the geometry of the device is independent of the direction out of the plane as shown in Fig. 4.2.

Note that the triangle of Fig. 4.2 has three vertices called *nodes*, labeled L , M , N . The unknown $A_z = A$ must be found at the three nodes, and thus the triangle of Fig. 4.2 is called a *nodal* finite element.

The triangular finite element of Fig. 4.2 is assumed to be a *first-order finite element* by assuming the following *shape function*

$$A(x, y) = \sum_{k=L,M,N} [A_k(a_k + b_kx + c_ky)] \quad (4.8)$$

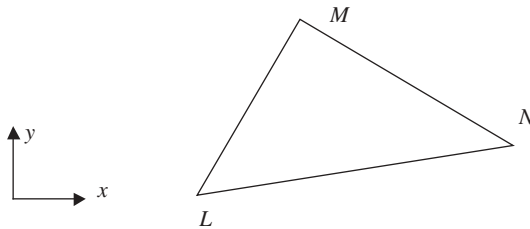


Figure 4.2 Triangular finite element lying in the xy plane.

where the first-order shape function is a first-order polynomial over the plane of interest. From Fig. 4.2, the unknown $A = A_K$ at $x = x_K$ and $y = y_K$, with two more such equalities at the other two nodes. Thus one obtains the matrix relation for the constants of (4.8):

$$\begin{pmatrix} a_L & a_M & a_N \\ b_L & b_M & b_N \\ c_L & c_M & c_N \end{pmatrix} = \begin{pmatrix} 1 & x_L & y_L \\ 1 & x_M & y_M \\ 1 & x_N & y_N \end{pmatrix}^{-1} \quad (4.9)$$

Hence for any triangle, the polynomial constants of (4.8) are known.

Substituting the shape function of (4.8) into the functional minimization equation (4.7) yields

$$\int \frac{\partial}{\partial A_k} \left(\frac{B^2}{2\mu} - \frac{1}{2} JA \right) dv = 0 \quad (4.10)$$

where evaluation of the curl of \mathbf{A} for the triangle gives

$$B^2 = \left(\frac{\partial A}{\partial x} \right)^2 + \left(\frac{\partial A}{\partial y} \right)^2 \quad (4.11)$$

4.3 MATRIX EQUATION

The final step of finding the unknown vector potentials at the three nodes of the triangle of Fig. 4.2 is to integrate over its volume, which is actually its area times the depth into the page. If the triangle area is denoted as S , one can show [1] that a 3×3 matrix equation is obtained

$$(S/\mu) \begin{pmatrix} (b_L b_L + c_L c_L) & (b_L b_M + c_L c_M) & (b_L b_N + c_L c_N) \\ (b_M b_L + c_M c_L) & (b_M b_M + c_M c_M) & (b_M b_N + c_M c_N) \\ (b_N b_L + c_N c_L) & (b_N b_M + c_N c_M) & (b_N b_N + c_N c_N) \end{pmatrix} \begin{bmatrix} A_L \\ A_M \\ A_N \end{bmatrix} = (S/3) \begin{bmatrix} J \\ J \\ J \end{bmatrix} \quad (4.12)$$

which is commonly denoted as

$$[K] \{A\} = \{J\} \quad (4.13)$$

The matrix K is commonly called the “stiffness matrix” from its origin in structural finite-element analysis. The column vector J is usually known, and then (4.13) enables the unknown column vector A to be found.

When several triangles are used to discretize the region analyzed, then the 3×3 matrix equation of (4.12) and (4.13) becomes an $n \times n$ matrix equation, where n is the total number of nodes. Usually many triangles are required, each of which may have a different constant permeability and applied current density (zero or nonzero). With modern software and hardware, matrices with thousands of rows and

columns (and millions of matrix entries) can be solved within a few minutes. In general, both storage requirements and computer solve times are proportional to the number of unknowns n to a power between 2 and 3.

After all nodal vector potentials are found using (4.13), the magnetic flux density in each triangle can be found using (4.11). Substituting the first order shape function into (4.11), it is seen that the \mathbf{B} in first-order triangles is a constant value. Since each first-order triangle has constant flux density, more and smaller triangular finite elements are needed wherever the magnetic field varies the most. Since the field is expected to vary the most near fine steel geometries such as corners, which must naturally be modeled with many triangles, the finite-element method is practical and can be very accurate.

To increase accuracy over each finite element, shape functions with higher polynomial order (called p) can be used. For example, a second-order or *quadratic* shape function for magnetic vector potential over a triangle is

$$A(x, y) = \sum_{k=L,M,N,O,P,Q} [A_k(a_k + b_kx + c_ky + d_kx^2 + e_ky^2 + f_kxy)] \quad (4.14)$$

In most cases the three extra variables create three extra nodes placed at the middle of each triangle edge and thus called *midnode* variables.

Extensions of the equations above enable better analysis of real-world magnetic problems. For saturable nonlinear materials, Newton's iterative method is used [1]. For conducting materials with eddy current power losses, an additional energy term can be added to the energy functional. For true 3D problems, often the triangular finite element is replaced by a tetrahedron. With only corner nodes, the tetrahedron has 4 nodes, whereas with midedge nodes, it has 10 nodes. However, to allow discontinuity in the normal component of 3D magnetic vector potential, for highest accuracy the variables preferred in tetrahedrons are the tangential components of \mathbf{A} along its edges. Such finite elements are called *edge elements* or *tangential vector elements* [5]. In some finite-element matrix derivations, as an alternative to the energy methods described here, the differential equation is directly used in Galerkin's method [3].

Example 4.1 Matrix Equation for Two Finite Elements Two first-order triangular finite elements are used to model a region made of copper wire and containing current density of 40,000 A/m² in the direction normal to the plane of the elements. The first element connects node numbers 1, 2, and 3. It has the following coefficient values: $b_1 = 1$, $b_2 = 2$, $b_3 = 3$, $c_1 = 4$, $c_2 = 5$, $c_3 = 6$, and area $S = 1\text{E-}4\text{ m}^2$.

The second element connects node numbers 3, 4, and 5. It has coefficient values (for those nodes in that order): $b_1 = 1$, $b_2 = 2$, $b_3 = 3$, $c_1 = 4$, $c_2 = 5$, $c_3 = 6$, and area $S = 2\text{E-}4\text{ m}^2$.

The matrix equation for all unknown vector potentials is to be written in a form amenable to ready solution.

Solution: Set up (4.12) for each element, and then combine the matrices into a sin-

gle 4×4 matrix equation. For the first element, (4.12) is

$$(1\text{E-}4/12.57\text{E-}7) \begin{pmatrix} (1+16) & (2+20) & (3+24) \\ (2+20) & (4+25) & (6+30) \\ (3+24) & (6+30) & (9+36) \end{pmatrix} \begin{bmatrix} A_1 \\ A_2 \\ A_3 \end{bmatrix} = (1\text{E-}4/3) \begin{bmatrix} 40\text{E}3 \\ 40\text{E}3 \\ 40\text{E}3 \end{bmatrix} \quad (\text{E4.1.1})$$

$$\begin{pmatrix} (1352) & (1750) & (2148) \\ (1750) & (2307) & (2864) \\ (2148) & (2864) & (3580) \end{pmatrix} \begin{bmatrix} A_1 \\ A_2 \\ A_3 \end{bmatrix} = \begin{bmatrix} 1.333 \\ 1.333 \\ 1.333 \end{bmatrix} \quad (\text{E4.1.2})$$

where the rows and columns correspond to the numbers 1, 2, and 3 respectively. For the second element, the rows and columns correspond to the numbers 3, 4, and 5 respectively, with the matrix equation:

$$(2\text{E-}4/12.57\text{E-}7) \begin{pmatrix} (1+16) & (2+20) & (3+24) \\ (2+20) & (4+25) & (6+30) \\ (3+24) & (6+30) & (9+36) \end{pmatrix} \begin{bmatrix} A_1 \\ A_2 \\ A_3 \end{bmatrix} = (2\text{E-}4/3) \begin{bmatrix} 40\text{E}3 \\ 40\text{E}3 \\ 40\text{E}3 \end{bmatrix} \quad (\text{E4.1.3})$$

$$\begin{pmatrix} (2704) & (3500) & (4296) \\ (3500) & (4614) & (5728) \\ (4296) & (5728) & (7160) \end{pmatrix} = \begin{bmatrix} 2.667 \\ 2.667 \\ 2.677 \end{bmatrix} \quad (\text{E4.1.4})$$

Combining (E4.1.2) for rows and columns 1, 2, 3 with (E4.1.4) for rows and columns 3, 4, 5 gives the final 5×5 matrix equation:

$$\begin{pmatrix} 1352 & 1750 & 2148 & 0 & 0 \\ 1750 & 2307 & 2864 & 0 & 0 \\ 2148 & 2864 & (3580+2704) & 3500 & 4296 \\ 0 & 0 & 3500 & 4614 & 5728 \\ 0 & 0 & 4296 & 5728 & 7160 \end{pmatrix} \begin{bmatrix} A_1 \\ A_2 \\ A_3 \\ A_4 \\ A_5 \end{bmatrix} = \begin{bmatrix} 1.333 \\ 1.333 \\ 4 \\ 2.667 \\ 2.677 \end{bmatrix} \quad (\text{E4.1.5})$$

Note that zero entries exist for nodes that are not directly connected by a finite element. As more elements are added, more zeros occur, and the matrix becomes dominated by zeros. A zero-dominated matrix is said to be *sparse*. Modern matrix solution software takes advantage of the *sparsity* to reduce storage requirements and solution time [6].

4.4 FINITE-ELEMENT MODELS

For the magnetic fields to be found in any magnetic device, a *finite-element model* of that device must be created. Making a finite-element model consists of four steps.

1. *Geometry, Subdivided into Finite Elements.* All 2D or 3D geometry must be specified, and the user and/or the software must subdivide it into finite ele-

ments. Geometry specification is difficult for many real world devices of complicated shape. For example, Fig. 4.3 shows a magnetic actuator with 2D geometry. If the geometry already exists in drawing software, then some finite element software will accept it. However, either the finite-element software or the user must subdivide all geometric regions, including air for magnetic fields, into finite elements, such as those shown in Fig. 4.4.

2. *Materials.* For electromagnetic fields, the three material properties of Chapter 2 may be required: permeability, conductivity, and permittivity. Recall that for nonlinear magnetic materials, the $B-H$ curve is required. For magnetostatics, (4.12) shows that conductivity and permittivity are not required.
3. *Excitations.* For magnetic fields, the excitations or sources input are current densities and/or currents according to (4.12). As will be seen in later chapters, voltages can be used instead if desired.
4. *Boundary Conditions.* On the outer boundary of the region analyzed, boundary conditions are required. For example, since Fig. 4.4 is a one-half model of the right side of an actuator, the left (symmetry) boundary must be specified. On the other three sides of the outer boundary, one must specify whether magnetic flux will enter. If flux does not enter at the boundary of a 2D model, then, as shown in the next chapter, that boundary has constant A_z , usually set to zero. Modeling only one-half reduces the computer time substantially. In some magnetic devices with multiple poles, periodic boundary conditions enable even smaller fractions to be modeled. In many cases, the magnetic field extends beyond the region modeled into surrounding airspace, and special

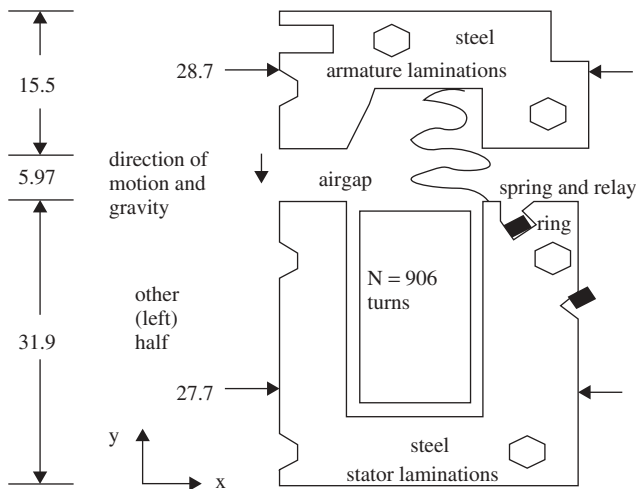


Figure 4.3 Magnetic actuator manufactured by Eaton Corporation [7], showing the geometry and materials of the right half. Dimensions are in millimeters. The steel laminations are stacked to a depth of 28.5 mm into the page.

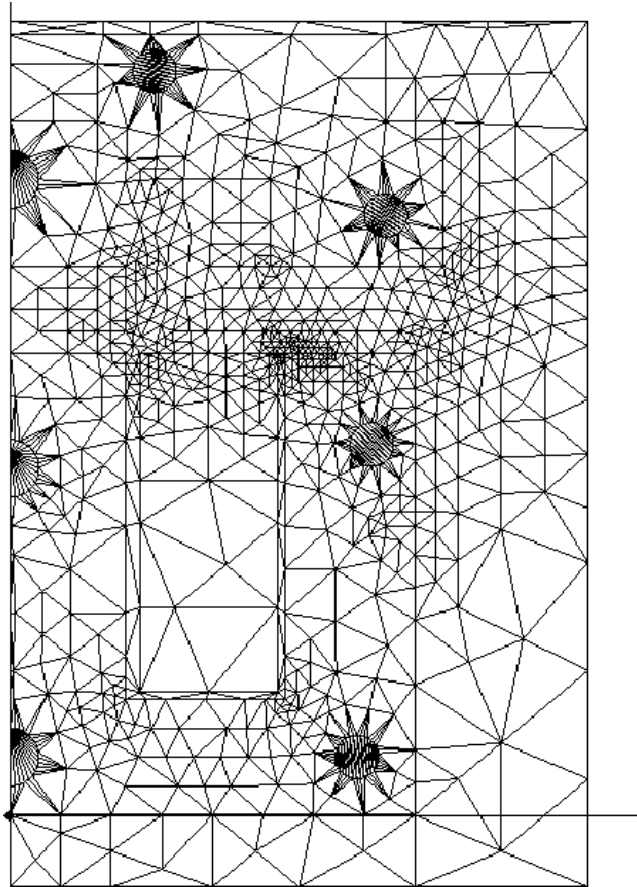


Figure 4.4 Computer display of triangular finite elements used to model Fig. 4.3.

open boundaries are appropriate.

In some finite-element software, the four steps listed above appear in a task menu. The four steps are often called *preprocessing*, because they must be accomplished in order for the matrix equation to be set up and solved for the magnetic vector potential distribution throughout the device analyzed. The 2D finite element software Maxwell SV (Student Version) is presently available for students at no cost at the Ansoft Corporation Website www.ansoft.com. The Website also contains instructional material with detailed worked examples. The Maxwell SV main menu contains these four steps, although step 1 has a different name and steps 3 and 4 are combined into one menu item. This book uses Maxwell SV for several examples in several chapters.

Example 4.2 Finite-Element Analysis of the “C” Steel Path with Airgap of

Example 3.1 The problem shown in Fig. E3.1.1 and solved by the reluctance

method in Example 3.1 is to be solved here using Maxwell SV.

Solution: Follow the four steps listed above to construct a finite-element model of the problem in Maxwell SV:

1. Enter the geometry. Maxwell requires a *background* that must be at least as big as the device modeled. The overall background chosen is the same as in Fig. E3.1.1, 0.8 m horizontally and 0.6 m vertically. The geometry is entered as straight lines that are connected to form the various parts. Make sure that the xy plane is selected on the upper left tab on the main menu just below the tab selecting the *magnetostatic* problem type.
2. Enter the materials. Since the steel is to have a relative permeability of 2000, you must add a special linear steel material.
3. Enter the excitations, called *sources* in the menu. The coil region in the center of the “C” is set to 10,000 A. Its return on the left side of the “C” must then have $-10,000$ A.
4. Enter the boundary conditions. Here the flux is assumed confined to the 0.8×0.6 -m region analyzed, and thus the vector potential is set to zero on the entire outer boundary.

You should now note on the Maxwell main menu that these four steps all have checkmarks next to them, indicating that you can now click on its “Solve” command. Maxwell then automatically places triangular finite elements in the geometry that you have entered. It adds elements in passes as shown in Table E4.2.1. For each pass, it computes both the total stored energy and the estimated energy error in percent. Its default energy error is 1%, but in Table E4.2.1 it has been reduced to 0.1%, requiring 11 passes. The corresponding finite element model or *mesh* is shown in Fig. E4.2.1.

The energy listed in Table E4.2.1 is for a depth of 1 m. To compare its energy of 141.65 J with that of the reluctance solution of Example 3.1, use the right-hand side

TABLE E4.2.1 Convergence of “C” Core Example Finite-Element Analysis in Maxwell SV

Pass	Triangles	Total Energy (J)	Energy Error (%)
1	46	1.331176E+002	8.8755
2	124	1.38127 E+002	2.6007
3	160	1.38824 E+002	1.2903
4	206	1.39575 E+002	0.8061
5	262	1.40271 E+002	0.7050
6	340	1.40619 E+002	0.4578
7	440	1.41122 E+002	0.3302
8	572	1.41274 E+002	0.2237
9	737	1.41454 E+002	0.1833
10	965	1.41588 E+002	1.1220
11	1241	1.41651 E+002	0.0851

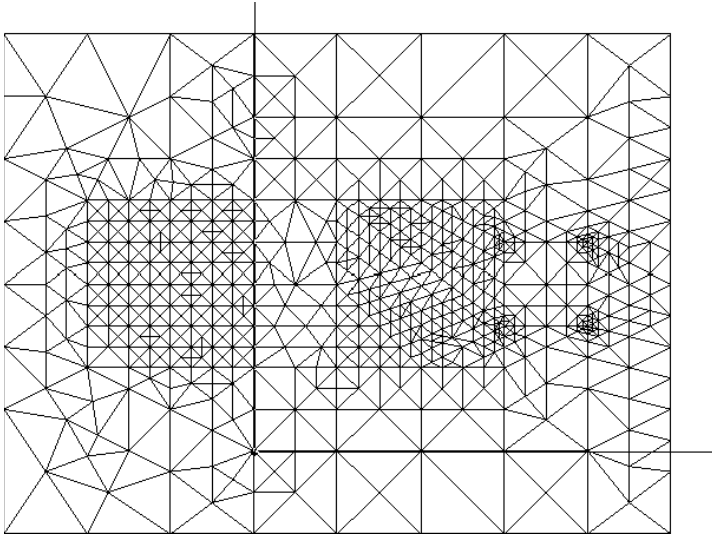


Figure E4.2.1 Computer display of finite-element model of steel path with airgap of Examples 3.1 and 4.2 produced by 11 adaptive passes.

of (4.2):

$$W = \int \frac{B^2}{2\mu} dv \quad (\text{E4.2.1})$$

Since the reluctance method of Example 3.1 obtained $B = 0.125$ T, and most of the energy is in the airgap volume of 0.1×0.1 m by a depth of 1 m (to agree with Maxwell software), (E4.2.1) becomes

$$W = (0.125)^2 / (12.57\text{E-}7)(0.1)(0.1)(1) = 124.3 \text{ J} \quad (\text{E4.2.2})$$

This energy of the reluctance method is about 12% lower than the 141.65 J computed by Maxwell. The finite element solution is thus considerably more accurate than the reluctance method solution.

PROBLEMS

- 4.1** Repeat Example 4.1 with the second finite element (of area $2\text{E-}4 \text{ m}^2$) changed to steel with relative permeability 1000 and containing no current. Assuming that the first element remains the same, find the final matrix equation.
- 4.3** Substitute the first-order triangular shape function of (4.8) into $\mathbf{B} = \nabla \times \mathbf{A}$ to show that \mathbf{B} is constant in each such finite element.

- 4.3 Use Maxwell SV to solve Example 4.2 with the steel having the nonlinear B – H curve called “steel_1010” in the Maxwell material list.
- 4.4 Use Maxwell SV to solve Example 4.2 with the steel having the nonlinear B – H curve called “steel_1020” in the Maxwell material list.

REFERENCES

1. J. R. Brauer, ed., *What Every Engineer Should Know about Finite Element Analysis*, 2nd ed., Marcel Dekker, New York, 1993.
2. J. K. Hastings, M. A. Juds, and J. R. Brauer, Accuracy and economy of finite element magnetic analysis, *Proc. Nat. Relay Conf.*, Stillwater, OK, April 1985.
3. N. Ida and J. P. A. Bastos, *Electromagnetics and Calculation of Fields*, 2nd ed., Springer-Verlag, New York, 1997.
4. J. P. Holman, *Heat Transfer*, McGraw-Hill, New York, 1963.
5. J. F. Lee, D. K. Sun, and Z. J. Cendes, Tangential vector finite elements for electromagnetic field computation, *IEEE Trans. Magn.*, **27**:4032–4035 (Sept. 1991).
6. L. Komzsik, *What Every Engineer Should Know about Computational Techniques of Finite Element Analysis*, Taylor & Francis, Boca Raton, FL, 2005.
7. M. A. Juds and J. R. Brauer, AC contactor motion computed with coupled electromagnetic and structural finite elements, *IEEE Trans. Magnetism*, **31**:3575–3577 (Nov. 1995).

Magnetic Force

The magnetic vector potential \mathbf{A} and magnetic flux density \mathbf{B} computed by the finite-element method of the preceding chapter can be used to find magnetic forces of magnetic actuators and sensors. Related to magnetic force are magnetic flux plots, magnetic energy, magnetic pressure, permanent magnets, and magnetic torque. All are discussed in this chapter, and all are examples of *postprocessing* of finite-element solutions.

5.1 MAGNETIC FLUX LINE PLOTS

Magnetic vector potential \mathbf{A} in the 2D planar triangular finite elements of the preceding chapter has been shown to consist of only one component: A_z . This component is directed perpendicular to the xy plane of the finite elements.

Plots of contours of constant A_z can be shown to be very useful plots for 2D planar models. They are called *magnetic flux line plots*, or *magnetic flux plots* for short. Figure 5.1 shows a magnetic flux line plot for the Eaton actuator of the preceding chapter. It is obtained by drawing contour lines connecting constant values of A_z , similar to plots of constant temperature appearing in weather maps. One can choose as many contour lines as one likes, but useful plots have all contours spaced by equal increments.

The 2D plot of contours of constant A_z is called a magnetic flux line plot because it shows the same pattern as obtained by sprinkling iron filings on a sheet of paper. Each iron filing is long and thin, resembling a compass needle. Like a compass needle, each filing will align itself in the direction of the magnetic flux density \mathbf{B} , and hence flux lines are sometimes called *lines of force*. Also, the filings will concentrate in the regions of highest flux density magnitude. Thus the closer flux lines in Fig. 5.1 represent higher-flux-density regions. A key advantage of finite-element flux plots over iron filing flux plots is that finite element flux plots enable the engineer to visualize the flux flow within steel, where iron filings cannot be sprinkled.

Since most magnetic devices contain parts made of steel with nonlinear B – H curves, the flux densities in the steel are of particular interest. If the flux line plots show steel regions with densities less than about 1.5 T, the approximate knee of most steel B – H curves, then some of the steel may be wasted. Some of the steel in

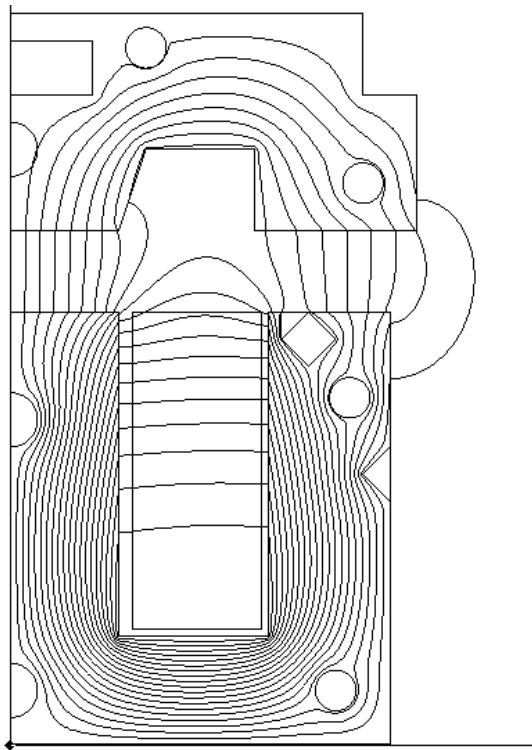


Figure 5.1 Computer display in black and white showing flux line plot for 2D planar Eaton actuator model of the preceding chapter.

those regions can be removed, thereby saving the cost and weight of that steel and/or the copper coil that surrounds it. On the other hand, if the flux plot shows steel with flux densities much greater than the knee at approximately 1.5 T, then that steel is saturated, and it is likely that more steel should be added to reduce the current required and the associated I^2R power loss in the coil. Hence flux plots and flux density distributions are very helpful in the design of magnetic devices.

Besides problems modeled with planar triangular finite elements, another type of 2D problem is not planar but is *axisymmetric*. Figure 5.2 shows a magnetic actuator originally developed by Bessho et al. in Japan [1]. Note that its parts all revolve around the central axis of symmetry, usually called the z axis. Thus its finite-element model, shown in Fig. 5.3, lies in a plane (usually called the rz plane) but consists of axisymmetric finite elements. Instead of each element having the same depth into the page, the depths are proportional to radius from the axis of symmetry, and thus the volume integrals for the finite-element matrix equation differ from those of the 2D planar finite elements of the preceding chapter. Similarly, the flux line plots must take into account the effects of the radius on volume. Accordingly, flux line plots for axisymmetric models are contours of constant radius times vector

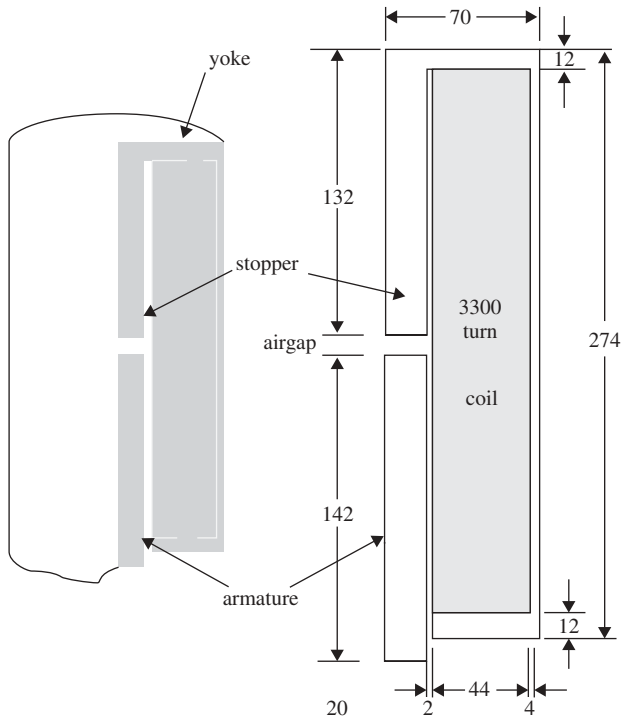


Figure 5.2 Axisymmetric magnetic actuator developed by Bessho et al. Dimensions shown are in millimeters.

potential, where the vector potential only has a component in the direction around the axis of symmetry.

For 3D models, flux line plots are not as meaningful because no piece of paper with iron filings can represent 3D flux flow. Thus contours of constant magnitude of vector potential are not very meaningful for 3D problems. Instead, color plots of the magnitude of flux density are very useful in 3D (and 2D) problems; usually red is used for high flux density and blue or black for low flux density.

For both 2D and 3D finite-element models, it is vital that flux line plots and/or flux density plots be obtained and examined. The engineer should never report results without doing so, because the plots can reveal mistakes in the model. Typical mistakes might include

- Wrong material selection
- Wrong boundary condition
- Wrong units (millimeters instead of meters, etc.)
- Wrong input excitation (current or voltage)
- Wrong number of turns

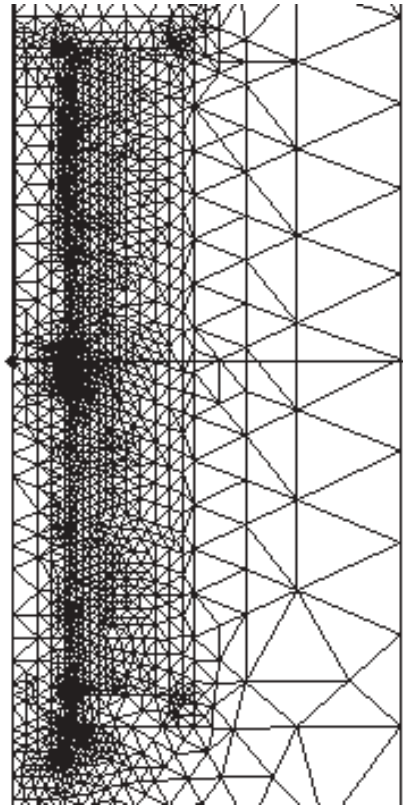


Figure 5.3 Computer display of 2D axisymmetric finite-element model of actuator of Fig. 5.2.

Any mistake must be corrected and the model rerun until the flux display appears reasonable, which is required for finite-element model validation. An additional check would be to compare the finite-element flux with the flux estimated by the reluctance method of Chapter 3, if such an estimate can be made.

Example 5.1 Relation between \mathbf{A} and \mathbf{B} for 2D Planar Problem Given a 2D planar finite-element solution of $A_z = y$, find the corresponding magnetic flux density \mathbf{B} and describe the flux line plot.

Solution: To find \mathbf{B} , use the curl of \mathbf{A} of (2.8), which for A_z only becomes

$$\mathbf{B} = \frac{\partial A_z}{\partial y} \mathbf{u}_x - \frac{\partial A_z}{\partial x} \mathbf{u}_y \quad (\text{E5.1.1})$$

Substituting the given expression for A_z , the partial with respect to x is zero, and thus the flux density has only an x component:

$$\mathbf{B} = \frac{\partial y}{\partial y} \mathbf{u}_x = 1 \mathbf{u}_x \quad (\text{E5.1.2})$$

Note that the flux density is a uniform 1 T in the x direction. The corresponding flux line plot connects constant vector potential values and also shows uniformly spaced lines directed in the x direction. Figure E5.1.1 shows the flux line plot for a typical number of lines.

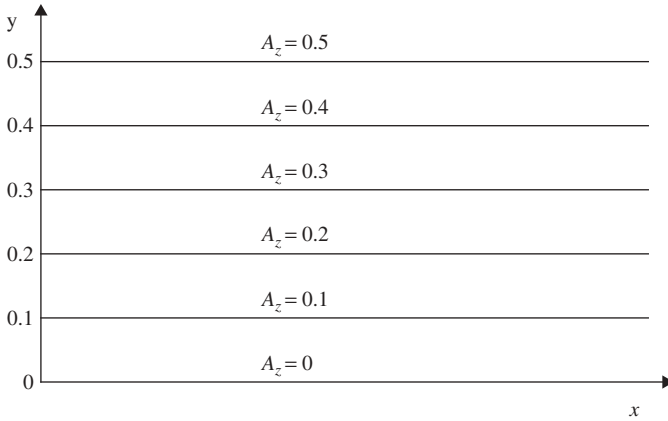


Figure E5.1.1 Flux line plot of Example 5.1, shown over a finite region of the xy plane.

Example 5.2 Flux Line Plot of the “C” Steel Path with Airgap of Examples 3.1 and 4.2 Given the “C”-shaped steel path with airgap and winding of Examples 3.1 and 4.2, obtain the flux line plot using Maxwell SV.

Solution: After clicking on “Solve” in the main menu of Maxwell and obtaining the convergence Table E4.2.1 of Example 4.2, click on the next main menu item “Post process.” On the top of the screen, choose “Plot.” On the popup that appears, choose “Flux lines” on “Surface—all” in area “All.” On the next popup, choose all defaults, except make 21 divisions (and thus 20 flux lines) with spectrum color type “magenta.”

The plot you obtain should be that of Fig. E5.2.1. Note that it has four flux lines that pass through the center coil region without reaching the airgap of the “C” core. These four flux lines to the left of the airgap region are thus called *leakage flux*. They are a type of leakage flux sometimes called “partial” flux since it does not fully surround the coil. Note that Fig. E5.2.1 also has four flux lines on the outside (to the right of the “C” airgap) that flow through the surrounding air without passing through the airgap region directly between the steel poles. These 4 lines represent *fringing flux* since their pattern extends outward much like fringe, as mentioned in Chapter 3.

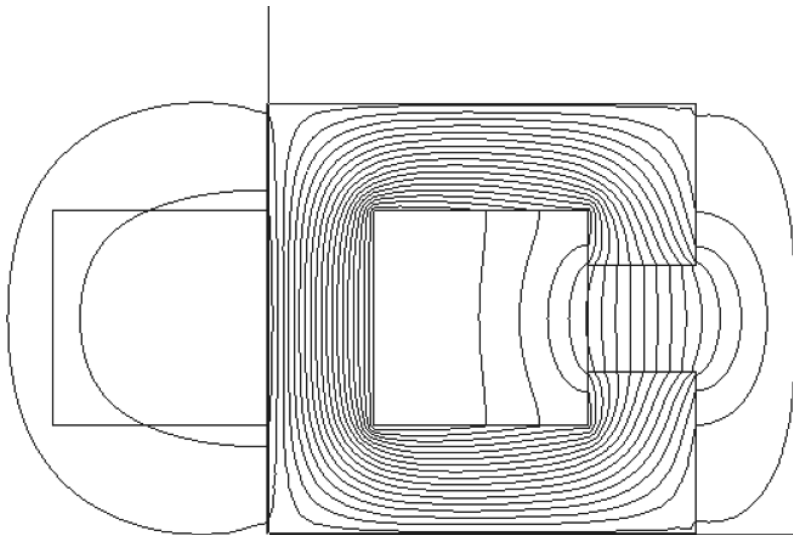


Figure E5.2.1 Computer display in black and white showing flux line plot of Examples 5.2, 4.2, and 3.1.

5.2 MAGNETIC ENERGY

The expression for energy stored in a magnetic field has been presented in (4.2) of the preceding chapter as

$$W_{\text{mag}} = \int \frac{B^2}{2\mu} dv \quad (5.1)$$

where constant permeability μ is assumed. In general, all types of energy W can be found by integrating energy density w over a volume:

$$W = \int w dv \quad (5.2)$$

Hence the energy density, in joules per cubic meter, for constant permeability material of (5.2) is easily seen to be

$$w_{\text{mag}} = \frac{B^2}{2\mu} = \frac{1}{2}BH \quad (5.3)$$

For materials with nonlinear B - H curves, the energy density can be shown to be

$$w_{\text{mag}} = \int H \cdot dB \quad (5.4)$$

Figure 5.4 shows that this energy density is the area to the left of the B - H curve. Note that Fig. 5.4 also shows an area under the B - H curve called the *co-energy*

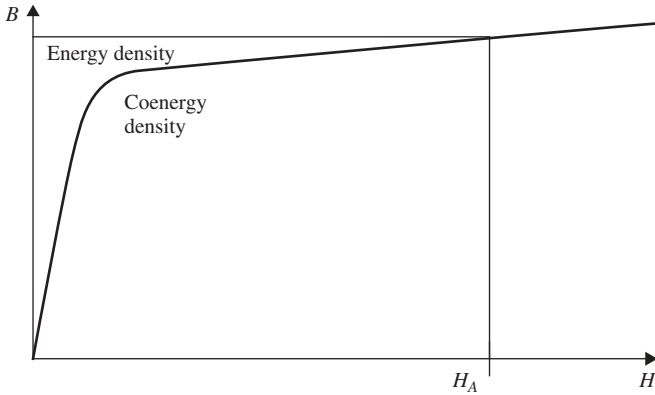


Figure 5.4 Energy density and co-energy density for a typical operating point on a typical nonlinear B – H curve.

density w_{co} . The sum of coenergy density and energy density is seen in Fig. 5.4 to obey

$$w_{\text{mag}} + w_{\text{co}} = HB \quad (5.5)$$

For constant-permeability materials, energy density and coenergy density become equal and are given by (5.3).

5.3 MAGNETIC FORCE ON STEEL

Force is related to energy. Indeed, energy is in units of force times distance. One of the most basic methods to determine force is to use the method of virtual work. It states that force in a given direction, say, the vertical y direction, equals the partial derivative of stored energy with respect to that direction:

$$F_y = \frac{\partial W}{\partial y} \quad (5.6)$$

An example of virtual work determining the force of a typical magnetic actuator or sensor is shown in Fig. 5.5. Assuming for now that the steel (or other material) has permeability that is thousands of times that of air, then the energy density in the air is thousands of times that in the steel, and is given by

$$w_{\text{mag}} = B^2/(2\mu_0) \quad (5.7)$$

To determine the magnetic force acting in the vertical y direction in Fig. 5.5, one may replace the derivative of (5.6) by its approximation

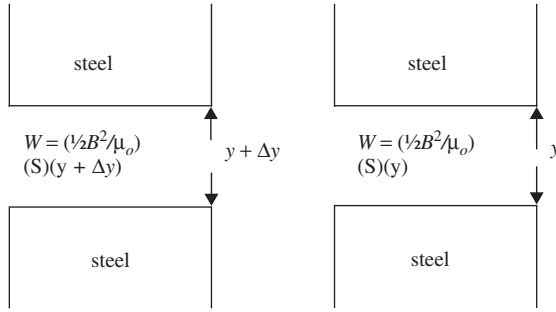


Figure 5.5 Typical magnetic actuator or sensor with steel poles and the energy stored in the air gap between them for two vertical positions.

$$F_y = \frac{\Delta W}{\Delta y} \quad (5.8)$$

where W is as always the volume integral of w . Assuming the flux density B in the air-gap of Fig. 5.5 is uniform, then magnetic energy W_{mag} is simply w_{mag} times volume:

$$W_{\text{mag}} = [B^2/(2\mu_0)]v \quad (5.9)$$

As shown in Fig. 5.5, during a *virtual displacement* Δy of a steel pole in the y direction, the volume of the airgap changes from its surface area S times $(y + \Delta y)$ to S times y . Hence from (5.9) we obtain

$$F_y = \frac{\Delta W}{\Delta y} = \frac{S(y + \Delta y)B^2/(2\mu_0) - SyB^2/(2\mu_0)}{\Delta y} \quad (5.10)$$

and thus the magnetic force is

$$F_{\text{mag}} = SB^2/(2\mu_0) \quad (5.11)$$

This magnetic force equation is very simple and useful, even though it assumes that the steel has infinitely high permeability. Note that the force is proportional to the square of flux density. The direction of the force causes the steel pole to move toward the airgap; that is, the steel poles of Fig. 5.5 are attracted to each other independent of the direction of B . Because this force tends to reduce the reluctance of the magnetic circuit, it is sometimes called a *reluctance force*.

If the steel poles have finite permeability μ_s , then from Fig. 5.5 the virtual displacement will produce an additional force term, because the steel volume changes with a virtual displacement. Thus the force of (5.11) becomes

$$F_{\text{mag}} = S[B^2/(2\mu_0) - B^2/(2\mu_s)] \quad (5.12)$$

Since $\mu_s > \mu_0$, the force direction remains such that the steel tends to move toward the air. In many cases, since $\mu_s > 1000\mu_0$, the simpler equation (5.11) is sufficiently accurate.

When materials with nonlinear B – H curves are present, the magnetic force can be derived with the aid of Fig. 5.6, which shows two B – H relations for an entire device with variable airgap. Curve 1 in Fig. 5.6 represents a high-reluctance position with large airgap and curve 2, a lower-reluctance position with the airgap reduced. Since current is a common input for the magnetostatic finite-element analyses of Chapter 4, it is assumed to be constant in Fig. 5.6, obtaining a constant field intensity H_A . The area between the two curves is the energy difference needed to obtain the force by the virtual work method, but is seen to actually be the difference in coenergies. Thus when nonlinear materials are present the force equation becomes

$$F_y = \left. \frac{\partial W_{co}}{\partial y} \right|_{I=\text{const}} \quad (5.13)$$

where W_{co} is the total magnetic coenergy and the applied current is assumed to be held constant.

Example 5.3. Force on One Pole of the “C” Steel Path with Airgap of Examples 3.1, 4.2, and 5.2 Given the “C”-shaped steel path with airgap and winding of Examples 3.1, 4.2, and 5.2, obtain the magnetic force on one of its two steel poles using Maxwell SV and compare it with the reluctance method result and the simple force formula (5.11).

Solution: Maxwell uses the virtual work method of (5.6) in an algorithm designed to obtain total magnetic force on any geometric part. The entire “C” of steel of Fig.

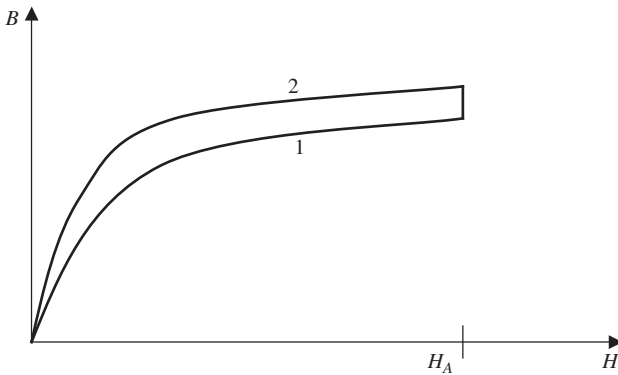


Figure 5.6 Nonlinear B – H relation of a typical magnetic device at positions 1 and 2. The applied current and thus applied field intensity H_A are constant.

E5.2.1 is expected to have zero total force, because the upper steel pole (above the airgap) will experience a downward force canceled by the equal upward force on the lower steel pole. Thus, to determine the force on one pole, a one-half model must be constructed.

The upper half is modeled by either altering the geometry of the model of Example 4.2 or by starting a new Maxwell project. Since only the upper half is modeled, the half-coil must contain half the ampere-turns, or 5000. Also, the boundary condition along the symmetry boundary (the horizontal plane at the bottom of the modeled upper half) must be specified as *even symmetry* or left unconstrained to allow flux to cross it. Finally, before clicking on the “Solve” button, the button “Set up executive parameters” must be clicked. Within this setup, the force on the upper half of the “C” must be requested. After solution, the resulting flux line plot is shown in Fig. E5.3.1.

In the “Convergence data” table the energy stored is 70.82 J, agreeing closely with one-half the 141.65 J obtained by Maxwell for the full model of Example 4.2. The magnetic force in the table is approximately 993 N. Under the tab “Solutions” the “Force/torque” is seen to contain a small F_x and $F_y = -992.5$ N. Note that the force is downward, because steel pole faces always experience outward magnetic force. The force output by Maxwell is for 1 m depth, and for the actual 0.1 m depth the force computation would be 99.3 N.

To compare the Maxwell computation with the reluctance method and (5.11), recall from Example 3.1 that its predicted $B = 0.125$ T. Substituting in (5.11) gives

$$F_{\text{mag}} = [(0.125)^2 / (2 * 12.57 \text{E-}7)] (0.1) (0.1) = 62.15 \text{ N} \quad (\text{E5.3.1})$$

This approximate force differs considerably from the accurate 99.3 N force computed by Maxwell.

5.4 MAGNETIC PRESSURE ON STEEL

Pressure is defined as force per unit area. Thus from (5.11) for infinitely high-permeability steel poles, the magnetic pressure acting on the pole area is:

$$P_{\text{mag}} = B^2 / (2\mu_0) \quad (5.14)$$

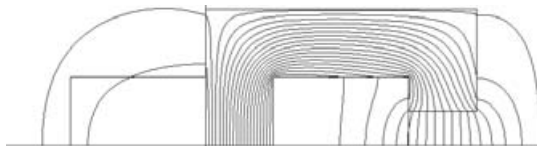


Figure E5.3.1 Computer display of flux lines in model of upper half of steel “C” with airgap.

This pressure is normal to the pole area and is one component of the *Maxwell stress tensor*. For steel of finite permeability, (5.12) gives the pressure:

$$P_{\text{mag}} = B^2/(2\mu_0) - B^2/(2\mu_s) \quad (5.15)$$

Since B is typically limited by most steel B – H curves to a practical maximum of approximately 2 T, the magnetic pressure is accordingly limited. However, instead of using (5.15) in the nonlinear case, the less well-known *nonlinear* Maxwell stress tensor should be used [4,5], which gives

$$P_{\text{mag}} = B^2/(2\mu_0) - (\mathbf{B} \cdot \mathbf{H} - w_m) \quad (5.16)$$

where w_m is magnetic energy density in the steel given in (5.4). Applying (5.5) yields an even simpler expression

$$P_{\text{mag}} = B^2/(2\mu_0) - w_{\text{co}} \quad (5.17)$$

where coenergy appears as in (5.13).

Using (5.17) instead of (5.15) further limits the maximum magnetic pressure. Figure 5.7 is a graph of the magnetic pressures in bar ($= 10^5 \text{ N/m}^2 = 10^5 \text{ Pa}$) computed using (5.14) and (5.15) for SAE 1010 steel, using its B – H curve, which is assumed to be isotropic. This commonly used steel has $B = 2.4 \text{ T}$ at $H = 320 \text{ kA/m}$. Note that the nonlinear pressure (5.17) gives pressures considerably lower than (5.15). At 2.4 T, (5.17) gives a pressure of 19.09 bar, which is 16.75% less than that given by (5.15). Figure 5.7 shows that magnetic pressures on typical steel have a practical limit of 20 bar or less. Recall that one bar is the standard pressure of air at sea level; the pressure varies with weather conditions but one bar is an approximate average.

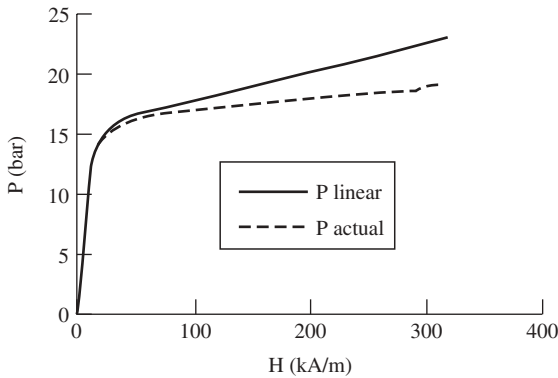


Figure 5.7 Magnetic pressures (bar) versus H (kA/m) in SAE 1010 steel. The upper curve graphs the pressure using the linear formula (5.15), whereas the lower (dashed) curve is from the actual nonlinear Maxwell stress tensor (5.17).

5.5 LORENTZ FORCE

In addition to the magnetic force and pressure on steel described in the preceding two sections and called a *reluctance force*, a magnetic force called *Lorentz force* exists on currents. On any part, such as a wire, of length l and cross-sectional area s carrying current density \mathbf{J} , the Lorentz force is

$$\mathbf{F}_L = \int (\mathbf{J} ds) \times (\mathbf{B} dl) \quad (5.18)$$

where \mathbf{B} is the magnetic flux density acting on the current density. Because (5.18) contains the cross product, the force direction is normal to both \mathbf{J} and \mathbf{B} . The force direction follows the right-hand rule as shown in Fig. 5.8. Note that an alternative expression of (5.18) is

$$\mathbf{F}_L = \int (\mathbf{J} \times (\mathbf{B}) dv) \quad (5.19)$$

where the integration is over the volume of the current density.

If \mathbf{J} and \mathbf{B} are perpendicular to each other, then the current I is perpendicular to \mathbf{B} as well. In this perpendicular case, the Lorentz force magnitude obeys the simple expression

$$F = BIl \quad (5.20)$$

where l is the length of the wire. In Fig. 5.8, the wire is coming out of the page.

Lorentz force can be computed by the method of virtual work, but is more easily and accurately computed using (5.19). Maxwell SV can be used to compute Lorentz force. Chapter 7 contains a further discussion of Lorentz force in magnetic actuators.

5.6 PERMANENT MAGNETS

A common magnetic actuator that uses Lorentz force is a voice coil actuator in loudspeakers. Such actuators obtain their magnetic flux density B using *permanent magnets*.

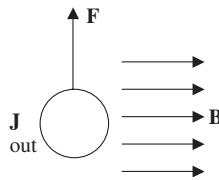


Figure 5.8 Lorentz force vectors. If the right hand is laid flat with its fingers in the direction of flux density \mathbf{B} and the thumb in the direction of current density \mathbf{J} , then the force is in the direction of the palm of the right hand.

The key to understanding permanent magnet behavior is the B – H curve. Figure 5.9 shows a typical B – H relationship for a material that can behave as a permanent magnet. After starting at the origin $(0,0)$ and increasing H by applying an increasing DC current in a nearby coil, the arrow to the right indicates the portion of the relation called the *magnetization curve*. Next, after H reaches a maximum, it is decreased and follows the arrow to the left. The curve going to the left is called the *demagnetization curve*. Since the demagnetization curve depends on the magnetization curve, demagnetization depends on the material history, a phenomenon called *hysteresis*. In contrast, the soft steel B – H relationship of Chapter 2 exhibited negligible hysteresis and was essentially a single-valued curve, unlike the multiple curves of Fig. 5.9.

Figure 5.10 is a labeled view of the second quadrant of Fig. 5.9. Note that the intercept point of the demagnetization curve with the B axis occurs at B_r , usually called the *residual flux density* (sometimes called the *remanent flux density*). The intercept point of the demagnetization curve with the negative H axis occurs at $-H_c$, where H_c is usually called the *coercive field intensity* (sometimes misleadingly called the *coercive force*).

Table 5.1 lists some of the main types of permanent magnets and their typical properties. Also listed are the approximate years of first development. Table 5.1 shows that the earliest permanent magnets were made of steel that had been hardened [5] by adding elements other than iron and by quenching (heating followed by very rapid cooling). Such hardened steels are in contrast to the soft steels of Chapter 2, which have much smaller values of B_r and H_c . Besides listing B_r and H_c , Table 5.1 also lists the maximum second quadrant product of B times H ; this energy product is the best indicator of the overall strength of a permanent magnet.

Table 5.1 shows that the first nonsteel permanent magnets developed were Alnico magnets. Alnico stands for aluminum, nickel, and cobalt, the elements used in such magnets. Note that Alnico properties are definitely superior to steels.

Next developed were ceramic magnets made of barium ferrite [6]. Both barium and ferrite (iron oxide) are low-cost, and thus ceramic magnets are inexpensive yet provide good permanent magnet properties.

The next breakthrough was the samarium cobalt magnet [6]. More expensive than ceramics, its properties are clearly superior.

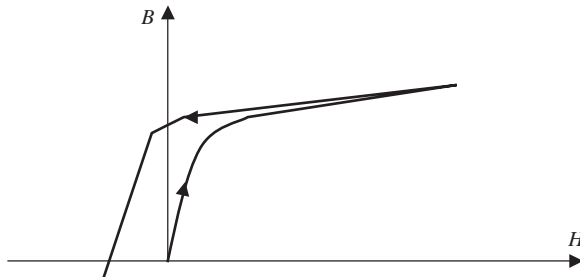


Figure 5.9 B – H relation of typical material that can exhibit permanent magnetization.

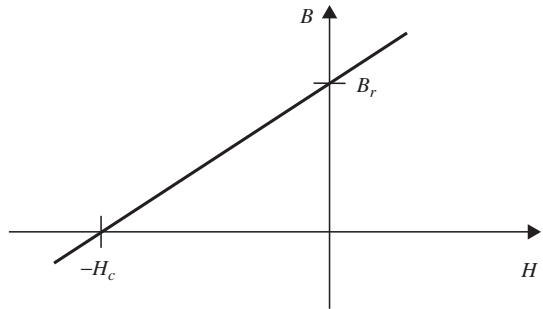


Figure 5.10 Linearized second quadrant of Fig. 5.9 with definitions of B_r and H_c .

Perhaps the best modern permanent magnet is made of elements neodymium, iron, and boron. While neodymium is an expensive rare earth, less of it is required than of inexpensive iron. Note that the latest neodymium iron magnets have H_c exceeding one million amperes per meter (1E6 A/m).

Disadvantages of permanent magnets include the need to magnetize them and the fact that most of the properties of Table 5.1 may vary significantly with temperature. A key advantage of permanent magnets over electromagnets (current-carrying coils) is that after magnetization they require no input energy and consume no power. This loss-free property is similar to that of superconductors, yet permanent magnets usually function well at room temperature and above.

Permanent magnets provide magnetic flux by means of internal currents circulating around their domains. Usually these currents cancel inside a permanent magnet and exist only on magnet surfaces. Thus in finite-element and reluctance models, a permanent magnet can be replaced by an equivalent electromagnet with currents located on certain surfaces. Figure 5.11 shows a simple rectangular permanent magnet with two poles, north (N) and south (S). North poles produce flux coming out, while south poles produce flux going into the magnet. Figure 5.11 also shows the

Table 5.1 Permanent Magnet Types and Typical Properties

Type	Approximate Year	B_r [T (teslas)]	H_c (A/m)	$(BH)_{\max}$ (T-A/m)
Carbon steel (quenched)	1600	0.9	4.E3	1.6E3
Cobalt steel (quenched)	1916	0.96	18.E3	7.2E3
Alnico3	1931	0.68	39.E3	11.1E3
Alnico5	1948	1.03	49.E3	51.7E3
Ceramic5 (ferrite)	1952	0.38	192.E3	24.E3
Ceramic8 (ferrite)	1955	0.39	240.E3	28.E3
Samarium cobalt	1970	0.88	640.E3	150.E3
Neodymium iron (early)	1990	1.08	800.E3	223.E3
Neodymium iron (latest)	2004	1.43	1080.E3	400.E3

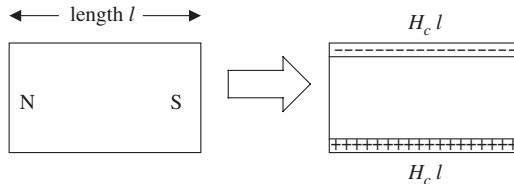


Figure 5.11 Simple permanent magnet and its equivalent coil.

equivalent electromagnet with a sheet current on two surfaces. Inside the sheet current, the equivalent electromagnet has the permeability equal to the slope of the demagnetization curve, which for most modern magnets is close to that of air.

The equivalent electromagnet of Fig. 5.11 has ampere-turns that obey [2,7]

$$NI = H_c l \quad (5.21)$$

where l is the length of the permanent magnet in the direction of magnetization. With the high H_c values of the modern magnets of Table 5.1, a typical modern permanent magnet has the equivalent of many thousands of ampere-turns.

Most finite-element software, including Maxwell SV, automatically analyzes permanent magnets using equivalent currents [7] such as those of (5.21). If the reluctance method is used, the equivalent current of permanent magnets is implemented by means of load lines, and results are usually much less accurate.

As experiments show, permanent magnets exhibit forces of attraction and repulsion between other magnets and steel. These forces can be very useful in magnetic actuators, and they can be calculated using the force equations and finite-element techniques presented and discussed earlier in this chapter.

Example 5.4 Force between Two Permanent Magnets Given two identical cylindrical neodymium iron permanent magnets with a straight line B – H curve with $B_r = 1.23$ T and $H_c = 8.9\text{E}5$ A/m. They both have radius 20 mm and height 10 mm, and are spaced 20 mm apart as shown in Fig. E5.4.1. If both magnets have their north poles on their top, obtain the magnetic force on the lower magnet using Maxwell SV.

Solution: Set the Maxwell “Solver” to “Magnetostatic” and its “Drawing” to “RZ plane.” In “Define model” enter two boxes along the left (z) axis for the two magnets. In “Set up materials” choose “NdFe35” for both magnets, and set their angle of magnetization as 90° , which is vertical with the north pole on top. Under “Set up boundaries/sources” no sources need be specified, since the permanent magnets have been defined as materials. However, the boundary condition “balloon” should be specified on the outer boundary of the model, since there is no steel to confine the flux. A balloon boundary is a type of open boundary that allows flux to leave the finite-element model space. Next, use “Set up executive parameters” to specify force computation on the lower magnet.

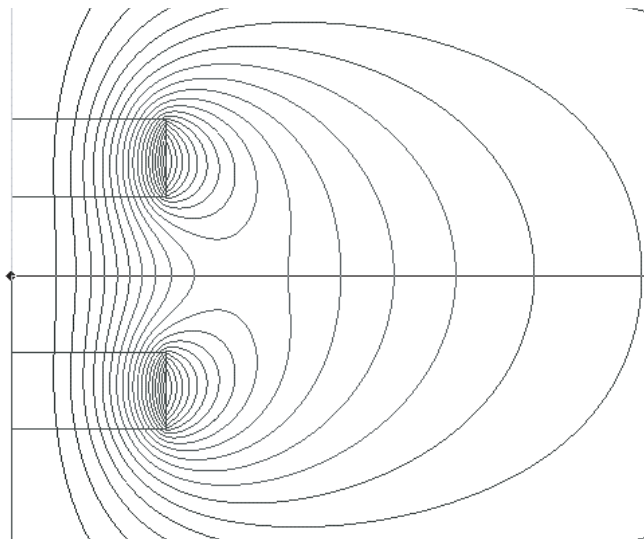


Figure E5.4.1 Computer display of two cylindrical permanent magnets and their flux lines.

Under “Set up solution options,” change the number of passes to 23. This high number is needed so that when “Solve” is clicked, the energy error will be below 2%. The computed force on the lower magnet is 30.92 N in the vertical upward direction. As expected, the north pole on the lower magnet is strongly attracted to the adjacent south pole on the upper magnet. The computed flux lines are shown in Fig. E5.4.1.

5.7 MAGNETIC TORQUE

The final topic of this chapter is magnetic torque, which is closely related to magnetic force. As before, the virtual work method may be used.

The virtual work method for magnetic torque requires the partial derivative with respect to *angle in radians* (rad):

$$T = \frac{\partial W}{\partial \theta} \quad (5.22)$$

The MKS (meter–kilogram–second) unit of both energy W and torque T is the newton-meter. For magnetic devices with constant ampere-turn excitation and materials with nonlinear B – H curves, the coenergy must be used as explained previously for magnetic force. Thus for magnetic devices, the torque is found using

$$T = \frac{\partial W_{\text{co}}}{\partial \theta} \quad (5.23)$$

The finite-element software Maxwell uses (5.23) to compute torque on parts selected by the user.

PROBLEMS

- 5.1 Redo Example 5.1 but with $A_z = x$.
- 5.2 Redo Example 5.1 but with $A_z = x + 5$.
- 5.3 Redo Example 5.1 but with $A_z = y^2$.
- 5.4 Redo Example 5.2 but with 31 divisions to obtain 30 flux lines.
- 5.5 Find the total normal magnetic pressure in pascals (newtons per square meter) acting on steel surfaces in air with $B = 1.1$ T and steel relative permeability $\mu_r = 1500$.
- 5.6 Find the total normal magnetic pressure in pascals (newtons per square meter) acting on steel surfaces in air with $B = 1.2$ T and steel relative permeability $\mu_r = 500$.
- 5.7 (a) Redo Example 5.3 but with steel relative permeability = 500; (b) also, use (5.12) as well as (5.11) to find the force using the reluctance method.
- 5.8 Redo the Maxwell computation of Example 5.3 using steel with the nonlinear curve of steel_1010.
- 5.9 A wire carrying a current of 100 A in the x direction is subjected to a magnetic flux density $\mathbf{B} = 0.8$ T in the y direction. Find the Lorentz force, a vector.
- 5.10 Find the equivalent ampere-turns of a permanent magnet with $H_c = 1$ MA/m (1E6 A/m). Its length in the direction of magnetization is 2.0 cm.
- 5.11 Redo Example 5.4 but with the permanent magnets changed to “Ceramic8D” ferrite magnets.
- 5.12 Redo Example 5.4 but with the permanent magnets changed to “SmCo28” samarium cobalt magnets.
- 5.13 Redo Example 5.4 but with the permanent magnet spacing reduced to 10 mm.
- 5.14 A rotating actuator is analyzed at two positions with constant ampere-turns applied. At 0° , the total coenergy is 2.02 J. At 1° , the total coenergy is 2.03 J. Find the torque and its direction. (*Hint:* Be sure to use radians, not degrees.)

REFERENCES

1. K. Bessho, S. Yamada, and Y. Kanamura, Analysis of transient characteristics of plunger type electromagnets, *Electric. Eng. Japan* **98**: 56–62 (July 1978).

2. J. R. Brauer, ed., *What Every Engineer Should Know about Finite Element Analysis*, 2nd ed., Marcel Dekker, New York, 1993.
3. J. R. Brauer and J. H. Lumkes, Coupled model of a magnetic actuator controlling a hydraulic cylinder and load, *IEEE Trans. Magn.* **38**: 917–920 (March 2002).
4. J. R. Brauer, J. J. Ruehl, M. A. Juds, M. J. VanderHeiden, and A. A. Arkadan, Dynamic stress in magnetic actuator computed by coupled structural and electromagnetic finite elements, *IEEE Trans. Magn.* **32**: 1046–1049 (May 1996).
5. R. M. Bozorth, *Ferromagnetism*, Wiley, New York, 1951; reprinted by Wiley IEEE Press.
6. R. J. Parker, *Advances in Permanent Magnetism*, Wiley, New York, 1990.
7. R. H. VanderHeiden, J. R. Brauer, J. J. Ruehl, and G. A. Zimmerlee, Utilizing permanent magnets in nonlinear three-dimensional finite element models, *IEEE Trans. Magn.* **24**: 2931–2933 (Nov.1988).

Other Magnetic Performance Parameters

The preceding chapter discussed force and related performance parameters of magnetic devices. This chapter discusses other magnetic performance parameters. After defining these key parameters, they are evaluated using reluctance and finite-element methods. Their relations with energy and force are also explained.

6.1 MAGNETIC FLUX AND FLUX LINKAGE

6.1.1 Definition and Evaluation

Magnetic flux through any surface s can be determined by integrating magnetic flux density \mathbf{B} , using the surface integral from Chapter 2:

$$\phi = \int \mathbf{B} \cdot d\mathbf{S} \quad (6.1)$$

If magnetic vector potential \mathbf{A} is used as in Chapter 4, then the flux can be expressed as

$$\phi = \int (\nabla \times \mathbf{A}) \cdot d\mathbf{S} \quad (6.2)$$

Using Stokes' vector identity of Chapter 2, the surface integral can be changed to a closed-line integral around the surface:

$$\phi = \oint \mathbf{A} \cdot d\mathbf{l} \quad (6.3)$$

The closed-line integral of this equation is easily evaluated from finite-element solutions of \mathbf{A} . For 2D planar solutions of depth d and vector potential component A_z obtained as described in Chapter 4, (6.3) becomes

$$\phi_{12} = (A_{z1} - A_{z2})d \quad (6.4)$$

where the flux is found that flows between any points 1 and 2 on the planar model.

Recall from Chapter 2 [Eq. (2.30)] that flux linkage is defined as flux times the number of turns of a coil:

$$\lambda = N\phi \quad (6.5)$$

Thus if the flux of (6.1)–(6.4) is found through a coil, the flux linkage is easily evaluated.

Example 6.1 Finding Flux in Example 5.3 Using Maxwell Software Given the one-half model of the “C” steel path with airgap of Example 5.3, find the flux passing through the steel pole face using Maxwell SV finite-element software and compare it with the reluctance solution of Example 3.1.

Solution: In the main Maxwell menu click on “Set up executive parameters,” and then select “Flux lines.” Enter the points on the left and right corners of the pole face, separated 0.1 m apart in the x direction, thereby forming “line1.” Then return to the main menu and click on “Solve.” You may have to request a smaller error under “Set up solution options” in order to execute a new finite-element solution. When the solution is completed, click on the upper “Solutions” tab and then on “Flux lines.” It displays “Flux linkage” = -0.014607 Wb. The Maxwell SV value is obtained using (6.4) for 1 m depth and for 1 turn. Thus the finite-element value for 0.1 meter depth is -0.00146 Wb for 1 turn. One would have to multiply by the number of turns to obtain the flux linkage of (6.5).

The reluctance method solution of Example 3.1 obtains a flux density of 0.125 T. Multiplying by the pole area of 0.1 m times 0.1 m gives a flux of 0.00125 Wb, or 125/146th the Maxwell flux. Thus, as before, the reluctance method is considerably less accurate than the finite element method.

6.1.2 Relation to Force and Other Parameters

Flux linkage is useful in several ways. One way, mentioned in Chapter 2, is to determine voltage induced by Faraday’s law (2.28):

$$V = -\frac{\partial \lambda}{\partial t} \quad (6.6)$$

Another application of flux linkage is to obtain alternative expressions for the energy, coenergy, and force of the preceding chapter. Energy input is power (voltage times current) integrated over time, giving [1]

$$W = \int VI \, dt = \int I \, d\lambda \quad (6.7)$$

where in general I versus λ is a nonlinear relation shown in Fig. 6.1. Figure 6.1 is similar to the nonlinear relation of B – H in a magnetic device graphed in Fig. 5.4. From (6.7), the energy stored is the area to the left of the curve:

$$W_{\text{mag}} = \int I d\lambda \quad (6.8)$$

Similarly to Fig. 5.4, the coenergy is the area below the curve, which is [1,2]:

$$W_{\text{co}} = \int \lambda dI \quad (6.9)$$

With the coenergy and energy known, the magnetic force may be obtained using techniques of the preceding chapter. As shown in Fig. 6.2, and in agreement with (5.13), the force in the x direction is

$$F_x = \left. \frac{\partial W_{\text{co}}}{\partial x} \right|_{I=\text{const}} \quad (6.10)$$

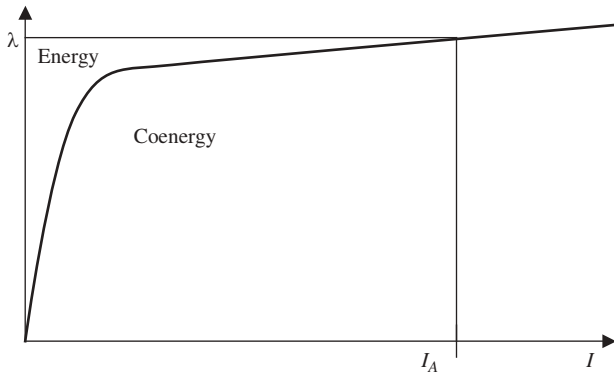


Figure 6.1 Magnetic energy and coenergy at a typical current value on a typical λ – I curve of a magnetic device.

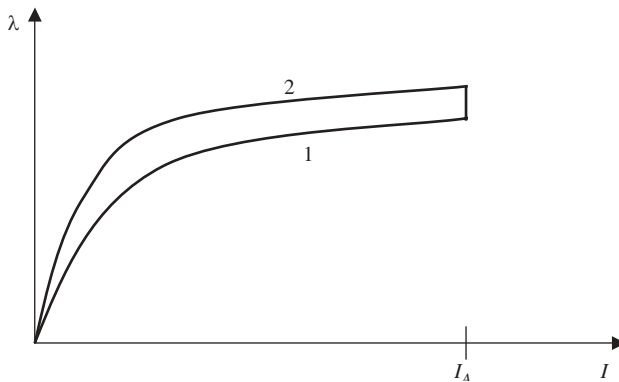


Figure 6.2 Nonlinear λ – I relation of a typical magnetic device at positions 1 and 2. The applied current is assumed to be held constant.

Similarly, torque can be found by the derivative with respect to angle as described at the end of the preceding chapter.

Example 6.2 Finding Force Given Flux Linkage versus Current and Position

Given the following relation for a magnetic actuator, find its magnetic force for $I = 2$ A and position $x = 0.05$ m:

$$\lambda = 0.15\sqrt{I/x} \quad (\text{E6.1.1})$$

Solution: The coenergy of the actuator is found using (6.9):

$$W_{\text{co}} = \int \lambda \, dI = \int 0.15I^{0.5}x^{-1} dI = (0.15/1.5)I^{1.5}x^{-1} = 0.1I^{1.5}x^{-1} \quad (\text{E6.1.2})$$

The magnetic force is then found using (6.10):

$$F_{\text{mag}} = \left. \frac{\partial W_{\text{co}}}{\partial x} \right|_{I=\text{const}} = 0.1I^{1.5} \frac{\partial}{\partial x} x^{-1} = -0.2I^{1.5}x^{-2} \quad (\text{E6.1.3})$$

which, evaluated for the given current and position, gives

$$F_{\text{mag}} = -0.2(2)^{1.5}/(0.05)^2 = -226\text{N} \quad (\text{6.1.4})$$

6.2 INDUCTANCE

6.2.1 Definition and Evaluation

The basic definition of *inductance* is

$$L = \lambda/I \quad (\text{6.11})$$

In the case of devices with purely linear B – H materials (of constant permeability), Ampere's law gives flux and flux linkage proportional to current. Hence, in linear devices, inductance is a constant, independent of current. Inductance units are henrys (H). All coils have inductance and can be called *inductors*.

For a coil with the flux linkage and current of (6.11), the inductance obtained is the *self-inductance*. For multiple coils, the ratios of different flux linkages and currents may be taken, expressed as

$$L_{jk} = \lambda_j/I_k \quad (\text{6.12})$$

If $j \neq k$, then L_{jk} is called *mutual inductance*. Self-inductance is for $j = k$. An inductance matrix is a way to express (6.12), where diagonal elements are self-inductances and off-diagonal elements are mutual inductances. The matrix is usually symmetric: $L_{kj} = L_{jk}$.

For devices with nonlinear B – H materials, flux linkage is not proportional to current and thus inductance is not uniquely defined. Figure 6.3 shows two inductances equal to two slopes. *Secant inductance* is the term often applied to the ratio λ/I at a particular current. *Incremental inductance* (also called differential inductance) is the slope of the λ – I curve:

$$L_{\text{inc}} = \frac{\partial \lambda}{\partial I} \quad (6.13)$$

Both secant and incremental inductances vary with current. Only if the current is low enough that no saturation occurs does a unique inductance apply, for in that case secant and incremental inductance are the same constant value.

Example 6.3 Finding an Inductance Matrix Using Maxwell SV Two coils are wound on a steel cylinder of length 20 mm and radius 10 mm. Both have cross section 4×4 mm and are placed flush with both ends of the cylinder as shown in Fig. E6.3.1. The steel has relative permeability of 2000. Each coil has 10 turns and carries one ampere. Make an axisymmetric finite-element model in Maxwell SV, and use it to find the inductance matrix.

Solution: In the main Maxwell menu click on “Solver” to make it “Magnetostatic” and click on “Drawing” to make it “RZ plane.” Then use “Define model” to enter the geometry, followed by “Set up materials” to enter the linear steel for the cylinder, and copper or vacuum for the coils. Next, under “Set up boundaries/sources,” give both coils 10 ampere-turns and select zero potential for the outer boundary.

Under “Set up executive parameters” click on “Matrix/flux.” Using its new window, select each coil region and (with the default return path) assign it to the ma-

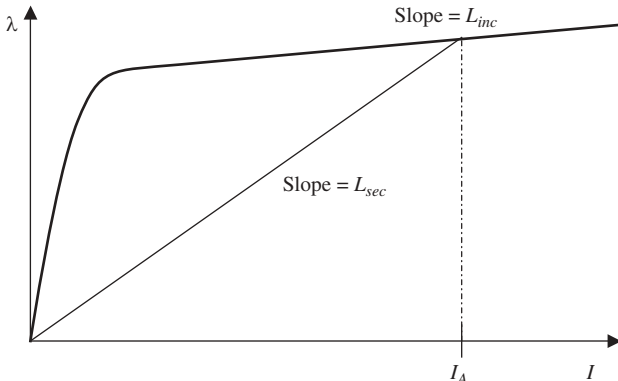


Figure 6.3 Inductances L_{sec} (secant) and L_{inc} (incremental) shown as slopes on a typical λ – I curve of a magnetic device.

trix. After allowing 13 passes under “Set up solution options,” click on “Solve.” Obtain the flux line plot shown in Fig. E6.3.1 using 21 divisions.

Finally, click on the upper “Solutions” tab to obtain “Matrix.” It shows an inductance matrix with $L_{11} = L_{22} = 6.063\text{E-}8$ H and with $L_{12} = L_{21} = 1.799\text{E-}8$ H. However, these inductances are for one turn in each coil. Each L_{jk} must be multiplied by $N_j N_k$, which is 100 in this problem, to obtain actual inductances. Note that the mutual inductances are much less than self-inductances, which is often the case. Note also that, due to the symmetry of this problem, both self-inductances are the same, and both mutual inductances are the same.

6.2.2 Relation to Force and Other Parameters

The relation between inductance and reluctance is obtained as follows. Rewriting (6.11) as

$$L = N\phi/I \quad (6.14)$$

and using the reluctance definition

$$\mathcal{R} = NI/\phi \quad (6.15)$$

to solve for N and substitute it into (6.14), we obtain

$$L = N^2/\mathcal{R} \quad (6.16)$$

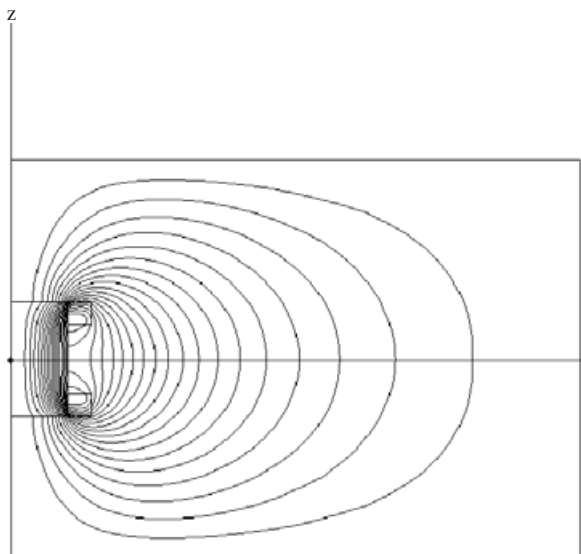


Figure E6.3.1 Computer display of two coils on a steel cylinder and the computed flux line plot for DC magnetostatics.

The magnetic energy stored in a constant (linear) inductor is [3]

$$W_{\text{mag}} = W_{\text{co}} = \int I d\lambda = \int \lambda dI = \int LI dI = \frac{1}{2}LI^2 \quad (6.17)$$

When inductance is constant over a current range but varies with position, it can be used to obtain magnetic force as follows. From (6.10), we obtain

$$F_x = \left. \frac{\partial W_{\text{co}}}{\partial x} \right|_{I=\text{const}} = \frac{\partial}{\partial x} \left[\frac{1}{2}L(x)I^2 \right]_{I=\text{const}} \quad (6.18)$$

$$F_x = \frac{1}{2}I^2 \frac{dL(x)}{dx} \quad (6.19)$$

This force equation is valid for a magnetic device with a single coil and single self-inductance. When multiple coils are energized, energies and forces are added as a result of the other self-inductances and mutual inductances. For example, for two coils coupled through mutual inductance L_{12} , magnetic energy is

$$W_{\text{mag}} = \frac{1}{2}L_{11}I_1^2 + \frac{1}{2}L_{22}I_2^2 + L_{12}I_1I_2 \quad (6.20)$$

and the related force is

$$F_x = \frac{1}{2}I_1^2 \frac{dL_{11}(x)}{dx} + \frac{1}{2}I_2^2 \frac{dL_{22}(x)}{dx} + I_1I_2 \frac{dL_{12}(x)}{dx} \quad (6.21)$$

6.3 CAPACITANCE

6.3.1 Definition

Coils and other parts of magnetic devices possess *capacitance*. The basic definition of capacitance is

$$C = Q/V \quad (6.22)$$

where Q is the charge in coulombs and V is the voltage. The unit of capacitance is the farad (F), and a device possessing capacitance is called a capacitor.

A typical capacitor has been shown in Fig. 2.7. As discussed in Chapter 2, capacitors are electric field devices, not magnetic field devices. Thus this book does not discuss capacitors in detail. However, because capacitance plays a role in the performance of magnetic actuators and sensors, especially at high frequencies, a few basics of capacitance are needed here.

The capacitance of (6.22) is called *self-capacitance* if the voltage is across two conducting plates (as in Fig. 2.7) and the charge is the magnitude of the charge on each plate. A capacitance matrix, analogous to an inductance matrix, is important if there are more than two plates.

Capacitance can be evaluated using the finite-element method for electrostatic fields, as will be shown in the next subsection.

6.3.2 Relation to Energy and Force

The electric field energy stored in a capacitor is

$$W_{\text{el}} = \frac{1}{2} \int \mathbf{D} \cdot \mathbf{E} \, dv = \frac{1}{2} \int \epsilon E^2 \, dv = \frac{1}{2} CV^2 \quad (6.23)$$

where the various parameters, including permittivity ϵ , have been defined in Chapter 2.

When capacitance varies with position, an electric field force is created. The virtual work method can again be used to obtain the force as the derivative of energy:

$$F_x = \left. \frac{\partial W_{\text{el}}}{\partial x} \right|_{V=\text{const}} = \left. \frac{\partial}{\partial x} \left[\frac{1}{2} C(x) V^2 \right] \right|_{V=\text{const}} \quad (6.24)$$

$$F_x = \frac{1}{2} V^2 \frac{dC(x)}{dx} \quad (6.25)$$

If the force is desired in terms of fields rather than capacitance, then the change in stored electric field energy in Fig. 2.7 can be found for a virtual displacement Δy of either plate. By observing the change in stored energy as was done for magnetic fields in Fig. 5.5, the pressure due to an electric field E in air is found to be

$$P_{\text{el}} = \frac{1}{2} \epsilon_0 E^2 \quad (6.26)$$

Because the electric field intensity of (6.23) is usually limited because of material breakdown (arcing and similar destructive behavior), electric field forces and pressures are usually much smaller than magnetic field forces and pressures. For example, in air the breakdown E is approximately 3 MV/m, varying somewhat with humidity, temperature, and pressure. Substituting that E into (6.26) gives an electric field pressure of 39.8 Pa, far below the maximum 20.E5 pascals produced by magnetic fields on steel poles in air.

Example 6.4 Finding Capacitance Using Maxwell SV Two aluminum plates 2 m wide are separated by 1 m as shown originally in Fig. 2.7 and also in Fig. E6.4.1. The lower plate is at 0 V and the upper, at 1 V. The region between the two plates is assumed filled with polystyrene, which has a relative permittivity of 2.6. Find the voltage contours, electric field, energy stored, and capacitance using Maxwell SV. Validate the energy stored using (6.23).

Solution: In the main Maxwell menu make sure that “Solver” is set to its default “Electrostatic” and “Drawing” to “XY plane.” The geometry of Fig. E6.4.1 is en-

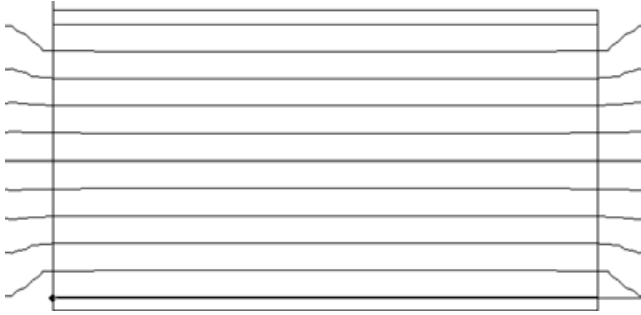


Figure E6.4.1 Computer display of capacitor with computed voltage contours.

tered using three “Box” commands. The material properties of aluminum and polystyrene are selected from the material list. The boundary conditions are then entered, consisting solely of setting the lower plate to 0 V and the upper plate, to 1 V. The solution, obtained in one pass, has an energy stored of $2.41\text{E-}11$ J. Postprocessing gives contours of constant phi (voltage) shown in Fig. E6.4.1. A color plot of the magnitude of E shows it to be 1.0 V/m between the plates, as expected from Fig. 2.7. The expected electric energy stored from (6.23) is

$$W_{\text{el}} = \frac{1}{2} \int \epsilon E^2 dv = (0.5)(2.6)(8.854\text{E-}12)(1)^2(1)(2)(1) = 2.3\text{E-}11 \text{ J} \quad (\text{E6.4.1})$$

which is in reasonable agreement with the $2.41\text{E-}11$ J output by Maxwell SV. Using this Maxwell energy value in (6.23) gives

$$W_{\text{el}} = 2.41\text{E-}11 = \frac{1}{2} CV^2 = 0.5C \quad (\text{E6.4.2})$$

$$C = 2(2.41\text{E-}11) = 48.2 \text{ pF} \quad (\text{E6.4.3})$$

6.4 IMPEDANCE

Many magnetic devices carry sinusoidal alternating current, often of frequency 50 or 60 Hz. For AC devices and systems, impedance is a complex number (in ohms) defined as

$$Z = V/I \quad (6.27)$$

where V is complex phasor voltage and I is complex phasor current.

In magnetic devices, voltage obeys Faraday’s law (6.6), which for AC frequency f (in Hz), becomes

$$V = -j2\pi f\lambda \quad (6.28)$$

where the time derivative of (6.6) has been replaced by $j2\pi f$, where j is the square root of minus one [4]. The imaginary number j causes the voltage V to be 90° out of phase from the flux linkage λ . In Chapter 2, such a 90° phase shift was shown in Example 2.7, in which a time derivative caused a sine to become a cosine.

In AC analyses, it is common to call $2\pi f$ the angular frequency ω [in radians per second (rad/s)], and thus (6.28) becomes

$$V = -j\omega\lambda \quad (6.29)$$

Substituting (6.3) and (6.5) gives

$$V = -j\omega N \oint \mathbf{A} \cdot d\mathbf{l} \quad (6.30)$$

and hence the impedance (with the sign reversed to follow normal sign conventions) of (6.27) is

$$Z = j\omega N \oint \mathbf{A} \cdot d\mathbf{l} / I = j\omega\lambda / I \quad (6.31)$$

Z is in general a complex number, and can be split into real and imaginary components:

$$Z = R + jX \quad (6.32)$$

X is called *reactance* and is shown using (6.14) to be proportional to inductance:

$$X = j\omega L \quad (6.33)$$

As discussed in Chapter 2, the resistance R can account for power losses due to induced eddy currents in conducting materials. Maxwell SV has a solution type “eddy current,” which solves for AC fields and impedance. Similar to the inductance and capacitance matrices discussed above, impedance matrices can be obtained for multiple coils. AC fields are discussed further in Chapter 8.

Example 6.5 Finding an Impedance Matrix Using Maxwell SV As in Example 6.3, two coils are wound on a steel cylinder of length 20 mm and radius 10 mm. Both have cross section 4×4 mm and are placed flush with both ends of the cylinder as shown in Figs. E6.3.1 and E6.5.1. The steel has relative permeability of 2000 and conductivity $2.E6$ S/m. Each coil has 10 turns of stranded wire (the stranding eliminates eddy currents in the wire) and carries one ampere real of AC current of frequency 60 Hz. Construct an axisymmetric finite-element model in Maxwell SV, and use it to find the impedance matrix.

Solution: (*Hint:* If you have already solved Example 3.3, copy it to a new project.) In the main Maxwell menu click on “Solver” to make it “Eddy current” and click on “Drawing” to make it “RZ plane.” If you have not previously defined the geometry,

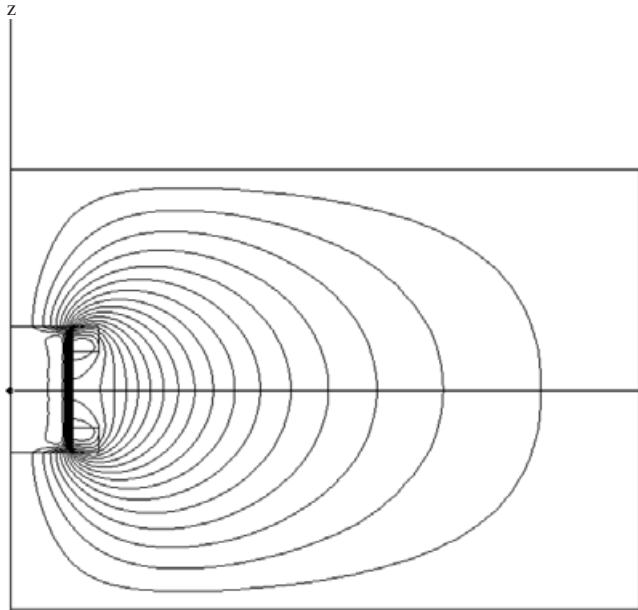


Figure E6.5.1 Computer display of two coils on a conducting steel cylinder and the computed 60-Hz flux line plot.

use “Define model” to enter the geometry. Next use “Set up materials” to enter the linear steel for the cylinder, and copper or vacuum for the coils. Make sure that the steel has the conductivity $2.E6$ S/m. Next, under “Set up boundaries/sources,” give both coils 10 ampere-turns (be sure to select stranded and phase angle 0) and select zero potential for the outer boundary.

Under “Set up executive parameters” click on “Matrix/flux.” Using its new window, select each coil region and (with the default return path) assign it to the matrix. After allowing 14 passes under “Set up solution options,” click on “Solve.” Obtain the flux line plot shown in Fig. E6.5.1 using 21 divisions. Note that it is very different from the DC flux line plot of Fig. E6.3.1, especially in the steel, evidently due to its eddy currents. Chapter 8 will explain that the eddy currents force the flux to flow near the skin of the conducting steel.

Finally, click on the upper “Solutions” tab to obtain “Matrix.” It shows a matrix with $L_{11} = L_{22} = 6.046E-8$ H and with $L_{12} = L_{21} = 1.785E-8$ H. However, these values are for one turn in each coil. Each L_{jk} must be multiplied by $N_j N_k$, which is 100 in this problem, to obtain actual inductances. Note that the mutual inductances are much less than self-inductances, and are only slightly different from the DC case of Example 6.3. Note also that because of the symmetry of this problem, both self-inductances are the same, and both mutual inductances are the same. To obtain reactance components of impedance, all inductances must be multiplied by $\omega = 2\pi f = 2\pi 60 = 377$.

The matrix also contains resistances $R_{11} = R_{22} = 8.916\text{E-}8 \Omega$ and $R_{12} = R_{21} = 6.246\text{E-}8 \Omega$. Again, these values are for one turn in each coil. Each R_{jk} must be multiplied by $N_j N_k$, which is 100 in this problem, to obtain the actual resistances. These resistances account for eddy current power loss in the conducting steel.

PROBLEMS

- 6.1 Redo the flux computation of Example 6.1, but find the flux in the steel along the horizontal symmetry plane.
- 6.2 Recalculate the force of Example 6.2 at the same current and voltage but with a new relation:

$$\lambda = 0.3I^{0.7}/x \quad (\text{P6.2.1})$$

- 6.3 Prove that an alternative formula for magnetic force is

$$F_{\text{mag}} = \left. \frac{\partial W_{\text{mag}}}{\partial x} \right|_{\lambda = \text{const}} \quad (\text{P6.3.1})$$

Then use it to obtain the same force value found in Example 6.2.

- 6.4 Redo Example 6.3 with the steel changed to the nonlinear “steel_1010.”
- 6.5 Redo Example 6.3 with the number of turns of the lower coil changed to 20.
- 6.6 Redo Example 6.3 with the upper coil moved up by 4 mm.
- 6.7 From the results of Example 3.1 using the reluctance method, find the inductance of the coil assuming that its number of turns is 100.
- 6.8 From the results of Example 3.2 using the reluctance method, find the inductance of the coil for both positions assuming the number of turns is 100.
- 6.9 Given the complex flux linkage $\lambda = 2 + j3$ weber-turns and current $I = 0.5$ A, find the impedance, resistance, reactance, and inductance (for 8 turns and 60 Hz).
- 6.10 Redo Example 6.5 with with the steel changed to the nonlinear “steel_1010.”
- 6.11 Redo Example 6.5 with the number of turns of the lower coil changed to “steel_1020.”
- 6.12 Redo Example 6.5 with the upper coil moved up by 4 mm.

REFERENCES

1. P. C. Sen, *Principles of Electric Machines and Power Electronics*, 2nd ed., Wiley, New York, 1997.

2. A. E. Fitzgerald, C. Kingsley Jr., and S. D. Umans, *Electric Machinery*, 6th ed., McGraw-Hill, New York, 2003.
3. Gordon R. Slemon, *Magnetoelectric Devices*, Wiley, New York, 1966.
4. C. K. Alexander and M. N. O. Sadiku, *Fundamentals of Electric Circuits*, McGraw-Hill, New York, 2000.

PART II

ACTUATORS

Magnetic Actuators Operated by Direct Current

Magnetic actuators use magnetic fields to transform electrical energy into mechanical energy. Thus they are a type of *transducer*, which is any device that transforms one type of energy into another [1]. However, the mechanical motion of the magnetic actuators discussed in this book is over a limited range of motion. This limited range is commonly assumed for actuators, unlike electric motors and other rotary electromagnetic machines, which have large unlimited motion over multiple revolutions. This part of the book, Part II, is devoted to magnetic actuators.

This chapter discusses in detail the most common types of magnetic actuators operated by direct current, in the following order: solenoid actuators, voice coil actuators, other linear actuators, proportional actuators, and rotary actuators.

7.1 SOLENOID ACTUATORS

Solenoid actuators have a *solenoidal coil*, which is a coil of wire wound to a shape that is sometimes cylindrical. All solenoid actuators also have a steel *armature*, a term for the moving part. In solenoid actuators, the armature moves along a straight line, and thus produces *linear motion*.

7.1.1 Clapper Armature

A solenoid actuator with a *clapper* armature functions similarly to a clapping hand. The armature acts like one hand that is drawn by magnetic force to the second hand. Because the second “hand” is stationary, it is called the *stator*.

Like a clapping hand, the clapper armature usually contacts the stator at two areas. In one area, magnetic flux enters the armature, while it leaves the armature through the other area, producing useful magnetic force over both areas. Since magnetic flux must always both enter and leave the armature (or any other volume as discussed in Chapter 1), the clapper armature is often more compact than other designs. The clapper may be either flat, like a flat hand, or may have ridges, like a cupped hand.

The coil may be excited by either a DC voltage (and current) or by an AC voltage (and current). This chapter deals only with actuators operated by DC, while AC

actuators are discussed in the next chapter. However, any such voltage (and current) must be turned on and off at some time in the past and future, and such transient effects are discussed in Chapter 9.

An example of a DC clapper solenoid is shown in Fig. 7.1a. It is somewhat similar to the Eaton Cutler–Hammer AC solenoid [2] shown in Chapter 2. Its magnetic flux pattern computed by finite-element analysis is shown in Fig. 7.1b.

As shown in the solenoid of Fig. 7.1, the clapper and the stator can be made of steel laminations. Laminating the steel minimizes eddy current effects that reduce force and increase power loss. If laminations are used, they are usually stacked to form a geometry that must be two-dimensional, or planar.

Instead of planar geometry, axisymmetric geometry is very common. Solenoidal coils are often cylindrical and thus axisymmetric. If these coils are surrounded by axisymmetric steel, an axisymmetric solenoid is created. However, since axisymmetric geometries cannot be laminated at low cost, axisymmetric solenoids are commonly made of solid steel.

The magnetic force produced by a solenoid actuator usually varies considerably with airgap and with coil current. Assuming for illustrative purposes that the steel permeability is infinite (and thus the MMF drop in the steel is zero) and that the two air gaps each have length g and poles of equal area, Ampere's law gives the following formula for H in both airgaps

$$H = NI/(2g) \quad (7.1)$$

and thus the flux density in both airgaps is

$$B = \mu_0 NI/(2g) \quad (7.2)$$

The normal (perpendicular) magnetic pressure from Maxwell's stress tensor of Chapter 5 is equal to the flux density squared divided by twice the permeability of air. Assuming that the S values of the two pole surface "seen" areas are the same, the total magnetic force is

$$F = (\mu_0 NI)^2 (2S)/(4g^2 2\mu_0) = \mu_0 N^2 I^2 S/4g^2 \quad (7.3)$$

Note that this approximate inherent magnetic force is inversely proportional to the square of the airgap, and thus varies tremendously with respect to airgap. It also is proportional to the square of the coil current, and thus increases greatly with increasing current. When this force is plotted against x (armature position), a *pull curve* is produced. A set of pull curves for various currents on one plot is often used by actuator designers and users, as will be shown in Example 7.1 and in Chapter 15.

In reality, due to actual steel B – H curves and complex shapes of steel and air, most solenoid actuators have pull curves that do not closely follow (7.3). For most solenoid actuators, the pull curves are indeed curves, that is, the force varies nonlinearly with both airgap and current.

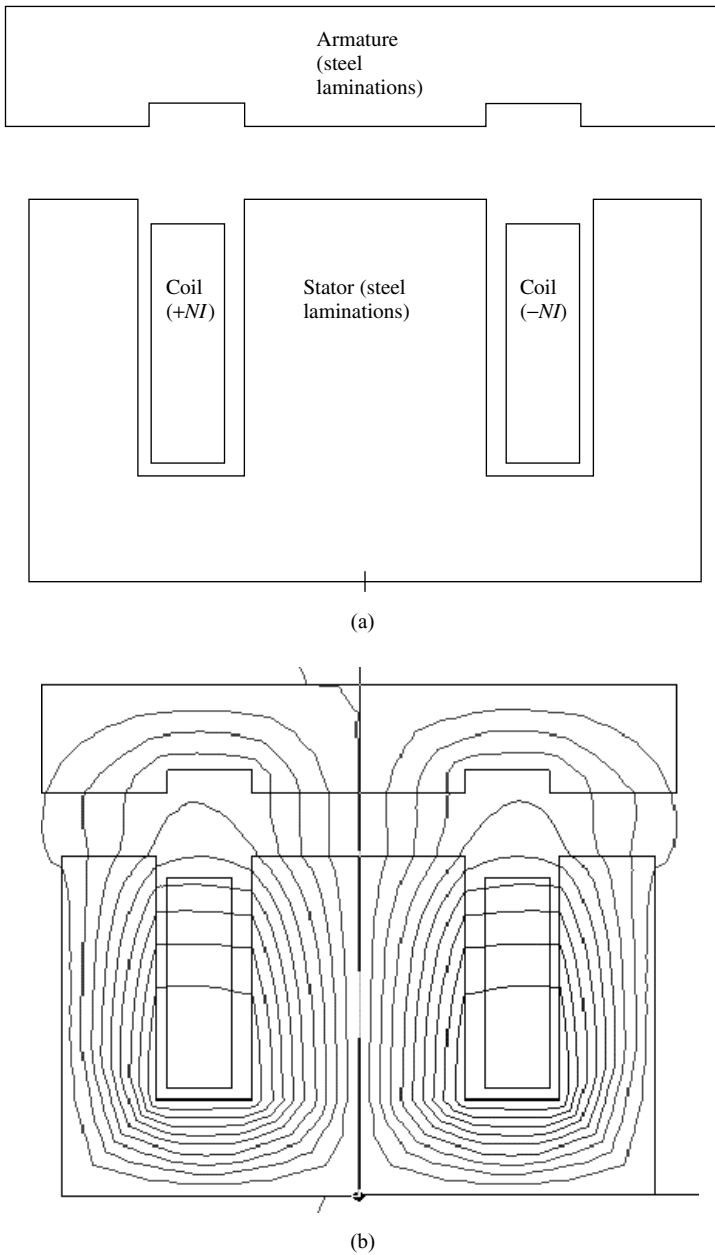


Figure 7.1 Typical clapper type solenoid actuator: (a) geometry, where steel is made up of thin laminations lying in the plane of the page and stacked in the direction out of the page; (b) computer display of flux lines obtained by finite-element analysis.

Example 7.1 Fluxes and Forces on Clapper Armature Solenoid of Planar Geometry Figure E7.1.1 shows a planar solenoid with a clapper armature. The stator winding shown has 200 turns and has an end (return) current path (not shown) outside the core. The dimensions are $w = 10$ mm, $Al_1 = 5$ mm, $Al_2 = 30$ mm, $Al_3 = 5$ mm, $Sl_1 = 15$ mm, $Sl_2 = 30$ mm, $Sl_3 = 15$ mm, and $g = 2$ mm.

- Use the reluctance method, assuming no leakage or fringing fluxes, to find the approximate values of the vectors \mathbf{B} and \mathbf{F} on left side of clapper for $I = 2$ A. Find \mathbf{F} in newtons per meter depth of the solenoid into the plane of the page.
- Repeat (a) to find the vectors \mathbf{B} and \mathbf{F} on right side of clapper.
- Obtain the answers with finite-element software by using high-permeability material (relative permeability = 2000) in the steel.
- Obtain force \mathbf{F} as given above with finite-element software with steel relative permeability = 10,000, and comment on why the results differ from those in (c).
- Repeat (d) for the gap varying from 4 to 0.5 mm in 0.5-mm increments and the current varying from 2 to 4 A in 1-A increments.

Solution

- The total reluctance is the sum of the stator reluctance \mathcal{R}_s , the left airgap reluctance \mathcal{R}_{gL} , the armature reluctance \mathcal{R}_a , and the right airgap reluctance \mathcal{R}_{gR} . Finding each from length over (permeability times area) gives

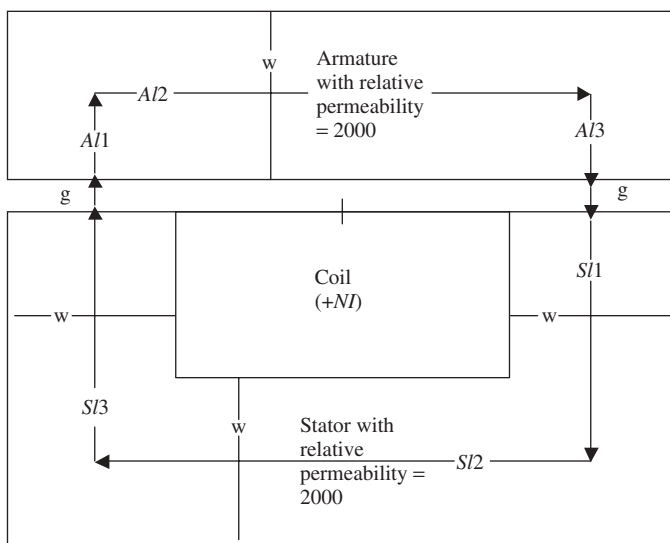


Figure E7.1.1 Example 7.1 clapper solenoid actuator of planar geometry.

$$\mathcal{R}_s = (Sl_1 + Sl_2 + Sl_3)/[(2000 \cdot 12.57\text{E-}7)(w \cdot 1)] = (0.06)/(25.14\text{E-}6) = 2387$$

$$\mathcal{R}_{gL} = g/[(12.57\text{E-}7)(w \cdot 1)] = (0.002)/(12.57\text{E-}9) = 159,109$$

$$\mathcal{R}_a = (Al_1 + Al_2 + Al_3)/[(2000 \cdot 12.57\text{E-}7)(w \cdot 1)] = (0.040)/(25.14\text{E-}6) = 1591$$

$$\mathcal{R}_{gR} = g/[(12.57\text{E-}7)(w \cdot 1)] = (0.002)/(12.57\text{E-}9) = 159,109$$

The flux is then $NI/(\text{total reluctance}) = (200 \cdot 2)/(322,196) = 1.2415\text{E-}3$ Wb. The flux density in each airgap (and in most of the steel) is the flux divided by $(w \cdot 1) = 0.12415$ T. From the right-hand rule, the direction of \mathbf{B} in the left gap is in the $-y$ direction. The pressure on each airgap is thus $B^2/(2 \cdot 12.57\text{E-}7) = 6131$ Pa, which, when multiplied by the airgap area of 0.01 m², gives the force on the left gap = 61.31 N. The force is always attractive, and thus the armature force is in the $-y$ direction.

- (b) By symmetry, \mathbf{B} is reversed in direction but force \mathbf{F} is the same on the right side of the clapper. Thus the total force by the reluctance method is 122.62 N. For a solenoid depth of d meters into the page, the force must be multiplied by d .
- (c) For the airgap shown of 2 mm, a model was quickly made using Ansoft's Maxwell SV, with modeling steps for magnetostatics described in previous chapters. The computed force on the armature for $I = 2$ A is 135.97 N per meter depth. This is larger than the force estimated by the reluctance method, partly because the reluctance method does not account for fringing near the poles.
- (d) The higher permeability raises the Maxwell SV computed force to 143.33 N. The increase is small because the steel reluctance is small compared with the airgap reluctance for the 2 -mm gap.
- (e) The force curves obtained using Maxwell's parametric capability are shown in Fig. E7.1.2. These pull curves show that the force is highly nonlinear (even for the assumed linear steel B - H curve of constant permeability), increasing greatly with small gap and high current.

Example 7.2 Fluxes and Forces on Clapper Armature Solenoid of Axisymmetric Geometry Figure E7.2.1 shows an axisymmetric solenoid with a clapper armature. The number of turns $N = 2000$ and the current $I = 1$ A. The dimensions are $g = 2$ mm, $w_a = 8$ mm, $R_1 = 15$ mm, $R_2 = 25$ mm, $R_3 = 30$ mm, $Z_1 = 8$ mm, and $Z_2 = 23$ mm.

Use the reluctance method, assuming no leakage or fringing fluxes, to find the approximate values of (a) \mathbf{B} and \mathbf{F} on inside of clapper and (b) \mathbf{B} and \mathbf{F} on outside of clapper. Then obtain the answers to (a) and (b) with finite element software (c) by using high-permeability material (relative permeability = 2000) in the steel and (d) with finite-element software with steel relative permeability = $10,000$, and comment on why the results differ.

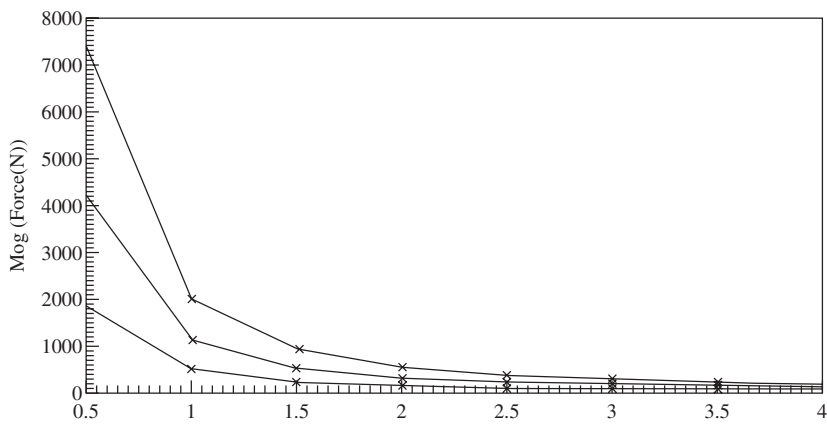


Figure E7.1.2 Pull curves computed for Example 7.1. The curves are for currents of 2, 3, and 4 A. The force (N) on the vertical (ordinate) axis is plotted against the airgap (mm) on the horizontal axis.

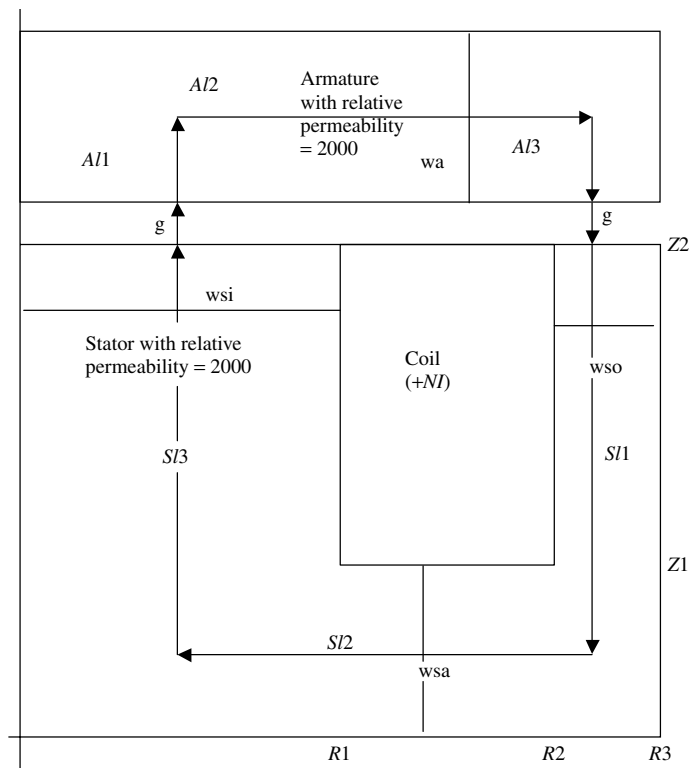


Figure E7.2.1 Example 7.2 clapper solenoid actuator of axisymmetric geometry. As customary, the axis of symmetry is the vertical line on the left border.

Solution

- (a) Pathlengths for the reluctance method are seen to be $Al_1 = 4$ mm, $Al_2 = 20$ mm, $Al_3 = 4$ mm, $Sl_1 = 19$ mm, $Sl_2 = 20$ mm, $Sl_3 = 19$ mm, $w_{si} = 15$ mm, $w_{sa} = 8$ mm, $w_{so} = 5$ mm. The total reluctance is the sum of the stator reluctance \mathcal{R}_s , the left airgap reluctance \mathcal{R}_{gL} , the armature reluctance \mathcal{R}_a , and the right airgap reluctance \mathcal{R}_{gR} . Finding each from length over (permeability times area) gives

$$\begin{aligned}\mathcal{R}_s &= (Sl_1)/[(2000 \cdot 12.57\text{E-}7)(\pi(R_3^2 - R_2^2))] + (Sl_2)/[(2000 \cdot 12.57\text{E-}7)\pi(R_1 + R_2)w_{sa}] \\ &\quad + (Sl_3)/[(2000 \cdot 12.57\text{E-}7)(\pi R_1^2)] \\ &= (0.019)/[(2.514\text{E-}3)\pi(0.03^2 - 0.025^2)] + (0.02)/[(2.514\text{E-}3)\pi(0.04)(0.008)] \\ &\quad + (0.019)/[(2.514\text{E-}3)\pi(0.015)^2] \\ &= 8748 + 7913 + 10692 = 27,353\end{aligned}$$

$$\mathcal{R}_{gL} = g/[(12.57\text{E-}7)(\pi R_1^2)] = (0.002)/[(12.57\text{E-}7)(\pi 0.015^2)] = 2.251\text{E}6$$

$$\begin{aligned}\mathcal{R}_a &= (Al_1 + Al_2 + Al_3)/[(2000 \cdot 12.57\text{E-}7)(w_a)\pi(R_1 + R_2)] \\ &= (0.028)/(2.514\text{E-}3)(1\text{E-}3) = 11,138\end{aligned}$$

$$\mathcal{R}_{gR} = g/[(12.57\text{E-}7)\pi(R_3^2 - R_2^2)] = (0.002)/[(12.57\text{E-}7)(864\text{E-}6)] = 1.842\text{E}6$$

The flux is then $NI/(\text{total reluctance}) = (2000 \cdot 1)/(4.132\text{E}6) = 48.41\text{E-}5$ Wb. The flux density in the left gap is the flux divided by (πR_1^2) and thus is 0.685 T. The pressure on the left airgap is thus $B^2/(2 \cdot 12.57\text{E-}7) = 187\text{E}3$ Pa, which, when multiplied by the airgap area of $707\text{E-}6$ m², gives the force on the left gap = 132 N. The flux density in the right gap is the flux divided by $\pi(R_3^2 - R_2^2)$ and thus is 0.56 T. The pressure on the right airgap is thus $B^2/(2 \cdot 12.57\text{E-}7) = 124.7\text{E}3$ Pa, which, when multiplied by the airgap area of $864\text{E-}6$ m² gives the force on the left gap = 108 N. The total force is 240 N and is always attractive, and thus the armature force is in the $-z$ direction.

- (b) B is about 0.82 T on the inner pole and 0.45 T on the outer pole. $F = 279.41$ N.
(c) The force increases to 285.1 N because of the higher permeability of steel.

7.1.2 Plunger Armature

Unlike a clapper armature, a plunger armature is not flat or cupped like a hand, but is basically a brick or cylinder, often shaped like a piece of chalk [3]. Figure 7.2 shows a typical cylindrical plunger actuator in a DC solenoid.

Unlike a clapper armature, where magnetic force in the direction of linear motion is produced where the flux both enters and leaves, the plunger armature has useful magnetic force on only one area. The useful force is produced only at the end of the plunger, which is usually either a flat rectangular or circular area or a conical



Figure 7.2 Photo of typical plunger-type axisymmetric solenoid actuator. A sector of the stator has been sawed away to show the coil cross section.

area. The flux usually leaves this end area, and enters the armature through the sides of the plunger. Little or no useful magnetic force is produced by the flux on the sides of the plunger, and thus the plunger armature solenoid might have less force per unit volume than the clapper armature solenoid of Section 7.1.1.

While the plunger is often a pure cylindrical shape as shown in Fig. 7.2, it can also be shaped for “constant force” as the armature moves. Such “constant force” or “proportional” solenoids will be discussed in later sections of this chapter.

If the plunger is cylindrical as in Fig. 7.2, then the solenoid is usually axisymmetric, and is thus made of solid steel. However, if the plunger is a rectangular brick shape, then it can be inexpensively laminated and placed in a laminated stator to form a planar solenoid. As mentioned previously, eddy currents are reduced when steel is laminated. Reducing eddy currents gives reduced losses and increased magnetic forces, as will be discussed further in Chapters 8 and 9.

Finite-element analysis of axisymmetric plunger armature solenoids has been combined with *design optimization methods* to mathematically obtain optimum designs [4]. Design optimization software has been developed [5] and is becoming increasingly powerful and available. A simpler way, however, to optimize design of magnetic devices is to run multiple finite-element analyses with varying design parameters such as pole width and armature length, and choose the design that produces the highest force. Such multiple runs are called *parametric finite-element analysis*.

Example 7.3 Fluxes and Forces on Planar Plunger Armature Solenoid

Figure E7.3.1 shows a planar solenoid with a plunger armature. The number of turns $N = 1000$ and the current $I = 2$ A. The dimensions are $w = 8$ mm, $g = 4$ mm, $g_s = 1$ mm, $Al_1 = 4$ mm, $Al_2 = 22$ mm, $Sl_1 = 8$ mm, $Sl_2 = 20$ mm, $Sl_3 = 34$ mm, and $Sl_4 = 15$ mm.

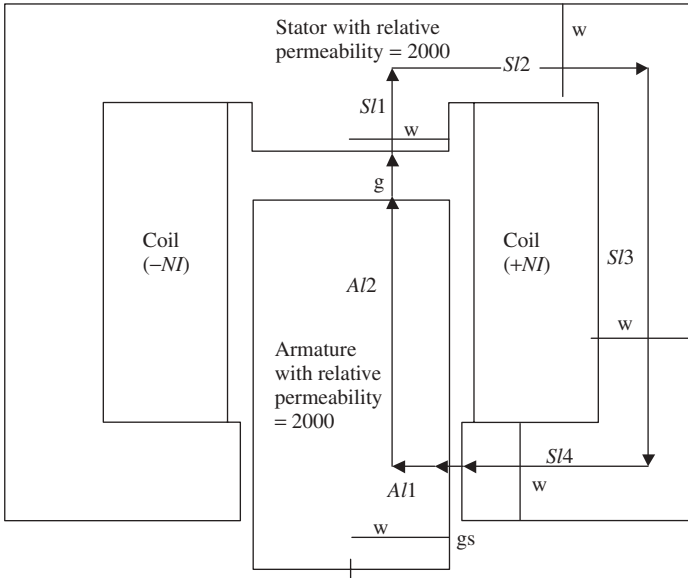


Figure E7.3.1 Example 7.3 plunger solenoid actuator of planar geometry.

- Use the reluctance method, assuming no leakage flux, to find the approximate values of \mathbf{B} and \mathbf{F} on the end of the plunger.
- Compute \mathbf{B} and \mathbf{F} using finite-element software with relative permeability = 2000 in the steel.
- Obtain the answers with finite-element software with steel relative permeability = 10,000, and comment on why the results differ.

Solution

- There are two flux paths—left and right—of equal lengths, areas, and reluctances. The total reluctance of the right path is the sum of the stator reluctance \mathcal{R}_s , the working airgap reluctance \mathcal{R}_g , the armature reluctance \mathcal{R}_a , and the side airgap reluctance \mathcal{R}_{gs} . Finding each from length over (permeability times area) gives

$$\mathcal{R}_s = (SI_1 + SI_2 + SI_3 + SI_4) / [(2000 \cdot 12.57\text{E-}7)(w \cdot 1)]$$

$$= (0.077) / [(2.514\text{E-}3)(0.008)] = 3829$$

$$\mathcal{R}_g = g / [(12.57\text{E-}7)(w \cdot 1)] = (0.004) / (10.06\text{E-}9) = 397,614$$

$$\mathcal{R}_a = (AI_1 + AI_2) / [(2000 \cdot 12.57\text{E-}7)(w \cdot 1)] = (0.026) / [(2.514\text{E-}3)(0.008)] = 1293$$

$$\mathcal{R}_{gs} = g_s / [(12.57\text{E-}7)(w \cdot 1)] = (0.001) / (10.06\text{E-}9) = 99,443$$

The right flux is then $NI/(\text{total reluctance}) = (1000 \cdot 2)/(502,179) = 3.983\text{E-}3$ Wb. The flux density in the working airgap g (and in most of the steel) is the flux divided by $(w \cdot 1) = 0.498$ T. From the right-hand rule, the direction of \mathbf{B} in the working gap is in the $-y$ direction. The pressure on each airgap is thus $B^2/(2 \cdot 12.57\text{E-}7) = 98582$ Pa, which, when multiplied by the total working airgap area of 0.016 m², gives the force on the armature = 1577 N (for one meter depth). The force is always attractive, and thus the armature force is in the y direction. To find the force on the solenoid of depth d meters, the 1577 N must be multiplied by d .

- (b) $F = 1863$ N for one meter depth using Maxwell SV, and B at the plunger end varies by ~ 0.51 T.
- (c) $F = 1900$ N per meter depth using Maxwell SV, higher because of the higher permeability of steel.

Example 7.4 Fluxes and Forces on Axisymmetric Plunger Armature Solenoid

Figure E7.4.1 shows an axisymmetric solenoid with a plunger armature. The number of turns $N = 400$ and the current $I = 4$ A. The dimensions are: plunger and pole outer radius $R_P = 20$ mm, side airgap outer radius $R_{PG} = 22$ mm, stator yoke outer radius $R_{YO} = 70$ mm, stator yoke inner radius $R_{YI} = 66$ mm, working airgap $g = 10$ mm, plunger length $L_P = 42$ mm, stator stopper length $L_S = 16$ mm, coil axial length $L_C = 46$ mm, and stator yoke axial thickness $t = 12$ mm (on top; same on bottom).

- (a) Use the reluctance method, assuming no leakage flux, to find the approximate values of \mathbf{B} and \mathbf{F} in the working air gap on the end of the plunger.
- (b) Compute \mathbf{B} and \mathbf{F} using finite-element software, with the relative permeability = 2000 in the steel.
- (c) Obtain the answers with finite-element software with steel relative permeability = 10,000, and comment on why the results differ.

Solution

- (a) The total reluctance is the sum of the stator reluctance \mathcal{R}_s , the working airgap reluctance \mathcal{R}_{gW} , the armature reluctance \mathcal{R}_a , and the side airgap reluctance \mathcal{R}_{gs} . Each is found from length over (permeability times area), where the areas are the average areas. The reluctances are then

$$\begin{aligned}
 \mathcal{R}_s &= (SL_1 + SL_3)/[(2000 \cdot 12.57\text{E-}7)[t \cdot \pi(R_{PG} + R_{YI})] \\
 &\quad + (SL_2)/[(2000) \cdot 12.57\text{E-}7)(\pi(R_{YO}^2 - R_{YI}^2))] + (SL_4)/[(2000) \cdot 12.57\text{E-}7)(\pi R_{YO}^2)] \\
 &= (0.046 + 0.058)/[2.514\text{E-}3 \cdot \pi(0.022 + 0.066)] \\
 &\quad + (0.046 + 0.012)/[2.514\text{E-}3 \cdot \pi(0.07^2 - 0.066^2)] \\
 &\quad + (0.016 + 0.006)/[2.514\text{E-}3(\pi \cdot 0.07^2)] = 12,470 + 13,500 + 568 = 26,538
 \end{aligned}$$

$$\mathcal{R}_{gW} = g/[(12.57\text{E-}7)(\pi R_P^2)] = 6.3307\text{E}6$$

- (c) The computed F using Maxwell SV is now 19.66 N, with air gap $B = 0.174$ T. These are both raised because of the higher permeability of steel.

7.2 VOICE COIL ACTUATORS

Instead of forces on steel, Lorentz force on current-carrying coils is used in many actuators. They are called “voice coil actuators” because of their common use in loudspeakers.

From the Lorentz force equation of Chapter 5, the force on an N -turn coil of average turn length l is

$$F = NBIl \quad (7.4)$$

where B is the magnetic flux density perpendicular to the coil direction and F is perpendicular to both \mathbf{B} and the coil direction. The directions follow the right-hand rule as shown in Fig. 7.3 for a typical voice coil in a loudspeaker. Note that when the current direction is reversed, then (assuming that the direction of \mathbf{B} is unchanged), the direction of the force is reversed. The reversible force of a voice coil actuator is an advantage over the force of moving iron actuators of the preceding sections, which is directed to attract the iron armature toward the iron stator regardless of the direction of the current. Another advantage over solenoid actuators is that voice coil force is much more independent of armature position and is proportional to current. A minor disadvantage is that the voice coil current must be supplied via a flexible lead, and thus the proper stranded wire must be selected for reliable long-term operation.

Because coils are most easily wound on cylindrical bobbins, voice coil actuators usually have axisymmetric geometry. No laminations are needed because the mag-

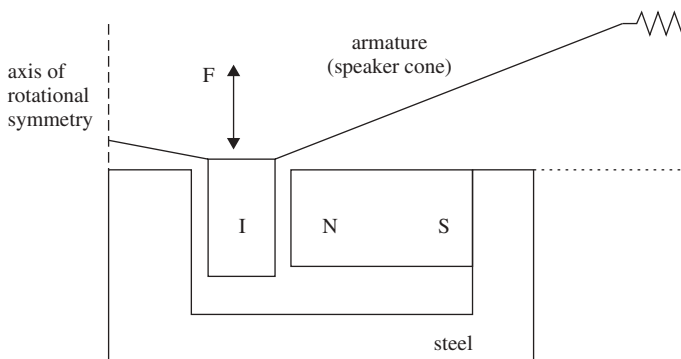


Figure 7.3 Typical voice coil actuator, shown driving a loudspeaker. The movable voice coil carries the current I and is subjected to the magnetic field from a permanent magnet with north (N) and south (S) poles.

netic flux density \mathbf{B} is constant and is almost always produced by a permanent magnet. There is some \mathbf{B} produced by the voice coil current, but it is usually negligibly small compared to the \mathbf{B} produced by the permanent magnet. An advantage of permanent magnets is that their \mathbf{B} is produced without any current or associated power loss and temperature rise.

Besides loudspeakers, another very popular use of voice coil actuators for DC (not AC) operation is for computer disk drive head actuation as in Fig. 1.3. The current applied is a DC step or pulse to position the voice coil armature at the desired radius (track) on the disk. Often the coil is on a pivot, like old-fashioned turntable arms. The time to move to the desired position is called *seek time* and should be as small as possible to enable high-speed computation. Because voice coils are made of copper or aluminum, both of which are lighter than steel or iron, voice coil actuators are preferred over moving iron solenoid actuators for disk head operation. Also, because voice coil force is proportional to current and is relatively independent of position, feedback control based on linear systems can be readily applied [6].

Example 7.5 Force of Voice Coil Actuator A voice coil has a resistance of $20\ \Omega$ and 400 turns. A permanent magnet provides a DC magnetic flux density of $0.8\ \text{T}$ in the radial r direction. The average radius of the voice coil is $15\ \text{mm}$. Given $12\ \text{V}$ DC applied to the voice coil, find the steady-state force produced.

Solution: From Ohm's law, the DC current $I = \frac{12}{20} = 0.6\ \text{A}$. The average length of a coil turn is 2π times the average radius $= 0.015\ \text{m}$, giving $l = 0.0942\ \text{m}$. Thus the desired $F = 400(0.8)(0.6)(0.0942) = 18.1\ \text{N}$.

7.3 OTHER ACTUATORS USING COILS AND PERMANENT MAGNETS

Besides solenoid and voice coil actuators, other actuators are available that use both permanent magnets and coils. The advantage of using permanent magnets is that the \mathbf{B} they produce does not require current or power loss as do coils. The \mathbf{B} of the permanent magnets interacts with the \mathbf{B} of coils to produce the force.

Many different designs are possible. Figure 7.4 shows a design from a 1990 paper by Lesquesne [7]. It is a long-stroke actuator with one radially magnetized permanent magnet, a steel or iron armature, and two coils. The coils are wound and connected so that they both carry current in the same direction. For example, if they both carry current out of the page, then the lower pole of the moving iron armature has higher flux than the upper pole, and the armature experiences a downward force. Reversal of the current gives an upward force, and no current gives zero (balanced) force on the armature. Thus the armature experiences bidirectional force. The force varies with position because of the variation in both airgaps.

Other possible designs can have armatures that are permanent magnets [8,9]. Besides permanent magnets, materials that are magnetostrictive are occasionally used in actuators, but are more often used in sensors, as will be described in Chapter 11.

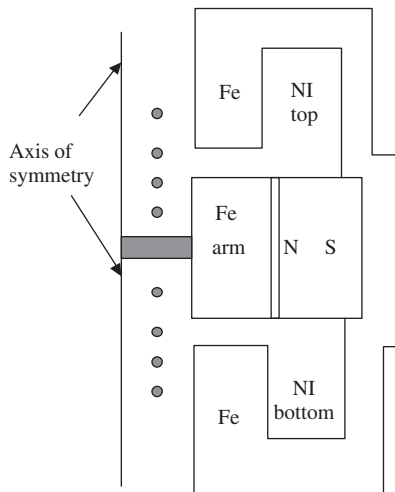


Figure 7.4 Actuator with both permanent magnet and coils in stator. The armature labeled “arm” moves either up or down.

Another type of actuator using permanent magnets and/or coils is the *magnetic separator*. Its stator produces magnetic force on multiple “armatures” consisting of ore particles or other matter. Many designs are possible [10]. Besides mineral separation, other applications include environmental waste processing and medical devices. High-field-gradient magnetic separation is used to separate red blood cells from blood and cancer cells from bone marrow. Other biomedical magnetic actuators are being investigated to target drug delivery and to remove toxins [11]. In some cases ferrite particles are added to liquids to form *ferrofluids* that can be actuated by magnetic fields [12].

7.4 PROPORTIONAL ACTUATORS

In many applications, proportional actuation is desired. Such actuation ideally produces a position x that is directly proportional to current or voltage, for example

$$x = kI \quad (7.5)$$

where k is the proportionality constant. Note that x is independent of inertia, load forces, and other external forces. Such ideal proportional positioning is highly desired for valve operation and other applications.

A graphical depiction of proportional actuation is given in Fig. 7.5, which shows force F as a function of x and I for both positive and negative currents I . Note that the slopes for all currents I are ideally infinite, that is, the lines are vertical and indicate no effect of external force.

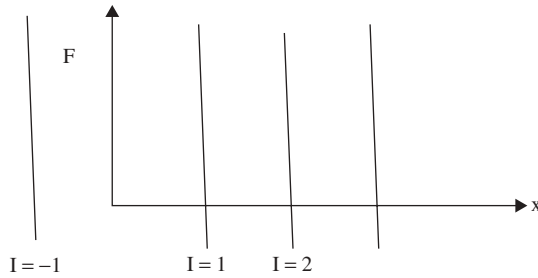


Figure 7.5 Ideal proportional actuator force.

In the real world, infinite slopes are not possible. Instead, a fairly high value of negative slope can be obtained by use of a mechanical spring. Figure 7.6 shows that the combination of a spring that produces a spring force:

$$F_s = k_x x \quad (7.6)$$

along with a magnetic actuator that produces a force F_{mag} that is independent of x and proportional to I , obtaining a total force F that approximates the desired set of proportional force lines. Note that the bigger the spring constant, the steeper are the total force lines, which is desirable. However, the bigger the spring, the larger is the magnetic force required for a specified total force, since the spring and magnetic forces are in opposition.

The required magnetic force that is independent of x and proportional to I is produced by what is commonly called a *constant-force magnetic actuator*. From the various types of magnetic actuators discussed in preceding sections, the type that inherently provides constant force is the voice coil actuator.

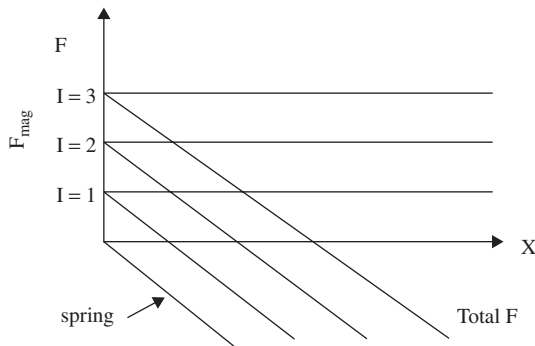


Figure 7.6 Nonideal proportional actuator produced by constant magnetic force and opposing spring force.

However, solenoid actuators can also be specially designed for proportional actuation. Without special design, solenoid actuators tend to produce force that varies greatly with position according to (7.3). To obtain force that is independent of position and proportional to current, much design work is required, usually involving electromagnetic finite-element analysis of various possible shapes of steel armatures and pole pieces. With such design work, the magnetic force can be made approximately “constant,” that is, independent of position x over a fairly wide variation of x . Some nonconstant regions, called *deadbands*, are present and must be avoided during operation. Figure 7.7 shows a typical design of a “constant force” plunger-type solenoid actuator. As pointed out by Lesquesne [13], the plunger is usually conical (not cylindrical), and the stator poles usually are angled as well. The exact angles and shapes must be carefully computed using finite-element software or (with less certainty) reluctance methods. Also, steel saturation must occur at the proper level to produce a force that is proportional not to the current square of Eq. (7.3) but to the first power of current.

Since steady-state current (from Ohm’s law) is V/R , a proportional actuator also has steady-state position proportional to applied voltage. Thus proportional actuators can be readily controlled by linear feedback control systems.

The lowest cost way to vary applied voltage is to use a chopper circuit to obtain *pulsewidth modulation* (PWM). A given DC voltage, such as battery voltage in an automobile, is switched on and off. Figure 7.8 shows a typical PWM voltage waveform. In this case the battery voltage is 24 V and the switching frequency is 1 kHz. Also in the figure, the “duty cycle” is approximately 33%, that is, that the voltage is

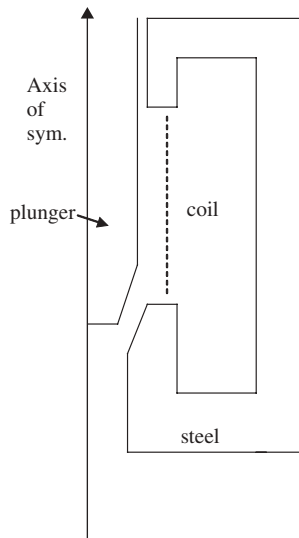


Figure 7.7 Plunger solenoid shaped for approximately constant force.

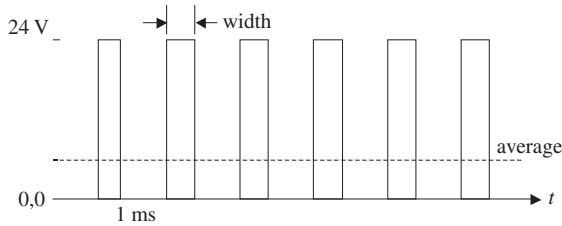


Figure 7.8 Typical PWM voltage waveform.

in ON state about one-third of the time. The average, or DC, voltage, equals duty cycle times battery voltage, and thus is 8 V in this case.

The choice of switching frequency f involves tradeoffs. Its period $T = (1/f)$ should be much faster than the desired actuation time, yet not so high as to produce significant eddy currents. The switching frequency produces corresponding pulses in magnetic force, which is not necessarily bad. The force pulsations, called *dither*, can often help overcome static friction, often called *stiction*.

7.5 ROTARY ACTUATORS

Many applications need rotary motion, that is, motion along a circular arc instead of the straight line of linear actuators. Rotary actuators are also sometimes called *torquers*, because they produce torque. This book is restricted to limited motion, and thus rotary actuators or torquers are studied, but not electric motors in general, because they produce motion that is many times $360^\circ/\text{min}$.

Rotary magnetic actuators are used at times in electrohydraulic servo valves and in computer disk drives. As mentioned in Section 7.3, voice coil actuators in disk drives sometimes operate on a pivoted arm, thus producing rotary motion.

The most common rotary magnetic actuator is the *step motor*. It is also called a *stepper motor* or *stepping motor*. Step motors are so called because they provide rotary motion in incremental steps. They are very popular because their incremental motion is easily controlled by microprocessors or other digital devices that produce digital pulses, that is, steps of DC current.

Figure 7.9a shows one quadrant of a typical step motor. Like most step motors, the rotor (armature) is on the inside and is made up solely of steel laminations. Over all four quadrants, the rotor shown here has 8 teeth, and the outer stator has 12 teeth. When a step of current is applied to the proper stator winding, the rotor wants to align its teeth for minimum reluctance for the flux of that winding. Hence they are also called *variable-reluctance motors*. Thus Figure 7.9b shows that for flux produced by current in the stator slots at approximately 20° and 70° , the rotor tends to move to the position shown. For highest torque, the airgap between stator and rotor is usually quite small, on the order of 0.1 mm. For the 12 stator teeth and 8 rotor teeth shown, each step (increment) in motion is $\frac{360}{12} = 15^\circ$. Other numbers of teeth

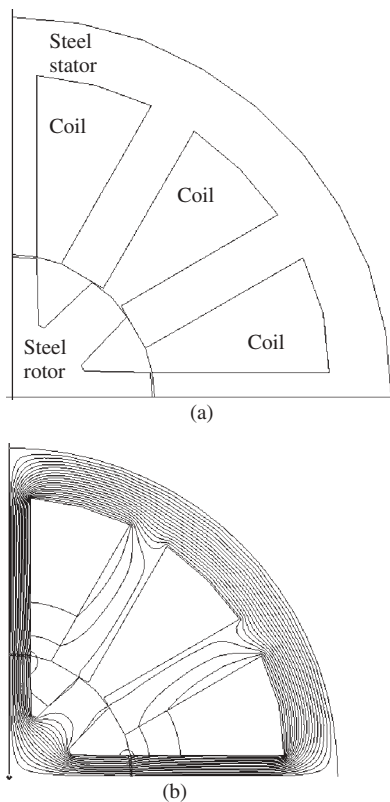


Figure 7.9 Typical step motor. (a) Geometry of one quadrant, (b) computer display of calculated flux lines.

can be chosen, but the rotor and stator must never have the same number of teeth.

Step motors can also be operated continuously, that is, over multiple revolutions. Under continuous operation they are commonly called *switched reluctance motors*. Again their advantage is the simple rotor construction, requiring only steel laminations and no coil or permanent magnet.

Another rotary actuator with a rotor made only of steel is shown in Fig. 7.10. Its stator has a solenoidal coil embedded in steel that provides three-dimensional flux paths. The design shown in Fig. 7.10 has been used by Sandia National Laboratories [14] and has four teeth on both the stator and rotor. Its maximum rotation with four poles is less than 90° . Its flux paths and torques have been computed by three-dimensional finite-element analysis [14]. Many design variations are possible.

Rotary motion requires bearings, and *magnetic bearings* feature long life due to their avoidance of mechanical wear. Magnetic bearings are a type of magnetic actuator designed to suspend a rotating axle with no mechanical contact. A more recent design of magnetic bearing shown in Fig. 7.11 maintains both radial and axial position of the rotor. Usually magnetic bearings require a control system that must be

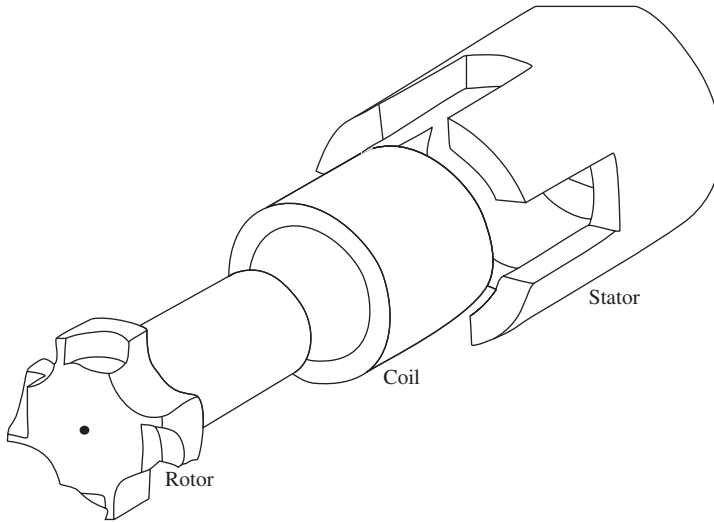


Figure 7.10 Rotary actuator with solenoidal winding and three-dimensional flux paths.

continuously active [15,16]. Some magnetic bearings also serve as *magnetic couplings*, which transfer torque between two rotating members without mechanical contact through seals and walls [17,18]. Also required for many rotating systems are magnetic brakes and clutches, which are often operated by clapper armature solenoids [19,20].

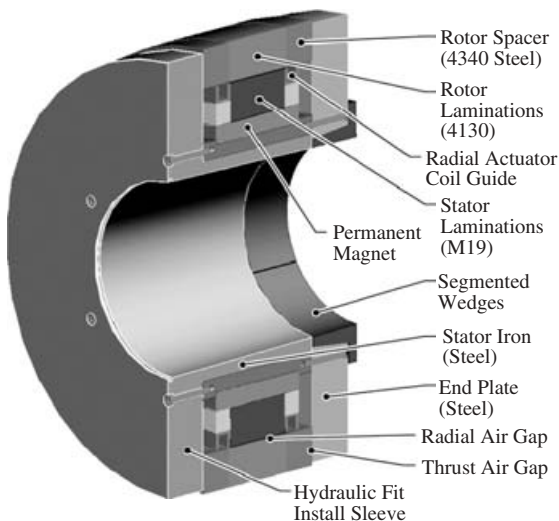


Figure 7.11 Magnetic bearing for both radial and axial positioning [15].

PROBLEMS

7.1 Assume that the planar solenoid with the clapper armature shown in Fig. E7.1.1 has the following dimensions: $w = 12$ mm, $Al_1 = 6$ mm, $Al_2 = 40$ mm, $Al_3 = 6$ mm, $Sl_1 = 20$ mm, $Sl_2 = 40$ mm, $Sl_3 = 20$ mm, $g = 1$ mm. It also has $N = 300$ and $I = 2$ A. Use the reluctance method, assuming no leakage or fringing fluxes, to find the approximate values of the following:

- Vector **B** and **F** on left side of clapper,
- Vector **B** and **F** on right side of clapper.
- Obtain the preceding answers with Maxwell SV finite element software (available for free at www.ansoft.com) by using high-permeability material (relative permeability = 2000) in the steel.
- Obtain the answers for the preceding with finite-element software with steel relative permeability = 10,000, and comment on why the results differ.
- Repeat (c) for $I = 2, 3$, and 4 and airgap $g = 0.5, 1, 1.5, 2, 2.5, 3, 3.5$, and 4 mm and plot the resulting pull curves.

7.2 The axisymmetric solenoid with a clapper armature as shown in Fig. E7.2.1 has the following dimensions: $g = 1$ mm, $w_a = 7$ mm, $R_1 = 15$ mm, $R_2 = 25$ mm, $R_3 = 30$ mm, $Z_1 = 7$ mm, and $Z_2 = 23$ mm. It also has $N = 1500$ and $I = 1$ A. Use the reluctance method, assuming no leakage or fringing fluxes, to find the approximate values of the following:

- B** and **F** on inside of clapper
- B** and **F** on outside of clapper

Then obtain

- The answers for (a) and (b) with finite-element software by using high-permeability material (relative permeability = 2000) in the steel.
- The answers for (a) and (b) with finite-element software with steel relative permeability = 10,000, and comment on why the results differ.

7.3 The planar solenoid with a plunger armature shown in Fig. E7.3.1 has the following dimensions: $w = 8$ mm, $g = 3$ mm, $g_s = 1.5$ mm, $Al_1 = 4$ mm, $Al_2 = 22$ mm, $Sl_1 = 8$ mm, $Sl_2 = 20$ mm, $Sl_3 = 34$ mm, and $Sl_4 = 15$ mm. It also has $N = 800$ and $I = 2$ A.

- Use the reluctance method, assuming no leakage flux, to find the approximate values of **B** and **F** on the end of the plunger.
- Compute the preceding values of **B** and **F** using finite-element software with the relative permeability = 2000 in the steel.
- Obtain the answers for the preceding with finite-element software with steel relative permeability = 10,000, and comment on why the results differ.

7.4 The axisymmetric solenoid with a plunger armature shown in Fig. E7.4.1 has the following dimensions: plunger and pole outer radius $R_p = 18$ mm, side air-gap outer radius $R_{pG} = 20$ mm, stator yoke outer radius $R_{YO} = 70$ mm, stator

yoke inner radius $R_{yl} = 66$ mm, working airgap $g = 8$ mm, plunger length $L_P = 42$ mm, stator stopper length $L_S = 16$ mm, coil axial length $L_C = 46$ mm, and stator yoke axial thickness $t = 12$ mm (on top; same on bottom). It also has $N = 400$ and $I = 3$ A.

- (a) Use the reluctance method, assuming no leakage flux, to find the approximate values of \mathbf{B} and \mathbf{F} on the end of the plunger.
 - (b) Compute the \mathbf{B} and \mathbf{F} from (a) using finite-element software, with the relative permeability = 2000 in the steel.
 - (c) Obtain the answers for (a) and (b) with finite element software with steel relative permeability = 10,000, and comment on why the results differ.
- 7.5** A voice coil has a resistance of $15\ \Omega$ and 300 turns. A permanent magnet provides a DC magnetic flux density of 0.6 T in the radial r direction. The average radius r of the voice coil is 20 mm. Assuming that 10 V DC is applied to the voice coil, find the steady-state vector force produced.
- 7.6** A voice coil lies from radius 10 to 14 mm. It has 200 turns and a resistance of $20\ 15\ \Omega$. It is subjected to a DC magnetic flux density of 0.5 T in the radial r direction. If 6 V DC is applied to the coil, what is its steady-state vector force?
- 7.7** A proportional actuator is made of a voice coil actuator with $F = 100I$ and a spring with $F_s = 1E5x$ in opposition. On a graph of total force versus x , for $x = 0$ to 0.010 m, draw the force lines for I varying from -1 A to $+10$ amperes.
- 7.8** A step motor has 10 stator teeth and 8 rotor teeth. Find its incremental (step) angle of motion.

REFERENCES

1. F. Jay, ed., *IEEE Standard Dictionary of Electrical and Electronics Terms*, 2nd ed., Wiley-Interscience, New York, 1977.
2. M. A. Juds and J. R. Brauer, AC contactor motion computed with coupled electromagnetic and structural finite elements, *IEEE Trans. Magn.* **31**: 3575–3577 (Nov. 1995).
3. K. Bessho, S. Yamada, and Y. Kanamura, Analysis of transient characteristics of plunger type electromagnets, *Electric. Eng. Japan* **98**: 56–62 (July 1978).
4. S.-B. Yoon, J. Hur, Y.-D. Chun, and D.-S. Hyun, Shape optimization of solenoid actuator using the finite element method and numerical optimization technique, *IEEE Trans. Magn.* **33**: 4140–4142 (Sept. 1997).
5. J. R. Brauer, ed., *What Every Engineer Should Know about Finite Element Analysis*, 2nd ed., Marcel Dekker, New York, 1993, Chapter 7, Design optimization, by R. S. Lahey.
6. R. T. Ratliffe and P. R. Pagilla, Design, modeling, and seek control of a voice-coil motor actuator with nonlinear magnetic bias, *IEEE Trans. Magn.* **41**: 2180–2188 (June 2005).
7. B. Lesquesne, Fast acting, long-stroke solenoids with two springs, *IEEE Trans. Indust. Appl.* **26**: 845–856 (Sept. 1990).

8. B. Lesquesne, Permanent magnet linear motors for short strokes, *IEEE Trans. Indust. Appl.* **32**: 161–168 (Jan. 1996).
9. B. Lesquesne, Fast acting, long-stroke bistable solenoids with moving permanent magnets, *IEEE Trans. Indust. Appl.* **26**: 401–407 (May 1990).
10. C. Hoffmann and M. Franzreb, A novel repulsive-mode high gradient magnetic separator—I. Design and experimental results, *IEEE Trans. Magn.* **40**: 456–461 (March 2004).
11. A. Hoffman, Magnetic viruses for biological and medical applications, *Magn. Bus. Technol.* 24 ff. (Spring 2005).
12. R. E. Rosensweig, *Ferrohydrodynamics*, Dover Publications, Mineola, NY, 1985.
13. B. Lesquesne, Finite element analysis of a constant force solenoid for fluid flow control, *IEEE Trans. Indust. Appl.* **24**: 574–581 (July 1988).
14. J. R. Brauer, E. A. Aronson, K. G. McCaughey, and W. N. Sullivan, Three dimensional finite element calculation of saturable magnetic fluxes and torques of an actuator, *IEEE Trans. Magn.* **24**: 455–458 (Jan. 1988).
15. M. A. Pichot and M. D. Driga, Loss reduction strategies in design of magnetic bearing actuators for vehicle applications, *IEEE Trans. Magn.* **41**: 492–496 (Jan. 2005).
16. S.-L. Chen, S.-H. Chen, and S.-T. Yan, Experimental validation of a current-controlled three-pole magnetic rotor-bearing system, *IEEE Trans. Magn.* **41**: 99–112 (Jan. 2005).
17. P. Eliès and G. Lemarquand, Analytical study of radial stability of permanent-magnet synchronous couplings, *IEEE Trans. Magn.* **35**: 2133–2136 (July 1999).
18. W. Wu, H. C. Lovatt, and J. B. Dunlop, Analysis and design optimization of magnetic couplings using 3D finite element modeling, *IEEE Trans. Magn.* **33**: 4083–4085 (Sept. 1997).
19. L. J. Kamm, *Understanding Electro-Mechanical Engineering*, IEEE Press, New York, 1996.
20. E. Kallenbach, R. Eick, P. Quendt, T. Ströhla, K. Feindt, and M. Kallenbach, *Elektromagnete*, 2nd ed., B. G. Teubner Verlag/Springer, Wiesbaden, Germany, 2003 (in German).

Magnetic Actuators Operated by Alternating Current

Because AC (alternating current) voltage is commonly available, many magnetic actuators are designed for AC operation. In most cases, the DC actuators of the preceding chapter must be substantially modified for AC operation. Armatures of clapper type and plunger type are still common, but changes to both the steel core and the coils are usually required.

8.1 SKIN DEPTH

Chapter 2 has shown that time-varying magnetic fields induce eddy currents in conducting materials. Since AC currents produce time-varying magnetic fields, eddy currents are a key issue in AC magnetic actuators. An easy way to examine AC eddy current effects is to calculate *skin depth*.

Faraday's law of Chapter 2 can be used to find the skin depth [1]

$$\delta = \frac{1}{\sqrt{\pi f \mu \sigma}} \quad (8.1)$$

where f is the AC frequency in hertz, μ is permeability, and σ is electrical conductivity. Both the steel core and the coils of magnetic actuators are made of conducting materials, and thus the skin depth is often less than the typical core or wire dimensions. Skin depth in wires will be discussed in Chapter 12, while here skin depth in steel cores is examined. For example, the 60 Hz magnetic flux in Example 6.5 was seen in Fig. E6.5.1 to be concentrated near the outer skin of its cylindrical steel core. Such flux concentration on the skin, and lack of flux in the interior, is called *skin effect*. The skin depth of (8.1) is the depth at which flux density and eddy currents have decayed to $1/e$ of their surface value, or 36.8%. The decay from surface into the interior is exponential [1].

Note that skin depth of (8.1) is infinite for DC (0 frequency), but decreases inversely proportional to the square root of frequency. It is also inversely proportional to the product of permeability times conductivity. This product is especially high for steel. Steel in magnetic actuators and sensors typically has permeabilities thousands of times that of air, and has conductivities on the order of $1.E6$ S/m. In Example 6.5, the

relative permeability of 2000, conductivity of $2.E6$ S/m, and frequency 60 Hz in (8.1) give a skin depth of 1.0 mm. Note that the flux lines in Fig. E6.5.1 are indeed concentrated in the outer 1 mm or so of the 10-mm-radius steel core. The inner 9 mm steel region is essentially unused for AC, and it could be removed to save weight and cost.

To carry more flux than just the skin will allow, most AC steel cores are laminated as was shown in Fig. 2.6 and described in Chapter 2. The lamination thickness should be less than approximately 0.5–1 skin depth. Thus most steel laminations for 60 Hz AC operation are less than 1 mm thick. For example, the Eaton AC magnetic actuator of Fig. 4.3 has steel of depth 28.5 mm into the page and is made of approximately 46 laminations, each approximately 0.62 mm thick. Both its stator and its armature are made of laminations that have been punched from sheet steel and then stacked and held together by rivets.

8.2 POWER LOSSES IN STEEL

8.2.1 Laminated Steel

Laminating steel does not completely eliminate steel eddy currents and their losses, but greatly reduces them. As long as the lamination thickness t is considerably less than skin depth, the eddy power loss density can be shown to obey [2] the following rule

$$\frac{P_e}{v} = \frac{t^2 \omega^2 B^2 \sigma}{24} \quad (8.2)$$

where B is the peak magnetic flux density, $\omega = 2\pi f$, P_e is power in watts, and v is the volume of the conducting material in cubic meters. The above loss equation holds true when the eddy currents cause negligible changes in the magnetic field. If the skin depth is less than the lamination thickness, more complicated relations often apply [2], and the laminations do not carry nearly as much flux.

In addition to eddy current loss, steel carrying AC flux has *hysteresis loss*. As explained in Chapter 5, areas on B – H planes correspond to energy, and hysteresis causes the B – H relation to have more than one single-valued curve. Thus in Fig. 8.1, which shows typical B – H loops for AC current and H , the energy density lost per cycle is the area enclosed by the B – H loop. Hysteresis loss is significant whenever eddy loss of (8.2) is small as a result of small lamination thickness. The sum of hysteresis loss and eddy current loss is called *core loss*.

Because the energy density lost per cycle is the area of Fig. 8.1, hysteresis loss is proportional to frequency. Also, for typical steel the area of Fig. 8.1 is approximately proportional to the peak B to the power n , where n varies from about 1.5 to about 2.5 [3]. Hence the hysteresis power loss density obeys

$$\frac{P_h}{V} = K_h f B^n \quad (8.3)$$

where K_h is approximately constant.

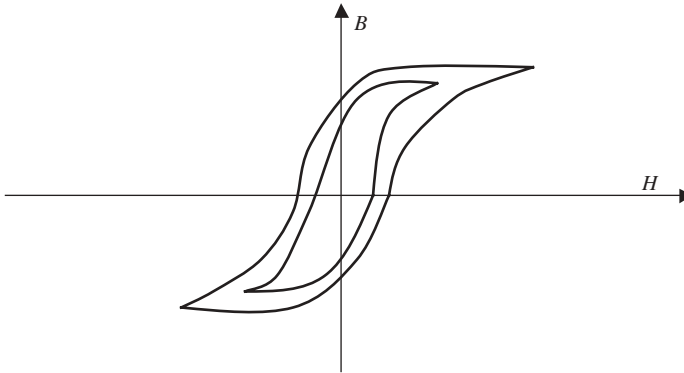


Figure 8.1 B – H hysteresis loops for AC H due to AC current. The area enclosed is the energy lost per cycle. Two loops are shown for two different peak AC current values.

Manufacturers of steel laminations for magnetic devices, often called *electrical steels*, customarily measure and publish *core loss curves*. Such curves are commonly available for 50 and 60 Hz over a range of peak B values.

Steel manufacturers also measure and publish B – H curves for AC devices called *normal AC B – H curves*. Such a normal curve is the locus of the tips of B – H loops such as shown in Fig. 8.1. The normal AC curve may differ somewhat from the DC curve.

8.2.2 Equivalent Circuit

As discussed in Example 6.5, eddy current loss (and thus core loss) introduces a resistor in the impedance seen by the coil. Since the losses of (8.2) and (8.3) are proportional to B^2 , and V_L across an inductor is proportional to B (from Faraday's law), core loss is equivalent to the parallel resistor R_{core} shown in Fig. 8.2. Its power loss, like core loss, is proportional to the square of the voltage across the inductor:

$$P_{\text{core}} = V_L^2 / R_{\text{core}} \quad (8.4)$$

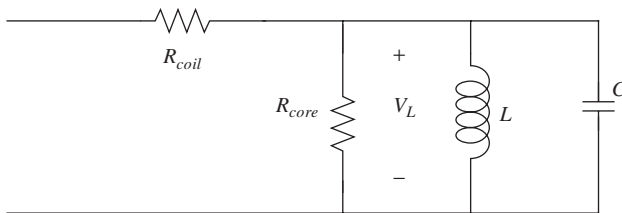


Figure 8.2 Equivalent circuit for a coil in a magnetic device. R_{core} accounts for core loss; R_{coil} accounts for coil loss. The nonlinear inductor accounts for flux and Faraday's law. The capacitor accounts for interwinding capacitance, which becomes important at high frequencies.

Note that Fig. 8.2 also includes a capacitor due to the interwinding capacitance mentioned in Chapter 6. It also includes a series resistor R_{coil} that equals the resistance of the coil itself. As explained further in Chapter 12, if skin effects in the coil are negligible R_{coil} is the DC coil resistance, but substantial coil AC skin effects may cause R_{coil} to change somewhat.

The impedance of the capacitor is typically negligible at 60 Hz, but becomes more important the higher the frequency. Since the capacitor C and inductor L are in parallel, the coil has a natural resonant frequency:

$$f_r = \frac{1}{2\pi\sqrt{LC}} \quad (8.5)$$

As discussed in Chapter 6, finite-element software usually outputs the impedance seen by each coil. This impedance is a sum of real and imaginary parts in series

$$Z_s = R_s + jX_s \quad (8.6)$$

and is assumed here to account only for the core loss and inductance of the coil; that is, the coil's DC resistance and capacitance are not included in (8.6). However, Fig. 8.2 needs the *parallel* impedance:

$$Z_p = R_{\text{core}} + j\omega L = R_p + jX_p \quad (8.7)$$

An advantage of the parallel impedance is that when the coil is excited by a voltage V_s , the core current loss draws an extra current, the current through the parallel resistor.

To find R_p and X_p of Fig. 8.2, apply the parallel circuit formula:

$$R_s + jX_s = \frac{(R_p)(jX_p)}{R_p + jX_p} \quad (8.8)$$

Using complex AC circuit methods, (8.8) can be expressed in terms of magnitudes and phase angles as follows:

$$R_s + jX_s = \frac{R_p X_p \angle 90^\circ}{(R_p^2 + X_p^2)^{1/2} \angle \arctan \frac{X_p}{R_p}} \quad (8.9)$$

$$(R_s^2 + X_s^2)^{1/2} \angle \arctan \frac{X_s}{R_s} = \frac{R_p X_p}{(R_p^2 + X_p^2)^{1/2}} \angle 90^\circ - \arctan \frac{X_p}{R_p} \quad (8.10)$$

The magnitudes on both sides must be the same, and the angles on both sides must also be the same. Also, in most cases the finite element results will find $R_s \ll X_s$. Thus from the first term of a series expansion:

$$\arctan \frac{X_s}{R_s} \cong 90^\circ - \frac{R_s}{X_s} \quad (8.11)$$

Assuming the above equality is exact, then equating the angles of (8.10) gives

$$\frac{R_s}{X_s} = \frac{X_p}{R_p} \quad (8.12)$$

Also, if $R_s \ll X_s$, then from the magnitudes of (8.10), it is approximately true that

$$X_p = X_s \quad (8.13)$$

Finally, from (8.12) and (8.13) we obtain

$$R_p = \frac{X_p^2}{R_s} \quad (8.14)$$

A major problem with AC equivalent circuits for devices made of nonlinear B – H materials is that the nonlinearity often causes the voltage and/or the current to become nonsinusoidal. The greater the current and voltage, the greater the saturation, and the more the waveforms can deviate from sinusoidal. Since the inductive reactances X_p and X_s in the equations above are constants, they cannot fully represent nonlinear behavior. However, these reactances can approximately simulate saturation effects when their magnitudes decrease as current and flux rise. These effective reactances are often obtained by AC finite-element software by use of “effective permeability,” which decreases with current magnitude [4]. For more exact modeling, and to obtain nonsinusoidal waveforms, nonlinear transient techniques of Chapters 9 and 14 are required.

8.2.3 Solid Steel

The equivalent circuit of Fig. 8.2 still applies if some or all of the steel is solid. However, the simple equations for the eddy current loss and hysteresis loss derived above for laminated steel no longer apply. In most cases, the eddy current loss in solid steel greatly exceeds the hysteresis loss, which can thus be neglected. The best way to predict the steel power loss and equivalent circuit parameters is to use the finite-element method.

Solid steel is sometimes used in AC actuators, depending on the type (from the previous chapter):

- *For planar actuators with clapper armatures*, the stator is easily laminated, but often the armature is made of solid steel, especially if the armature is steel plate (or steel scrap) to be lifted by a *lifting magnet*.
- *For axisymmetric actuators with clapper armatures*, lamination is difficult and expensive, and thus both stator and armature steels are usually solid.

- For planar actuators with plunger armatures, both stator and armature are usually laminated, but a solid armature is sometimes required due to its greater mechanical rigidity.
- For axisymmetric actuators with clapper armatures, lamination is difficult and expensive, and thus both stator and armature steels are usually solid.

The easiest way to design and manufacture an AC actuator is to simply apply AC to an existing DC solenoid. However, such a simple design method is usually unsatisfactory. Besides the need to laminate to reduce eddy power loss, the number of turns usually must be changed to obtain the proper current for the particular AC voltage applied. Further changes are discussed in the remainder of this chapter.

Example 8.1 AC Flux Linkage and Equivalent Circuits of Solenoid of Example 7.1 with a Solid Steel Clapper Figure E8.1.1 shows the solenoid of Example 7.1 turned upside-down to act as an AC lifting magnet. The stator is laminated but the clapper being lifted is solid steel. The stator winding shown has 200 turns carrying 2 A rms AC 60 Hz current. The dimensions are $w = 10$ mm, $Al_1 = 5$ mm, $Al_2 = 30$ mm, $Al_3 = 5$ mm, $Sl_1 = 15$ mm, $Sl_2 = 30$ mm, $Sl_3 = 15$ mm, $g = 2$ mm. Assuming that all steel has relative permeability of 2000, and the clapper has conductivity $2.E6$ S/m, find the AC fields and series and parallel equivalent circuits using Maxwell SV.

Solution: The flux linkage output by Maxwell is $\lambda = 1.814E-5 - j7.51E-7$ per turn. The series impedance for one turn is then found using (6.30)

$$Z = j\omega\lambda/I \quad (E8.1.1)$$

where $I = 2$ A and $\omega = 377$. The resulting series impedance (for 200 turns) is

$$Z_s = R_s + jX_s = (200)(141.6E-6 + j3.42E-3) = 28.32E-3 + j684E-3 \quad (E8.1.2)$$

Note that as expected, the resistive part is much smaller than the reactive part.

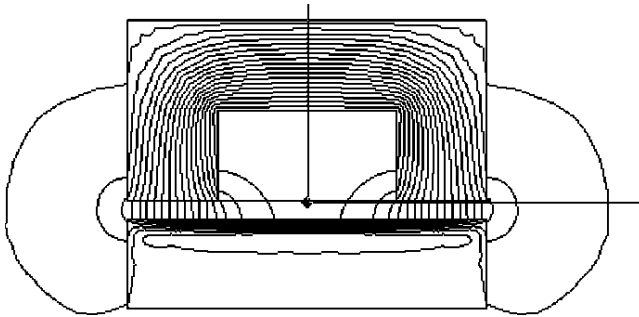


Figure E8.1.1 Computer display of AC magnetic actuator with a laminated steel stator and solid steel rotor. Its dimensions are the same as those in Fig. E7.1.1. The flux lines are computed for a frequency of 60 Hz.

To obtain the parallel equivalent circuit of Fig. 8.2, recall that $X_p = X_s$, so $X_p = 684\text{E-}3$ and $L_p = 684\text{E-}3/377 = 1.814\text{E-}3$ H. Also, use (8.14) to obtain the parallel core loss resistor:

$$R_p = \frac{X_p^2}{R_s} = 16.52 \, \Omega \quad (\text{E8.1.3})$$

Note that the parallel core loss resistor has much higher impedance than does the parallel inductive reactor, as expected.

The computed flux lines are shown in Fig. E8.1.1. Note the substantial skin effects in the solid steel armature.

8.3 FORCE PULSATIONS

8.3.1 Force with Single AC Coil

Because AC actuators have AC current that varies with time, Ampere's law shows that their magnetic fields B also vary with time. Since magnetic force of Chapter 5 is approximately proportional to the square of B , the time-varying B causes force variations called *pulsations*.

If eddy currents are small enough to not affect the field, then the magnetic field throughout the actuator is due solely to the current through the energized coil or coils. Often there is only one coil, and thus there is only one AC current, and all fields are in phase with the current. Since the current goes through zero twice per cycle, the magnetic fields throughout the actuator must go through zero twice per cycle.

For example, the current is often a sine wave:

$$I_1 = \sin(2\pi ft) \quad (8.15)$$

Figure 8.3 plots this AC sine wave over a few cycles, when the argument of the sine is varied from 0° to about $\sim 1000^\circ$. From (5.11), the force is then proportional to

$$F_1 = kI_1^2 = k \sin^2(2\pi ft) = \frac{k}{2} (1 - \cos 4\pi ft) \quad (8.16)$$

The force versus time waveform is also plotted in Fig. 8.3. Note that the force pulsates from its maximum, to zero, going through zero twice per cycle of current. The alternating component of the force has twice the electrical frequency. The average force value is one-half the maximum force, and the total force never reverses direction.

The preceding current and force relations assume that the current is sinusoidal, as often assumed for the reactances of Fig. 8.2. In actuality, most AC solenoids are voltage-driven, typically by 120 V 60 Hz in the United States. If saturation occurs, then the current may be nonsinusoidal, as mentioned in the previous subsection. However, in all cases the current goes through zero twice per cycle, and so will the force.

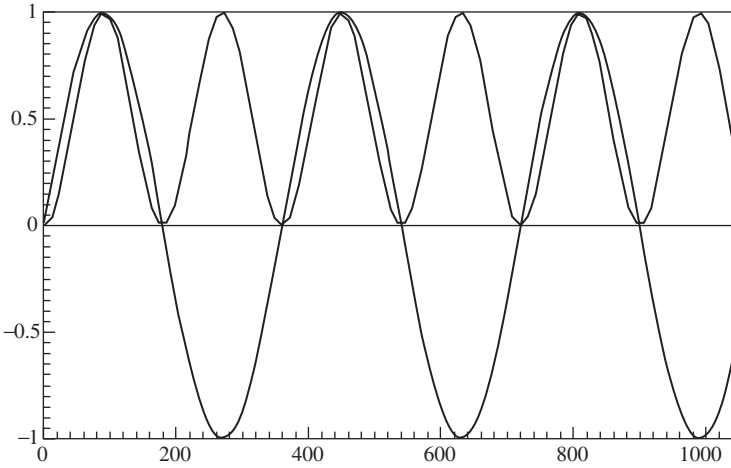


Figure 8.3 Current and force waveforms versus time for a single AC current in an actuator. The current swings positive and negative, while the force is always positive and has double frequency content.

8.3.2 Force with Added Shading Coil

If an additional significant current at a different phase angle exists in the AC solenoid, then it is possible that the force pulsations may be reduced. For example, suppose that one winding has the current of (8.15) and produces the force of (8.16) on its steel pole, but that there is also an additional current:

$$I_2 = \cos(2\pi ft) \quad (8.17)$$

Suppose also that this current produces an additional force on its own steel pole, giving the following total force:

$$F_1 = F_2 = k(I_1^2 + I_2^2) = k[\sin^2(2\pi ft) + \cos^2(2\pi ft)] = k \quad (8.18)$$

Note that a trigonometric identity has been used to obtain a magnetic force that is independent of time. Thus the force has no pulsations.

In practice, it is extremely difficult to obtain the constant force of (8.18). However, it is possible to raise the minimum force considerably above zero by a relatively inexpensive modification.

The inexpensive way of reducing the pulsation is to add a *shading coil* or a one-turn version called a *shading ring*. Figure 8.4 shows the aluminum shading rings added to the two poles in the Eaton AC actuator of Chapter 4. According to the time derivative in Faraday's law, the induced voltage in each ring will be 90° out of phase from the magnetic flux passing through it. If the induced current were in phase with that induced voltage, then the phase relation of (8.18) would be satisfied.

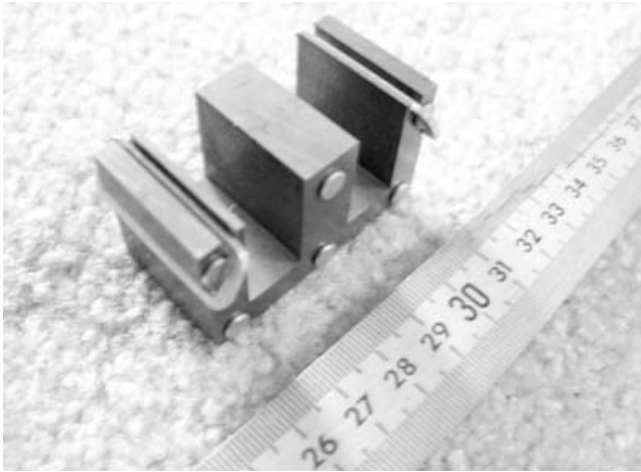


Figure 8.4 Photo of stator core with two shading rings in Eaton AC actuator of Chapter 4.

However, due to self-inductance, the current phase lags further behind. Also, the magnitude of the induced shading ampere-turns will always be less than the magnitude of the ampere-turns in the main coil. Thus a shading coil will not eliminate force pulsations, but can reduce them.

While reluctance techniques have been used to calculate shading coil effects [5], the easiest way to calculate them is to use finite-element analysis. The effects of the shading coil in the Eaton AC actuator of Fig. 8.4 have been calculated using nonlinear transient finite-element analysis, including the effects of armature motion, and will be discussed in Chapter 14.

Since induced currents in solid metals affect the force, armatures made of non-laminated high-conductivity metal experience large eddy current forces, which in some cases can be shown to be *repulsive* instead of attractive. Pure aluminum armatures placed above a steel stator with an AC stator coil can in some cases be *levitated* above the stator. That is, the magnetic repulsive force vertically upward balances the downward force of gravity [6,7], and can be used to levitate trains. Similarly, magnetic bearings can suspend a rotating shaft, working against gravitational and other forces.

Example 8.2 Fluxes and Forces on Axisymmetric Plunger Armature Solenoid of Example 7.4 with Added Shading Ring Figure E8.2.1 shows the axisymmetric solenoid with a plunger armature of Example 7.4 with an added shading ring on its stator pole. The number of turns of the main driven coil remain $N = 400$. The current I is now 4 A rms at 60 Hz. The dimensions remain the same as in Example 7.4, except that now there is an added shading ring. The steel has relative permeability 2000 and conductivity $5.E5$ S/m. The ring has an inner radius of 10 mm and a cross section of 4×4 mm. It is made of copper with conductivity $5.8E7$ S/m.

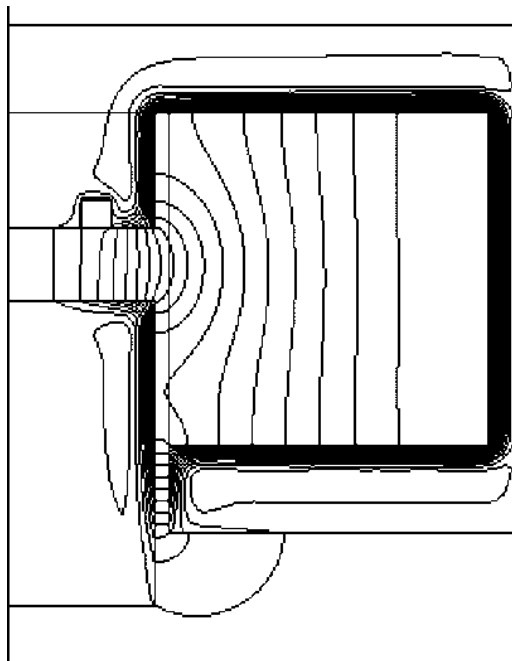


Figure E8.2.1 Computer display of geometry and computed flux lines of axisymmetric actuator with shading coil placed on stator pole face.

Compute the magnetic fields and the force using finite-element software Maxwell SV.

Solution: The easiest way to make this model is to modify the model of Example 7.4. The solution type must be changed to “eddy current.” The shading ring must be added using a rectangular box command. Be sure to change the steel conductivity to the specified nonzero value, and choose copper for the shading ring material. Also be sure to specify “Force” under “Set up executive parameters.” To allow convergence to small energy error, allow 16 passes under “Set up solution.”

The solution has the magnetic flux line plot shown in Fig. E8.2.1 at time equal to 0° phase angle. Note that skin effects are clearly visible. The force output by Maxwell has a time-average value of 8.46 N and an “AC fluctuation” of 8.40 N. Thus the fluctuation or pulsation is large, but somewhat less than the average value. Hence the shading ring prevents the force from going through zero twice per cycle.

8.4 CUTS IN STEEL

A way to improve the performance of AC magnetic devices made of solid steel is to put cuts in the steel. The cuts or slots partly block the eddy current circulation pattern, somewhat like laminations, and thereby reduce power loss and increase flux.

8.4.1 Special Finite-Element Formulation

To compute the magnetic fields and flux in slotted steel with eddy currents, an unusual finite-element formulation called “eddy axial” is available in Maxwell SV. Displacement currents are neglected because the frequency applied to actuators is usually 1 kHz or lower.

The formulation begins with Ampere’s law with $\mathbf{J} = \sigma \mathbf{E}$ from Chapter 2:

$$\nabla \times \mathbf{H} = \sigma \mathbf{E} \quad (8.19)$$

Premultiplying both sides by the inverse of the conductivity and then taking the curl of both sides, we obtain

$$\nabla \times \sigma^{-1} \nabla \times \mathbf{H} = \nabla \times \mathbf{E} \quad (8.20)$$

Applying Faraday’s law gives

$$\nabla \times \sigma^{-1} \nabla \times \mathbf{H} = -\frac{\partial \mathbf{B}}{\partial t} \quad (8.21)$$

which for sinusoidal fields of angular frequency $\omega = 2\pi f$ is

$$\nabla \times \sigma^{-1} \nabla \times \mathbf{H} = -j\omega\mu\mathbf{H} \quad (8.22)$$

where permeability μ is assumed constant; that is, the B – H curve is assumed to be operating in its linear region.

In comparison, the planar eddy current solution of Example 8.1 solves (8.19) by using $H = B/\mu$, obtaining

$$\nabla \times \mu^{-1} \mathbf{B} = \sigma \mathbf{E} \quad (8.23)$$

Substituting (2.39) and (2.41), and again assuming sinusoidal fields gives

$$\nabla \times \mu^{-1} \nabla \times \mathbf{A} = -j\omega\sigma\mathbf{A} \quad (8.24)$$

which is the differential equation for “eddy current” problems such as Example 8.1. In the two-dimensional case, the only component of \mathbf{A} is commonly the z component normal to the plane of the problem as described in Chapter 4.

The eddy axial solver uses planar two-dimensional finite elements (of default depth 1 m) in which only one component of \mathbf{H} exists, the component H_z perpendicular to the elements (out of the page). Computing only one unknown H_z at each finite-element node is much more computationally efficient than computing two components of \mathbf{A} (A_x and A_y) for planar eddy currents, as much as $3^2 = 9$ times less expensive. After H_z is computed, the software also computes the eddy current density \mathbf{J} using Ampere’s law to give:

$$\mathbf{J} = \nabla \times \mathbf{H} \quad (8.25)$$

In the two-dimensional case with $\mathbf{H} = H_z \mathbf{u}_z$, \mathbf{J} has only x and y components in the plane of the triangular finite elements. Contours of constant H_z correspond to eddy current flow lines.

8.4.2 Loss and Reluctance Computations

The finite-element method of the preceding subsection can be used to analyze a two-dimensional circular model of a cylindrical solid steel pole. While other steel shapes can also be analyzed, the cylinder is selected here because of its common use in axisymmetric magnetic actuators and sensors. Also, because equations have been derived for conductors that are perfect circles without cuts, some finite-element computations can be verified by comparing them with the equations.

Equations for the AC fields in circular conductors have been derived by Ramo et al. [8] as follows. Applying vector identities to (8.22) gives

$$\nabla^2 \mathbf{H} = j\omega\mu\sigma\mathbf{H} \quad (8.26)$$

For $\mathbf{H} = H_z \mathbf{u}_z$ as discussed in Subsection 8.4.1, (8.26) can be written in cylindrical coordinates as [8]

$$\frac{d^2 H_z}{dr^2} + \frac{1}{r} \frac{dH_z}{dr} - j\omega\mu\sigma H_z = 0 \quad (8.27)$$

where r is the radius, the only coordinate over which H varies.

The solution of (8.27) can be shown [8] to involve Bessel functions. Since (8.27) is a complex equation, Bessel functions of complex numbers are required. It is common to define [8] Bessel real and Bessel imaginary functions:

$$\text{Ber}(v) = \text{Re}[J_0(j^{-1/2}v)], \text{Bei}(v) = \text{Im}[J_0(j^{-1/2}v)] \quad (8.28)$$

Using the Ber and Bei definitions, the solution of (8.27) can be shown to be [8]

$$H_z = H_a[(\text{Ber}(2^{1/2}r/\delta) + j\text{Bei}(2^{1/2}r/\delta))/(\text{Ber}(2^{1/2}r_o/\delta) + j\text{Bei}(2^{1/2}r_o/\delta))] \quad (8.29)$$

where r_o is the outer radius at which H_a is applied by a coil, and δ is the skin depth.

To compare the results of (8.29) with those of the finite elements of (8.22), a steel cylinder of radius 2.5 mm is selected as shown in Fig. 8.5. The steel is assumed to have relative permeability 2000 and electrical conductivity $2.E6$ S/m. The H_z applied to the outside the model of Fig. 8.5 is 398.1 A/m at 60 Hz, which corresponds to 1 T flux density just inside the outer radius of the steel cylinder. The computed flux lines are also shown in Fig. 8.5 at the instant that the applied 398.1 A/m is peaking.

The computed flux lines in Fig. 8.5 are nonuniform, due to the eddy currents in the steel. To compare the computed field distribution with the theory of (8.29), the ratio of the magnitude of H over the applied $H = 398.1$ A/m is plotted in Fig. 8.6.

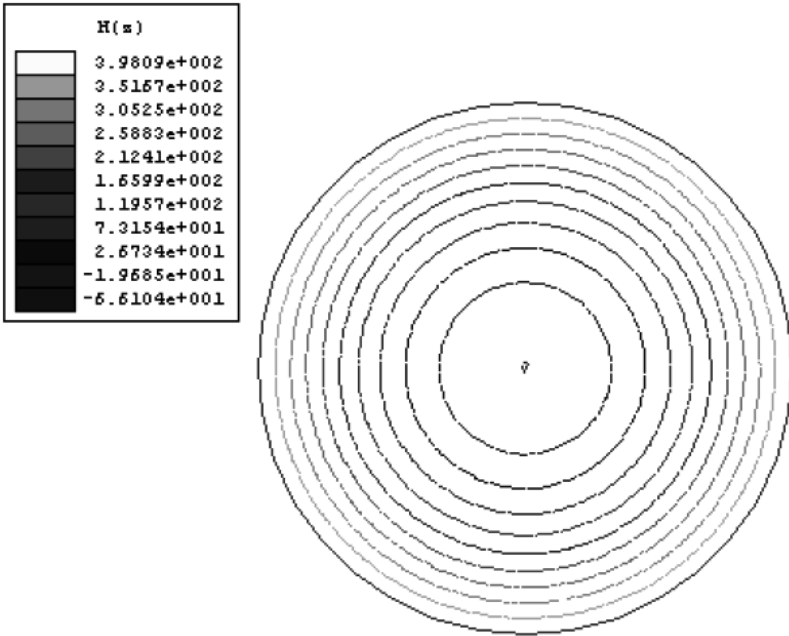


Figure 8.5 Computer display of conducting steel cylinder (without cuts) of radius 2.5 mm. The eddy current flow lines are displayed at the instant when the applied outer H of frequency 60 Hz is 398.1 A/m, corresponding to 1 T just inside the outer steel. The contour values show that the real part of H varies from 398.1 down to -66 A/m. The magnetic flux is directed normal to the plane of this figure.

Also plotted is the theoretical magnitude of H from (8.29), using Ber and Bei function values interpolated from tables [9]. In all cases the computed value is within 0–1% higher than the theoretical value obtained using (8.29).

As an additional verification of the finite-element formulation, the conductivity of the steel cylinder of Fig. 8.5 is changed to zero. The computed flux is $19.65 \mu\text{Wb}$ (microwebers), which, substituted in (3.8) along with $H = 398.1$ A/m and depth 1 m, gives computed DC reluctance $\mathcal{R}_{\text{DC}} = 20.26\text{E}6$ A/Wb. This value agrees exactly with the value obtained using the conventional magnetostatic reluctance formula (3.9) with area equal to that of the circle.

As mentioned in Chapter 3, AC eddy currents cause reluctance to become complex. The magnetostatic reluctance \mathcal{R}_{DC} presented here can be compared with the 60 Hz reluctance of Fig. 8.5. Using the definition of \mathcal{R}_{RE} , the real part of the complex reluctance of (3.16), the software finds $\mathcal{R}_{\text{RE}} = 47.57\text{E}6$ A/Wb. This is 234.8% of $\mathcal{R}_{\text{DC}} = 20.26\text{E}6$ A/Wb, and is listed as that percentage in the first row of Table 8.1. As expected from Lenz' law, eddy currents cause the AC reluctance to be higher than the magnetostatic reluctance. Thus the finite element computations have been verified.

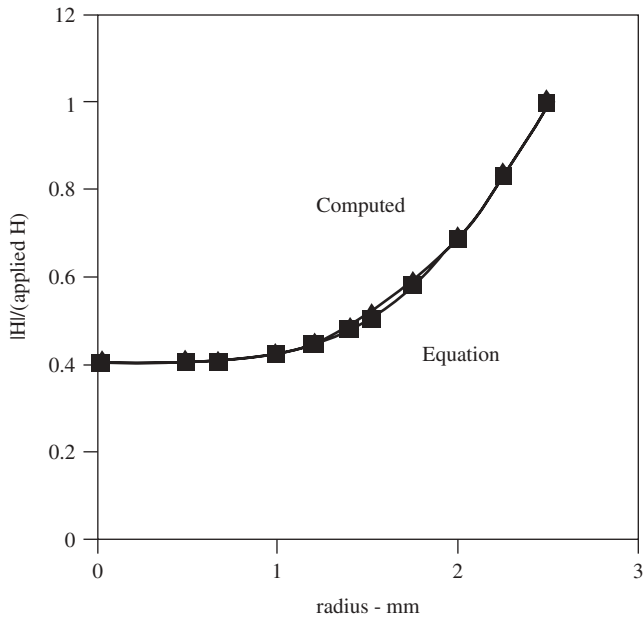


Figure 8.6 Ratio of magnitude of H inside steel cylinder over applied H of frequency 60 Hz. The cylinder has a radius of 2.5 mm, a conductivity of 2.E6 S/m, and a relative permeability of 2000. The lower curve is from Eq. (8.14); the upper curve was computed using finite elements.

To reduce the AC reluctance and associated eddy power loss, cuts have often been made in solid steel poles and armatures [10]. A similar technique is to use *tape-wound* steel, as shown in the spiral steel pole of Fig. 8.7. The eddy current flow lines computed by the “eddy axial” solver of Maxwell are shown. Note that the circular eddy flow patterns are well blocked by the spiraling. Table 8.1 lists the computed power loss and AC reluctance, both of which are greatly reduced by the

Table 8.1 Losses and Reluctances Computed for Various (or No) Cuts in Cylinders of Radius 2.5 mm^a

Cuts	Power Loss (W)	$\mathcal{R}_{RE}/\mathcal{R}_{DC}$ (%)
None	0.481	234.8
Spiral	0.111	100.5
4	0.411	115.7
8	0.198	105.2
36	0.021	111.7

^aAll values are at 60 Hz and with solid steel of conductivity 2.E6 S/m and $B = 1$ T in steel skin.

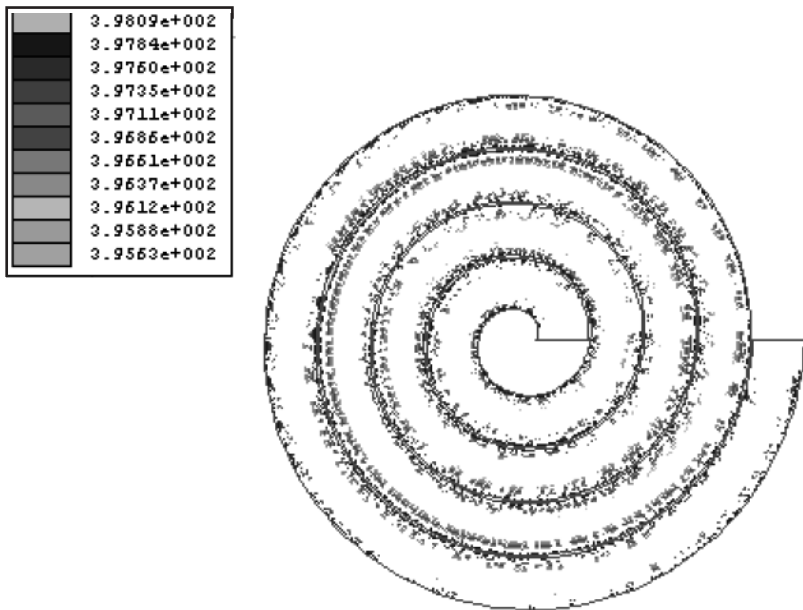


Figure 8.7 Computer display of spiral steel pole of radius 2.5 mm and outer $B = 1$ T at 60 Hz, showing computed eddy current flow patterns and contours of constant real H .

spiraling. Thus placing cuts in steel poles can greatly improve their AC performance.

Example 8.3 Loss and Reluctance of a Cylindrical Pole with Added Radial Slots Figure E8.3.1 shows the cross section of a cylindrical steel pole of radius 2.5 mm. The steel is again assumed to have relative permeability 2000 and conductivity $2.E6$ S/m. A 60 Hz magnetic field of 1 T is applied just inside the surface of the cylinder. As shown in Fig. E8.3.1, in an attempt to reduce eddy currents, four radial slots of width 0.03 mm are cut spaced equally. To maintain some mechanical integrity, the slots are only cut down to a radius of 0.55 mm.

Compute the eddy power loss and real AC reluctance \mathcal{R}_{RE} using the finite-element software Maxwell SV.

Solution: Maxwell SV's "eddy axial" is selected as the "solver," along with the default xy plane. The applied outer boundary condition is $H_z = 398.1$ A/m to obtain 1 T just inside the steel surface. The resulting plot of contours of real H_z is shown in Fig. E8.3.1. The power loss is 0.411 W for 1 meter depth and is entered in Table 8.1, where it is seen to be somewhat less than the power loss for no slots. Table 8.1 also lists the computed real AC reluctance as a percentage of the DC reluctance. Note that slotting has significantly reduced the AC reluctance. Table 8.1 also lists computed results with increased numbers of equally spaced slots.

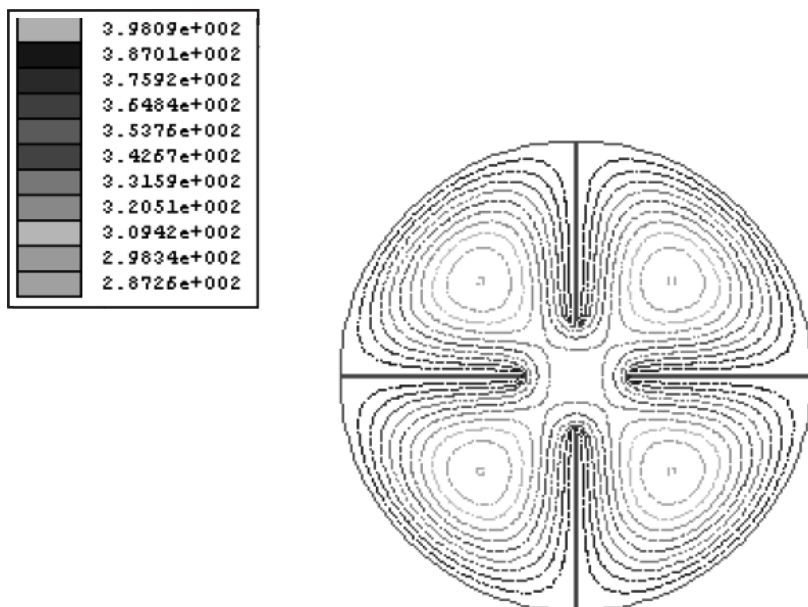


Figure E8.3.1 Computer display of steel cylinder with four radial slots and outer $B = 1$ T at 60 Hz, showing computed eddy current flow patterns and contours of constant real H .

PROBLEMS

- 8.1 Redo Example 6.5 but at a frequency of 10 Hz.
- 8.2 Redo Example 6.5 but with a conductivity of $2.E5$ S/m.
- 8.3 Calculate the skin depth at 60 Hz of material with
 - (a) A semiconductor with conductivity = 1 S/m and relative permeability = 1
 - (b) Copper with conductivity = $5.8E7$ S/m and relative permeability = 1
 - (c) A high-conductivity ($5.E6$ S/m) steel with relative permeability = 8000
- 8.4 Find (in a book containing mathematical series) the complete trigonometric series for (8.11).
- 8.5 Redo Example 8.1 but with Maxwell's nonlinear "steel_1010."
- 8.6 Repeat Problem 8.5 but with the current increased to 5 A. Note that Maxwell SV handles nonlinear B – H characteristics in AC eddy current problems, and that saturation can affect the equivalent circuit parameters.
- 8.7 Redo Example 8.2 but with the shading ring moved to an inner radius of 9 mm.

- 8.8** Redo Example 8.2 but with the shading ring moved to an inner radius of 11 mm.
- 8.9** Redo Example 8.3 but with eight equally spaced radial slots. Besides obtaining the numerical values in Table 8.1, also obtain a plot of the eddy current flow pattern.
- 8.10** Redo Example 8.3 but with 36 equally spaced radial slots. Besides obtaining the numerical values in Table 8.1, also obtain a plot of the eddy current flow pattern. Explain why the AC reluctance has not decreased further.

REFERENCES

1. M. Sadiku, *Elements of Electromagnetics*, 3rd ed., Oxford Univ. Press, New York, 2001.
2. J. R. Brauer, Z. J. Cendes, B. C. Beihoff, and K. P. Phillips, Laminated steel eddy current losses versus frequency computed with finite elements, *IEEE Trans. Indust. Appl.* **36**: 1132–1137 (July/Aug. 2000).
3. A. E. Fitzgerald and C. Kingsley, *Electric Machinery*, 2nd ed., McGraw-Hill, New York, 1961, pp. 346–347.
4. N. A. Demerdash and T. W. Nehl, Use of numerical analysis of nonlinear eddy current problems by finite elements in the determination of parameters of electrical machines with solid iron rotors, *IEEE Trans. Magn.* **15**: 1482–1484 (Nov. 1979).
5. M. A. Juds, A nonlinear magneto dynamic model for AC magnets with shading coils, *Proc. Int. Relay Conf.*, 1994.
6. E. R. Laithwaite, *Propulsion without Wheels*, 2nd ed., English Univ. Press Ltd., London, 1970, Chapter 10.
7. E. R. Laithwaite, *Induction Machines for Special Purposes*, Chemical Publishing Co., New York, 1966, Chapter 9.
8. S. Ramo, J. R. Whinnery, and T. Van Duzer, *Fields and Waves in Communication Electronics*, Wiley, New York, 1965, pp. 292–293.
9. H. B. Dwight, *Tables of Integrals and Other Mathematical Data*, Macmillan, New York, 1961, pp. 324–325.
10. H. C. Roters, *Electromagnetic Devices*, Wiley, New York, 1941.

Magnetic Actuator Transient Operation

While the preceding two chapters analyzed magnetic actuators under DC and AC operation, they did not consider the transient effects of turning on (or off) the DC and AC currents or voltages. This chapter is the first to investigate transient operation of actuators. Its techniques will help determine actuator performance for any applied voltage or current versus time.

9.1 BASIC TIMELINE

The basic timeline for transient operation of magnetic actuators is

1. An energizing circuit turns on, supplying voltage and current.
2. The coil current rises, determined partly by an electrical time constant.
3. The magnetic flux density rises, determined partly by a time constant called the *magnetic diffusion time*.
4. The force rises as the magnetic flux density rises.
5. The force produces acceleration of the armature and/or attached mass.
6. After a certain time, during which the armature may or may not reach the end of its stroke, the energizing circuit may be turned off.

Each of these steps may introduce a time delay. For many applications, a time delay is undesirable because it slows the speed of response.

This chapter studies the basics of steps 3, 4, and 5, and 6 above. Steps 1 and 2 will not be investigated until Chapters 12, 14, and 15, which will examine further aspects of transient operation.

9.2 SIZE, FORCE, AND ACCELERATION

Magnetic force is the most important parameter of magnetic actuators, and it determines the mechanical acceleration and speed of response of the actuator. While many aspects of the mechanical performance will not be studied until Chapters 14–16, here some basic relations between force and actuator size are presented.

The force for axisymmetric plunger actuators of the type shown in Fig. E7.4.1 is related to the actuator of a more general design shown in Fig. 9.1. In both designs the plunger and its stopper extend to the same radius, but in Fig. 9.1 their inner radius may be greater than zero. Thus the cylindrical plunger of radius R_p may be hollow, with its end having area $k_a \pi R_p^2$ instead of πR_p^2 , where k_a is an area constant less than or equal to one.

For a cylindrical plunger of length L_p , the optimum design would have the same area for magnetic flux entering through the side and leaving the circular end of the plunger:

$$2\pi R_p L_p = k_a \pi R_p^2 \quad (9.1)$$

$$\text{Hence} \quad L_p = k_a R_p / 2 \quad (9.2)$$

would be the minimum plunger length. However, in many cases, such as in the actuator of Fig. 9.1, the actual plunger length is longer. Denoting the actual length as $k_L L_p$, where k_L is a constant greater than or equal to 1, the plunger volume is

$$v = k_L L_p (k_a \pi R_p^2) = k_L (\pi k_a^2 R_p^3) / 2 \quad (9.3)$$

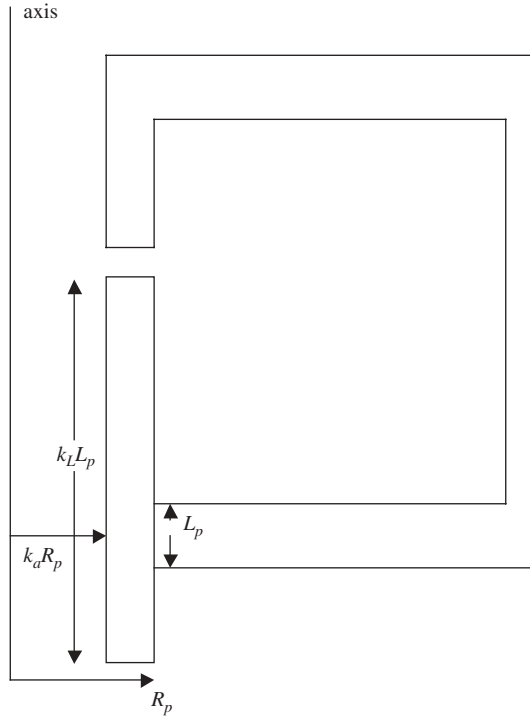


Figure 9.1 Dimensional parameters of axisymmetric plunger actuator.

The acceleration is

$$a = F/m = P(\pi k_a R_p^2)/(\rho v) \quad (9.4)$$

where P is the magnetic pressure and ρ is the mass density of the plunger material. It was shown in Chapter 5 that for typical steel the maximum magnetic pressure $P = 20\text{E}5 \text{ N/m}^2$. Therefore the maximum acceleration of the cylindrical plunger is

$$a = 20\text{E}5(\pi k_a R_p^2)/[\rho(\pi k_L k_a^2 R_p^3)/2] \quad (9.5)$$

$$a = 40\text{E}5/(\rho k_L k_a R_p) \quad (9.6)$$

For steel $\rho = 7800 \text{ kgm per cubic meter}$, and thus

$$a = 513/(R_p k_L k_a) \quad (9.7)$$

Thus, to maximize acceleration, $k_L k_a R_p$ should be minimized; that is, the smaller the plunger, the faster it will move, assuming there are no other forces than the magnetic force. This speedier acceleration of small objects is commonly observed in nature; for example, a 2-g hummingbird accelerates much faster than does a 10-kg turkey.

If the actuator of Fig. 9.1 is the Bessho actuator of Fig. 5.2, then the abovementioned dimensions are known. With $R_p = 20\text{E}-3 \text{ m}$, the area constant $k_a = 1$, and the length constant $k_L = 2\pi(0.02)(0.142)/\pi(0.02)^2 = 7.1$. Then (9.7) gives $a = 3613 \text{ m/s}^2$. If this acceleration exists over the entire stroke s , then

$$s = \frac{1}{2}at^2 \quad (9.8)$$

or

$$t = (2s/a)^{1/2} \quad (9.9)$$

For example, if $s = 10\text{E}-3 \text{ m}$, (9.9) gives $t = 2.35 \text{ ms}$. Note that this is the *minimum possible stroke time* for the Bessho actuator with no opposing forces or masses on the armature. Actual stroke times either experimentally observed [1] or computed using time-stepping finite element analysis [2] are 51 ms or greater.

For other types of actuators, such as the clapper types of Chapter 7, similar simple equations can be developed. Thus the maximum forces and minimum operation times can be estimated.

The minimum stroke time presented above assumes that the magnetic pressure is always the maximum. Thus it requires high current, which usually requires a significant risetime, and zero time for the magnetic field to diffuse through the plunger. The actual time for the magnetic field to diffuse is the subject of the next sections. Throughout this chapter, unless otherwise indicated, the hysteresis loop of the steel is assumed to be negligibly small.

9.3 LINEAR MAGNETIC DIFFUSION TIMES

Magnetic diffusion time τ_m is the time required for the fundamental component of flux density B at every point in a conducting material to rise from zero to at least approximately 63% of its final value after an applied step function in $H(t)$ [3]. The step in $H(t)$ is usually due to a current step applied to a coil.

Diffusion time τ_m is a useful parameter for predicting eddy current delay effects on transient magnetic fields and related parameters such as inductance and force. Diffusion time has been derived analytically using (8.26) for several simple one-dimensional (1D) geometries of *linear* materials [3].

9.3.1 Steel Slab Turnon and Turnoff

For planar devices with B varying only over one planar dimension x , the diffusion time for materials with permeability μ and conductivity σ is [3]

$$\tau_m = \mu\sigma(w/\pi)^2 \quad (9.10)$$

where w is the width of the conducting slab between two coil regions. When the step rise in $H(t)$ is applied, the magnetic flux density B diffuses inward from both slab sides (coil regions), for example, moving in the x direction from its left side to the right and from its right side to the left, as shown in Fig. 9.2. The fundamental Fourier component of the flux reaches 63% of its final value in the middle of the conducting slab at $t = \tau_m$. The flux density is y -directed and obeys [3]:

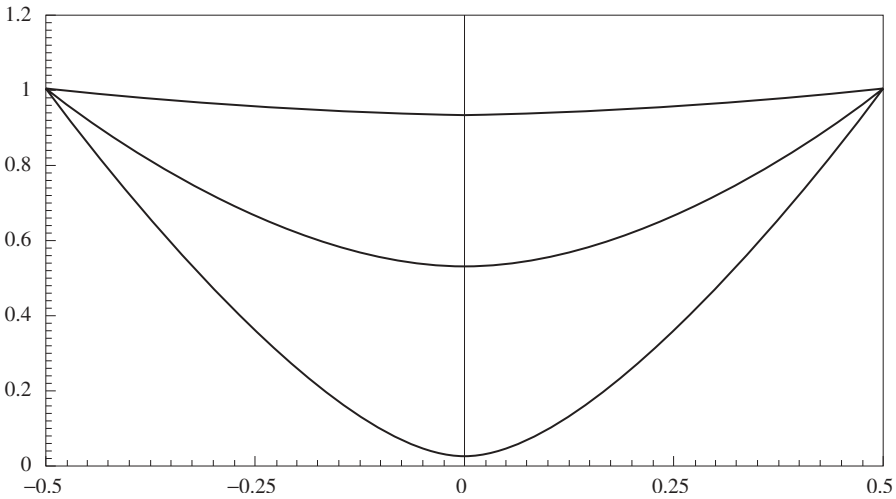


Figure 9.2 Computer display of analytical results using (9.11) for diffusion into a steel slab with constant permeability. The top curve is for $t = 3 \tau_m$, the middle curve is for $t = \tau_m$, and the lower curve is for $t = 0.3 \tau_m$. The vertical axis is $B(t)/B_F$, and the horizontal axis is x/w .

$$B_y = B_F \left[1 - \sum_{n=\text{odd}} (4/(n\pi)) \cos(n\pi x/w) e^{-n^2 t/\tau_m} \right] \quad (9.11)$$

where B_F is the final flux density long after the step current is incremented and x is the distance from the slab center. Figure 9.2 plots the magnetic flux density versus position of (9.11) at various times, showing the inward diffusion. Note that the *total* flux density in the middle of the conducting slab at $t = \tau_m$ reaches 53.2% of the final value, a change from the 63% due to only the fundamental component.

If the DC coil current has existed over many diffusion times and is suddenly switched off, the current and $H(t)$ then undergo a step decrement. The magnetic flux density B diffuses outward to both slab sides, decaying most slowly in the center of the slab. Thus the magnetic force will also eventually decay to zero. However, if the steel is a hard magnetic material as discussed in Chapter 5, then it will have significant coercive field intensity H_c and residual flux density B_r , and there may be a significant permanent magnet force. For soft steels, however, the permanent magnet force is usually less than 1% of the steady-state force when energized. For a current step decrement at time zero, the flux density of (9.11) becomes

$$B_y = B_0 \sum_{n=\text{odd}} (4/(n\pi)) \cos(n\pi x/w) e^{-n^2 t/\tau_m} \quad (9.12)$$

where B_0 is the initial flux density (in the y direction). At time $t = \tau_m$ the maximum flux density B_y in (9.12) is 47% of B_0 .

Example 9.1 Magnetic Diffusion into Linear Steel Slab during Turnon and Turnoff Figure E9.1.1 shows a large planar magnetic device made up of one coil, solid steel, and laminated steel. All steel is of depth 1 m. There is no airgap between the solid armature (rotor) and laminated stator. The laminations have relative permeability of 100,000 and zero conductivity. Figure E9.1.2 shows a 1D slice through the right half of Fig. E9.1.1 with width $w = 0.447$ m. The slice is used because the diffusion time of (9.10) is a 1D concept. The conductivity of the armature is assumed to be $1.7\text{E}6$ S/m, and its B – H curve is assumed to obey an equation for cast steel of Chapter 2:

$$H = (49.4e^{1.46B^2} + 520.6)B \quad (\text{E9.1.1})$$

which for low B – H has a relative permeability of 1344.

Assuming that $NI = 264$ ampere-turns has existed for a long time in Fig. E9.1.1, and is switched off at time zero, the following are to be found:

- Use (9.10) to calculate the diffusion time.
- Use Maxwell SV to obtain the flux line plot and energy at time zero for the entire device and for the slice.
- If you have access to Maxwell 2D, which has a transient finite-element solver, then find the flux line plot at $t = 100$ s, and also graph B versus x at $t = \tau_m$, and compare it with (9.12).

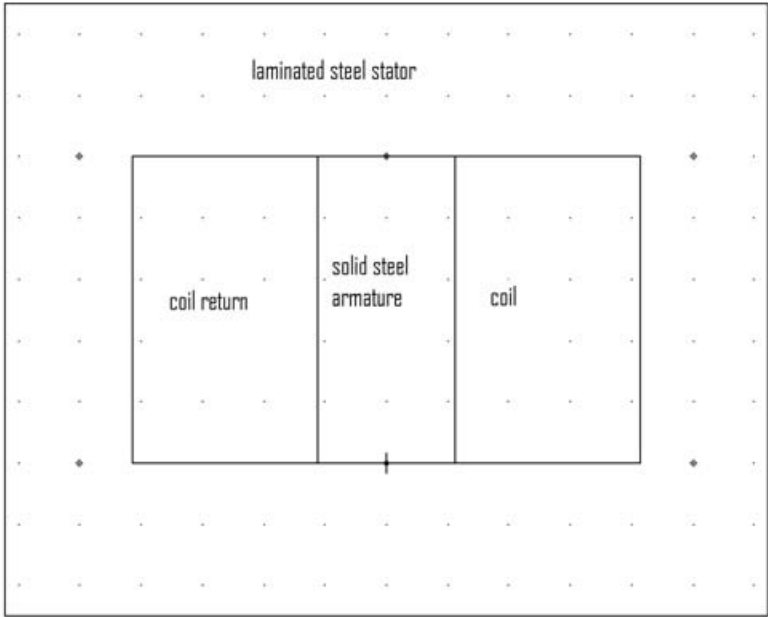


Figure E9.1.1 Computer display of large magnetic device. Its depth is 1 m. The solid armature is of (x,y) dimensions 0.447×1.0 m. Both coil regions are of dimension 0.6055×1.0 m. The laminated stator has overall dimensions 2.49×2.0 m.

Solution

- (a) The diffusion time τ_m for Fig. E9.1.2 is found using (9.10) with $w = 0.447$ m to be 58.14 seconds.
- (b) For the entire device, Maxwell SV obtains an energy of 25.74 J. For the slice, which has only 5% of the ampere-turns, the ampere-turns are reduced to 13.2, and the energy computed by Maxwell SV is reduced to 0.65 J, which is approximately 2.5% of the energy of the entire device, as it should be. In both models, the flux density in the armature is approximately 0.4427 T.
- (c) The “transient” solver in Maxwell 2D was used to obtain the flux density distribution computed in Fig. E9.1.2 at $t = 100$ s. Note that the laminated stator has uniform flux density but the solid armature has a nonuniform flux density with the lowest value on its surface.



Figure E9.1.2 Computer display of slice of Fig. E9.1.1 for use in determining diffusion. The rotor core has half-width equal to the dimension $T_1 = 0.2235$ m in Fig. E9.1.1. The rotor has conductivity $1.7E6$ S/m and relative permeability 1344. The stator has zero conductivity and relative permeability 100,000. The computed magnetic flux lines are shown at $t = 100$ s after the winding current decrement.

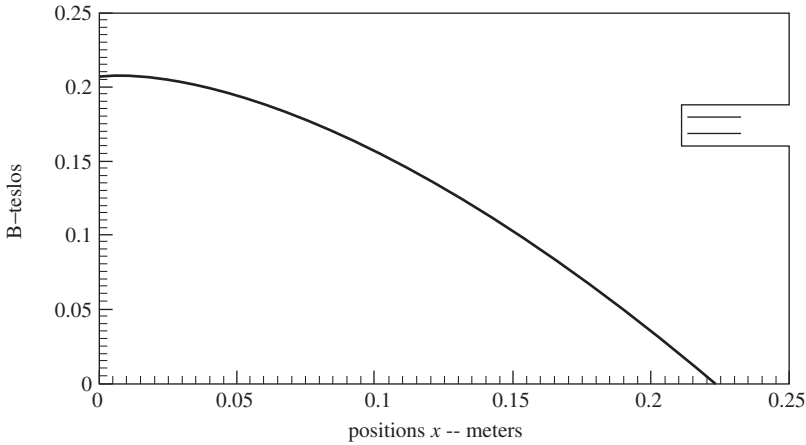


Figure E9.1.3 Graph of B versus x for model of Fig. E9.1.2 at time $t = 58$ s, which is close to the computed diffusion time using (9.12). Note that the dark theoretical curve of (9.12) lies on top of the lighter curve computed by transient finite-element analysis.

The computed flux density at 58 s for the finite-element model of Fig. E9.1.1 is graphed by the postprocessor in Fig. E9.1.3. The center value of 0.2073 T is 47% of the initial $B_0 = 0.4427$ T throughout the armature, and thus the computed diffusion time agrees closely with the 58.14 s predicted by (9.10). In Fig. E9.1.3 the curve of finite-element results lies on top of the analytical curve from (9.12).

9.3.2 Steel Cylinder

Because many actuators, including the Bessho actuator of Fig. 5.2, have cylindrical plunger armatures and cylindrical stoppers made of solid steel, magnetic diffusion in cylinders is important. The magnetic diffusion time τ_m for a cylinder with constant permeability obeys [3]

$$\tau_m = \mu \sigma R^2 / (2.4048)^2 \quad (9.13)$$

where σ is electrical conductivity, R is the cylinder radius, and the value 2.4048 is the root of the first-order Bessel function.

For the Bessho actuator of Fig. 5.2, the conductivity of all steels is specified as $1.7\text{E}6$ S/m [1]. Two different B - H curves are specified. One is for the armature and stopper of Fig. 5.2, and the other is for the yoke. The cylindrical armature B - H curve begins with a constant permeability of 630 times that of air. The resulting magnetic diffusion time τ_m using (9.13) is 93 ms. However, nonlinear finite-element computations [2] have obtained closing times with the abovementioned steel as low as 51 ms, so the diffusion time τ_m of (9.13) appears to be longer than actual nonlinear diffusion time.

The analytic equation for the flux density in a linear steel cylinder as a function of time after a step increment in current is [3]

$$B_z(t) = B_F \left[1 - \sum_{n=1}^{\infty} [c_n J_0(\sqrt{\mu\sigma\alpha_n r}) e^{-\alpha_n t}] \right] \quad (9.14)$$

where the alphas involve roots of Bessel functions:

$$\alpha_n = \frac{1}{\mu\sigma} (v_n/R)^2 \quad (9.15)$$

The constants in (9.14) can be shown to be $c_1 = 1.602$, $c_2 = -1.066$, $c_3 = 0.851$, followed by less important ones. Using (9.14), at time $t = \tau_m$ the flux density along the cylinder axis has the fundamental component of 63% of the final value B_F , but the total flux density at that time along the axis is only 41.62% of B_F .

9.4 NONLINEAR MAGNETIC DIFFUSION TIME

The formulas for magnetic diffusion time τ_m in the preceding section all contain permeability μ . Many magnetic devices contain steel operating in the nonlinear region of its B - H curve, and thus the value of μ cannot be determined. The effect of a nonlinear B - H curve on diffusion time must be investigated.

9.4.1 Simple Equation for Steel Slab with “Step” B - H

To obtain an approximate formula for τ_m in nonlinear planar slabs, first assume a “step” B - H curve [4] with infinite slope from $B = 0$ to B_m and zero slope for $B > B_m$. This simple B - H curve has been shown to respond to an applied field intensity $H_0(t)$ by producing a traveling flux density wavefront of position $x_0(t)$ given by [4]

$$x_0(t) = [\int H_0(t) dt / (\frac{1}{2} \sigma B_m)]^{1/2} \quad (9.16)$$

where the $\frac{1}{2}$ is placed in the denominator because the applied $H_0(t)$ here starts at zero, not $-B_m$ as assumed in Ref. 4. Assuming a planar slab of width w with $H_0(t)$ stepped to H_0 on both slab sides ($x = 0$ and $x = w$), then $x_0(t) = w/2$ at time $t = \tau_m$. Then the integral is replaced by $H_0\tau_m$, resulting in the formula for nonlinear planar magnetic diffusion time with step B - H :

$$\tau_m = \sigma w^2 B_m / (8H_0) \quad (9.17)$$

9.4.2 Transient Finite-Element Computations for Steel Slabs

The diffusion time τ_m for devices with nonlinear B - H curves may be computed using transient finite-element analysis of the type used in Example 9.1. Various

B – H curves may be input, both the preceding “step” curve and curves of actual steels.

Example 9.2 Magnetic Diffusion in Nonlinear Rectangular Inductor The first example of applying (9.17) is to the rectangular inductor shown in Fig. E9.2.1. The entire rectangular core of this inductor is 45 mm wide and 90 mm high and assumed to be made of solid steel. The magnetic field and eddy currents are assumed to be invariant with dimension z (out of the page), and thus the fields vary only in the xy plane. To achieve such independence of z , the depth of the inductor into the page must be much greater than its dimensions in the xy plane. The eddy currents in the steel core of conductivity $1.7\text{E}6$ S/m flow in the z direction and must sum to zero according to Kirchhoff’s current law. Each of the two coils in Fig. E9.2.1 has 660 turns. Then

- (a) The nonlinear diffusion time is to be found using (9.17) assuming a step

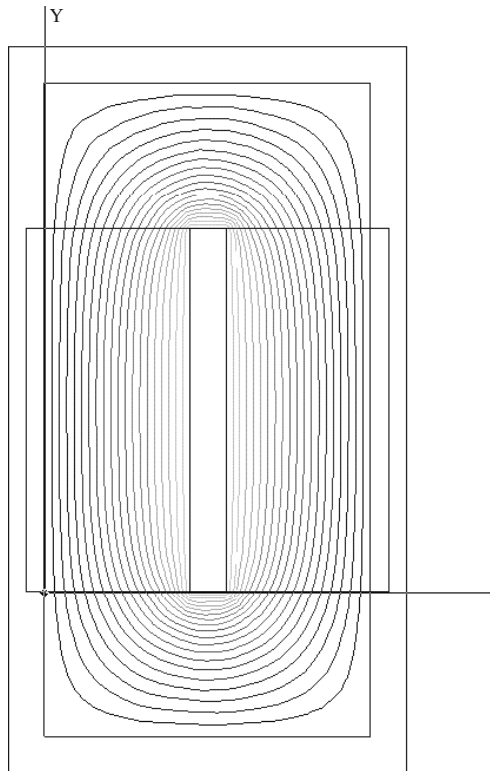


Figure E9.2.1 Computer display of rectangular planar inductor, showing typical magnetostatic flux lines computed by two-dimensional planar finite-element analysis. The solid steel is a hollow rectangle consisting of four legs of width 20 mm, with copper windings on its left and right legs carrying currents that produce magnetic flux as shown. The window in the center of the legs is 5×50 mm.

curve at $B_m = 2$ T for coil currents of 0.5, 1, and 2 A. Also, find its magneto-static flux lines using Maxwell SV and constant steel relative permeability of 2000.

- (b) Using Maxwell 2D or other available nonlinear transient finite-element software, confirm the results of (9.17) and then use the actual armature steel B – H curve given in Ref. 1. To save computer time, a slice model can be used as in Example 9.1.

Solution

- (a) The diffusion time τ_m for Fig. E9.2.1 is found using (9.17) as follows. The width $w = 0.020$ m in Fig. E9.2.1. The applied field intensity H_0 is found using Ampere's law:

$$(H_0)(2 \times 0.050) = 2(660)I \quad (\text{E9.2.1})$$

$$H_0 = 13,200 I \quad (\text{E9.2.2})$$

The resulting three τ_m values are listed in Table E9.2.1. Note that all three values are much less than the 54.6 ms obtained by the linear formula (9.13), and that the higher the current, the smaller the diffusion time. The computed flux lines are shown in Fig. E9.2.1.

- (b) Rather than model the entire planar region of Fig. E.9.2.1, because the inductor dimension in the y direction is considerably greater than that in the x direction, the slice model of Fig. E9.2.2 can be used. Its dimension in the y direction is only 2 mm. Because eddy currents and skin effects must be modeled, a fairly fine finite element mesh is required, and thus the reduced computer time obtained by the reduced model of Fig. E9.2.2 is helpful.

The windings in Fig. E9.2.2 contain a step current $I(t)$ and number of conductors N . The N in Fig. E9.2.2 must be $(2 \text{ mm})/(50 \text{ mm})$ times the 660 turns of Fig. E9.2.1, and thus $N = 26.4$.

Transient finite-element analysis was first used to obtain the diffusion time for low H_0 values, for which the relative steel permeability is 630. Ansoft's Maxwell software computed the time for the flux density in the center of both steel legs to reach approximately half of its final value as 56 ms. This agrees well with the 54.6 ms obtained using the linear formula (9.10).

Next, nonlinear transient analyses were performed. Since the slope of the B – H curve is used at each timestep in Newton's method of Chapter 4, the infinite slope

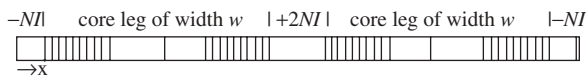


Figure E9.2.2 A 2-mm-high section of Fig. E9.2.1. Computed flux lines are for $t = 4$ ms and real B – H curve. Note that the flux lines diffuse inward from the four outer steel core surfaces with windings of conductors N containing current $I = 1$ A.

assumed for the step B – H curve of (9.17) must be replaced by a large finite slope. Here B_m is assumed to be 2 T and the slope from $B = 0$ to 1.93 T is assumed to be 100,000 times that of air. Above 1.93 T, the slope is gradually decreased to that of air at 2.07 T and higher. Table E9.2.1 lists the values of τ_m for a range of H_0 . The theoretical values of (9.17) are compared with finite-element analysis (FEA) computed values with the approximate step B – H curve. Note that the computed times agree closely with those of (9.17).

Table E9.2.1 also lists the computed nonlinear diffusion times with the specified real steel B – H curve [1]. The real steel has an initial permeability of 630 times that of air for $B \leq 1$ T, and has a typical saturation knee that approaches the slope of air for $B \gg 2$ T. As expected, the real B – H curve produces different nonlinear diffusion times.

Figure E9.2.3 plots B versus position x in Fig. E9.2.2 at two timesteps of the finite-element analysis for 2 A and the step B – H of Table E9.2.1. Note the inward diffusion of the step B from all four steel surfaces, as expected [5]. Figure E9.2.4 plots magnetic flux versus time for the same case. Since inductance is flux times N/I , the effective inductance also varies with time in the same manner.

9.4.3 Simple Equation for Steel Cylinder with “Step” B – H

To obtain an approximate formula for τ_m in nonlinear steel cylinders, first assume a “step” B – H curve as in the preceding section. Assuming the step curve for a steel cylinder of radius R and conductivity σ , it has been found [4] that the magnetic field diffuses into the cylinder following a step wavefront at moving position $r_0(t)$. A formula [4] for the wavefront $r_0(t)$ derived for a field switched between $-B_m$ and $+B_m$ is altered here to account for a field switched from 0 to $+B_m$ by an applied $H_0(t)$

$$2\int H_0 dt / [\frac{1}{2} \sigma R^2 B_m] = \lambda (\ln \lambda - 1) + 1 \quad (9.18)$$

where

$$\lambda = r_0^2(t)/R^2 \quad (9.19)$$

These two formulas are here applied to determine magnetic diffusion time. Because the current is a step applied at time zero, H_0 is also a step, and thus the left-hand side of (9.18) has its integral over time replaced by $H_0 \tau_m$. The value of λ is zero, since $r_0(t) = 0$ when $t = \tau_m$. Thus (9.18) becomes

TABLE E9.2.1 Nonlinear Magnetic Diffusion Times for Fig. E9.2.2 (ms)

I (A)	H_0 (A/m)	Analytical (9.17)	FEA (Step B – H)	FEA (Real B – H)
0.5	6600	25.8	25.0	18.9
1.0	13200	12.9	12.5	9.0
2.0	26400	6.4	6.2	5.0

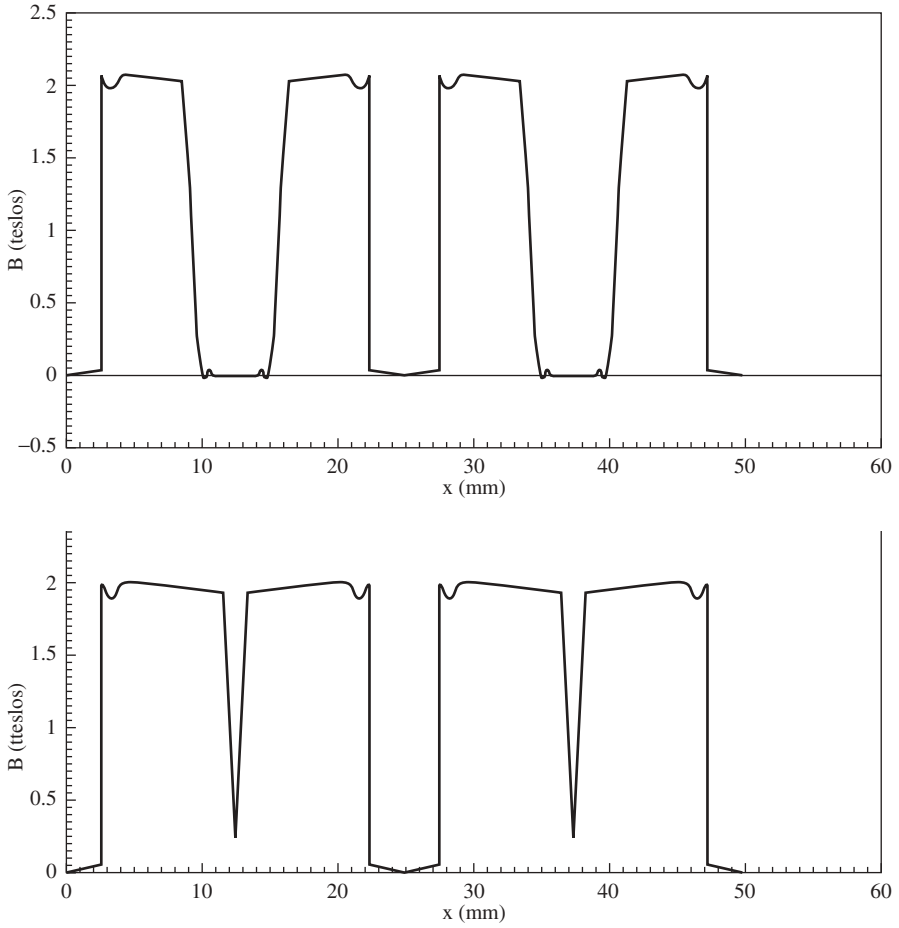


Figure E9.2.3 Computed magnetic flux density B versus position x in Fig. E9.2.2 for $I = 2$ A and step B – H curve at times (a) $t = 3$ ms, (b) $t = 6$ ms.

$$4H_0 \tau_m / [\sigma R^2 B_m] = 1 \quad (9.20)$$

giving

$$\tau_m = [\sigma R^2 B_m] / [4H_0] \quad (9.21)$$

9.4.4 Transient Finite-Element Computations for Steel Cylinders

Transient finite-element analysis of the type used in Examples 9.1 and 9.2 can be used to compute diffusion into nonlinear steel cylinders. Various B – H curves may be input, both the “step” curve of (9.21) and curves of actual steels.

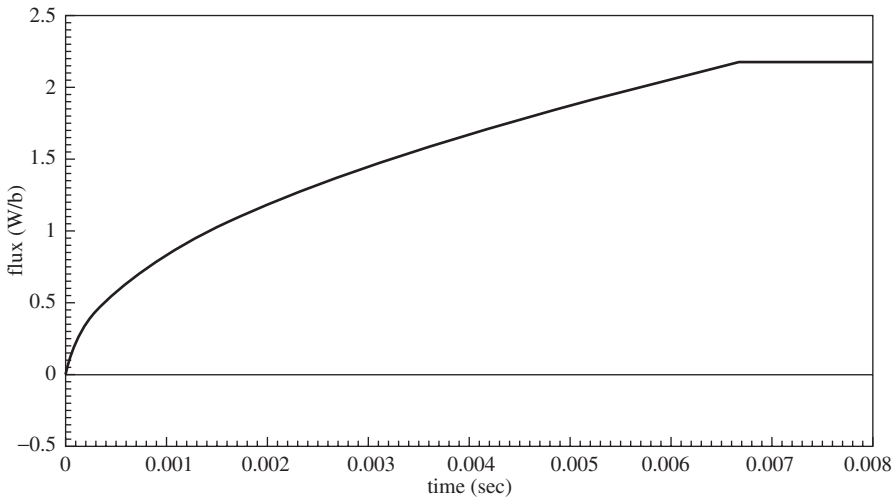


Figure E9.2.4 Computed magnetic flux versus time for $I = 2$ amperes and step B - H curve in Fig. E9.2.2 with depth into page assumed to be 1 m.

Further studies of transient behavior of magnetic actuators will be presented in Chapters 14–16. They will show that mechanical motion can greatly affect the current waveform, magnetic flux, and magnetic force.

Example 9.3 Magnetic Diffusion in Nonlinear Bessho Actuator Plunger An example of applying (9.21) is to the Bessho axisymmetric plunger actuator of Fig. 5.2. Rather than model the entire actuator, a thin (10-mm) slice as shown in Fig. E9.3.1 is to be modeled with two-dimensional finite elements. The slice represents the armature (here assumed stationary with zero airgap), the coil, and the yoke. The purpose of the slice is to model only the variation of B with radial position r .

Then

- (a) The nonlinear diffusion time is to be found using (9.21) assuming a step curve at $B_m = 2$ T for coil currents of 0.5 and 2 A. Also, find its magnetostatic flux lines using Maxwell SV and constant steel relative permeability of 630.

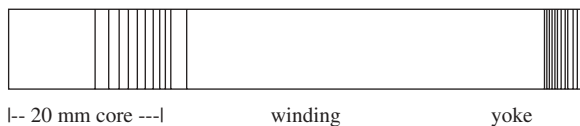


Figure E9.3.1 Slice (height 10 mm) of Bessho magnetic actuator, showing computed magnetic flux lines at $t = 20$ ms with actual B - H and $I = 0.5$ A.

- (b) Using Maxwell 2D or other available nonlinear transient finite-element software, confirm the results of (9.18) and then use the actual armature steel B – H curve given in Ref. 1 for 0.5- and 2-A coil currents.

Solution

- (a) The diffusion time τ_m for Fig. E9.3.1 is found using (9.21) as follows. The radius $R = 0.020$ m from Fig. 5.2. The applied field intensity H_0 is found using Ampere’s law for Fig. 5.2

$$H_0 = NI/l \tag{E9.3.1}$$

- where $N = 3300$. The pathlength l is assumed to be the 250 mm axial length of the coil window, meaning that the cylindrical core of radius 20 mm drops all ampere-turns (the outer yoke is assumed to have negligible MMF drop). The assumed B_m in steel is 2 T. Thus $I = 0.5$ A gives $H_0 = 6600$ A/m. Substituting in (9.18) with the steel $\sigma = 1.7\text{E}6$ S/m gives $\tau_m = 51.5$ ms, which is listed in Table E9.3.1. The other analytical value listed in Table 9.3.1 is for the current quadrupled to 2 A, for which (9.21) obtains one fourth the diffusion time, $\tau_m = 12.9$ ms. Note that both values are much less than the 93 ms obtained by the linear formula (9.13), and that the higher the current, the smaller the diffusion time.
- (b) For the step B – H curve, finite-element analyses of Fig. E9.3.1 were made with input currents of 0.5 and 2 A. Figure E9.3.2 shows the computed magnetic flux density waveshape in the core at a typical instant; note that it is a steep step to 2 T as expected. The time when the wavefront reaches zero radius is the magnetic diffusion time entered in Table E9.3.1. The computed diffusion times agree well with the times predicted using (9.18).

Other transient finite-element computations were then made using the actual Bessho core and yoke B – H curves. Figure E9.3.3 shows the computed flux density waveshape at a typical instant; note that it now has a more gradual rise. The computed diffusion time constants with the actual B – H curves are also listed in Table E9.3.1. Note that the B – H curve shape has a significant effect on the computed nonlinear diffusion time.

PROBLEMS

- 9.1** Find the maximum acceleration and minimum operation time for a smaller version of the Bessho actuator, in which all dimensions are reduced by 50%.

TABLE E9.3.1 Bessho Actuator Nonlinear Magnetic Diffusion Times (ms)

Current (A)	Analytical (9.21)	Finite Element (Step B – H)	Finite Element (Real B – H)
0.5	51.5	53.0	42.0
2.0	12.9	13.4	11.5

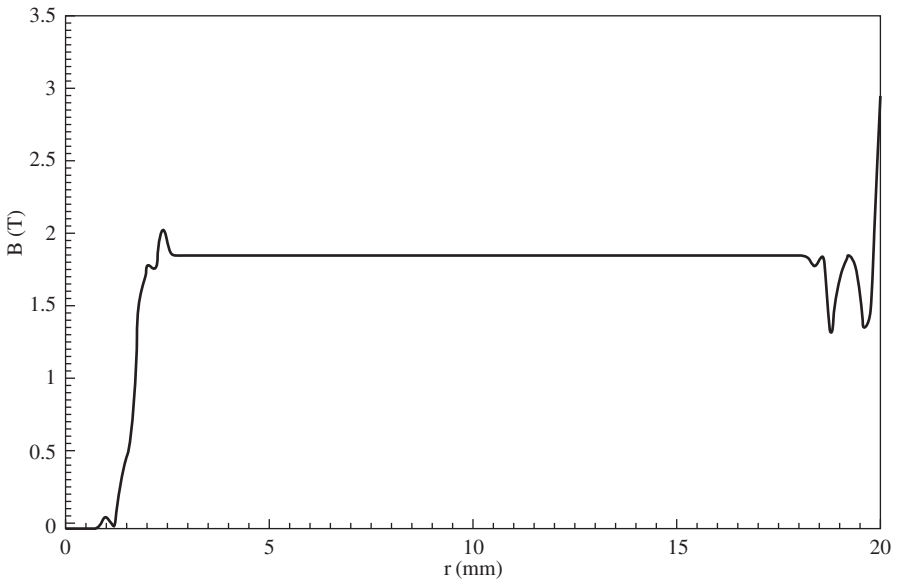


Figure E9.3.2 Flux density B (teslas) versus radius (mm) in core computed by nonlinear transient finite elements with step B - H curve at $t = 51$ ms.

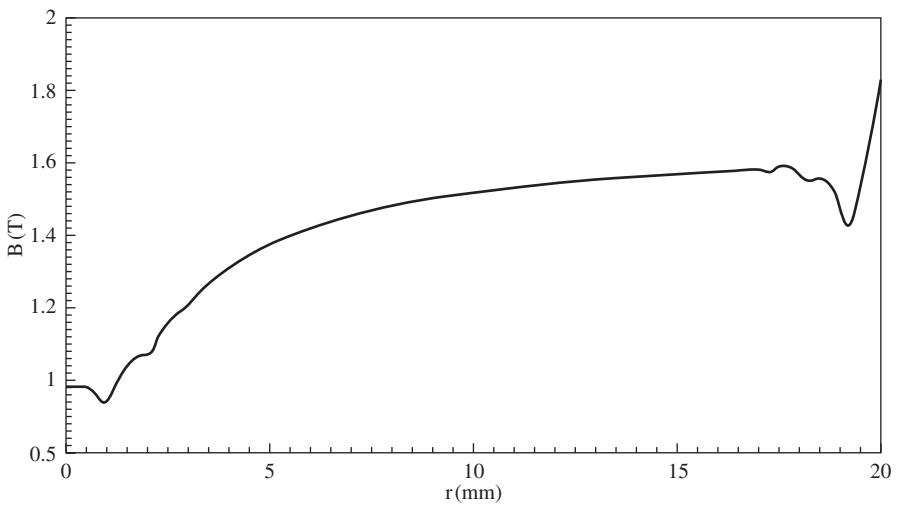


Figure E9.3.3 Flux density B (teslas) versus radius (mm) in core computed by nonlinear transient finite elements with actual B - H curve at $t = 40$ ms.

- 9.2 Find the analytic diffusion time for the steel with the properties of Example 9.1 case (a) but with its width reduced by a factor of (a) 10, (b) 100, (c) 1000.
- 9.3 Redo Example 9.1 cases (b) and (c) using Maxwell software but with its width reduced by a factor of 10.
- 9.4 Redo Example 9.1 cases (b) and (c) using Maxwell software but with its width reduced by a factor of 100.
- 9.5 Redo Example 9.1 cases (b) and (c) using Maxwell software but with its width reduced by a factor of 1000.
- 9.6 Put a 1-mm airgap at the upper armature–stator interface of Problem 9.3 and repeat the computations of Problem 9.3. Show that the airgap produces significant changes in the flux pattern.
- 9.7 Figure P9.7.1 shows a sector of a toroidal inductor with a circular (cylindrical) core. It extends into the page to a depth of 1 m. The core is made of solid steel and has inner radius $r_i = 10$ mm and outer radius $r_o = 30$ mm. Only a 4° sector of the 360° of the circular inductor is shown and to be modeled; this smaller model saves computer time. Inside the inner radius is a coil carrying ampere-turns NI in the $+z$ (out) direction, where $NI = 4.608$ or 9.215 ampere-turns. Outside the 30-mm core radius, to a radius of 31.6 mm, the coil ampere-turns are returned as $-NI$. The eddy currents in the core must sum to zero.
- Apply the nonlinear diffusion time formula to find diffusion times for both given ampere-turns. Note that because two different H_0 values exist because of the inductor's differing inner and outer pathlengths, you will find a range of diffusion times only for each value of ampere-turns.
 - Use Maxwell 2D to obtain diffusion times by nonlinear transient finite-element analyses with the real B – H curve of the Bessho armature steel.
- 9.8 Figure P9.8.1 shows a laminated core inductor mounted in a solid steel cabinet. The cabinet is made of solid steel panels on all of its six sides. Inductors are often placed inside such cabinets to house them mechanically and to confine their magnetic fields and thereby reduce electromagnetic interference. The cabinet (also called a “box” or a “housing”) is known to often increase the inductance. However, the inductance increase is delayed by the magnetic diffusion time of the solid steel panels. The inductor of Fig. P9.8.1 has N_T total turns placed in

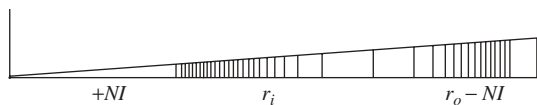


Figure P9.7.1 A 4° sector of circular inductor with inner core radius $r_i = 10$ mm and outer core radius $r_o = 30$ mm. The flux lines at 10 ms are computed with windings of $NI = 4.608$ A and with the real B – H curve. Note that the flux lines diffuse inward from both steel core surfaces.

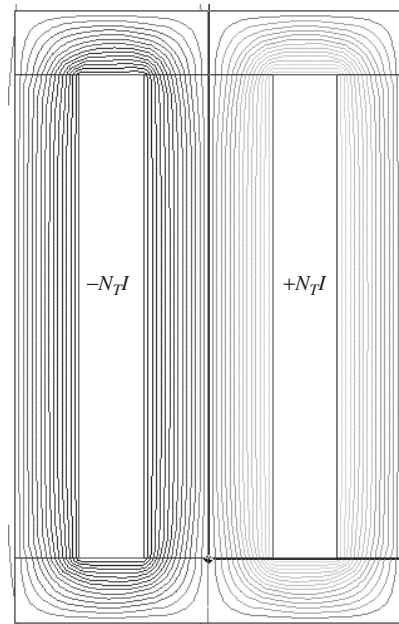


Figure P9.8.1 Computer display of laminated inductor core surrounded by solid steel panels on all four sides, showing typical magnetostatic (no eddy current) flux lines computed by Maxwell SV. The overall dimensions are 95 mm high and 60 mm wide. The four panels are all 10 mm thick. The laminated center core is 20 mm thick.

the center of a steel cabinet. Because the inductor core is laminated or made of composite ferromagnetic material with extremely low electrical conductivity, the electrical conductivity of the core is assumed to be zero. Thus eddy currents exist only in the solid steel panels. Figure P9.8.2 is a 2-mm-high slice of the right half of Fig. P9.8.1. It includes only the right half of the center leg, the right coil half, and the right panel, which has an eddy current that does not sum to zero. The eddy current in the right panel is returned through the other five cabinet panels. Because the coil is only on the inside of the steel panel and its eddy currents can be returned through the other five cabinet panels, diffusion

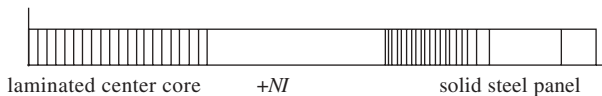


Figure P9.8.2 A 2-mm-high section of right half of inductor of Fig. P9.8.1 with computed flux lines at time $t = 6$ ms and $I = 0.5$ A for real $B-H$ curve. Note that the flux lines are diffusing into the panel from the coil ampere-turns NI , but that the flux lines in the laminated core are uniform because of its lack of eddy currents.

occurs only into the inside of the panel. Thus w must be considered to be twice the panel thickness T , giving

$$\tau_m = \sigma(2T)^2 B_m / (8H_0) = \sigma T^2 B_m / (2H_0) \quad (\text{P9.8.1})$$

The core material is assumed here to be laminated SAE 1010 steel with a curve given in Maxwell SV. The outer shell is assumed to be made of solid steel with conductivity $1.7\text{E}6$ S/m. The number of conductors N in Fig. P9.8.2 is assumed to be 26.4.

- (a) Find the analytic diffusion times for a step B – H curve at 2 T and currents of 0.5, 1.0, and 2.0 A.
- (b) Verify the results of (a) using Maxwell 2D or other software, and then repeat using the actual Bessho armature B – H curve [1].

REFERENCES

1. K. Bessho, S. Yamada, and Y. Kanamura, Analysis of transient characteristics of plunger type electromagnets, *Electric. Eng. Japan* **98**: 56–62 (July 1978).
2. J. R. Brauer, Magnetic actuator models including prediction of nonlinear eddy current effects and coupling to hydraulics and mechanics, *Proc. Congresso Brasileiro de Eletromagnetismo*, Gramado, Brazil, Nov. 2002.
3. H. H. Woodson and J. R. Melcher, *Electromechanical Dynamics*, Wiley, New York, 1968, Part II.
4. I. Mayergoyz, *Nonlinear Diffusion of Electromagnetic Fields*, Academic Press, San Diego, CA, 1998.

PART III

SENSORS

Hall Effect and Magnetoresistive Sensors

As mentioned in Chapter 1, magnetic sensors use magnetic fields to sense motion. Input energy in the form of mechanical energy and/or electromagnetic energy is converted to electrical energy, and thus magnetic sensors are a type of transducer. Usually magnetic sensors output a signal voltage along with little or no current.

Magnetic sensors using the Hall effect are very common, small, and inexpensive. This chapter examines the behavior, accuracy, and construction of typical Hall sensors. Along with the Hall effect, it also investigates a related parameter called *magnetoresistance*.

10.1 SIMPLE HALL VOLTAGE EQUATION

The Hall effect was discovered in 1879 by E. H. Hall. He found that a voltage is developed across a current-carrying semiconductor in a direction normal to the current flow and proportional to the magnetic flux density that is normal to both the current and the voltage difference. The Hall voltage across terminals spaced in the y direction is

$$V_y = k_H B_z J_x d_y \quad (10.1)$$

where d_y is the terminal (electrode) spacing shown in Fig. 10.1, which also shows the current density J_x flowing in the x direction, along with the flux density B_z . The Hall voltage is developed because the current experiences the Lorentz force of Chapter 2. It can be shown that the Hall electric field \mathbf{E} in volts per meter balances the motional electric field of (2.31) [1].

The Hall coefficient k_H in (10.1) can be shown for a narrow bar with $d_x \gg d_y$ to equal approximately [1]

$$k_H = -\frac{1}{ne} \quad (10.2)$$

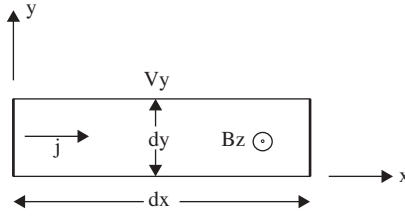


Figure 10.1 Hall effect voltage in a narrow semiconductor bar.

where n is the electron concentration in electrons per cubic meter and e is the charge on an electron = 1.602×10^{-19} C (coulombs). The electron concentration varies with the semiconductor material used. Typically, silicon is used because it is so widely available, thermally stable, and inexpensive, and has conductivity in the semiconductor range. In fact, many Hall sensors are built within CMOS (complementary metal oxide semiconductor) or other integrated silicon circuits. The semiconductor range of conductivity is within several orders of magnitude of 1 S/m, and can be varied by doping with impurities. If doped so as to contain holes, the Hall constant of (10.2) becomes

$$k_H = \frac{1}{pe} \quad (10.3)$$

where p is the hole concentration in holes per cubic meter.

Practical Hall sensors often have many large electrodes and a wide range of geometries, which can make the accuracy of (10.1) poor. To analyze a wide range of geometries and materials, a numerical technique is required that will solve for current flow in Hall sensors.

10.2 HALL EFFECT CONDUCTIVITY TENSOR

Current flow is governed by Ohm's law for fields given in Chapter 2. When conductivity σ is anisotropic (dependent on direction), then it must be expressed as a matrix called a *tensor*, and Ohm's law becomes

$$\begin{bmatrix} J_x \\ J_y \\ J_z \end{bmatrix} = \begin{pmatrix} \sigma_{xx} & \sigma_{xy} & \sigma_{xz} \\ \sigma_{yx} & \sigma_{yy} & \sigma_{yz} \\ \sigma_{zx} & \sigma_{zy} & \sigma_{zz} \end{pmatrix} \begin{bmatrix} E_x \\ E_y \\ E_z \end{bmatrix} \quad (10.4)$$

Because an applied magnetic field produces a Lorentz force on moving electrons, the conductivity tensor described above is indeed anisotropic. Fermi gas theory of free electrons [3] experiencing \mathbf{B} in the z direction produces the following matrix elements of (10.4)

$$\sigma_{xx} = \sigma_{yy} = \frac{\sigma_0}{1 + (\omega_c \tau)^2} \quad (10.5)$$

$$\sigma_{xy} = \frac{-\omega_c \tau \sigma_0}{1 + (\omega_c \tau)^2} \quad (10.6)$$

$$\sigma_{yx} = \frac{\omega_c \tau \sigma_0}{1 + (\omega_c \tau)^2} \quad (10.7)$$

$$\sigma_{xz} = \sigma_{yz} = \sigma_{zx} = \sigma_{zy} = 0 \quad (10.8)$$

$$\sigma_{zz} = \sigma_0 \quad (10.9)$$

where ω_c is the cyclotron frequency for a free electron, τ is the collision time, and σ_0 is the *bulk conductivity* [3]

$$\sigma_0 = ne^2 \tau m \quad (10.10)$$

where m is electron mass = 9.1085E-31 kg. The cyclotron frequency of the free electrons due to the force of the magnetic field is

$$\omega_c = eB/m \quad (10.11)$$

Because (10.6) and (10.7) differ for $B > 0$, Hall effect and magnetoresistance create an *unsymmetric* conductivity tensor.

The Hall voltage equation (10.1) can be derived by making the following assumptions:

1. Assuming $E_z = 0$, then (10.4)–(10.9) give

$$J_y = \frac{\sigma_0}{1 + (\omega_c \tau)^2} (\omega_c \tau E_x + E_y) \quad (10.12)$$

2. Assuming $J_y = 0$, then (10.12) and (10.11) give

$$E_y = -\omega_c \tau E_x = -\frac{eB}{m} E_x \quad (10.13)$$

Next, (10.4)–(10.9) give

$$J_x = \frac{\sigma_0}{1 + (\omega_c \tau)^2} (E_x - \omega_c \tau E_y) \quad (10.14)$$

Substituting (10.13) into (10.14) gives

$$J_x = \sigma_0 E_x \quad (10.15)$$

3. Assuming that E_y is uniform in y , then (10.13) gives

$$V_y = E_y d_y = -d_y \frac{eB_z \tau}{m} E_x \quad (10.16)$$

Substituting (10.15) and then (10.10), we obtain the Hall voltage:

$$V_y = -d_y \frac{eB_z \tau}{m\sigma_0} J_x = -d_y \frac{B_z J_x}{ne} \quad (10.17)$$

Note that (10.17) agrees with (10.1) and (10.2). However, these three assumptions have to hold true for the simple equation (10.1) to apply. These assumptions are valid only for narrow bars with infinitesimal Hall voltage sensing electrodes.

Example 10.1 Simple Hall Equation Applied to Semiconducting Bar A wide bar of semiconductor material as shown in Fig. 10.1 has dimensions $8 \times 10 \times 0.25$ mm in x , y , and z , respectively. The measured current I in the x direction is 2.5 mA for 1 V applied across the current-carrying electrodes at $x = 0$ and $x = d_x$.

- Calculate the bulk resistance and σ_0 .
- A narrow bar of the same material and current density placed in a magnetic field of 1 T yields a Hall electric field of -23.8 V/m. Find the Hall coefficient and the conductivity tensor.

Solution

- The bulk resistance is $R = V/I = 1/0.0025 = 400 \Omega$. Analogous to reluctance of Chapter 3, resistance of a bar obeys

$$R = l/(\sigma S) \quad (\text{E10.1.1})$$

where as in Chapter 3, l is length, and S is cross-sectional area. Substituting the length and area of the wide bar yields the bulk conductivity $\sigma_0 = 8$ S/m, which is within the wide conductivity range of semiconductors.

- From (10.17), (10.1), and (10.2), the Hall electric field for the narrow bar is

$$E_y = k_H B_z J_x \quad (\text{E10.1.2})$$

In terms of resistivity ρ , the inverse of conductivity, where $1/\sigma_0 = \frac{1}{8} = 0.125$:

$$\begin{bmatrix} E_x \\ E_y \end{bmatrix} = \begin{pmatrix} 0.125 & -k_H B_z \\ k_H B_z & 0.125 \end{pmatrix} \begin{bmatrix} J_x \\ J_y \end{bmatrix} \quad (\text{E10.1.3})$$

Given the -23.8 V/m measurement for $J_x = I/S = 1000$ A/m², the off-diagonal terms can be filled in to give

$$\begin{bmatrix} E_x \\ E_y \end{bmatrix} = \begin{pmatrix} 0.125 & 0.0238 \\ -0.0238 & 0.125 \end{pmatrix} \begin{bmatrix} J_x \\ J_y \end{bmatrix} \quad (\text{E10.1.4})$$

The Hall coefficient is thus $k_H = -0.0238$. The tensor conductivity is the inverse of the above resistivity tensor matrix

$$\begin{pmatrix} \sigma_{xx} & \sigma_{xy} \\ \sigma_{yx} & \sigma_{yy} \end{pmatrix} = \begin{pmatrix} \rho_{xx} & \rho_{xy} \\ \rho_{yx} & \rho_{yy} \end{pmatrix}^{-1} \quad (\text{E10.1.5})$$

which means that the product of the resistivity and conductivity tensors is unity:

$$\begin{pmatrix} \rho_{xx} & \rho_{xy} \\ \rho_{yx} & \rho_{yy} \end{pmatrix} \begin{pmatrix} \sigma_{xx} & \sigma_{xy} \\ \sigma_{yx} & \sigma_{yy} \end{pmatrix} = \begin{pmatrix} 1 & 0 \\ 0 & 1 \end{pmatrix} \quad (\text{E10.1.6})$$

The conductivity tensor can be easily found in the case when (10.5)–(10.8) render diagonal terms equal and off-diagonal terms equal but opposite in sign:

$$\begin{pmatrix} \rho_{xx} & \rho_{xy} \\ -\rho_{xy} & \rho_{xx} \end{pmatrix} \begin{pmatrix} \sigma_{xx} & \sigma_{xy} \\ -\sigma_{xy} & \sigma_{xx} \end{pmatrix} = \begin{pmatrix} 1 & 0 \\ 0 & 1 \end{pmatrix} \quad (\text{E10.1.7})$$

Multiplying out the left side and using Cramer's rule gives

$$\sigma_{xx} = \rho_{xx}/(\rho_{xx}^2 + \rho_{xy}^2) \quad (\text{E10.1.8})$$

$$\sigma_{xy} = -\rho_{xy}/(\rho_{xx}^2 + \rho_{xy}^2) \quad (\text{E10.1.9})$$

which for the resistivity tensor of (E10.1.4) gives the desired conductivity tensor

$$\begin{pmatrix} \sigma_{xx} & \sigma_{xy} \\ \sigma_{yx} & \sigma_{yy} \end{pmatrix} = \begin{pmatrix} 7.72013 & -1.46991 \\ 1.46991 & 7.72013 \end{pmatrix} \quad (\text{E10.1.10})$$

10.3 FINITE-ELEMENT COMPUTATION OF HALL FIELDS

To predict Hall voltages for arbitrary geometries, including bars that are not narrow, as well as for arbitrary materials, a numerical method is needed. Similar to the finite elements of Chapter 4 for magnetic fields, here finite elements are applied to current flow problems with anisotropic tensor conductivity.

10.3.1 Unsymmetric Matrix Equation

From Ohm's law, voltages and currents are related by the matrix equation

$$[C] \{V\} = \{I\} \quad (10.18)$$

where $[C]$ is the conductance matrix. Chapter 4 showed that finite elements have shape functions. For a shape function N of any type, it can be shown that the conductance matrix is of the form

$$[C] = \sum dv [\nabla N]^T [\sigma] [\nabla N] \quad (10.19)$$

where the summation is over volume integrals of individual finite elements. Note that the tensor conductivity appears, postmultiplied by the gradient of N and pre-multiplied by the matrix transpose of the gradient of N . Because the Hall effect conductivity tensor of (10.4) is unsymmetric, the conductance matrix $[C]$ is also unsymmetric for nonzero magnetic fields.

Most finite-element software will not solve problems with unsymmetric matrices. For example, Maxwell SV will solve problems obeying (10.18), called *current flow problems*, but not with unsymmetric anisotropic tensor conductivity.

10.3.2 2D Results

Finite-element software that solves DC current flow problems with unsymmetric conductivity tensors has been used to analyze Hall effect and the related magnetoresistance. Here 2D finite-element analysis is applied to several examples.

Example 10.2 Hall Voltage Computed for Wide 2D Semiconductor Bar of

Example 10.1 The wide bar of semiconductor material of Example 10.1 has the conductivity tensor determined in that example. Use the unsymmetric conductivity tensor in 2D finite-element software to compute the actual Hall electric field in the wide bar along with the resistance of the bar.

Solution: The results are shown in Fig. E10.2.1 and included in Table 10.1. Note that quadrilateral finite elements are used, all squares 1 mm on a side. The voltage contours in Fig. E10.2.1a are “S” shaped because of the Hall effect, which produces the y components of electric field in Fig. E10.2.1b. The current density has both x and y components as shown in Fig. E10.2.1c. The top row of Table 10.1 shows that the actual Hall electric field is -13.39 V/m, considerably reduced from the -23.8 V/m obtained for the narrow rod as described in Example 10.1. Table 10.1 lists the voltage V_T in the top Hall electrode and the voltage V_B in the bottom Hall electrode, whose difference is the Hall voltage. Note also in the top row of Table 10.1 that the resistance is now 408.51Ω , an increase from the 400Ω without a magnetic field. The increased resistance is called *magnetoresistance*.

Example 10.3 Hall Voltage Computed for More Narrow 2D Semiconductor

Bar The semiconductor material with the conductivity tensor of Examples 10.1 and 10.2 is used in a bar of size $8 \times 2 \times 0.25$ mm. Use the unsymmetric conductivity tensor in 2D finite-element software to compute the actual Hall voltage and magnetoresistance.

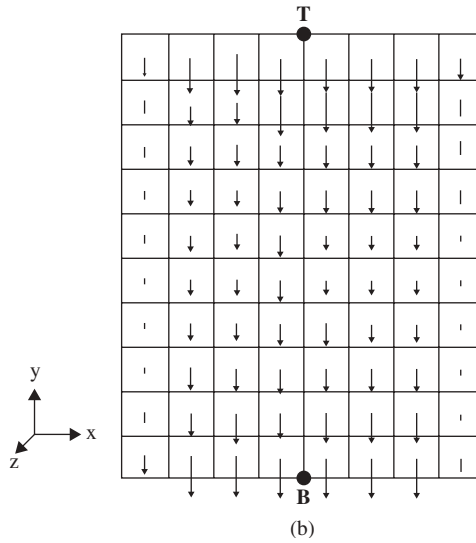
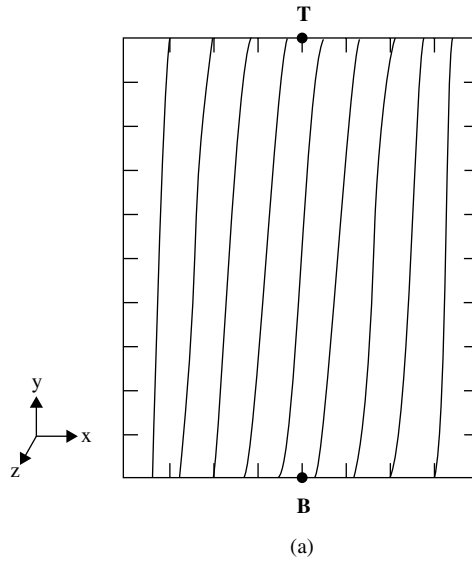


Figure E10.2.1 Finite-element model with 1-mm^2 elements and computed results for Hall sensor of dimensions 8 mm in x and 10 mm in y ; \mathbf{B} is in the z direction and applied \mathbf{J} in x direction. The top electrode is indicated by T and the bottom electrode is indicated by B. (a) Voltage contours; (b) Hall electric field in y direction. (*continued*)

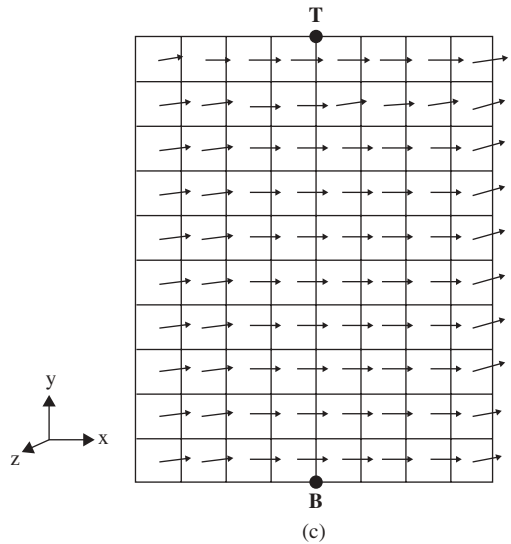


Figure E10.2.1 (cont.) (c) Current density vectors.

Solution: The results are shown in Fig. E10.3.1 and included in Table 10.1. The voltage contours in Fig. E10.3.1a are slanted as a result of the Hall effect, which produces the y components of the electric field in Fig. E10.3.1b. The second row of Table 10.1 shows that the actual Hall electric field is -23.65 V/m, very close to the -23.8 V/m obtained for the narrow rod as described in Example 10.1. Note also in the second row of Table 10.1 that the resistance is now $2011.5\ \Omega$, a small percentage increase from the $2000\ \Omega$ without a magnetic field.

Example 10.4 Effect of Finite Hall Electrodes on Current Flow The wide bar of semiconductor material of Example 10.1 is placed where there is no magnetic field. Maxwell SV is to be used to find its voltage contours and current flow pattern for two cases. The first case has no Hall electrodes. The second case has two Hall aluminum electrodes of size 1 mm in x and 1 mm in y . In both cases the

TABLE 10.1 Calculated Hall Fields and Magnetoresistance R_M

Model						
Dimensions (mm)	A_{el} (mm ²)	V_B (V)	V_T (V)	$E_{y,\text{av}}$ (V/m)	R_M (Ω)	R_M (%)
2D $8 \times 10 \times 0.25$	0	0.43304	0.56696	-13.39	408.51	102.13
2D $8 \times 2 \times 0.25$	0	0.47635	0.52365	-23.65	2011.5	100.58
3D $8 \times 10 \times 2$	2	0.44575	0.55425	-10.85	48.978	102.26
3D $8 \times 2 \times 2$	2	0.48489	0.51511	-15.11	187.66	100.98

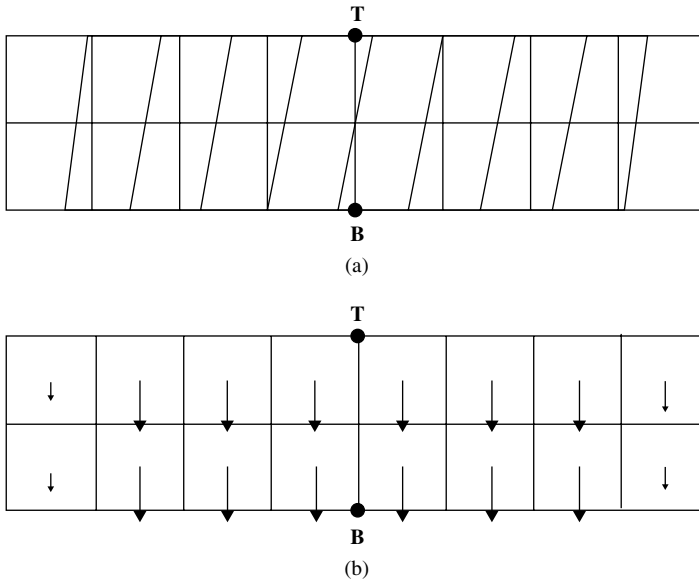


Figure E10.3.1 Finite-element model with 1-mm² elements and computed results for Hall sensor of dimensions 8 mm in x and 2 mm in y . \mathbf{B} is in the z direction and applied \mathbf{J} , in the x direction. The top electrode is indicated by T and the bottom electrode, by B: (a) voltage contours; (b) Hall electric field in y direction.

applied magnetic field is assumed to be zero, and the power loss is also to be found.

Solution: First, change the “solver” in Maxwell SV to “DC conduction.” Next, enter the 8×10 -mm rectangular box for the geometry, and also use boxes for both electrodes. Under “Set up materials,” since there is no magnetic field, the bulk conductivity of 8 S/m is entered. The electrodes are first made the same 8 S/m, and later changed to aluminum. Finally, boundary conditions of 1 V on the left edge and 0 V on the right edge are specified.

The computed voltage contours without aluminum electrodes are shown in Fig. E10.4.1a, and the computed current density arrows are shown in Fig. E10.4.1b. The computed power loss is exactly 10 W for 1 m depth. Since for 1 m depth the resistance from (P10.1.1) is $0.1 \, \Omega$, the expected power loss is $I^2/0.1 = 10 \, \text{W}$, agreeing with the computed power loss.

The computed voltage contours with aluminum electrodes are shown in Fig. E10.4.2a, and the computed current density arrows are shown in Fig. E10.4.2b. Both patterns show that the aluminum electrodes perturb the field. The computed power loss is now 10.7365 W for 1 m depth. The power loss has increased for 1 V because some of the semiconductor is replaced by aluminum, reducing the resistance.

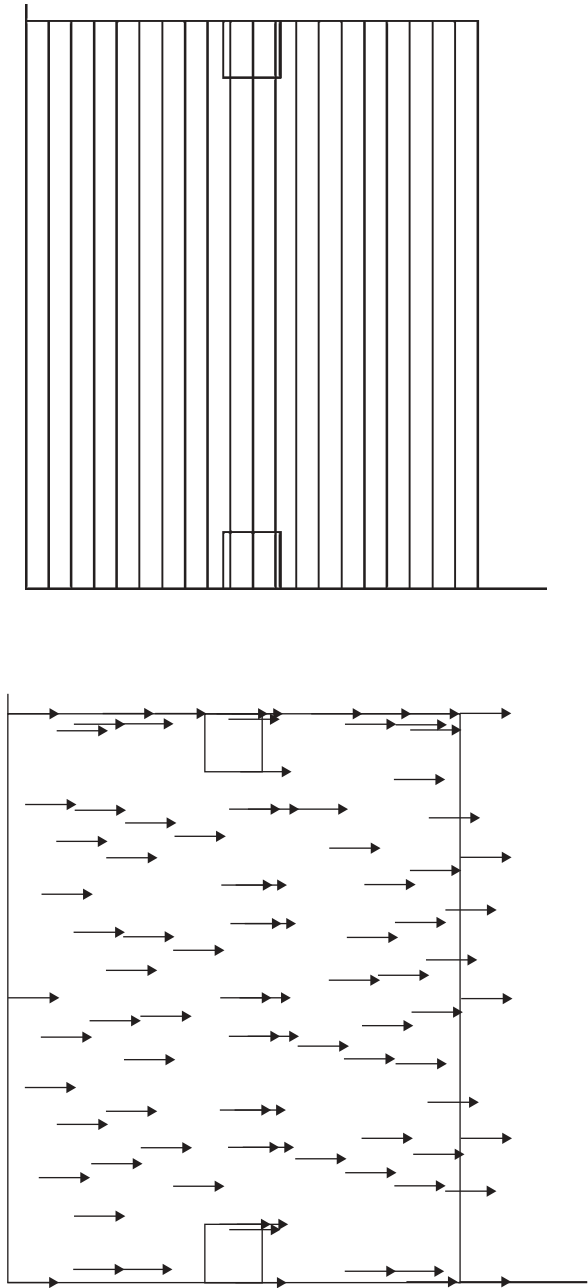


Figure E10.4.1 Computer display of wide semiconductor bar of Example 10.4 with no applied magnetic field: (a) computed voltage contours; (b) computed current density arrows.

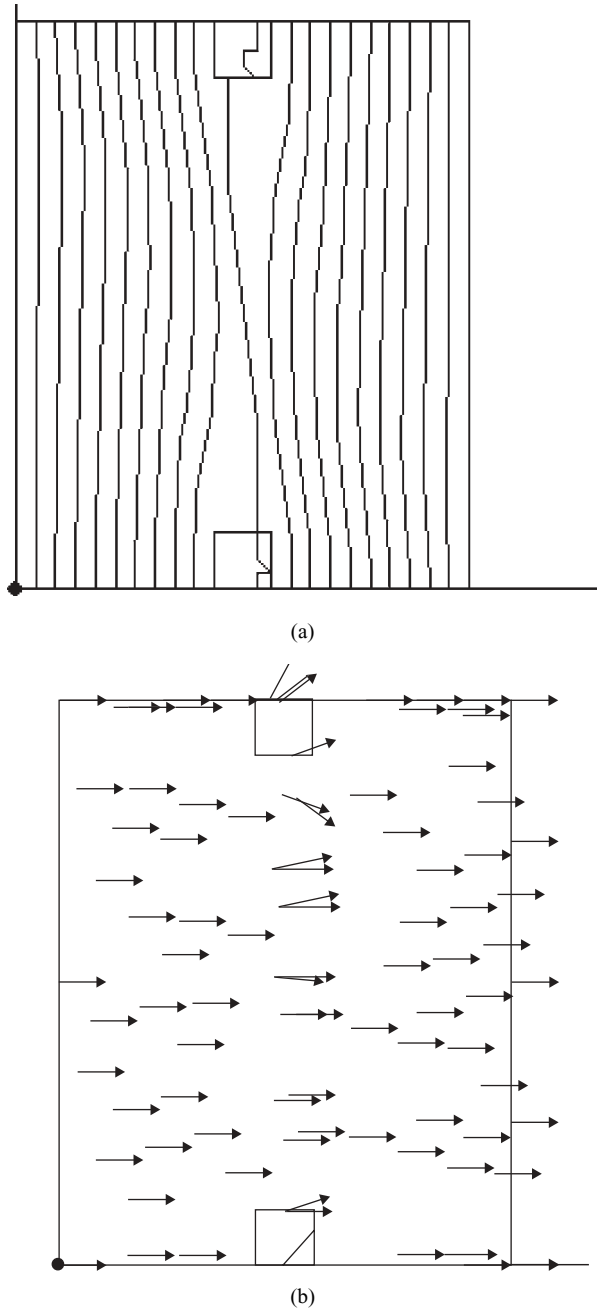


Figure E10.4.2 Computer display of wide semiconductor bar of Example 10.4 with no applied field but with 1×1 -mm aluminum electrodes: (a) computed voltage contours; (b) computed current density arrows.

10.3.3 3D Results

To compute the voltage contours, Hall electric field and voltage, and resistance of sensors with 3D geometries, 3D finite elements are used to assemble the matrix equation of (10.18). The shape function of (10.19) for the first-order 3D finite elements used here obtains a voltage within an element obeying the following rule:

$$V(x, y, z) = \sum_{k=L,M,N,O} V_k(1 - a_k x)(1 - b_k y)(1 - c_k z) \quad (10.20)$$

Thus the shape function of (10.19) is

$$N = (1 - a_k x)(1 - b_k y)(1 - c_k z) \quad (10.21)$$

The 3D finite elements in the examples below are all hexahedrons, which are six-sided solids. In the examples below the hexahedrons are all cubes, but they could be any shape not distorted greatly from a rectangular box. Other 3D finite elements include the tetrahedrons discussed in Chapter 4.

Example 10.5. Hall Voltage Computed for Wide 3D Semiconductor Bar with Finite Hall Electrodes The wide bar of semiconductor material of Example 10.1 has the conductivity tensor determined in that example. The Hall electrodes are thin highly conducting plates of area 2×1 mm as shown in Fig. E10.5.1, which shows a bar thickness of 2 mm. Use the unsymmetric conductivity tensor in 3D finite-element software to compute the actual Hall voltage contours and electric field in the wide bar along with the resistance of the bar.

Solution: The computed voltage contours are shown in Fig. E10.5.1, in which the electrodes were assumed to be perfectly conducting. Other computed results are listed in row 3 of Table 10.1. Note that the Hall electrodes and other 3D effects have reduced the Hall electric field to -10.85 V/m, even further from the predicted -23.8 V/m of (10.1).

Example 10.6 Hall Voltage Computed for Narrower 3D Semiconductor Bar with Finite Hall Electrodes The narrower bar of semiconductor material of Example 10.2 is made 2 mm thick in the third (z) dimension. It has thin highly conducting plates of area 2×1 mm for Hall electrodes, as shown in Fig. E10.6.1. Use the unsymmetric conductivity tensor in 3D finite-element software to compute the actual Hall voltage contours and electric field in the narrower bar along with the resistance of the bar.

Solution: The computed voltage contours are shown in Fig. E10.6.1, in which the electrodes were assumed to be perfectly conducting. Other computed results are listed in row 4 of Table 10.1. Note that the Hall electrodes and other 3D effects have reduced the Hall electric field to -15.11 V/m, much farther from the predicted -23.8 V/m of (10.1) than the -23.65 V/m of the 2D case.

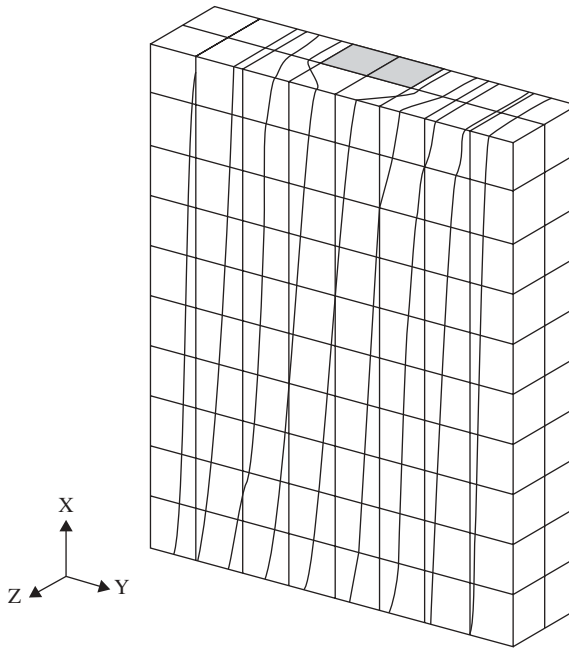


Figure E10.5.1 Finite-element model with 1-mm³ elements and computed voltage contours for Hall sensor of dimensions 8 × 10 × 2 mm.

10.4 TOOTHED WHEEL HALL SENSORS FOR POSITION

The Hall sensor element can be used in a magnetic circuit to sense position. The most popular magnetic circuit has the toothed wheel, which may be a gear, shown in Fig. 10.2. The sensor of Fig. 10.2 is commonly used in the automotive industry for wheel position and speed sensing. Four-wheel sensing is essential for the following automotive safety systems:

- *Antilock braking*, in which zero or low speed of one or two wheels indicates sliding on ice and other surfaces and therefore triggers rapid pumping actuation of the brakes
- *Traction control*, in which high speed of one or two wheels indicates spinning on ice or another surface and therefore triggers changes in engine torque applied to the wheels
- *Brake force distribution*, in which higher speed of certain wheels carrying a heavier cargo load indicates that they need greater braking force
- *Stability control*, in which zero or low speed of one or two wheels during turning indicates a side skid and therefore triggers changes in engine torque applied to the wheels

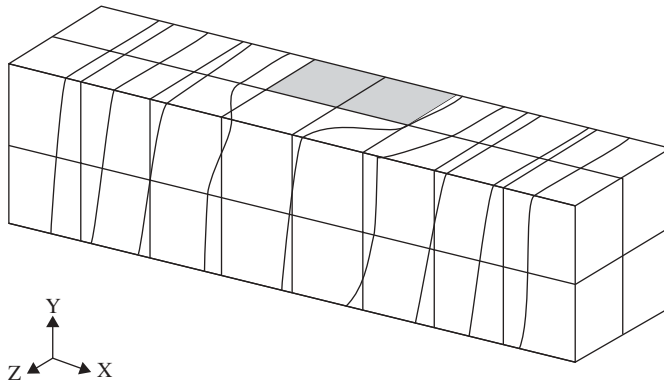


Figure E10.6.1 Finite-element model with 1-mm³ elements and computed voltage contours for Hall sensor of dimensions 8 × 2 × 2 mm.

In most of these systems, feedback control as shown in Fig. 1.4 is used with both the magnetic sensor and an actuator. The actuator may be purely magnetic or may also involve an electrohydraulic system to be discussed in Chapter 16.

In Fig. 10.2 the magnetic field is supplied by a permanent magnet stator. In some cases, a coil winding on a steel stator can be used instead, as analyzed in Example 3.2. As described in Example 3.2, the reluctance changes as the steel wheel teeth rotate past the stator. This variable reluctance causes the magnetic flux and flux density to change. For simplicity, assume the Hall sensor is subjected to a sinusoidal B change with wheel angular position θ of the type

$$B(\theta) = B_{pk} \sin n_T \theta \tag{10.22}$$

where n_T is the number of teeth on the wheel.

Assume also that the flux density described above is in the z direction of Fig. 10.1 and (10.1), which applies along with a current density J_x and Hall sensor dimension d_y . Then (10.22) and (10.1) give the sensor output voltage:

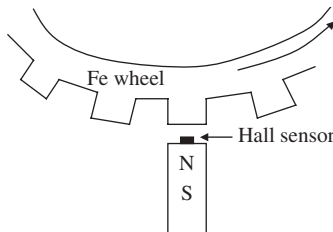


Figure 10.2 Toothed wheel position sensor with Hall effect magnetic field detector mounted on a permanent magnet with north (N) and south (S) poles.

$$V_y = k_{IF} J_x d_y B_{pk} \sin n_T \theta \quad (10.23)$$

Because the four coefficients above are all constants, the sensor output voltage is directly proportional to $\sin(n_T \theta)$. Thus the position θ is sensed over a tooth “pitch,” and speed is also easily sensed by taking the time derivative of the output voltage.

Actually, the simple sinusoid assumed in (10.22) is only an approximation. Finite-element analysis can determine the exact variation with position for any tooth shape. To sense absolute position, a particular tooth can be removed or the tooth pattern can be made nonuniform.

Example 10.7 Hall Sensor Output for Toothed Wheel of Example 3.2 A small Hall sensor is inserted in the airgap between the teeth of Example 3.2. Assume that the Hall sensor is supplied a current and is arranged as in Fig. 10.1 to sense the magnetic flux density, which is assumed to vary sinusoidally between the values of Example 3.2. Find the expression for the output voltage as a function of position.

Solution: From Example 3.2, the flux density varies from 0.06285 to 0.6285 T. Assuming a sinusoidal variation gives

$$B(\theta) = 0.06285 + (0.6285 - 0.06285) \sin n_T \theta \quad (10.24)$$

Substituting in (10.1) gives the output voltage

$$V_y = k_{IF} J_x d_y (0.06285 + 0.5656 \sin n_T \theta) \quad (10.25)$$

where the three coefficients are all constants.

10.5 MAGNETORESISTANCE

Both Hall effect and related magnetoresistance are extremely popular methods of sensing magnetic fields. Since the year 2000 or so, devices using magnetoresistance, commonly abbreviated MR, have become increasingly popular as new forms of MR are developed. The basic definition of magnetoresistance is the change in resistance due to application of a magnetic field.

10.5.1 Classical Magnetoresistance

Sections 10.1, 10.2, and 10.3 have shown that magnetic fields acting on semiconductors produce both Hall effect and magnetoresistance. This type of magnetoresistance is shown in Table 10.1 to be in the range of a 1–10% change. This type of “classical” magnetoresistance is commonly called “classical MR,” or simply MR.

Since the same semiconducting material produces both Hall effect and magnetoresistance, either can be used to make a sensor. Since the magnetoresistance

changes of Table 10.1 classical MR are only a few percent, most engineers prefer to use the Hall voltage, even though it requires addition of the two Hall electrodes.

10.5.2 Giant Magnetoresistance

In 1988 a much larger percentage change in magnetoresistance was discovered and appropriately named *giant magnetoresistance* (GMR). Throughout the 1990s, GMR was developed extensively, especially for sensing magnetic fields recorded on computer disk drives, magnetic stripes on credit cards, and so on [4,5].

GMR is very different from classical MR. It requires a multilayer structure of very thin films. It attains change in resistance as high as 65% due to the change in magnetization of the successive magnetic layers. For example, layers of Fe can be coupled antiferromagnetically (with opposite electron spins [3]) through nonmagnetic Cr layers. When the magnetic field to be sensed is applied, the antiferromagnetic coupling can be overcome, making the magnetic layers parallel. The resistance varies as the cosine of the angle between the magnetizations. Thus the resistance in the antiparallel case is much greater than the resistance in the parallel case.

There are several different designs for GMR sensors. One sensor has two ferromagnetic layers sandwiching the GMR material. The two layers are often called *soft adjacent layer* (SALs). Often one of the layers has fixed magnetization, while the other is varied by the field to be sensed. Maximum current (minimum resistance) occurs when the two layers have parallel magnetism.

GMR is now very commonplace for read heads for hard-disk computer drives. The latest development to increase storage density is called CPP-GMR [6,7]. CPP stands for current perpendicular to plane, in contrast with the present CIP-GMR, where CIP stands for current in plane.

10.5.3 Newest Forms of Magnetoresistance

There are additional forms of magnetoresistance. All are being investigated to possibly replace GMR in the near future.

- *Tunneling Magnetoresistance (TMR)*. Again placed between two SALs, the material used here is a very thin insulator carrying current by quantum tunneling of electrons when subjected to a magnetic field. This tunneling effect was first observed in 1975 but is presently being developed to replace GMR for disk drive read heads. Quantum-mechanical effects are beyond the scope of this book.
- *Colossal Magnetoresistance (CMR)*. Insulating manganese oxide crystals are changed from nonmagnetic insulators to ferromagnetic conductors by the magnetic field to be sensed. However, such a change requires very low temperatures and a field greater than 1 T. Thus CMR is not very promising at the present time.

some of the flux from the disk to the MR stripe. The magnetized medium typically has a B - H curve with a slope of 2 or 3 times the permeability of air and a residual flux density B_r of approximately 0.5 T.

Assuming the MR stripe exhibits classical MR, the anisotropic conductivity of (10.4)–(10.9) has been used in 3D finite-element software [11]. The computed MR due to the magnetized media was 2.1%, and the computed voltage contours have the slant of the type shown in Fig. E10.6.1.

The next chapter includes a discussion of other types of recording heads. It contrasts and compares them with magnetoresistive heads.

PROBLEMS

- 10.1** Redo Example 10.1 when the current measured is reduced to 2.0 mA.
- 10.2** Show all the steps between (E10.1.7), (E10.1.8), and (E10.1.9).
- 10.3** Redo Example 10.4 with the conductivity reduced to 4 S/m.
- 10.4** Redo Example 10.4 with the conductivity reduced to 1 S/m.
- 10.5** Redo Example 10.7 for the current of Example 3.2 reduced by 50%.

REFERENCES

1. R. A. Greiner, *Semiconductor Devices and Applications*, McGraw-Hill, 1961, pp. 80–81 and Problem 5-1 on p. 471.
2. J. R. Brauer, J. J. Ruehl, B. E. MacNeal, and F. Hirtenfelder, Finite element analysis of Hall effect and magnetoresistance, *IEEE Trans. Electron Devices* **42**: 328–333 (Feb. 1995).
3. C. Kittel, *Introduction to Solid State Physics*, 3rd ed., Wiley, New York, 1967, pp. 240–244.
4. R. L. White, Giant magnetoresistance: A primer, *IEEE Trans. Magn.* **28**: 2482–2487 (Sept. 1992).
5. R. L. White, Giant magnetoresistance materials and their potential as read head sensors, *IEEE Trans. Magn.* **30**: 346–352 (March 1994).
6. M. Takagishi, K. Koi, M. Yoshikawa, T. Funayama, H. Iwasaki, and M. Sahashi, The applicability of CPP-GMR heads for magnetic recording, *IEEE Trans. Magn.* **38**: 2277–2282 (Sept. 2002).
7. H. Fukuzawa et al., MR ratio enhancement by NOL current-confined-path structures in CPP spin valves, *IEEE Trans. Magn.* **40**: 2236–2238 (July 2004).
8. J. Moussa, L. R. Ram-Mohan, J. Sullivan, T. Zhou, D. R. Hines, and S. A. Solin, Finite element modeling of enhanced magnetoresistance in thin film semiconductors with metallic inclusions, *Phys. Rev.* **B64**: 184410 (2001).
9. J. Moussa, L. R. Ram-Mohan, A. C. H. Rowe, and S. A. Solin, Response of an extraordinary magnetoresistance read-head to a magnetic bit, *J. Appl. Phys.* **94**: 1110 (2003).

10. S. A. Solin, Magnetic field nanosensors, *Sci. Am.* 71–77 (July 2004).
11. J. R. Brauer and M. M. Jenich, Finite element analysis of a magnetoresistive head, *IEEE Magnetic Recording Conf.*, Minneapolis, MN, Sept. 13–15, 1993.
12. E. M. Williams, *Design and Analysis of Recording Magnetoresistive Heads*, Wiley-IEEE Press, New York, 2000.

Other Magnetic Sensors

Besides the Hall effect and magnetoresistive sensors of the preceding chapter, many other types of magnetic sensors are commonly used. This chapter examines the major remaining types of magnetic sensors.

11.1 SPEED SENSORS BASED ON FARADAY'S LAW

The preceding chapter discussed how a toothed steel wheel rotating next to a Hall sensor is used in many automotive safety systems. In many cases the speed or velocity is to be sensed, not position, and thus a pickup coil can be used instead of the Hall sensor, as shown in Fig. 11.1. Note that, as in Fig. 10.2, a permanent magnet serves as the usual source of the magnetic field. The Hall sensor of Fig. 10.2 is replaced in Fig. 11.1 by a coil wound around a steel pole piece. A photograph of an actual automotive variable-reluctance velocity sensor is shown in Fig. 11.2. The cutaway in Fig. 11.2 shows the coil, which is wound of hundreds of turns of very thin copper wire.

The voltage induced in the coil is determined by Faraday's law of Chapter 2

$$V = -N \frac{d\phi}{dt} \quad (11.1)$$

where N is the number of turns and ϕ is the flux passing through the coil. As the toothed steel wheel in Fig. 11.1 rotates with angular position θ , the reluctance changes as analyzed in Example 3.2, producing a changing flux through the coil. Assume for simplicity that the flux ϕ is sinusoidal

$$\phi(\theta) = \phi_{pk} \sin n_T \theta \quad (11.2)$$

where n_T is the number of teeth on the wheel. Assume that the toothed wheel is rotating at constant mechanical angular velocity Ω in radians per second:

$$\theta = \Omega t \quad (11.3)$$

Substituting (11.2) and (11.3) into (11.1) gives

$$V = -\Omega N n_T \phi_{pk} \cos(n_T \Omega t) \quad (11.4)$$

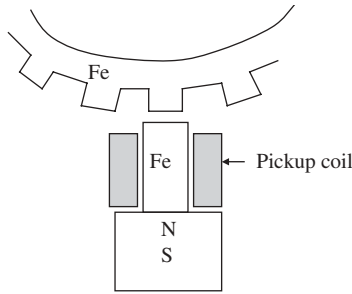


Figure 11.1 Toothed wheel speed sensors.

Note that the magnitude of the induced voltage is proportional to the speed. At very low speed, the voltage is very small. Thus the sensors of Figs. 11.1 and 11.2 are indeed speed sensors. While it is true that their voltages can be integrated over time to obtain position, they are inherently speed sensors, not position sensors. In most cases the coil is open-circuited so that the voltage observed is that of (11.4).

Example 11.1 Speed Sensor Output for Toothed Wheel of Example 3.2 Example 3.2 is to be used as a speed sensor by winding an open-circuited pickup coil of N turns on top of the exciting coil in Fig. E3.2.1. Assume that the magnetic flux varies sinusoidally between the values of Example 3.2 and that its armature has n_T teeth equally spaced around 360° . Find the expression for the output voltage as a function of the armature speed Ω .



Figure 11.2 Actual automotive speed sensor stators, consisting of a coil wound around steel adjacent to a permanent magnet. A cutaway stator is shown next to a complete stator.

Solution: From Example 3.2, the flux varies from 62.85E-6 to 628.5E-6 W. Assuming a sinusoidal variation gives

$$\phi(\theta) = 62.85\text{E} - 6 + (628.5 - 62.85)\text{E} - 6 \sin n_T\theta \quad (\text{E11.1.1})$$

Substituting in (11.2) and (11.4) gives the output voltage:

$$V = -\Omega N n_T (566\text{E} - 6) \cos(n_T \Omega t) \quad (\text{E11.1.2})$$

11.2 INDUCTIVE RECORDING HEADS

The preceding chapter examined magnetoresistive heads for reading (sensing) magnetized media such as hard disks. Besides magnetoresistive heads, inductive heads are commonly used. Inductive heads have a voltage induced by Faraday's law.

Inductive heads are the most common means of writing on (i.e. magnetizing) the disk medium. A typical inductive head is shown in Fig. 11.3. Its coil is wound with many turns of very fine wire, and therefore for a given current the coil can create a much higher magnetizing field intensity than can a magnetoresistive head with its single current-carrying conductor. The ampere-turns in the head coil create magnetic flux lines in the disk medium. Inductive heads can also be used for reading, that is, sensing the magnetic field pattern written on the disk. However, their reading performance is usually inferior to magnetoresistive heads.

The inductive head read signal is based on Faraday's law, as is the signal produced by a moving-magnet microphone. For simplicity, assume that a sinusoidal pattern is magnetized on the recording disk and produces the flux of (11.2) linking the head coil

$$\phi(\theta) = \phi_{pk} \sin n_C \theta \quad (11.5)$$

where the number of teeth n_T of (11.1) is changed to n_C , the number of cycles of magnetization along the disk track circumference. Assuming the disk is traveling at

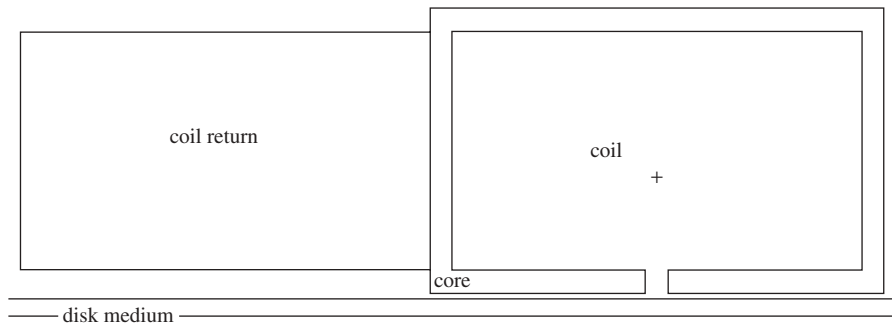


Figure 11.3 Typical inductive head and adjacent disk medium.

angular speed Ω in radians per second, then from Faraday's law the signal volts "read" at the head coil is similar to (11.3), becoming

$$V = -\Omega n_c N \phi_{pk} \cos(n_c \Omega t) \quad (11.6)$$

Since ϕ_{pk} is produced by one magnetized bit (half-cycle) on the disk, it equals B_{pk} times the area of a half cycle. Thus

$$\phi_{pk} = B_{pk} (2\pi r_{\text{disk}} w_{\text{track}}) / (2n_c) \quad (11.7)$$

where r_{disk} is the disk radius and w_{track} is the disk magnetization track width. The flux density B_{pk} is limited by saturation and other factors. Substituting (11.7) in (11.6) gives

$$V = -\Omega r_{\text{disk}} \pi w_{\text{track}} N(B_{pk}) \cos(n_c \Omega t) \quad (11.8)$$

Note that the magnitude of the voltage sensed is proportional to the product of the angular speed Ω times the disk radius. When the radius is reduced by disk drive miniaturization the read voltage of (11.8) is reduced. In contrast, the voltage of a magnetoresistive read head is proportional only to the change in flux density, not speed. Thus magnetoresistive read heads have almost totally replaced inductive read heads in hard-disk drives.

The magnetization pattern produced on the disk medium in actual operation depends on the history of all previous write operations. Predicting all such hysteresis effects is a very challenging task. Several books and a huge number of technical papers continue to be written about magnetic recording [1,2] and magnetic hysteresis [3,4]. Also, all permanent magnets used in actuators and sensors must undergo magnetization, and modeling their *magnetizing fixtures* requires similar techniques [5].

As mentioned in Chapter 1, disk drives often utilize the read signal of the head as a position sensor for the voice coil actuator in a feedback control servo system [1]. The voice coil actuator must *seek* the desired track in minimum time for rapid information transfer to or from the disk [6,7].

Example 11.2 Writing and Reading with an Inductive Head The inductive head of Fig. E11.2.1 is to be used for both writing and reading. It has 20 turns of wire carrying 0.05 A for writing. Assume that the disk medium has a relative permeability of 3 and has been previously unmagnetized. Dimensions of the head core, of relative permeability 2000, are 80 μm in x and 50 μm in y . The head core is 4 mm deep in the z direction. The medium is 3 mm thick in the radial direction and spaced by 1 mm from the head.

- Find the field in the disk medium during writing using Maxwell SV. Assume all eddy currents to be negligibly small.
- Assuming that the coil current is reset to zero, and the section of the disk between the head poles (below the head airgap) is magnetized with $B_r = 0.5$ T

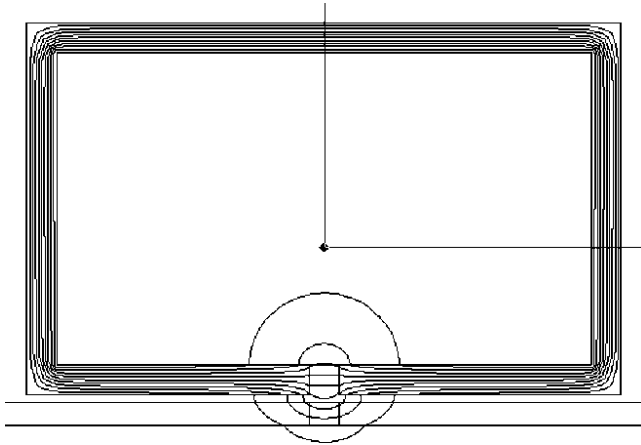


Figure E11.2.1 Computer display of inductive head with computed flux lines during write operation on previously unmagnetized disk.

in the direction parallel to the disk, find the flux pattern throughout the medium and head.

Solution: Maxwell SV's magnetostatic solver was first used with no permanent magnet materials, and later with the bit region being permanently magnetized with $B_r = 0.5$ T in the direction parallel to the disk.

- (a) Computed flux lines are shown in Fig. E11.2.1. All flux densities are less than 2 T, with the highest densities in the head core.
- (b) The computed flux lines are shown in Fig. E11.2.2. All flux densities are less than 0.3 T, with the highest density in the bit. Most of the head core has flux density on the order of 0.15 T, less than 10% of its flux density during writing.

11.3 PROXIMITY SENSORS USING IMPEDANCE

The AC impedance seen by a coil depends on its surroundings. If the adjacent surrounding vicinity, called the *proximity*, contains conducting and/or permeable objects, then the impedance can be significantly changed. Thus coils carrying AC currents are often used as *proximity sensors*.

Since metal objects are always conducting, proximity sensors are commonly used to detect their presence nearby. For example metal detectors for security systems commonly include proximity sensors. The impedance that they see—that is, their ratio of complex AC voltage to complex AC current—is affected by the eddy currents induced in the metal. Thus proximity sensors are also commonly called *eddy current sensors*.

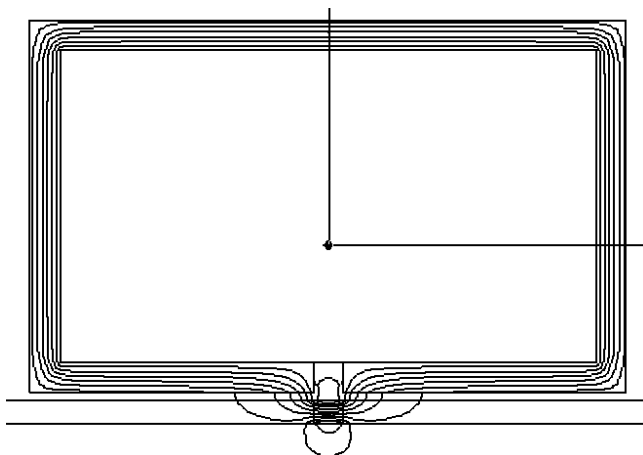


Figure E11.2.2 Computer display of inductive head with computed flux lines produced by single bit on the disk immediately below the head gap.

Besides security systems, proximity eddy current sensors are also commonly used in factory automation. For example, such sensors are used to determine when a metal part is approaching a station on an assembly line, so that a robot can find and work on the part. In both security and automation applications, the sensor output signal must undergo either simple or advanced signal processing to determine the next action.

The object being sensed is often called the *target*. Most eddy current proximity sensors detect the target using frequencies ranging from 50 to ~ 100 kHz. Both real and imaginary parts of the sensor impedance are usually monitored in order to detect the target and its location.

11.3.1 Stationary Eddy Current Sensors

The first step in understanding proximity sensors is to analyze such sensors when the target is not moving, or is moving so slowly that motional eddy current effects are negligible. The effects of higher-speed motion will be investigated later.

An example proximity sensor is shown in Fig. 11.4. It is basically a solenoid actuator with a clapper armature that is the target. The sense coil is wound on a steel stator core that is preferably laminated. The sensor of Fig. 11.4 was analyzed by two-dimensional planar AC finite-element analysis.

The plot of complex-plane impedance for two target materials and multiple positions is shown in Fig. 11.5 for frequency of 1 kHz. Ideally, the frequency should be selected to see the greatest impedance changes with variable target materials and positions. Note that the higher-permeability target material gives higher inductive reactance X than does the lower-permeability material, as one would expect. Note also that the resistive R (lossy) component in Fig. 11.5 rises as the target approach-

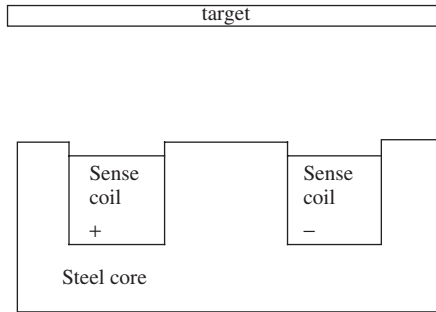


Figure 11.4 Typical proximity sensor.

es, due to the conductive losses in the target. The target material and its distance can thus be determined from the complex-plane impedance.

Note in Fig. 11.5 that as the target approaches, the impedance follows a path called a *locus*. The complex-plane impedance locus is thus very revealing of the target.

Complex-plane impedance loci are commonly used in *nondestructive testing* (NDT) and *nondestructive evaluation* (NDE). For example, an AC current-carrying coil can be moved along a steel pipe. Any changes in the eddy current flow patterns of the pipe due to cracks, imperfect geometries, or other anomalies will cause changes in the impedance locus. Many books and papers are devoted to electromagnetic sensors for NDT and NDE [8,9].

In NDE, the evaluation of the complex-plane impedance locus is a type of *inverse problem*. Signal processing software is employed to attempt to determine the type of

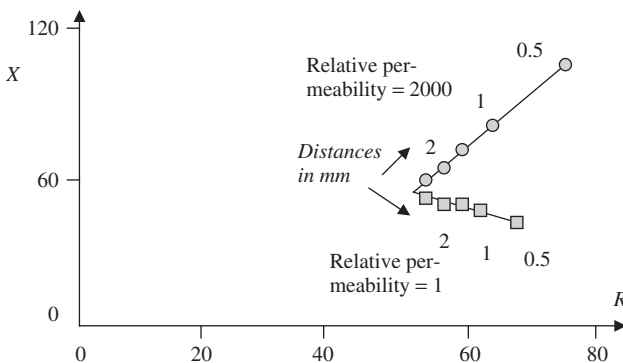


Figure 11.5 Impedance plane plots for proximity sensor of Fig. 11.4 with various targets and positions. The target has conductivity $1.E7$ S/m and a relative permeability of either 2000 or 1. The frequency is 1 kHz. The airgap distance between the stator poles and the target is 0.5 mm or greater.

any flaw and its severity. Examples include pipes in nuclear power plants and security checkpoints at airports. Certain NDE signals are caused by unacceptable metallic flaws that must be detected in order to register an alarm. Another example is eddy current sensors suspended down holes in the earth; their signals are determined by subterranean conductivities and can thus be processed to find petroleum.

Any sensor must to some extent perturb the object being sensed. Eddy current proximity sensors produce forces on their metallic targets. For example, the sensor of Fig. 11.4 is also a magnetic solenoid actuator with the target as the armature. The armature forces of Chapters 7 and 8 act on the target. Whereas the actuator designer usually seeks to maximize the force and resultant armature motion, in most cases the sensor designer seeks to minimize the target force and motion. Because eddy current prediction by hand calculation is extremely difficult, electromagnetic finite element analysis is usually carried out instead.

Example 11.3 Impedance of Proximity Sensor for Two Target Positions An eddy current proximity sensor of the type of Fig. 11.4 is to be used with an aluminum target. The stator is identical to the steel stator of Example 7.1, but it is now laminated. The stator coil consists of 10 turns, each carrying 0.2 A rms. The armature material is now aluminum of conductivity $3.6E7$ S/m. The target and sensor are shown in Fig. E11.3.1. The coil resistance is $0.1\text{ m}\Omega$ (milliohm). The impedance seen by the coil is to be found for airgap distances of 2 and 4 mm using Maxwell SV.

Solution: The easiest way to make this model is to begin with the model of Example 7.1. Changes required include making the solution type “eddy current” and

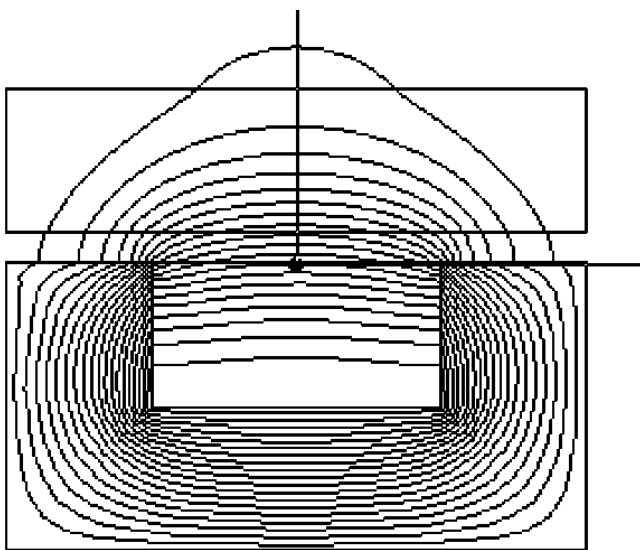


Figure E11.3.1 Computer display of proximity sensor and its computed flux lines.

changing the armature material. For the original 2-mm airgap, the flux linkage output for 1 turn is $\lambda = 2.375\text{E-}6 - j1.195\text{E-}7$. The series impedance for one turn is then found using (6.30)

$$Z = j\omega\lambda/I \quad (\text{E11.3.1})$$

where $I = 2$ A and $\omega = 377$. The resulting series impedance (for 10 turns) is

$$Z_s = R_s + jX_s = (10)(22.53\text{E} - 6 + j448\text{E} - 6) = 22.53\text{E} - 5 + j448\text{E} - 5 \quad (\text{E11.3.2})$$

The total impedance is found by adding the 0.1 m Ω coil resistance (as explained in Chapter 8), yielding

$$Z(0.002) = 32.53\text{E} - 5 + j448\text{E} - 5 \quad (\text{E11.3.3})$$

The corresponding flux lines are shown in Fig. E11.3.1.

To obtain results at the 4-mm position, the armature is moved upward by 2 mm using the “Arrange” and “Move” commands. The flux linkage output for 1 turn is $\lambda = 2.66\text{E-}6 - j8.215\text{E-}7$, greater evidently because the aluminum is farther away and repels less flux. The series impedance for one turn is then found using (6.31):

$$Z = j\omega\lambda/I \quad (\text{E11.3.4})$$

where $I = 2$ A and $\omega = 377$. The resulting series impedance (for 10 turns) is

$$Z_s = R_s + jX_s = (10)(155\text{E} - 6 + j501.4\text{E} - 6) = 155\text{E} - 5 + j501\text{E} - 5 \quad (\text{E11.3.5})$$

The total impedance is found by adding the 0.1 m Ω coil resistance to obtain

$$Z(0.004) = 165\text{E} - 5 + j501\text{E} - 5 \quad (\text{E11.3.6})$$

11.3.2 Moving Eddy Current Sensors

The effect of target velocity on the sensor signal is indicated by the *magnetic Reynolds number* [10]

$$R_m = \mu\sigma V l \quad (11.9)$$

where V is the velocity and l is the length of the conductive armature in the direction of the velocity and motion. The magnetic Reynolds number is dimensionless. If it is less than one, then the velocity effects are negligible, and the methods of the preceding section apply.

If R_m exceeds one, then the velocity effects are significant. The larger R_m , the more the magnetic flux distribution is altered by motional induced voltage. Hence magnetic actuators and sensors with high magnetic Reynolds numbers must be ana-

lyzed including velocity effects. Usually magnetic actuators have zero armature speed at time zero, and rarely reach speeds with high Reynolds numbers. However, in the case of *magnetic brakes* the speed is high and is reduced by eddy current braking forces [11,12].

Magnetic sensors often sense objects with high velocities and high Reynolds numbers. An example is NDE sensors for steel heat exchanger tubes in nuclear power plants or for pipelines made of steel. These eddy current sensors are often pulled through pipes at fairly high velocities, and thus R_m often exceeds one. A typical traveling sensor, often called a “pig,” is shown in Fig. 11.6. Note that if there is no defect in the pipe, then the geometry of Fig. 11.6 does not change with time, even though there is a relative velocity between the pig and the pipe. A perfect or *smooth* pipe becomes an imperfect pipe if there is any roughness on its surface due to corrosion cracks and other defects.

Finite-element methods have been developed for such problems with smooth conducting armatures traveling at constant high velocities [11,12]. In such formulations the matrix equation becomes unsymmetric [12]. For more general moving armatures with imperfect nonsmooth (changing) geometry with motion, finite-element methods will be discussed in Chapters 14 and 15.

11.4 LINEAR VARIABLE DIFFERENTIAL TRANSFORMERS

The variation of magnetic sensor signal with position is often nonlinear, whereas a linear correspondence between position and signal voltage is highly desirable. For example, the proximity sensor impedances of Fig. 11.5 and of Example 11.3 are not linear with position.

A sensor with an extremely linear relation between position and voltage magnitude is the *linear variable-differential transformer* (LVDT). A typical LVDT is shown in Fig. 11.7 and is made of “E”-shaped steel, laminated to render the mag-

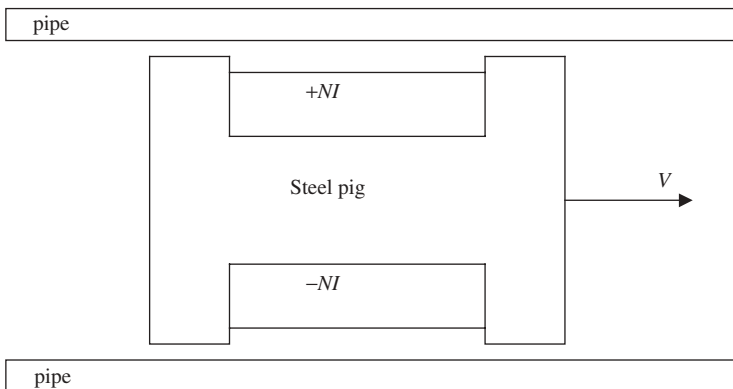


Figure 11.6 Typical AC eddy current NDT sensor traveling through a pipe.

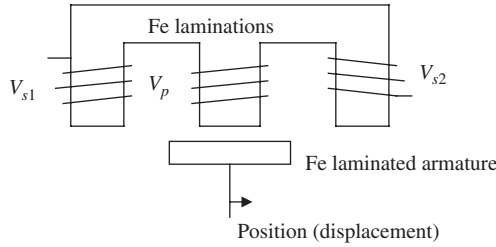


Figure 11.7 Typical LVDT.

netic Reynolds number equal to zero. The LVDT has a primary winding excited with AC voltage V_p . It also has two secondary windings with induced open-circuit voltages V_{s1} and V_{s2} .

The two secondary voltages are induced by Faraday's law transformer action, and are equal and opposite if the laminated steel armature is at zero position, that is, centered below the primary winding and its laminated steel pole. If the armature is positioned to the right (a positive position x), then the total induced voltage $V_{s2} - V_{s1}$ is positive and proportional to x . The relation between the LVDT voltage output $V_s = V_{s2} - V_{s1}$ and x is shown in Fig. 11.8.

Various LVDT designs are possible, and the frequency of operation may also vary. Typical frequencies range from 50 to 25 kHz. Figure 11.8 shows that the output voltage increases with frequency, but can be extremely linear with position. Note also that the voltage is reduced as the load impedance is reduced.

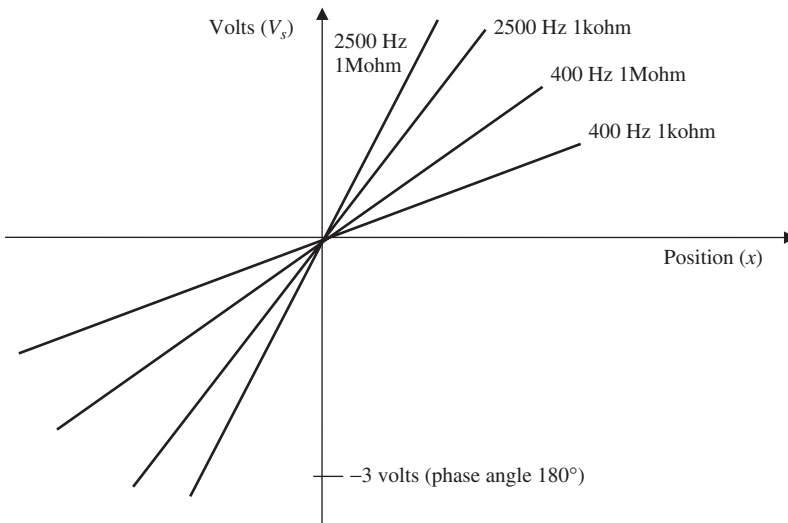


Figure 11.8 Typical voltage versus position curves of LVDT.

LVDTs are unfortunately quite expensive. Their optimum frequency usually ranges from 500 to 5 kHz. To generate this frequency, the electronics required includes

- A 60 Hz to DC power supply
- An oscillator of the desired frequency
- A phase shifter
- AC and DC amplifiers

Example 11.4 Simple LVDT An LVDT is shown in Fig. E11.4.1 as drawn in Maxwell SV's default window. The primary coil consists of 1000 turns, each carrying 2 A rms 1000 Hz. Both the stator and armature are made of laminated steel with relative permeability 2000. The two secondary coils indicated by the arrows are open-circuited and connected in series opposition, each having 500 turns. Use Maxwell SV to find the total secondary output voltage for the 20×6 -mm armature at centered (zero) position and moved 4 mm to the right. The depth into the page is 100 mm.

Solution: Since there are no significant eddy currents, a magnetostatic solution suffices. The model shown in Fig. E11.4.1 was input into Maxwell SV with “Set up executive parameters” and “Flux lines” to find the flux passing through the two secondary coils. The computed flux plot at zero armature position is shown in Fig. E11.4.2. The computed secondary fluxes are $-2.93\text{E-}3$ and $+2.94\text{E-}3$ W; the magnitudes differ due solely because the mesh is not perfectly symmetric. The induced voltage is thus approximately zero.

Next, the “Arrange” and “Move” commands were used to move the armature 4 mm to the right. The computed secondary fluxes are $-2.59\text{E-}3$ and $+3.58\text{E-}3$ W for

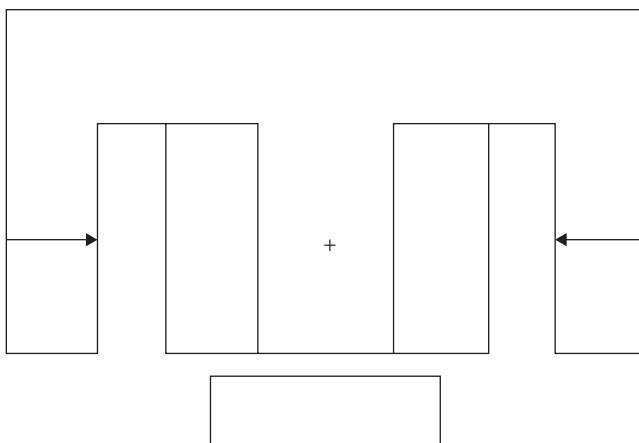


Figure E11.4.1 Geometry of LVDT to be modeled.

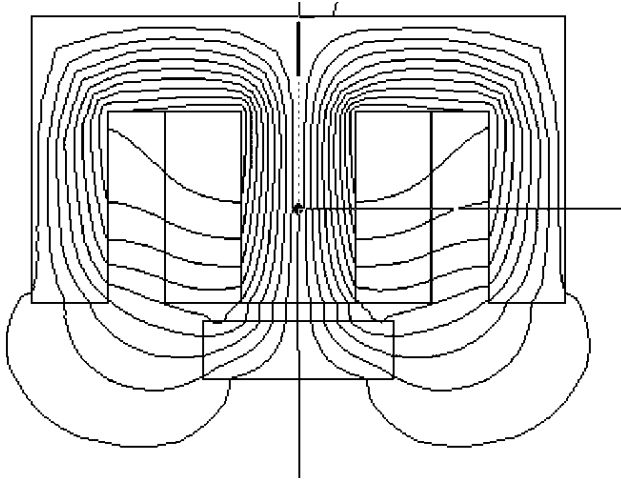


Figure E11.4.2 Computer display of flux lines in LVDT for armature position = 0.

1 m depth. For the actual 0.1 m depth, the total flux linking the secondary is thus $+0.99\text{E-}4$ W. To find the secondary voltage magnitude, use Faraday's law:

$$|V| = N d\phi/dt = N\omega\phi = 2\pi f N\phi \quad (\text{E11.4.1})$$

Substituting the total flux, the frequency, and 500 turns, the LVDT output for this position is 6.22 V.

11.5 MAGNETOSTRICTIVE SENSORS

Magnetostriction is the phenomenon of elastic deformation that accompanies magnetization [13]. Magnetic fields cause certain materials to deform. This deformation is a form of motion in magnetostrictive actuators. However, motions of such actuators are usually much less than one millimeter, and thus magnetostrictive actuators are not further discussed in this book.

Magnetostrictive sensors, on the other hand, are useful and fairly commonplace. They require, however, materials in which magnetic flux density and mechanical properties are strongly interdependent. While steel has small magnetostrictive effects, recently developed materials exhibit much stronger magnetostriction.

The material constitutive properties are determined by the following matrix equation for planar magnetostriction:

$$\begin{bmatrix} \sigma_{xx} \\ \sigma_{yy} \\ H_x \\ H_y \end{bmatrix} = \begin{pmatrix} K_1 & K_2 & X_1 & X_2 \\ K_3 & K_3 & X_3 & X_4 \\ X_5 & X_6 & M_1 & M_2 \\ X_7 & X_8 & M_3 & M_4 \end{pmatrix} \begin{bmatrix} \varepsilon_{xx} \\ \varepsilon_{yy} \\ B_x \\ B_y \end{bmatrix} \quad (11.10)$$

Note that the left-hand column vector contains both planar structural stresses σ and magnetic field intensities. The right-hand column vector contains both planar structural strains ε and magnetic flux densities. The 4×4 matrix is the material tensor, containing purely structural entries K , purely magnetic entries M , and magnetomechanical coupling cross-term entries X .

A strongly magnetostrictive material is terfenol, which is made up of rare-earth elements Tb (terbium), Dy (dysprosium), and also Fe. A typical terfenol actuator is shown in Fig. 11.9. Application of a magnetic field causes the terfenol membrane to bend.

A commonly used magnetostrictive position sensor is shown in Fig. 11.10. The magnetostrictive material acts as an acoustic waveguide. The linear position sensor is composed of four elements:

1. Waveguide sensing element
2. Sensing and output conditioning electronics module
3. Protective housing
4. External permanent magnet

A sonic strain pulse is induced in the magnetostrictive waveguide by the momentary interaction of two magnetic fields. One field comes from a movable permanent magnet that passes along the outside of the sensor tube, while the other field comes from a current pulse or interrogation pulse applied along the waveguide. The interaction of the two magnetic fields produces a strain pulse, which travels at sonic speed along the waveguide until the pulse is detected at the head of the sensor. The position of the magnet is determined with high precision by measuring the elapsed time between the application of the interrogation pulse and the arrival of the result-

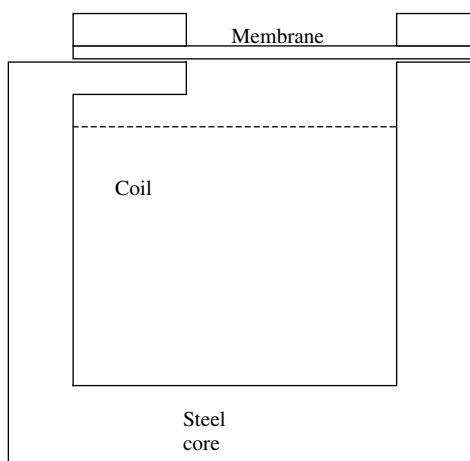


Figure 11.9 Magnetostrictive actuator.

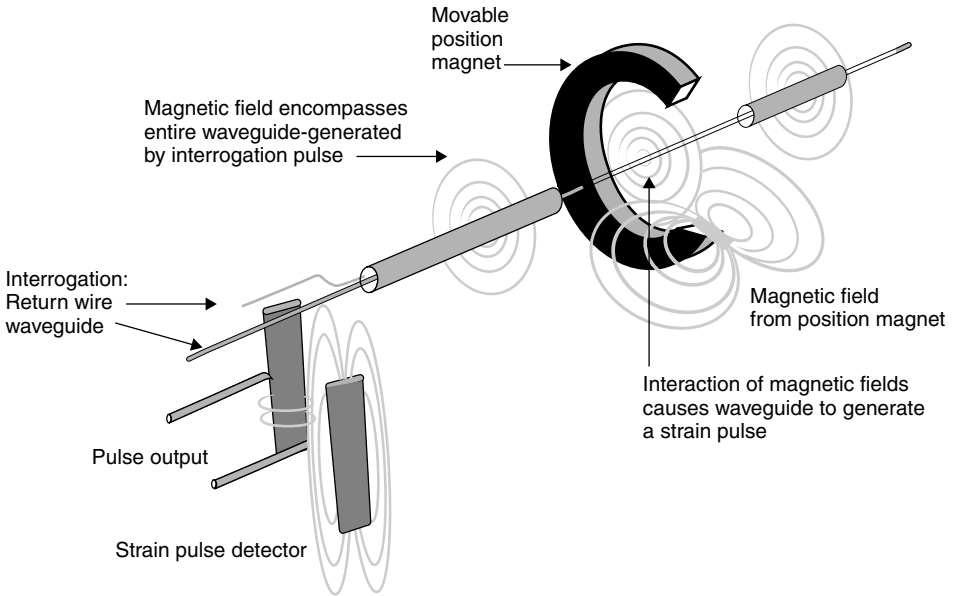


Figure 11.10 Magnetostrictive position sensor. (This picture of a Temposonics® sensor is courtesy MTS Sensors.)

ing strain pulse. Hence accurate noncontact position sensing is achieved without any wear to the sensing components.

Another popular use of magnetostrictive sensors is for torque sensing. For control of rotating electric motors or internal-combustion engines, accurate sensing of shaft torque is often required. Since the shaft is rotating, connecting it directly to electrical sensing wires is highly impractical. Instead, the strain in the shaft can be measured with a noncontact magnetostrictive sensor [14], and the strain is proportional to torque.

11.6 FLUX GATE SENSORS

Materials such as steel with nonlinear B - H curves can be used to produce *flux gate sensors*. The sensor material is driven between the constant permeability and the saturable regions of its B - H curve. A typical flux gate sensor is shown in Fig. 11.11. The inductance seen by its coil is a function both of its coil current and the external magnetic field to be sensed.

Flux gate sensors are used as proximity sensors, for navigational and geomagnetic field measurement instruments, and for position and speed sensing. A properly designed flux gate sensor has an output linearly proportional to the magnetic field being sensed.

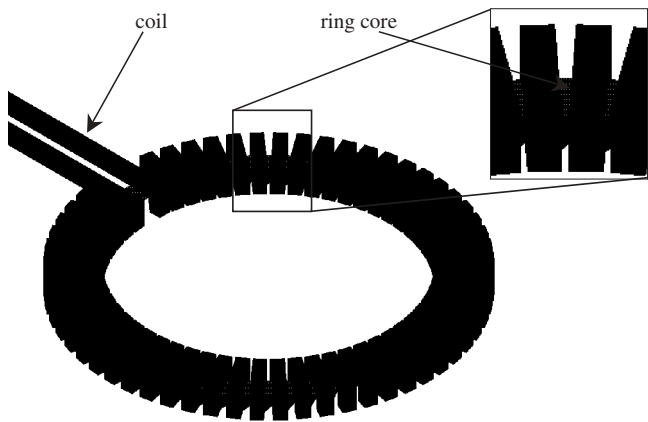


Figure 11.11 Computer display of typical flux gate sensor with a toroidal coil wound on a ring core.

Finite element analysis aids the design of flux gate sensors [15]. The inductance seen by the coil for various external magnetic flux densities computed for a typical flux gate sensor is plotted in Fig. 11.12. Note how the curves shift with the external field. The curves can then be exported from the Maxwell finite-element software to a circuit analysis program such as SPICE or Simplorer. SPICE, which stands for simulation program with *integrated circuit emphasis*, is widely available in several

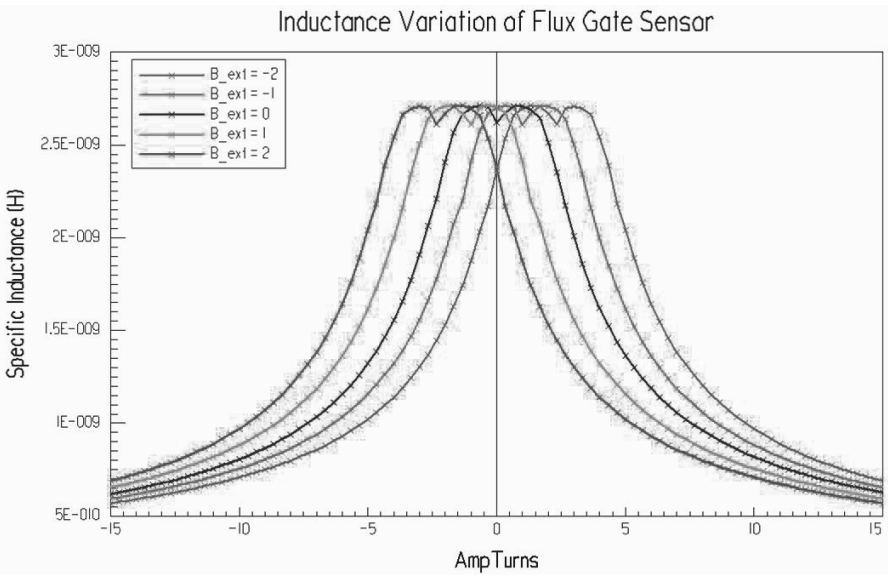


Figure 11.12 Typical flux gate sensor inductance variation.

forms. Simplorer, available from Ansoft Corporation, is a software package used to design and analyze complex technical systems.

Typical saturable sensor current response to an applied 2.5-V 100-kHz sinusoid is shown in Fig. 11.13 for no applied external field. When an external field is applied, the current response is shifted as shown in Fig. 11.14. The sensor behaves similarly when excited with a square wave voltage, as shown by the current in Fig. 11.15. Thus flux gate sensors are often driven by a square-wave voltage such as shown in Fig. 11.16. Such a voltage can be created by two alternately fired MOSFETs (metal oxide semiconductor field-effect transistors) as shown in Fig. 11.17. The sensing circuit Simplorer model, including SPICE models of op-amp (operational amplifier) integrated circuits, is shown in Fig. 11.18. The output voltage of Fig. 11.18 is shown in Fig. 11.19 for various fields to be sensed [15].

In many cases there are two external fields to be sensed, and the differential flux density between the two is to be found. The final flux gate sensor model for such a system is shown in Fig. 11.20. The MOSFETs are fired by state machines. The system model transient response to a change in the external field from 0 to -0.2 mT is shown in Fig. 11.21. Thus the response time of the flux gate sensor is shown to be in the millisecond range [15]. Flux gate sensors are able to detect even smaller flux densities, down to the 0.1 nT range.

11.7 MAGNETOMETERS AND NOTES

Magnetic sensors that are able to detect very small magnetic fields are called *magnetometers*. Besides flux gate magnetometers, SQUID magnetometers are commonly used. SQUID stands for *superconducting quantum interference device*. Since quantum mechanics is beyond the scope of this book, SQUIDs will not be further studied here. Quantum mechanics is also involved in magnetic resonance imaging (MRI), which has been analyzed elsewhere [16]. Sometimes magnetic ferrite

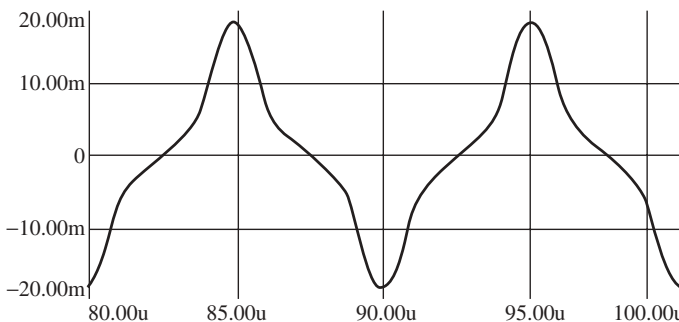


Figure 11.13 Typical flux gate sensor current response to an applied 2.5-V 100-kHz sinusoid with no external magnetic field. Note that the positive and negative areas are equal.

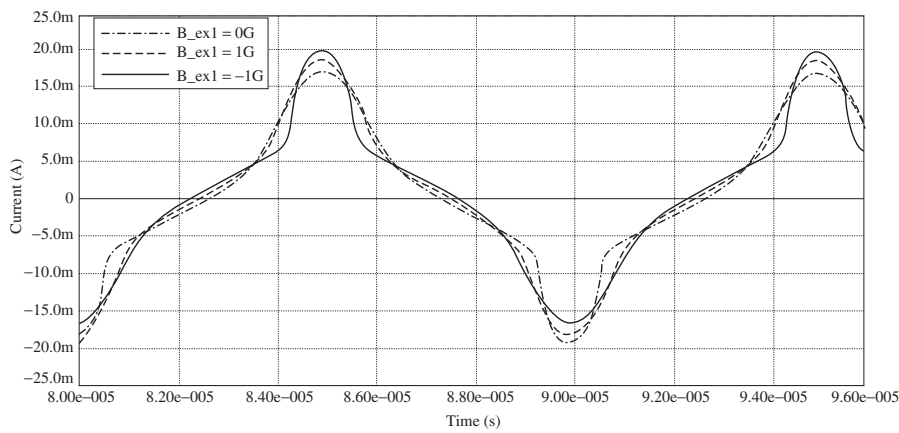


Figure 11.14 Typical flux gate sensor current response to an applied 2.5-V 100-kHz sinusoid with applied external magnetic fields. Note that the positive and negative areas are unequal when an external field is applied.

nanoparticles are used to provide contrast in MRI, and such particles are also being investigated for DNA testing [17].

Some of the newest developments in sensors are for *magnetoimpedance* (MI) sensors. MI sensors were developed in Japan on micromachined chips in 2001 and 2002 [18]. At that time they were made of amorphous FeCoSiB wire that had been tension-annealed for surface anisotropy. Their impedance changes as a result of skin effects and is proportional to the square root of the externally applied magnetic

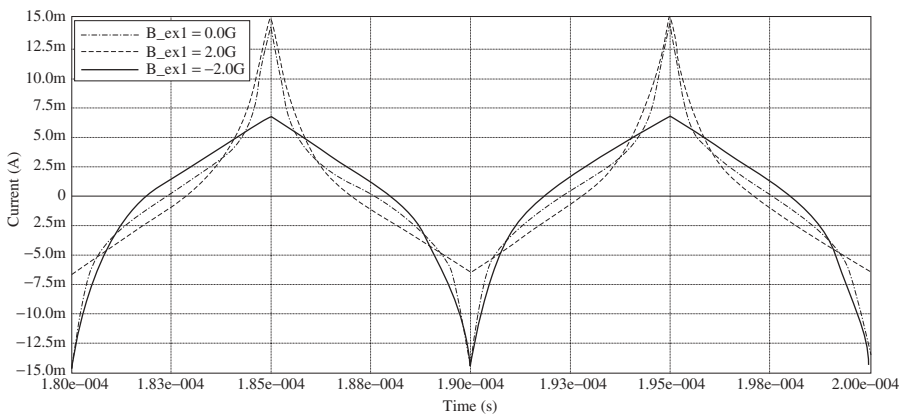


Figure 11.15 Typical flux gate sensor current response to an applied 1.5-V 100-kHz square wave with applied external magnetic fields. Note that the positive and negative areas are unequal when an external field is applied.

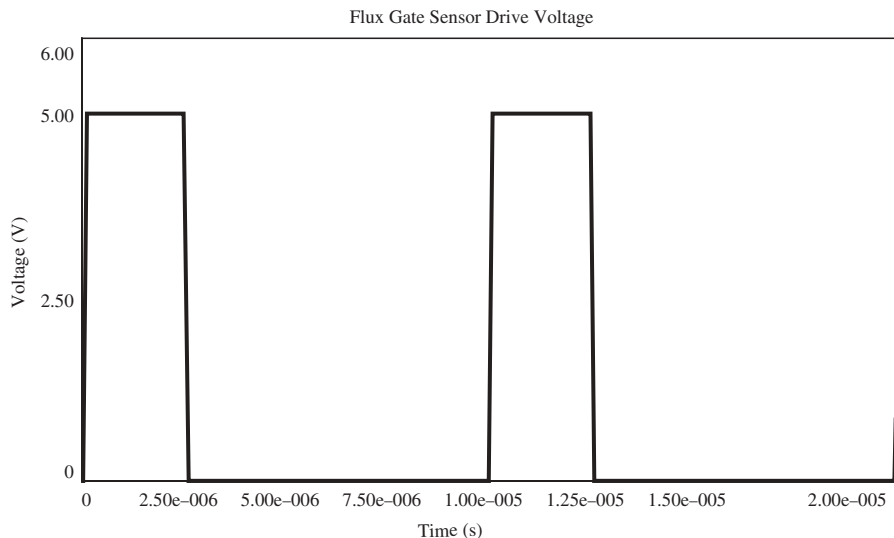


Figure 11.16 Typical square-wave voltage applied to flux gate sensor.

field. More recently, other materials have been used and the response has been made linear with the applied field [19–21].

Various magnetic sensor types are compared in Table 11.1. Note that MI sensors make excellent magnetometers, for their resolution is down to the same nanotesla range as in flux gate sensors. The speeds in Table 11.1 can be considered to be bandwidths; all are 1 MHz except for flux gate sensors. The lengths in the table are minimum dimensions; note that flux gate sensors require the most space, followed by MI sensors. Flux gate sensors also require more input power; the other types only require about 10 mW.

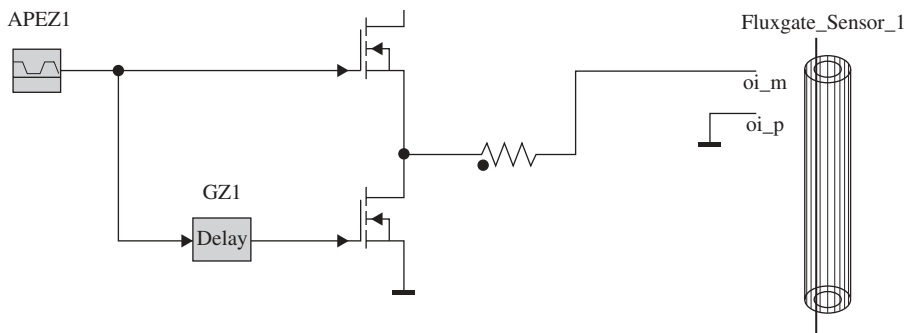


Figure 11.17 Typical flux gate sensor drive circuit containing two MOSFETs, modeled in Simpler.

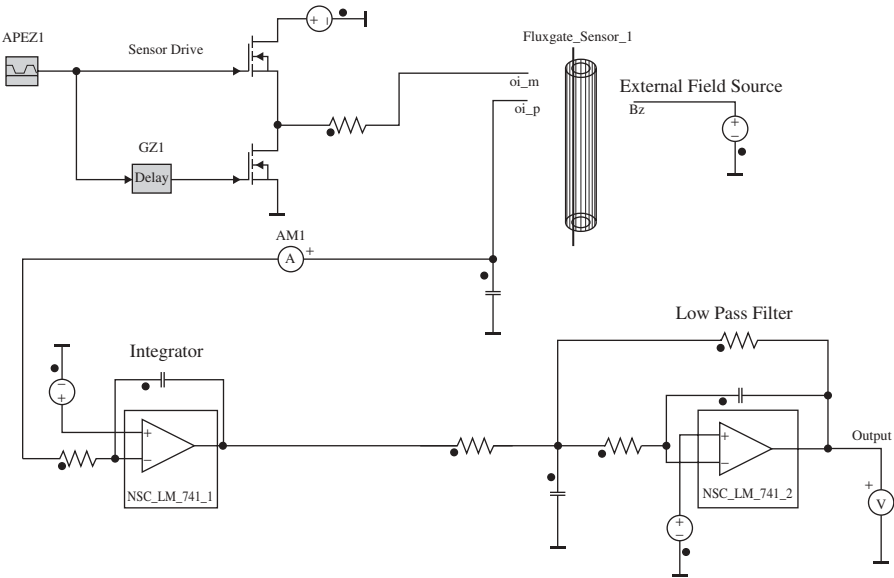


Figure 11.18 Typical Simplorer model of flux gate sensor, including op-amp integrated circuit models originally developed for SPICE.

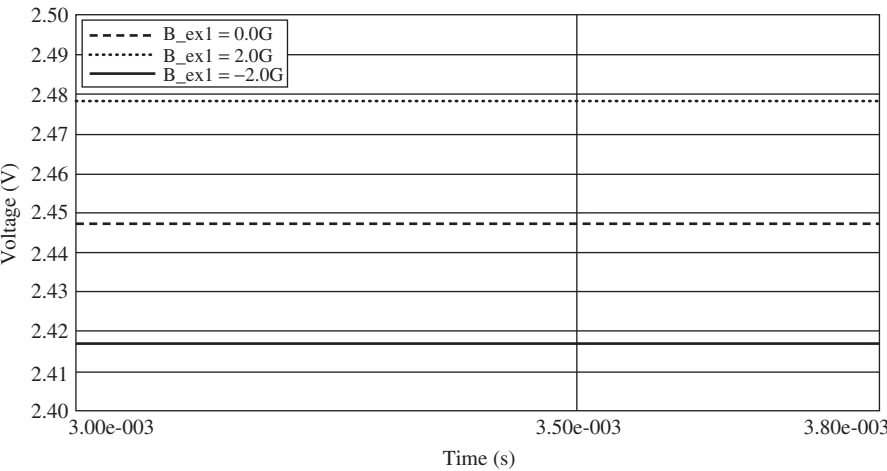


Figure 11.19 Computed output voltages of Fig. 11.18 model.

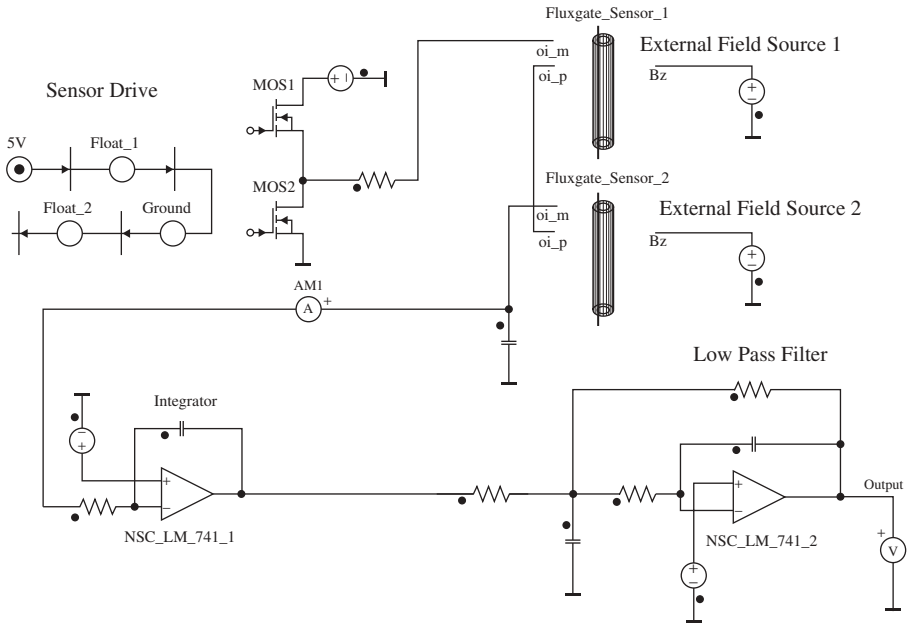


Figure 11.20 Systems model of two-field differential flux gate sensor. The MOSFETs are fired by a state machine model, commonly used in control systems.

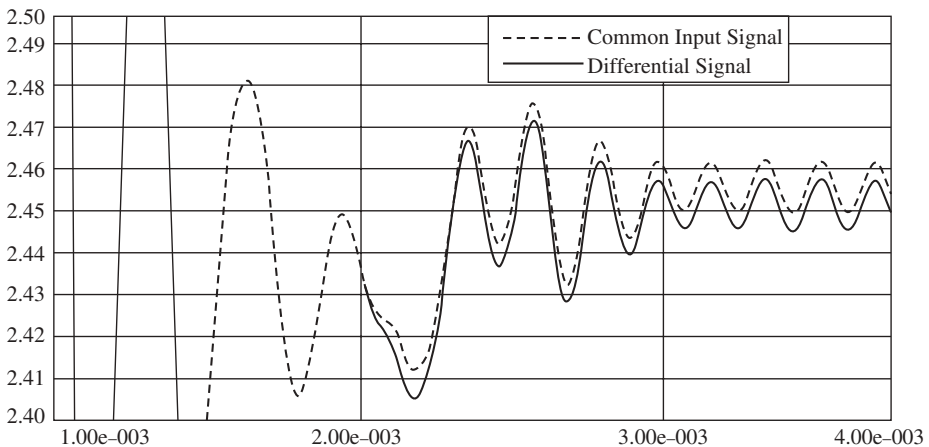


Figure 11.21 Computed transient response of sensor of Fig. 11.20 to a step change in external field from 0 to -0.2 mT (millitesla). The common and differential voltages are plotted on the vertical axis, and time in seconds is plotted along the horizontal axis.

TABLE 11.1 Comparison of Sensor Types.

Type	Length	Resolution	Speed	Wattage
Hall	100 μm	0.5 E-4 T	1 MHz	10 mW
MR	100 μm	0.1 E-4 T	1 MHz	10 mW
GMR	100 μm	0.01 E-4 T	1 MHz	10 mW
Flux gate	20 mm	0.1 E-9 T	5 kHz	1 W
MI	2 mm	0.1 E-9 T	1 MHz	10 mW

The sensors in Table 11.1 with lengths of 100 μm can be used to make *motes*, which are remote wireless sensors. Of very recent development, motes are sometimes called *smart dust*. If they were inexpensive enough, hundreds or more could be sprinkled around a region to monitor its detailed magnetic field distribution. IEEE Standard 802.15.4 covers wireless mesh networks called “Zigbee.”

Sensors can be interfaced to large systems through various interfaces. IEEE Standard P1451.4 enables *smart sensors* to *plug and play* into computers, including notebook and smaller computers. In automobiles, trucks, and construction equipment, sensors are commonly interfaced using CAN bus standard technology.

PROBLEMS

- 11.1** Redo Example 11.1 when the ampere-turns are reduced from 1000 to 500.
- 11.2** Redo Example 11.2 when the head core permeability is reduced to 200.
- 11.3** Redo Example 11.3 when the frequency is changed to (a) 100 Hz; (b) 200 Hz; (c) 400 Hz.
- 11.4** Redo Example 11.3 when the target material is changed to steel with relative permeability 100 and conductivity $1\text{E}6$ S/m.
- 11.5** Find the LVDT output voltage for Example 11.4 when the frequency is increased to 5 kHz.
- 11.6** Find the LVDT output voltage for Example 11.4 when the armature position is (a) -4 mm; (b) $+2$ mm; (c) $+6$ mm.

REFERENCES

1. F. Jorgensen, *The Complete Book of Magnetic Recording*, TAB Books, Blue Ridge Summit, PA, 1980.
2. R. L. Comstock, *Introduction to Magnetism and Magnetic Recording*, Wiley, New York, 1999.
3. I. D. Mayergoyz, *Mathematical Models of Hysteresis and Their Applications*, 2nd ed., Academic Press, New York, 2003.

4. E. Della Torre, *Magnetic Hysteresis*, Wiley-IEEE Press, New York, 2000.
5. R. H. VanderHeiden, A. A. Arkadan, and J. R. Brauer, Nonlinear transient finite element modeling of a capacitor discharge magnetizing fixture, *IEEE Trans. Magn.* **29**: 2051–2054 (March 1993).
6. M. Kobayashi and R. Horowitz, Track seek control for hard disk dual-stage servo systems, *IEEE Trans. Magn.* **37**: 949–954 (March 2001).
7. K. G. Ashar, *Magnetic Disk Drive Technology: Heads, Media, Channel, Interfaces, and Integration*, Wiley-IEEE Press, New York, 1996.
8. N. Ida, *Numerical Modeling for Electromagnetic Non-Destructive Evaluation*, Chapman & Hall, London, 1995.
9. Y. Gotoh and N. Takahashi, Proposal of detecting method of plural cracks and their depth by alternating flux leakage testing: 3D nonlinear eddy current analysis and experiment, *IEEE Trans. Magn.* **40**: 655–658 (March 2004).
10. H. H. Woodson and J. R. Melcher, *Electromechanical Dynamics*, Wiley, New York, 1968, Part II.
11. D. Rodger, P. J. Leonard, and T. Karaguler, An optimal formulation for 3D moving conductor eddy current problems with smooth rotors, *IEEE Trans. Magn.* **26**: 2370–2372 (Sep. 1990).
12. N. Ida and J. P. A. Bastos, *Electromagnetics and Calculation of Fields*, 2nd ed., Springer-Verlag, New York, 1997, pp. 420–422.
13. F. Jay, ed., *IEEE Standard Dictionary of Electrical and Electronic Terms*, 2nd ed., Wiley-Interscience, New York, 1977.
14. Y. Chen, J. E. Snyder, C. R. Schwichtenberg, K. W. Dennis, R. W. McCallum, and D. C. Jiles, Metal bonded Co-ferrite composites for magnetostrictive torque sensor applications, *IEEE Trans. Magn.* **35**: 3652–3654 (Sep. 1999).
15. D. Steward, Fluxgate sensor analysis, Power Point presentation prepared for Ansoft Corporation, Pittsburgh, PA, 2002.
16. J.-M. Jin, *Electromagnetic Analysis and Design in Magnetic Resonance Imaging*, CRC Press, Boca Raton, FL, 1998.
17. A. Hoffman, Magnetic viruses for biological and medical applications, *Magn. Bus. Technol.* 24 ff (Spring 2005).
18. K. Mohri et al., Amorphous wire and CMOS IC-based sensitive micromagnetic sensors utilizing magnetoimpedance (MI) and stress-impedance (SI) effects, *IEEE Trans. Magn.* **38**: 3063–3068 (Sept. 2002).
19. P. Delooze, L. Panina, D. Mapps, K. Ueno, and H. Sano, Sub-nano tesla resolution differential magnetic field sensor utilizing axymmetrical magnetoimpedance in multilayer films, *IEEE Trans Magn.* **40**: 2664–2666 (July 2004).
20. S. Sandacci, D. Makhnovskiy, L. Panina, K. Mohri, and Y. Honkura, Off-diagonal impedance in amorphous wires and its application to linear magnetic sensors, *IEEE Trans. Magn.* **40**: 3505–3511 (Nov. 2004).
21. X. Wang, W. Yuan, Z. Zhao, X. Li, J. Ruan, and X. Yang, Giant magnetoimpedance effect in CuBe/NiFeB and CuBe/insulator/NiFeB electroless-deposited composite wires, *IEEE Trans. Magn.* **41**: 113–115 (Jan. 2005).

PART IV

SYSTEMS

Coil Design and Temperature Calculations

Magnetic actuators and sensors are often components of large systems, such as automobiles. The actuators and sensors must perform reliably in the system environment and interface properly with the system.

To interface properly with system power supplies, the coils of the magnetic components must be properly designed, as described in this chapter. As part of the coil design, the temperatures developed by the coils and the components must be predicted. The relationship between electromagnetics (EM) and temperatures T is shown in Fig. 12.1 as a block diagram.

12.1 WIRE SIZE DETERMINATION FOR DC CURRENTS

Many DC power supplies consist of a fixed voltage. For example, automobiles have a standard 12-V supply, although the voltage under no load is actually 14 V, and other higher voltages are being added to accommodate ever-growing electrical demands.

As discussed in Chapter 7 and other previous chapters, the magnetic field and force are determined by ampere-turns NI . Ampere's law states that NI produces the field, not voltage. Thus the engineer designing a magnetic actuator or sensor must ensure that the coil carries the proper NI .

For DC voltages V , Ohm's law gives the relation between V and current I

$$I = V/R \quad (12.1)$$

where R is the coil resistance in ohms. Similar to reluctance of Chapter 3, resistance is related to geometry

$$R = l/(\sigma S_c) \quad (12.2)$$

where l is length of the conducting coil wire, σ is its conductivity, and S_c is the cross-sectional area of the wire.

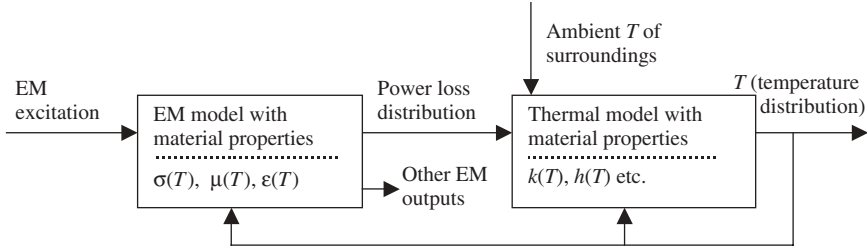


Figure 12.1 Modeling temperature and its effects on magnetic devices, to be discussed in this chapter.

For copper at room temperature (20°C), σ is 5.8E7 S/m. The other common coil material, aluminum, has a room-temperature conductivity of approximately 3.6E7 S/m. Both materials, however, change their conductivity with temperature T , as indicated in Fig. 12.1. For $0 < T < 100^\circ\text{C}$, the conductivity of copper obeys

$$\sigma = \frac{5.8\text{E7 S/m}}{1 + 0.00393(T - 20^\circ\text{C})} \quad (12.3)$$

that is, the conductivity of copper decreases by approximately 0.4% for each degree Celsius rise in temperature. The resistivity of copper, which is the reciprocal of conductivity, increases with temperature, having a positive temperature coefficient.

While square or rectangular wire is sometimes used, usually the wire used to wind coils has a circular cross section. Thus its cross sectional area S_c is related to wire diameter d :

$$S_c = \pi r^2 = \pi d^2/4 \quad (12.4)$$

Instead of choosing any wire diameter, one chooses an available *wire gauge*. Different countries can use different gauges. The American Wire Gauge (AWG) is a number, usually an integer, that gives the bare-wire diameter [1]:

$$d = (0.00826)(1.123^{-\text{AWG}}) \text{ m} \quad (12.5)$$

In AWG, every 6-gauge decrease gives a doubling of the wire diameter, and every 3-gauge decrease gives a doubling of the wire cross-sectional area. Also common is the metric wire gauge, which is simply 10 times the diameter in mm. Thus increasing wire size is accomplished by decreasing AWG or by increasing metric gauge.

However, all wires require insulation. The insulation can be a very thin enamel or other coating, consisting of one or more layers called *builds*. One can consult wire tables to determine insulated wire diameters.

The coil occupies a given coil winding area, as shown for example in any of the DC actuators of Chapter 7. The relation between the coil winding area S_w and the copper (or other wire material) area is the *packing factor*:

$$F_p = NS_c/S_w \quad (12.6)$$

For circular wires, even when they are tightly wound, the packing factor is typically only about 75%. Conservative designs assume a maximum $F_p = 0.70$ or less [1].

Various coil design procedures can be followed according to the preceding equations. Given a certain winding area and voltage, the desired NI can be obtained. However, if I is too high a value, then the coil temperature may become too high [2], as will be discussed later in this chapter. Maximum permissible current densities vary with cooling and other factors, but a reasonable value in some cases is 40 A/mm². All coil insulation is only capable of withstanding a certain temperature rise, for example, 40°C.

Example 12.1 Simple DC Coil Design at a Given Temperature An axisymmetric copper coil is to be designed to operate at a maximum temperature of 60°C. The available winding area S_w is 1.E-3 m² and the average coil radius is 5 cm. Assume a packing factor of 70% and a DC voltage of 12 V. If $NI = 1000$ ampere-turns, find the bare-wire diameter, the number of turns N , and the current density.

Solution: The length of a turn l_T is 2π times the 0.05-m radius, and thus $l_T = 0.31416$ m. The conductivity σ of the copper at 60°C is found using (12.3) to be $5.012\text{E}7$ S/m. This value can be used in the resistance equation from (12.2) and (12.4):

$$R = 4 \frac{NI_T}{\sigma \pi d^2} \quad (\text{E12.1.1})$$

The other key equation, based on (12.1), is

$$NI = NV/R \quad (\text{E12.1.2})$$

Substituting (E12.1.1) and solving for the bare diameter gives

$$d = \sqrt{\frac{4NI_T}{\sigma F_p \pi V}} \quad (\text{E12.1.3})$$

Inserting the known values of σ , F_p , V , l_T , and NI gives $d = 0.975$ mm. Then using (12.6), we obtain

$$N = F_p S_w / S_c = 4F_p S_w (\pi d^2) \quad (\text{E12.1.4})$$

Inserting the known values gives $N = 938$ turns. Thus each turn carries $1000/938 = 1.066$ amperes. The current density is the current per unit of area of copper, and here is 1.43 A/mm², a reasonably small value.

12.2 COIL TIME CONSTANT AND IMPEDANCE

In all DC and AC magnetic actuators and sensors, the time constant is important. When a DC voltage V is applied (as a step), the current rises exponentially according to

$$I = \frac{V}{R}(1 - e^{-t/\tau_e}) \quad (12.7)$$

where the electric time constant $\tau_e = L/R$. When an AC voltage V_{AC} is applied, then (ignoring capacitive effects), the steady-state AC current obeys the complex phasor relation

$$I_{AC} = \frac{V_{AC}}{Z} = \frac{V_{AC}}{R + j\omega L} \quad (12.8)$$

where Z is the complex AC impedance. Thus the current has the following phase angle:

$$\theta_I = -\arctan(\omega L/R) \quad (12.9)$$

Hence the L/R ratio is important for both DC and AC magnetic devices.

One expects that the coil design would affect the L/R time constant and the impedance. Thus this section investigates the design of a coil in a given coil winding area S_w . We seek to choose N for minimum time constant L/R and minimum energy W lost in ohmic power in the coil. Inductance L , resistance R , and the related τ_e and W can be calculated for a coil of given area S_w and ampere-turns NI . The derivation that follows ignores velocity effects.

From Chapter 3, L is proportional to the square of N and to permeance \mathcal{P} of (3.14):

$$L = N^2\mathcal{P} = (NI/I)^2\mathcal{P} = (NI)^2\mathcal{P}/(I^2) \quad (12.10)$$

Resistance R of the coil is proportional to length of wire (here N times the length of each turn l_T) divided by the product of conductivity and wire area times packing factor:

$$R = Nl_T/(\sigma F_p S_c/N) \quad (12.11)$$

$$R = N^2 l_T/(\sigma F_p S_c) \quad (12.12)$$

The related electric circuit time constant $\tau_e = L/R$ is then

$$\tau_e = N^2\mathcal{P}/(\sigma F_p S_c)/(N^2 l_T) \quad (12.13)$$

$$\tau_e = \mathcal{P}l_T/(\sigma F_p S_c) \quad (12.14)$$

Thus the time constant L/R is *independent of turns* N .

Energy loss W (power loss integrated over time) is proportional to the square of I and to resistance:

$$W = kI^2R = k(NI/N)^2N^2I_T/(\sigma S_c F_p) \quad (12.15)$$

$$W = k (NI)^2 I_T / (\sigma S_c F_p) \quad (12.16)$$

Hence W depends (as would be expected) on excitation NI , but does not depend on whether the coil designer chooses a high N and low I or a low N and high I .

Thus the engineer designing a high-speed actuator cannot vary N over a given area and expect the coil current risetime to be minimized. Instead, what must be done to reduce the time for the current to rise to a given amperage is to increase the voltage applied to the coil. This voltage increase is usually temporary to avoid excessive coil power loss and overheating.

For the Bessho actuator of Fig. 5.2, the time constant τ_e is 20 ms [3]. The inductance computed by magnetostatic finite element software [4] for a 10-mm airgap = 3.15 H, which then leads to a resistance $R = L/\tau_e$ = approximately 150 Ω , which is believed to be close to the actual R [4]. Even if the number of turns were changed from the 3300 of Fig. 5.2, the initial time constant would remain 20 ms.

12.3 SKIN EFFECTS AND PROXIMITY EFFECTS FOR AC CURRENTS

The DC resistance R described above can be increased significantly under AC operation. From Faraday's law, the magnetic fields produced by the AC current induce additional AC currents in the coil conductors. These additional currents produce additional losses, and sometimes change the current density distribution from uniform to nonuniform.

The skin depth equation (8.1) of Chapter 8 applies not only to steel but also to coil conductors, and is repeated here

$$\sigma = \frac{1}{\sqrt{\pi f \mu \sigma}} \quad (12.17)$$

where f is the AC frequency in hertz and σ is electrical conductivity. Coils of copper and aluminum have permeability $\mu = 12.57\text{E-}7$, the permeability of air. The derivation of the above skin depth assumes one-dimensional conducting slabs, but (12.17) is an approximate indicator of the depth of currents and magnetic fields for many practical problems.

When the skin depth is much greater than the wire radius, then AC magnetic flux density can be shown to produce losses similar to those of (8.2):

$$\frac{P_e}{v} = \frac{\omega^2 \sigma}{24} (w_y^2 B_x^2 + w_x^2 B_y^2) \quad (12.18)$$

where B_x and B_y are components of the peak AC magnetic flux density passing through the z -directed wire, $\omega = 2\pi f$, P_e is power in watts, v is the volume of the conducting material in cubic meters, w_x is the wire width in the x direction, and w_y is the wire width in the y direction. The losses of (12.18) are sometimes a significant addition to the I^2R losses of the DC resistance.

However, when the skin depth is smaller than the wire radius, then *skin effect losses* are said to occur. The current density distribution is no longer uniform. While the average of the current density J over the wire cross section remains the same, the average power loss density increases. The total power loss is

$$P = \int \frac{J^2}{\sigma} dv \quad (12.19)$$

Skin effect is usually considered to be associated with the magnetic field of a single isolated wire in air. Because other wires add contributions to the magnetic field, other wires in the proximity cause changes in the power losses. These effects of other wires are included in the *proximity effect*.

Since the magnetic fields are affected by all wires and all magnetic materials, the best way to analyze skin and proximity effects is to use finite-element analysis. The software must include eddy currents and must constrain the total current in each conductor to the same value.

Example 12.2 Skin Effect in an Isolated Conductor A circular copper wire carrying 100 A peak is placed in air, far from any other materials. If its radius is 10 mm, find its current density and magnetic flux density distributions at 400 Hz and 1 Hz using Maxwell SV. Also find the power loss and resistance per meter.

Solution: Use Maxwell SV's "eddy current" solver with the wire centered in its default model area, placing "balloon" boundaries around the area. At 400 Hz the power loss computed (per meter) is 0.49036 W. Thus the 400 Hz resistance $R = P/I^2$, where I is rms, is $0.98072\text{E-}4 \Omega/\text{m}$. Figure E12.2.1 shows the computed flux lines; note that they appear to be concentrated near the wire surface. Figure E12.2.2 graphs the computed current density versus wire radius. Note that the current density decays exponentially from the surface, as expected for an isolated wire. Since the skin depth at 400 Hz from (12.17) is 3.304 mm, the decay over the 10-mm radius appears reasonable.

At 1 Hz, the computed power loss is reduced to 0.2758 W/m. Thus the 1 Hz resistance is $0.5516\text{E-}4 \Omega/\text{m}$, which agrees closely with the DC resistance of $0.5488 \Omega/\text{m}$ obtained by (12.2). Thus the resistance at 400 Hz is approximately 1.8 times the DC resistance. Graphing the current density versus radius shows an essentially uniform current density throughout the wire at 1 Hz.

Example 12.3 Skin and Proximity Effects in Stator Coil with Clapper An axisymmetric copper coil is placed in a ferrite "cup core" inductor shown in Fig. E12.3.1 as created in Maxwell SV's default drawing area. The area is assumed to

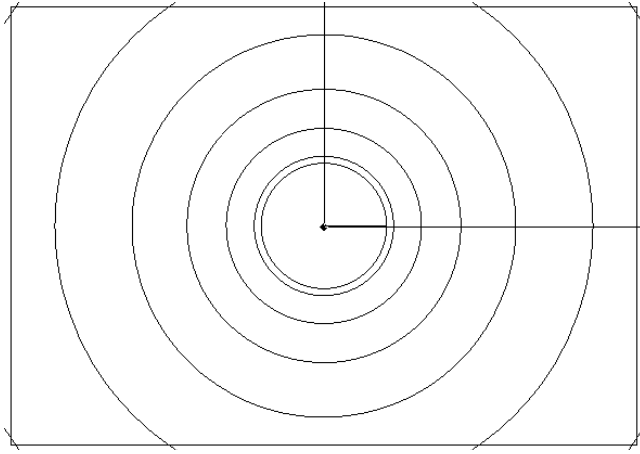


Figure E12.2.1 Computer display of computed flux lines in isolated wire at 400 Hz.

confine the flux. The ferrite in the lower stator and upper clapper armature has a relative permeability of 1000 and conductivity of 0.01 S/m. The coil has three copper conductors, each of radius 4 mm and carrying 50 A at 400 Hz. Use Maxwell SV to find the power loss, flux line plot, and current density distribution, showing skin and proximity effects in the three wires.

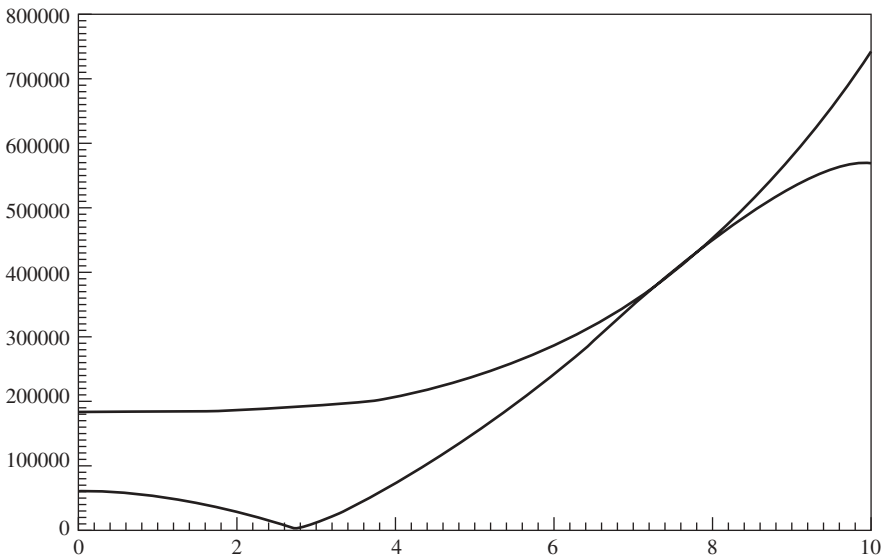


Figure E12.2.2 Computed current density at 400 Hz versus radius from center of wire. The upper curve is the total magnitude, and the lower curve is the magnitude at phase angle zero.

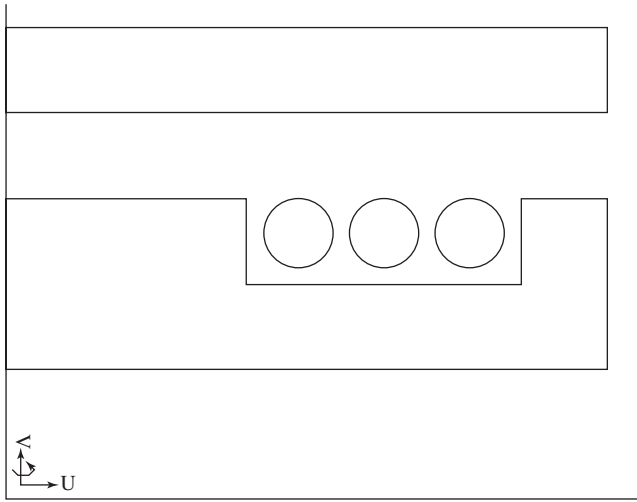


Figure E12.3.1 Three-turn winding in ferrite cup core inductor, as drawn in Maxwell's default window. The wire radius is 4 mm.

Solution: The model of Fig. E12.3.1 was solved by Maxwell SV's "eddy current" solver. The computed power loss is 0.635 W. The flux line distribution is shown in Fig. E12.3.2 at phase angle zero. The current density distribution can be plotted in color, but is instead graphed in Fig. E12.3.3 along a plane cutting all three wires. Note that each of the three wires has a different current density profile (because each has a different flux density), but that all appear to have the same average current density as they should.

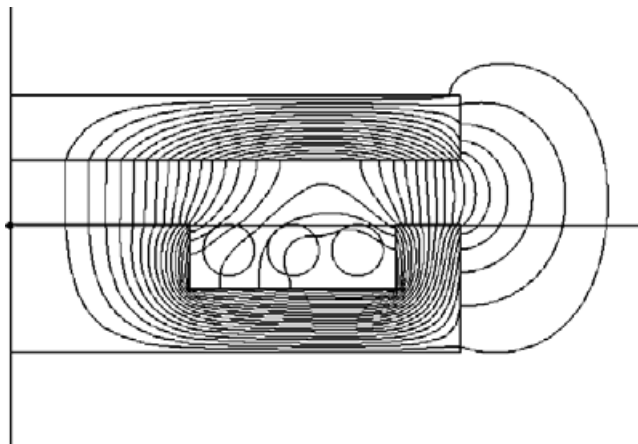


Figure E12.3.2 Computer display of flux line plot obtained for Fig. E12.3.1.

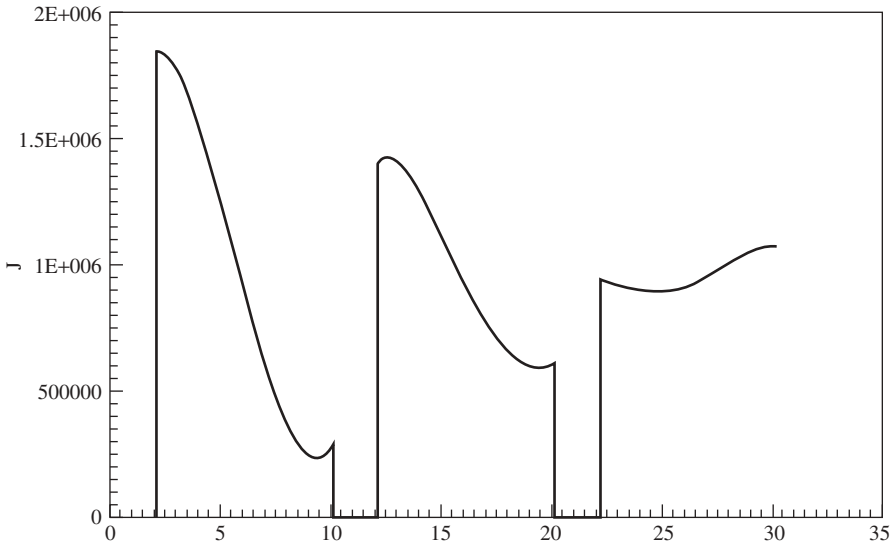


Figure E12.3.3 Graph of computed current density J in amperes per square meter versus position (mm) along plane cutting through the centers of the three wires in Fig. E12.3.1.

12.4 FINITE-ELEMENT COMPUTATION OF TEMPERATURES

As indicated in Fig. 12.1, the power losses in magnetic actuators and sensors determine their operating temperature. Since high temperatures can cause device failure and/or fire, it is important to be able to compute temperature distributions.

Thermal computations must in general include three means of heat transfer: conduction, convection, and radiation. This book will examine steady-state thermal computations. Time variation of temperature is studied elsewhere [5,6]. The Appendix includes the symbols, dimensions, and units of heat.

12.4.1 Thermal Conduction

Steady-state thermal conduction is governed by Poisson's differential equation [5,6]

$$\nabla \cdot k \nabla T = -\frac{P}{v} \quad (12.20)$$

where T is temperature, k is thermal conductivity, and the right-hand side is the negative power per unit volume. Thermal conductivities are similar to electrical conductivities in that they vary from high in metals to low in insulators and also vary somewhat with temperature. Approximate room temperature (20°C) values include 400 W/(m·°C) for copper and 80 W/(m·°C) for typical steel.

There is an analogy between (12.20) and one of Maxwell's equations of Chapter 2. Replacing the electric flux density of (2.44) by permittivity times electric field intensity E gives

$$\nabla \cdot \epsilon \mathbf{E} = \rho_v \quad (12.21)$$

where the right-hand side from Chapter 2 is volume charge density. Replacing \mathbf{E} by the negative gradient of electric scalar potential ϕ_v of (2.34) gives

$$\nabla \cdot \epsilon \nabla \phi_v = -\rho_v \quad (12.22)$$

Note that (12.22) is analogous to (12.20). Permittivity ϵ replaces thermal conductivity k , volume charge density replaces power per unit volume, and electric scalar potential replaces temperature.

Finite-element analysis of thermal conduction problems is commonplace [6,7]. Since Maxwell SV is used elsewhere in this book, its electrostatic solution of (12.22) will be used to solve thermal conduction by analogy.

Example 12.4 Steady Thermal Conduction Computation Using Analogy to Electrostatics An axisymmetric copper coil is surrounded by glastic insulation and a cylindrical steel core as shown in Fig. E12.4.1. The thermal conductivities are

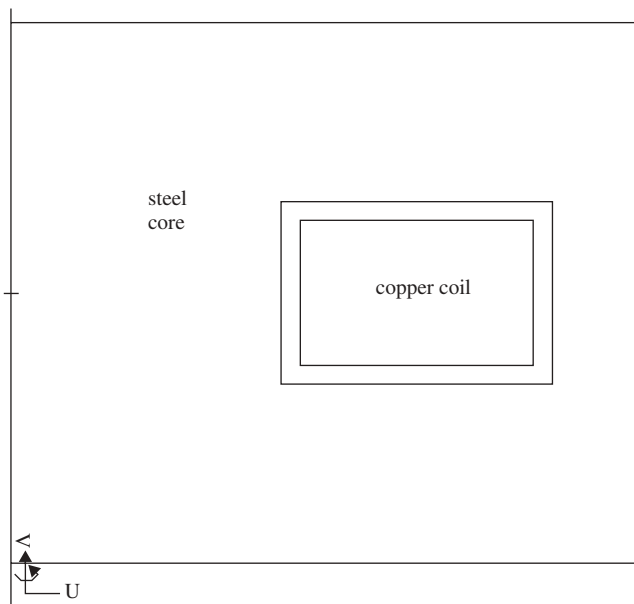


Figure E12.4.1 Axisymmetric inductor of radius 70 mm and height 60 mm. The temperature distribution is to be computed when there are power losses in the steel and in the copper coil of size 26 mm radially and 16 mm high, surrounded by glastic insulation 2 mm thick on all sides.

400, 10, and 79 W/(m·°C), respectively. The copper power loss density is 8000 W/m³ and the steel core loss density is 4000 W/m³. Use Maxwell SV's electrostatic solver to compute the temperature distribution, assuming that the outermost steel of the cylinder is at 25°C.

Solution: The relative permittivities to be entered are the preceding thermal conductivities divided by free-space permittivity 8.854E-12. Under “Sources and boundary conditions,” enter the charge densities of 8000 C/m³ in the copper coil and 4000 C/m³ in the steel core; then enter 25 Volts for the upper, lower, and outer steel boundaries. The computed voltage contours are shown in Fig. E12.4.2. Note that the maximum contour value is approximately 48 volts in the steel along the axis of symmetry. Thus the maximum temperature is 48°C. Alternatively, Maxwell's “thermal solver” can be used to also obtain 48°C.

12.4.2 Thermal Convection and Thermal Radiation

Besides thermal conduction, thermal convection and thermal radiation are usually very important in determining temperatures of magnetic actuators and sensors. The easiest way to analyze them is to use the film coefficient h defined by

$$Q = hA \Delta T \tag{12.23}$$

where Q is heat flow, A is the area of the surface, and ΔT is the temperature difference across the convective and/or radiative region. In many cases ΔT is the temperature rise above the temperature of the surroundings, called the *ambient temperature*. The coefficient h has SI units of W/(°C·m²).

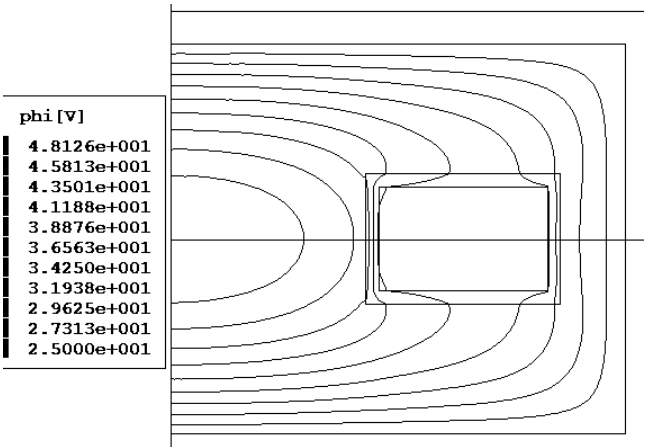


Figure E12.4.2 Computer display in black and white composed of computed voltage contours in inductor of Fig. E12.4.1, also available in color. The maximum temperature is approximately 48°C.

While the film coefficient varies tremendously with the available airflow paths and temperatures, a value often assumed is $10 \text{ W}/(^{\circ}\text{C}\cdot\text{m}^2)$ for free convection and radiation. *Free convection* is without fan cooling, while *forced convection* has a fan or wind. For more accurate determination of the convection portion of film coefficient h , computational fluid dynamics can be carried out, often using finite-element fluid analysis [6].

Thermal radiation is usually proportional to the fourth power of surface absolute temperature [6] in SI units of kelvin (see the Appendix). However, even at surface temperatures common to magnetic actuators and sensors, say, 60°C , the portion of film coefficient h due to radiation can be more than that of free convection. Radiation heat transfer is also determined by surface emissivity and geometric view factors [6]. Since both convection and radiation are commonly nonlinear functions of temperature, the nonlinear film coefficient h is often required in thermal finite-element computations [7].

Thermal finite-element software is widely available. Maxwell automatically includes electromagnetic power losses in its thermal computations.

12.4.3 AC Magnetic Device Cooled by Conduction, Convection, and Radiation

As an example of temperature computation in laminated magnetic devices, consider the three-phase inductor shown in Fig. 12.2. It has a core made of laminations of



Figure 12.2 Photograph of laminated three-phase 425-A rms 88- μH inductor for which temperatures are to be found.

Armco M6 grade steel of thickness 0.356 mm. To maintain inductance at frequencies above 60 Hz, the laminations are considerably thinner than the 0.635 mm thickness commonly used for 60-Hz laminations. The laminations are stacked to form a core of height of 190.5 mm.

The laminated core material has a B - H curve and core loss curves provided by Armco. To model the core loss using Maxwell's thermal finite element solver, the Armco core loss curves are fitted to the core loss equation [8,9]

$$p = K_h B^2 f + K_c (Bf)^2 + K_e (Bf)^{1.5} \quad (12.24)$$

where p = power loss density in watts per cubic meter, K_h = hysteresis coefficient, K_c = classical eddy current coefficient, K_e = excess (or anomalous) eddy current coefficient due to domains, B = peak magnetic flux density in teslas, and f = frequency in Hz. For the Armco steel laminations used, least-squares curve fitting gives $K_h = 66.9$, $K_c = 0.210$, and $K_e = 1.92$.

To reduce high-frequency losses in the copper windings of the three-phase inductor, the winding turns are made of multiple strands. Figure 12.3 shows the three phase windings, one on each arm of the laminated core. Each phase has 7 turns made of 8

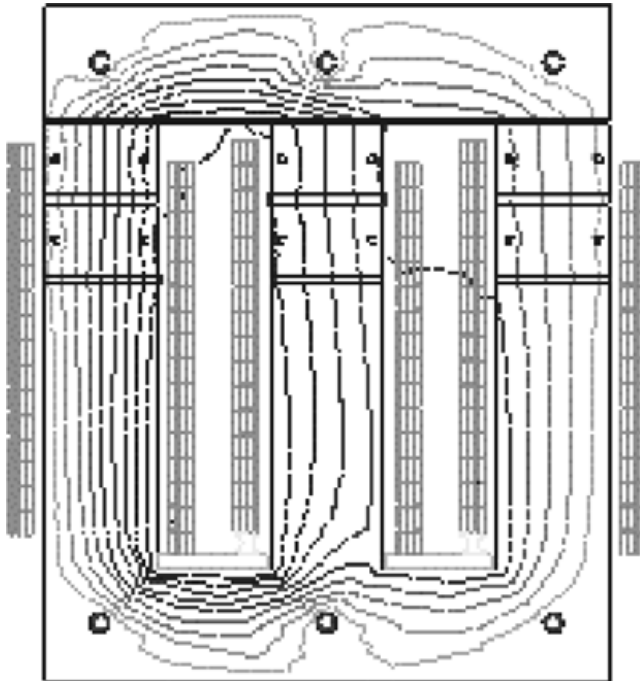


Figure 12.3 Computer display of geometry of laminated three-phase inductor, also showing computed magnetic flux lines at time zero, when 14.14 A (10 A rms) of frequency 100 Hz flows in the leftmost winding. Note that there are eight core segments.

strands of octagonal wire. The overall lamination width is 302 mm, and the total height (including the top “I” core segment) is 361 mm. The geometry of Fig. 12.3 was developed as an Autocad DXF file, which was then directly input into Maxwell.

Besides the core and copper losses, losses may occur in the bolts holding the laminations together. The bolts are made of solid steel with a $B-H$ curve and electrical conductivity (2.E6 S/m) assumed for SAE 1010 steel.

The three-phase laminated inductor of Figs. 12.2 and 12.3 was input to Maxwell, which was used to compute its electromagnetic performance followed by its thermal performance. The magnetic flux density distribution and related electrical parameters and losses were computed over a wide range of current amplitudes and frequencies. Figure 12.3 shows a typical computed magnetic flux line pattern.

The loss distributions in the various copper windings, the various segments of the steel core, and the steel bolts, were computed for frequencies ranging from 1 Hz to 20 kHz. Skin effects and proximity effects in the stranded copper windings were included in the computations. To check the copper loss computation of 0.0507 W at 1 Hz and 10 A rms, the simple DC resistance formula (12.2) was used where length $l = 0.1905$ m, electrical conductivity $\sigma = 5.8E7$ S/m for Cu, and S_c is the area of the octagon-shaped strand. Substituting the area and multiplying by I^2 gives a loss of 0.050 W, agreeing closely with the 0.0507 W computed by finite elements.

At higher frequencies for the same 10-A current, finite-element computations show that the copper loss increases from 1.184 W at 100 Hz to 32.266 W at 20 kHz. The increase is due to skin and proximity effects, which also cause changes in the magnetic field flux pattern shown in Fig. 12.4 at 4 kHz, which differs in the winding area from Fig. 12.3.

The inductance was also computed, which for 60 Hz currents below 750 A was 89.8 μ H. This agrees reasonably well with the manufacturer’s rated 88 μ H and measured 60 Hz inductance of approximately 96 μ H at low currents; the small difference is believed due at least in part to the inductance of the leads. Because of skin effects within steel laminations, inductance is expected to be greatly reduced at frequencies of 20 kHz and higher [10].

Next, the losses computed were used in a thermal finite-element model, again using the Maxwell software. The thermal model is made from the electromagnetic model by adding the necessary thermal materials, boundary conditions, and excitations.

The thermal material properties include the thermal conductivities. Even though the steel used is laminated, the thermal conductivity for solid steel was used; this is believed appropriate since most heat is expected to flow in the $x-y$ plane of the laminations. Other key thermal conductivities include 10.2 W/(m-°C) for the glastic insulation in the “airgaps” between the eight core segments.

The thermal boundary conditions are convective and radiative, involving a film coefficient. Because the inductor of Fig. 12.2 also has available airflow paths at its ends (in the z direction out of the figure), the film coefficient assumed here is $h = 15$ W/(°C-m²). The ambient temperature is assumed to be 25°C. The 60-Hz loss distributions were input for 425 A rms. The resulting computed temperature distribution is shown in Fig 12.5.

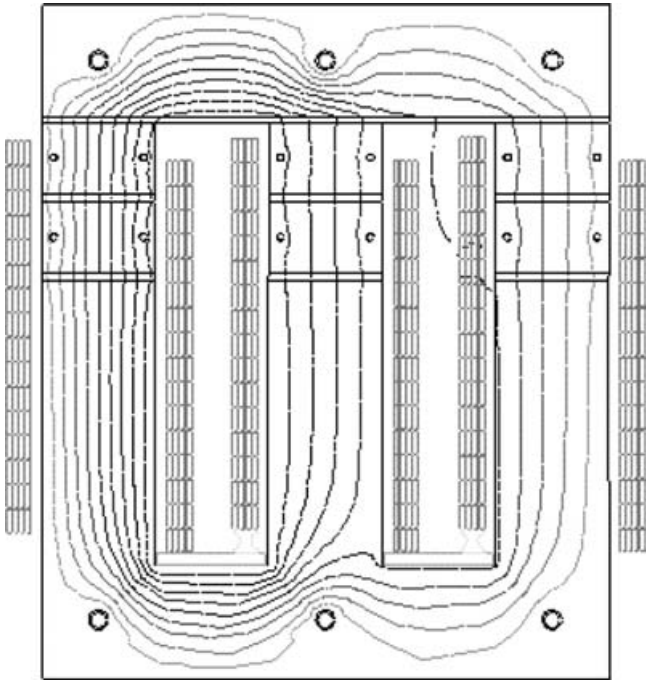


Figure 12.4 Computer display of computed flux lines for 14.14 A (10 A rms) of frequency 4 kHz in leftmost winding. Note that, as a result of skin and proximity effects the winding leakage flux lines differ from Fig. 12.3 low-frequency flux lines.

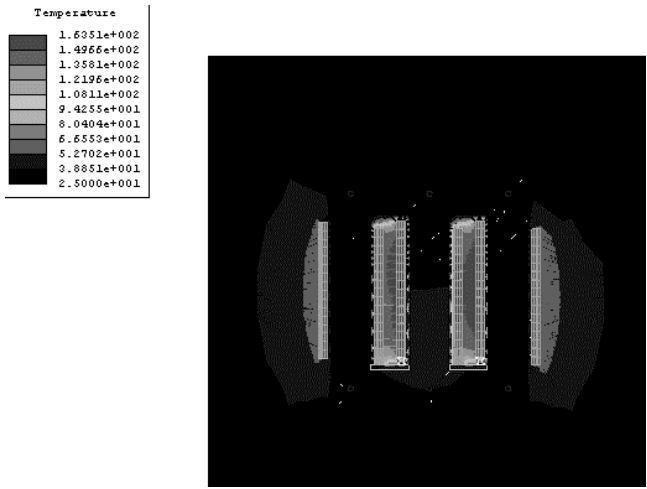


Figure 12.5 Computer display in black and white of computed temperature distribution in laminated inductor, also available in color.

The maximum computed temperature in Fig. 12.5 is 163.5°C, which agrees reasonably well with the measured maximum temperature of 156°C. The computed temperatures are significantly affected by the assumed film coefficient; for example, changing it from 15 to 20 W/(°C-m²) causes the maximum temperature to fall to 145°C.

PROBLEMS

- 12.1 Redo Example 12.1 assuming a temperature of 100°C.
- 12.2 Redo Example 12.1 when the winding area is increased to 1.5E-3 m².
- 12.3 Redo Example 12.1 when the packing factor is increased to 0.75.
- 12.4 Redo Example 12.1 when the voltage is increased to 14 V DC.
- 12.5 Redo Example 12.2 at 60 Hz.
- 12.6 Redo Example 12.2 with the wire made of aluminum with an electrical conductivity of 3.54E7 S/m.
- 12.7 Redo Example 12.3 at 60 Hz.
- 12.8 Redo Example 12.3 with the wires made of aluminum with electrical conductivity 3.54E7 S/m. Find the power lost in each of the three wires as well as the total loss.
- 12.9 Redo Example 12.4 with the power loss density doubled in the coil.
- 12.10 Redo Example 12.4 with the power loss density doubled in the steel core only.
- 12.11 Redo Example 12.4 with the power loss density doubled in both the coil and the core.
- 12.12 Redo Example 12.4 with the thermal conductivity of the insulation reduced to 4 W/(m-°C).

REFERENCES

1. M. A. Juds, *Notes on Solenoid Design*, Eaton Corporate R&D, Milwaukee, WI, July 15, 2004.
2. W. M. Flanagan, *Handbook of Transformer Design and Applications*, 2nd ed., McGraw-Hill, New York, 1993.
3. K. Bessho, S. Yamada, and Y. Kanamura, Analysis of transient characteristics of plunger type electromagnets, *Electric. Eng. Japan* **98**: 56–62 (July 1978).
4. J. R. Brauer, J. J. Ruehl, and F. Hirtenfelder, Coupled nonlinear electromagnetic and structural finite element analysis of an actuator excited by an electric circuit, *IEEE Trans. Magn.* **31**: 1861–1864 (May 1995).

5. J. P. Holman, *Heat Transfer*, McGraw-Hill, New York, 1963.
6. J. R. Brauer, ed., *What Every Engineer Should Know about Finite Element Analysis*, 2nd ed., Marcel Dekker, New York, 1993, Chapter 4, Thermal analysis, by V. D. Overbye; Chapter 5, Fluid analysis, by N. J. Lambert.
7. J. R. Brauer and P. Wallen, Coupled 3D electromagnetic, structural, and thermal finite element analysis as integral components of electronic product design, *Proc. IEEE Wescon Conf.*, Oct. 1996, pp. 358–364.
8. G. L. Skibinski, B. G. Schram, J. R. Brauer, and Z. Badics, Finite element prediction of losses and temperatures of laminated and composite inductors for AC drives, *Proc. IEEE Int. Electric Machines and Drives Conf.*, June 2003.
9. A. E. Fitzgerald, C. Kingsley, and S. D. Umans, *Electric Machinery*, 6th ed., McGraw-Hill, New York, 2003.
10. J. R. Brauer, B. C. Beihoff, Z. J. Cendes, and K. P. Phillips, Laminated steel eddy loss vs. frequency computed using finite element analysis, *IEEE Trans. Indust. Appl.*, **36**: 1132–1137 (July/Aug. 2000).

Electromagnetic Compatibility

Just as in the preceding chapter, the magnetic device design must be compatible with system voltages and temperatures, and the device must also possess *electromagnetic compatibility*. EMC, the common abbreviated term, is related to EMI, *electromagnetic interference*. Magnetic actuators and sensors must not produce unacceptable EMI, nor should their performance adversely be affected by EMI.

13.1 SIGNAL-TO-NOISE RATIO

EMI is electromagnetic interference or noise, where noise is any undesirable signal [1]. There are four general types of EMI:

- *Conducted emissions* are noises produced by the magnetic device that travel to other devices in any system via conductors such as power supply wires.
- *Radiated emissions* are noises produced by the magnetic device that travel to other devices in any system via electromagnetic radiation in air or free space.
- *Conducted susceptance* refers to noises produced in the magnetic device by conduction through wires from other devices.
- *Radiated susceptance* refers to noises produced in the magnetic device by electromagnetic radiation in air or free space.

Whether noise is produced by conduction or radiation, the important factor is whether it dominates the desired signal. For example, if a radio signal, such as a voice and/or music, is large compared with noise, such as static due to lightning, then performance is generally satisfactory. If the noise becomes almost as large as, or larger than, the signal, then performance is usually unsatisfactory. The signal-to-noise ratio, abbreviated as S/N or SNR, is thus a key parameter.

For best S/N, the noise should be reduced and/or the signal increased. If the noise has a frequency spectrum different from that of the signal, filtering circuits can be employed to reduce the noise. Hence most EMI and EMC specifications by regulatory agencies (such as the U.S. Federal Communications Commission) are in terms of frequency. However, if noise occupies the same frequency band as the signal, then other methods must be found.

Conducted noise can usually be reduced by proper circuit design. For example, conducted noise due to IR voltage drops caused by current pulses in an actuator coil can be reduced if the wires from the power supply to the actuator and other devices are large enough to reduce the resistance and if proper grounding is employed [1,2]. For automotive conducted susceptibility the biggest challenge often is alternator *load dump*, but careful filtering and shielding can prevent it from causing malfunction of proximity sensors [3].

Radiated noise is usually a more difficult problem, whether the magnetic device is emitting it or subjected to it. Magnetic actuators, which often have large ampere-turns, tend to emit EMI. Magnetic sensors, which often are very sensitive to magnetic fields, tend to be very susceptible to EMI.

Inductive magnetic sensors are especially susceptible to radiated EMI. For example, inductive pickup coils of the velocity sensors of Section 11.1 induce voltages proportional to frequency according to Faraday's law. Thus high frequency EMI can induce large noise voltages, larger than the desired signal at low speeds. In automotive EMI engineering [4] involving such velocity sensors on all four wheels, one method of noise suppression is to connect the four sensors so that *common-mode noise* voltages induced in all four wheels essentially cancel out, leaving mostly the desired signal voltage [5].

13.2 SHIELDS AND APERTURES

The best way to reduce radiated emissions and radiated susceptance is to use a shield. A *shield* is a highly conductive enclosure, almost always made of metal. Ideally, it would *completely* enclose and seal off the magnetic actuator or sensor.

From Chapter 8, conductive materials possess the skin depth

$$\delta = \frac{1}{\sqrt{\pi f \mu \sigma}} \quad (13.1)$$

where f is frequency in Hz, μ is permeability, and σ is electrical conductivity. The key parameter in a shield is the ratio of its thickness T to skin depth. The larger the ratio, the lower is the transmissibility of electromagnetic fields from one side of the shield to the other. Thus the larger the ratio of T to skin depth, the better the shield is at preventing EMI.

Shield thickness T equals skin depth at a frequency f_{\min} found from (13.1):

$$f_{\min} = \frac{1}{\pi \mu \sigma T^2} \quad (13.2)$$

For noise frequencies below the minimum frequency f_{\min} the shield is ineffective. Note that for lowest f_{\min} , the conductivity, permeability, and thickness should all be as high as possible.

Shield thickness is limited by weight, size, and cost considerations. To reduce the weight, aluminum is a very common shield material. However, the higher permeability of steel causes it to be chosen sometimes to shield low frequencies. In fact, it will be shown that steel shields even reduce DC magnetic field transmission from one side to the other.

For magnetic actuators and sensors, magnetic field EMI is usually the main concern, rather than electric field EMI. However, above a certain frequency range *coupled electromagnetic* radiation, mentioned in Chapter 2, becomes the most significant form of EMI. Thus electric fields are also important, and in fact are usually measured during EMC tests. The frequency at which coupled electromagnetic fields become significant is when the component size, including the shield size, has a dimension of approximately 10% of a wavelength. Wavelength λ is given by

$$\lambda = c/f \quad (13.3)$$

where c is the speed of light that equals 3.E8 m/s in air or free space.

Unfortunately, almost all shields must contain at least one *aperture*, a term meaning opening or hole. For magnetic sensors, the object or field to be sensed cannot be entirely separated from the sensor, so an aperture is usually required. For magnetic actuators, the object to be moved must usually be accessible, and thus an aperture is needed. For both magnetic actuators and sensors, electrical voltages or currents must be accessed through some sort of terminal.

A typical shield and aperture are shown in Fig. 13.1. The shield is a rectangular box with a top piece that is attached above a gasket [6,7]. To reduce computer mod-

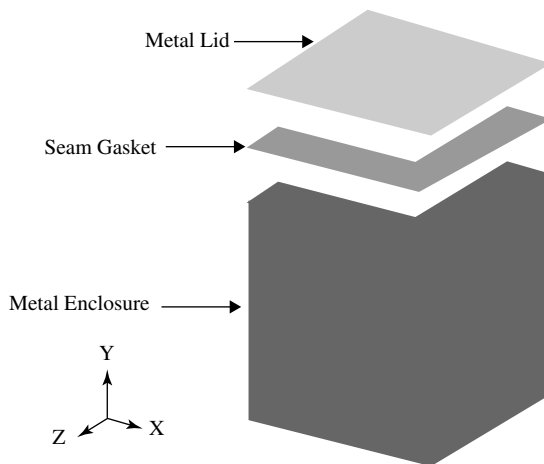


Figure 13.1 One-quarter of a rectangular shielding box that is 1 mm thick. The quadrant size is 110×110 mm of the 440-mm^2 box. The box height is 115 mm, on top of which is the 5-mm-thick gasket and the 1-mm-thick lid.

eling time, only one-fourth of the box is needed. The shield has a conductivity of $4.8\text{E}7$ S/m, and the gasket has a complex relative permeability of $100 - j 100$ along with a relative permittivity of 10. Inside the box is a vertically oriented half-loop current source lying in the $x = 0$ plane. The top of the loop is located 50 mm down from the top of the lid. The electric field outside the box is to be computed over the frequency range 100 kHz–100 MHz. At 100 MHz, the wavelength from (13.3) is 3 m. Since the box has maximum dimension of almost 0.5 m, coupled electromagnetic fields can be significant in the range of ~ 60 MHz and higher. Thus a coupled 3D electromagnetic finite-element formulation, to be presented in the next chapter, was used in all computations for Fig. 13.1.

The computed electric field intensity versus frequency is plotted in Fig. 13.2, where it is shown to compare fairly closely with measurements available to 1 MHz [6,7]. The computed 3D electric field distribution in three cut planes around the box is displayed in Fig. 13.3. Similar finite-element computations have been carried out for over 100 apertures at frequencies as high as approximately 10 GHz [8].

Some magnetic actuators and sensors inherently possess some shielding. For example, the axisymmetric plunger actuators discussed in Chapter 7 almost completely surround their coils by steel, and thus usually emit less EMI than planar actuators with clapper armatures.

Example 13.1 Cylindrical Shield without and with an Aperture A circular copper wire loop carrying 1000 ampere turns AC is shielded by a cylindrical metal can as shown in Fig. E13.1.1. The coil is stranded such that its skin and proximity effects are negligible; its inner radius is 1 mm, outer radius 2 mm, and height is 1 mm. The coil is centered in the can of inner radius 3 mm, inner height 3 mm, and thickness 0.4 mm. The can has an optional 1-mm airgap below its top. Use finite elements to find the magnetic flux density just inside and outside the top corner of the can for the following cases:

- (a) Aluminum can at 60 Hz and 10 kHz with no airgap. The aluminum electrical conductivity is $3.6\text{E}7$ S/m.

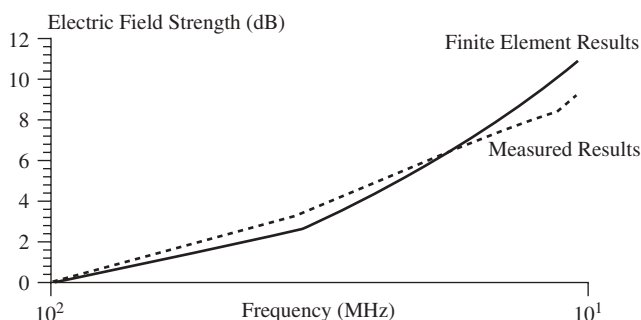


Figure 13.2 Computed and measured leakage electric field from shield of Fig. 13.1.

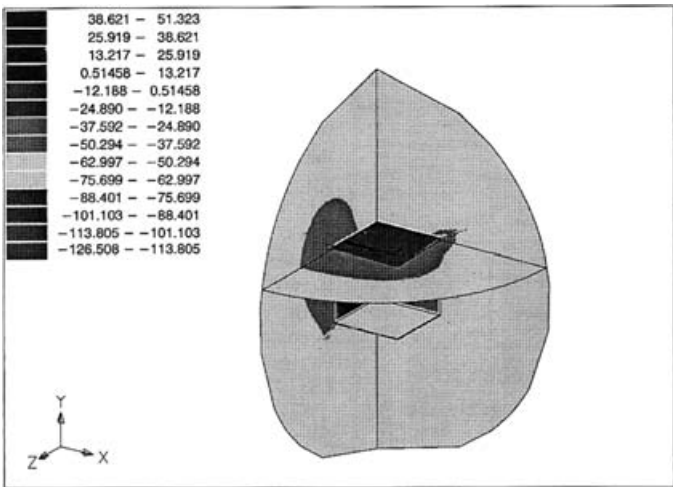


Figure 13.3 Computed electric field distribution in decibels emitted by shield of Fig. 13.1 at 1 MHz. This display appears in color on the computer screen but is shown here in black and white.

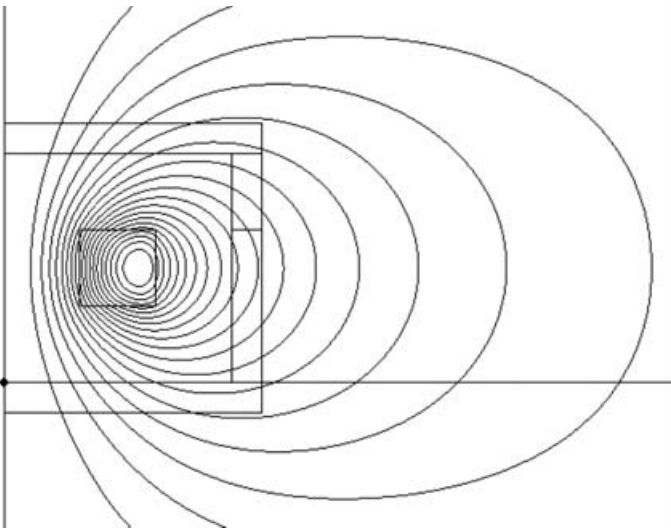


Figure E13.1.1 Computer display of cylindrical can with computed flux lines at 60 Hz with complete aluminum shield.

- (b) Aluminum can at 10 kHz with 1-mm airgap.
- (c) Steel can at 0.1 Hz (essentially DC) and 10 kHz. The steel has relative permeability of 1000 and electrical conductivity $2.E6$ S/m.
- (d) Steel can at 10 kHz with 1 mm airgap.

Solution: Since the overall shield size at the frequencies to be analyzed is much less than 10% of a wavelength, Maxwell SV's "eddy current" solver will be used. Under "Sources and boundary conditions" use a balloon outer boundary and stranded source. Results are as follows:

- (a) At 60 Hz the aluminum is not a good shield, as shown by its flux lines in Fig. E13.1.1. Note that they pass through the aluminum as if it were not present, because the skin depth in aluminum at 60 Hz using (13.1) is 10.8 mm, much greater than the shield thickness. Flux densities at the top right inner edge of the can are 0.029 T inside and 0.021 T outside, essentially natural decay with distance. At 10 kHz, some shielding occurs, because the skin depth is now 0.84 mm. The flux densities are 0.031 T inside and 0.015 T outside.
- (b) When the aperture is cut in the aluminum, there is more flux density outside. The flux density decays from 0.035 T inside the aperture to 0.020 T outside.
- (c) The skin depth in the steel is 0.113 mm at 10 kHz, less than the 0.4 mm thick shield. At 0.1 Hz, B is 1.1 mT just inside the shield and only 0.577 mT outside the shield; the shield itself has flux densities on the order of 0.6 T. At 10 kHz, B is 3.77 mT just inside the shield and only 0.163 mT outside the shield; the shield itself has inner flux densities of 1.6 T. The flux line plot is shown in Fig. E13.1.2, and shows how the shield confines most of the magnetic flux.

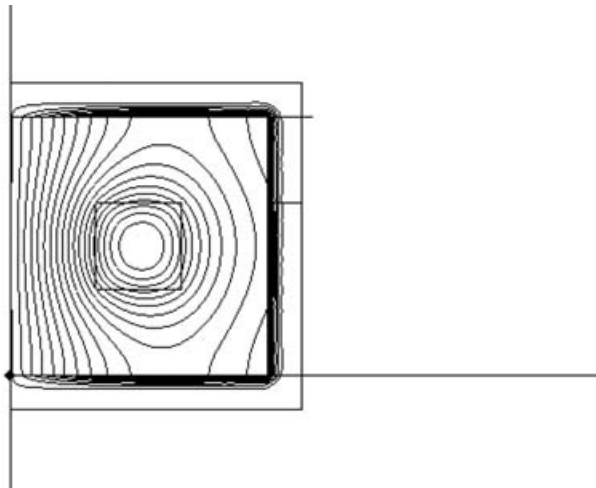


Figure E13.1.2 Computer display of cylindrical can with computed flux lines at 10 kHz with complete steel shield.

- (d) Cutting the aperture produces 97 mT in the same outside location that previously had only 0.163 mT. As shown in Fig. E13.1.3, the aperture allows a lot of flux to pass, although the shield still is helpful.

13.3 TEST CHAMBERS

Test chambers are commonly used to test radiated EMC behavior of magnetic actuators and sensors. To evaluate emissions, electromagnetic *absorption chambers* are often used. They are quite expensive and large, because they must contain a great deal of absorptive (also called electromagnetic anechoic) material, usually wedge-shaped pieces facing the emitting device. They absorb rather than reflect EMI, and thus simulate the “open air” environment in which many magnetic devices are placed. Smaller, less expensive chambers called *TEM cells* and *triplate cells* are often used to determine radiated susceptibility.

13.3.1 TEM Transmission Lines

A *transverse electromagnetic (TEM) field* has \mathbf{E} and \mathbf{H} vectors both lying in the plane transverse (perpendicular or normal to) the direction of energy propagation. \mathbf{E} and \mathbf{H} are perpendicular to each other, and the ratio of their magnitudes is called the *wave impedance*

$$Z_w = |E_F|/|H_F| = \sqrt{\mu/\epsilon} \quad (13.4)$$

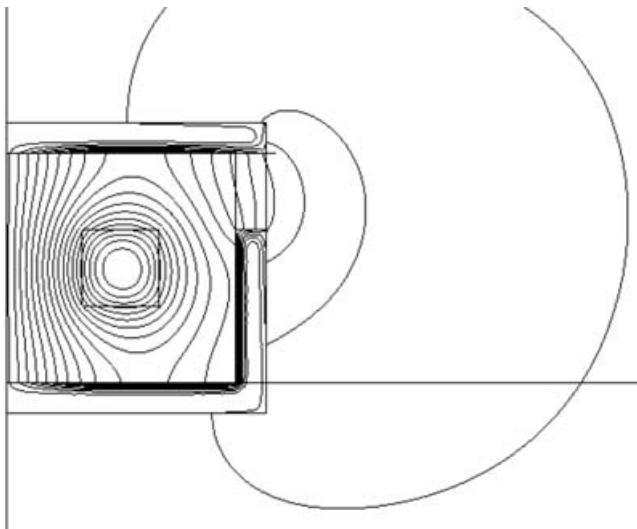


Figure E13.1.3 Computer display of cylindrical can with computed flux lines at 10 kHz with steel sheet with an aperture.

where the energy is propagating in the forward (F) direction in a lossless material with permeability μ and permittivity ϵ . Note that the subscript F on E and H indicates the forward-traveling “waves” of E and H . Substituting the material properties of air, its $Z_w = 377 \Omega$. Assuming no reflections or losses, the only components of \mathbf{E} and \mathbf{H} are those in (13.4), and thus the \mathbf{E} and \mathbf{H} fields are uniform and known.

TEM cells and triplate cells are basically modified *transmission lines*. A common basic TEM transmission line is a coaxial cable. It is essentially lossless, and has a characteristic impedance commonly denoted as Z_0 , given by

$$Z_0 = |V_F|/|I_F| = \sqrt{L/C} \quad (13.5)$$

where V_F is the forward-traveling voltage wave and I_F is the forward-traveling current wave. Also, L is the transmission line inductance per unit length in henrys per meter, and C is the transmission-line capacitance per unit length in farads per meter. Typical coax (coaxial cable) Z_0 values are 50 and 75 Ω . If a coax cable is matched with an impedance (including a Thevenin impedance) on its end equal to its Z_0 , then no reflections occur and the only voltages and currents are V_F and I_F . Thus impedance matching produces uniform and known V and I , as well as uniform and known \mathbf{E} and \mathbf{H} .

A coax cable has a grounded outer shield and a center conductor. The center conductor usually carries the signal voltage. The current passes down the center conductor and returns via the outer shield. The characteristic impedance can be altered by changing L and C . They are varied by

1. Changing the material between the shield and center conductor. For example, different plastics have different permittivities.
2. Changing the geometry of the center conductor and outer shield. For circular coax, varying these two radii changes Z_0 . For other shapes, such as elliptical or rectangular, other values of Z_0 can be obtained. Changing the geometry changes both L and C . It is possible, however, to vary the geometry along a transmission line and yet obtain the same L/C ratio, thereby maintaining a constant Z_0 . Maintaining constant Z_0 prevents reflections, thereby helping to maintain the desired uniform and known V, I and \mathbf{E}, \mathbf{H} .

Besides the abovementioned lossless transmission line, lossy (with loss) transmission lines also occur. Their characteristic impedance is given by [9]

$$Z_0 = |V_F|/|I_F| = \sqrt{(R + j\omega L)/(G + j\omega C)} \quad (13.6)$$

where R is the series resistance per unit length in ohms per meter and G is the parallel conductance per unit length in siemens per meter. Because j is the square root of minus 1, the characteristic impedance in the lossy case can be a complex number. The angular frequency $\omega = 2\pi f$, where f is the frequency in hertz.

In TEM transmission lines, the electric and magnetic fields are at right angles to each other and can be computed separately. If lossless, electrostatic and magneto-

static solutions apply. If lossy, the magnetic field computations should include eddy current losses at the frequency f as described in the preceding chapter.

13.3.2 TEM Cells

A TEM cell is a TEM transmission line that has a big “bulge” in it that serves as the cell, or chamber, for the device under test. There are many ways to make the “bulge” and thus many varieties and sizes of TEM cells exist. Figure 13.4 shows a typical small TEM cell. Note that the coax connectors on both ends are visible.

Note also in Fig. 13.4 that the TEM cell is completely enclosed. However, Fig. 13.4 shows that doors are placed in the enclosure walls to allow the device being tested to be inserted. Also couplings through the doors and walls enable measurements of the fields and the device performance.

Interiors of TEM cells can be of various designs. The field is only approximately uniform throughout the entire interior.

13.3.3 Triplate Cells

A triplate cell is a simplification of a TEM cell in which some walls are removed to create three metal “plates.” The device to be tested can thus be easily inserted and altered. The triplate in Fig. 13.5 has the coax connectors visible on both ends.

Both triplate cells and TEM cells bombard the device under test with both electric and magnetic fields. To find the ratio E/H for an arbitrarily shaped triplate or TEM cell, assume that the load impedance on the cell end matches the characteristic impedance, giving $V/I = Z_0$. Then, from (13.5), we obtain

$$V/I = (L/C)^{1/2} \quad (13.7)$$

$$V^2/I^2 = L/C \quad (13.8)$$

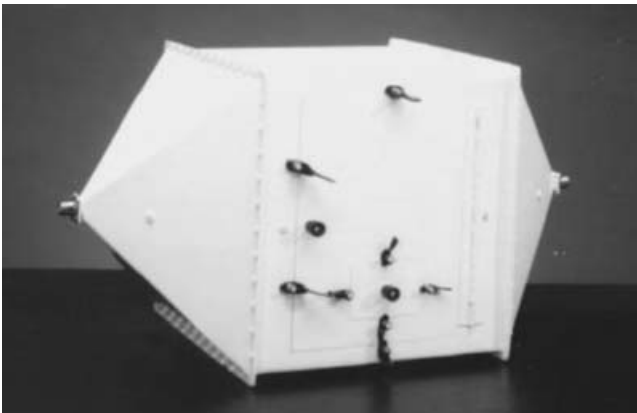


Figure 13.4 Typical small TEM cell ($33 \times 33 \times 64$ cm).



Figure 13.5 Typical triplate cell.

Substituting energy expressions (6.17) and (6.23) gives

$$V^2/I^2 = (2W_{\text{mag}}/I^2)/(2W_{\text{el}}/V^2) \quad (13.9)$$

Thus

$$W_{\text{mag}} = W_{\text{el}} \quad (13.10)$$

This equality has been verified using finite-element computations. Thus a feature of a matched triplate or TEM cell is that its *electric fields and magnetic fields have equal energies*.

Now the magnetic energy W_{mag} is the volume integral of magnetic energy density, or the average magnetic energy density times the volume:

$$W_{\text{mag}} = \frac{1}{2}\mu_0 H_{\text{av}}^2 v \quad (13.11)$$

where H_{av} is the average H and v is volume. The electric energy is the volume integral of electric energy density, or the average electric energy density times the volume

$$W_{\text{el}} = \frac{1}{2}\epsilon_0 E_{\text{av}}^2 v \quad (13.12)$$

where E_{av} is the average E .

Substituting (13.11) and (13.12) into (13.10) gives

$$\frac{1}{2}\mu_0 H_{\text{av}}^2 = \frac{1}{2}\epsilon_0 E_{\text{av}}^2 \quad (13.13)$$

Hence

$$E_{\text{av}}/H_{\text{av}} = (\mu_0/\epsilon_0)^{1/2} = 377 \quad (13.14)$$

Thus in any triplate cell or TEM cell that has a load equal to its characteristic impedance, that is $V/I = Z_0$, the average ratio of E/H is 377. Since the voltage contours (for the \mathbf{E} field) and the magnetic flux lines are identical as discussed in the example below, \mathbf{E} and \mathbf{H} fields obey this ratio everywhere in matched triplate cells and

TEM cells. Most commercial cells produce a specified \mathbf{E} field, but (13.14) obtains the cell \mathbf{B} field magnitude as follows:

$$B = \mu_0 E / 377 \quad (13.15)$$

Since magnetic sensors and actuators are usually more susceptible to \mathbf{B} field EMI than to \mathbf{E} field EMI, (13.15) is often useful.

Example 13.2 Characteristic Impedance of Triplate The cross section of the main center section of a triplate cell is shown in Fig. E13.2.1. Its dimensions are 60×60 cm. Its three plates are all 5 mm thick. Its center plate is 50.8 cm wide. Find its characteristic impedance using Maxwell SV. Also find its voltage contours and magnetic flux lines, assuming that it is matched, thereby indicating the variation of the fields over the cell cross section.

Solution: To find characteristic impedance using the preceding formulas, L and C must be found. First, Maxwell SV's "electrostatic" solver is used to find C and the electric field. Figure E13.2.1 shows computed voltage contours for $V = 10$ V between adjacent plates. In most regions $E = V/d = 33.3$ V/m in the vertical direction. However, near the corners of the plates E is much higher, and away from the plates E decays and changes direction ("fringes"). Maxwell also computes the electric energy stored W_E as $2.2564\text{E-}9$ J/m for $V = 10$ V between plates. Then from the capacitance energy formula (6.23), solving for capacitance gives

$$C = 2W_{\text{el}}/V^2 \quad (\text{E13.2.1})$$

the capacitance C is found to be 45.13 pF/m.

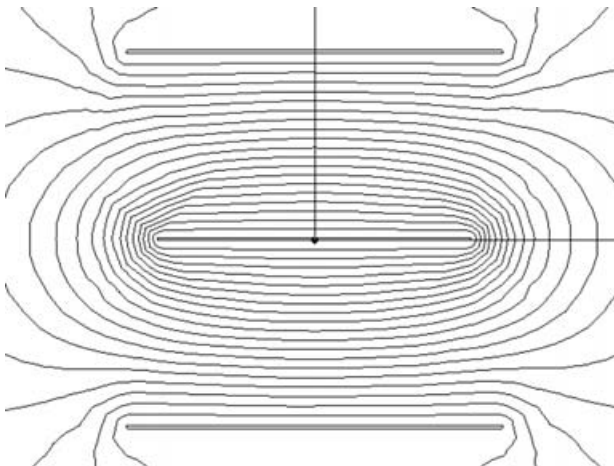


Figure E13.2.1 Computer display of triplate cell center cross section and its computed voltage contours or magnetic flux lines.

Next, the same tri-plate was analyzed for its magnetic fields and inductance using Maxwell's "eddy current" solver. To include skin effects expected at audiofrequencies (20 Hz–20 kHz) and higher, the plates are assumed to have their currents on their skin, and thus the plate permeability is assumed to be 0.1% that of air. The computed magnetic flux lines appear identical to Fig. E13.1.1. For 10 A, the computed magnetic energy is 1.2513E-5 J per meter depth. Then from the well known magnetic energy formula (6.17), solving for inductance gives

$$L = 2W_{\text{mag}}/I^2 \quad (\text{E13.2.2})$$

the inductance L is found as 250.3 nH per meter. Then from (13.5), the characteristic impedance of the triplate is 74.5 Ω . This agrees reasonably well with the 75 Ω specified by the triplate manufacturer.

The magnetic flux lines and voltage contours of Fig. E13.1.1 show that a large area of the region between plates has an approximately uniform field. The field is uniform in most locations away from plate corners. Thus, in using triplate cells, the magnetic device under test must be considerably smaller than the cell and should be placed near the center of the cell. If desired, finite-element models of the device under test can be developed and included in the model of the cell [10].

PROBLEMS

- 13.1 Redo Example 13.1 at a frequency of 20 kHz.
- 13.2 Redo Example 13.1 for steel with a relative permeability of 500 and conductivity 1.5E6 S/m.
- 13.3 Redo Example 13.2 when the center plate is expanded to the same width as the top and bottom plates.
- 13.4 Redo Example 13.2 when the top and bottom plates are expanded to 75 cm wide.
- 13.5 Redo Example 13.2 when the top and bottom plates are 75 cm wide and the center plate is 60 cm wide.
- 13.6 At a certain distance "down the line" from the center cross section of the triplate cell of Example 13.2, all dimensions are exactly one-half those of the center section. Use Maxwell SV to find the characteristic impedance of the smaller section. Also find its voltage contours and magnetic flux lines, assuming that it is matched, thereby indicating the variation of the fields over this smaller cross section.

REFERENCES

1. H. W. Ott, *Noise Reduction Techniques in Electronic Systems*, Wiley, New York, 1976.
2. C. R. Paul, *Introduction to Electromagnetic Compatibility*, Wiley, New York, 1992.
3. R. Repas, Prox sensors for vehicles, *Machine Design* (Feb. 3, 2005).

4. M. S. Markel, J. R. Brauer, and B. S. Brown, Using finite element software to predict automotive EMC, *Proc. EMC/ESD Int. Conf.*, Denver, CO, April 1993.
5. *Automotive Handbook*, 4th ed., Robert Bosch GmbH, Stuttgart, Germany, 1996; also available from SAE, Warrendale, PA, p. 638.
6. J. R. Brauer and B. S. Brown, Mixed-dimensional finite elements for models of electromagnetic coupling and shielding, *IEEE Trans. Electromagn. Compat.* **35**: 235–241 (May 1993).
7. T. Harada et al., Suppressing electromagnetic field leakage through gaps in metal enclosures using magnetic materials, *Proc. 9th Int. Zurich Symp. Tech. Exhib. on EMC*, March 1991, pp. 725–730.
8. J. R. Brauer, Homogenized finite element model of a beam waveguide resonator antenna with over one hundred coupling holes, *Proc. Applied Computational Electromagnetic Society Annual Review of Progress*, Monterey, CA, 1998.
9. J. R. Brauer, EMC of automotive wiring analyzed by finite elements, paper presented at SAE Passenger Car Meeting, Dearborn, MI, Sept. 1985; also in *SAE Transactions*.
10. J. E. Bracken, I. Bardi, A. Mathis, S. Polstyanko, and Z. J. Cendes, Analysis of system-level electromagnetic interference from electronic packages and boards, *Proc. IEEE Meeting on Electrical Performance of Electronic Packaging*, Austin, TX, Oct. 2005.

Electromechanical Finite Elements

For magnetic actuators and sensors, mechanical parameters usually influence performance more than do any other nonelectromagnetic parameters. For example, armature mass directly affects the speed of response of a magnetic actuator. Mechanical and electromagnetic behaviors are coupled together and described as *electromechanical* behavior.

This chapter and the next are devoted to electromechanical analysis. The present chapter uses electromechanical finite elements to analyze the behavior of magnetic actuators and sensors.

14.1 ELECTROMAGNETIC FINITE-ELEMENT MATRIX EQUATION

The magnetic finite elements described in Chapter 4 are not sufficient by themselves to completely analyze magnetic actuators and sensors. Subsequent chapters have described the use of finite elements to analyze electric fields and coupled electromagnetic fields. In addition, the electric circuit exciting the actuator or sensor must be included in many analyses.

An electromagnetic finite-element formulation that is capable of analyzing all types of electromagnetic fields is described here. While many other formulations exist, each with its own advantages, the formulation given here is easy to understand and is directly related to the structural finite-element formulation to follow.

The 3D electromagnetic finite-element formulation described here is based on three matrices: $[K_E]$, $[B_E]$, and $[M_E]$. They appear in the electromagnetic finite-element equation [1,2]

$$[M_E]\{\ddot{u}_E\} + [B_E]\{\dot{u}_E\} + [K_E]\{u_E\} = \{F_E(t)\} \quad (14.1)$$

where $[K_E]$ is the reluctance stiffness matrix of (4.13) and is defined here in terms of shape functions N by the finite-element volume integral

$$[K_E] = \int dV [\nabla \times N]^T [\nu] [\nabla \times N] \quad (14.2)$$

where the center factor, the reluctivity tensor matrix, is the inverse of the magnetic permeability tensor matrix $[\mu]$. The $[B_E]$ matrix of (14.1) is called the *conductance matrix* and is proportional to the conductivity tensor according to

$$[B_E] = \int dv [\nabla N]^T [\sigma] [\nabla N] \quad (14.3)$$

and accounts for energy (power) loss necessary to solve eddy current problems. Finally, to solve problems where electric field energy storage is included, the permittance matrix proportional to permittivity is defined as

$$[M_E] = \int dv [\nabla N]^T [\epsilon] [\nabla N] \quad (14.4)$$

and is needed in coupled electromagnetic problems.

The unknown electromagnetic vector $\{u_E\}$ in (14.1) contains in general four components at each finite-element node

$$\{u_E\} = \begin{bmatrix} A_1 \\ A_2 \\ A_3 \\ \Psi \end{bmatrix} \quad (14.5)$$

where the three components of magnetic vector potential A in many cases are x , y , and z components, but may also be in other coordinate systems. The fourth unknown component is the time integral of the electric scalar potential ϕ_v of (2.34):

$$\Psi = \int dt \phi_v \quad (14.6)$$

The right-hand side of (14.1) is the electromagnetic excitation vector:

$$\{F_E\} = \begin{bmatrix} J_{\text{vector}} \\ 0 \end{bmatrix} \Big|_{\text{node}} + \begin{bmatrix} H_{\text{tan}} \\ J_{\text{norm}} \end{bmatrix} \Big|_{\text{surface}} + \begin{bmatrix} \nabla \times H_c \\ 0 \end{bmatrix} \Big|_{\text{volume}} \quad (14.7)$$

where the vector J_{vector} includes the current densities at the finite-element nodes as described in two dimensions in (4.12), but here allowing for all three-dimensional components. The second term in (14.7) allows for 3D \mathbf{H} fields to be imposed on surfaces of finite-element models, as do the TEM cells and triplate cells of the preceding chapter. Finally, to allow permanent magnet excitations, the third term is added that involves the distribution of the coercive field intensity H_c of Chapter 5 as detailed elsewhere [1].

Note that (14.1) includes the permittance matrix times the second time derivative (indicated by the double dot) of $\{u_E\}$ and the conductance matrix times the first time derivative (indicated by the single dot) of $\{u_E\}$. It also includes the reluctance matrix times $\{u_E\}$ as expected from Chapter 4. Because of its time derivatives, (14.1) can solve both static and dynamic (time-varying) electromagnetic problems.

The derivation of the general electromagnetic matrix equation (14.1) is based on electromagnetic energy. Instead of minimizing an energy functional as in Chapter 4, an energy variational including all forms of energy is set to zero [1,2].

Because (14.1) includes all forms of electromagnetic energy as well as time derivatives, it can solve many types of electromagnetic problems:

1. Static problems: electrostatics, magnetostatics, current flow
2. AC problems, in which each dot is replaced by $j2\pi f$, where f is any frequency
3. Transient problems, in which the dots involve timesteps (as in Chapter 9)
4. Nonlinear magnetostatic problems (with nonlinear B - H curves)
5. Nonlinear transient problems, using time steps and nonlinear B - H curves
6. Modal solutions of resonance problems, usually at high frequencies encountered by magnetic actuators and sensors only when undergoing EMC tests

14.2 0D AND 1D FINITE ELEMENTS FOR COUPLING ELECTRIC CIRCUITS

The general formulation of (14.1) allows for 3D finite elements, 2D finite elements, and also 1D and 0D finite elements. The 1D and 0D finite elements allow electric circuits to be included in the finite-element model. While other methods of including electric circuits are available [3], the 0D technique described here is especially easy to understand.

Zero-dimensional (0D) finite elements connect nodes independent of their geometric dimensional distances [2]. Since conventional electric circuit elements R , C , and L connect circuit nodes independent of their distance and dependent only on topology, 0D finite elements can model circuit elements. Thus the general formulation (14.1) includes the three 0D finite elements labeled as “res,” “cap,” and “ind” in Fig. 14.1. Because circuit nodes have voltage as their potential, the res, cap, and ind elements have the time integral of voltage (14.6) as their potential.

The cap 0D finite element of C farads contributes the following terms to the permittance $[M_E]$ matrix:

$$[M_c] = C \begin{bmatrix} 1 & -1 \\ -1 & 1 \end{bmatrix} \quad (14.8)$$

The res 0D finite element of R ohms contributes the following to the conductance $[B_E]$ matrix:

$$[B_R] = \frac{1}{R} \begin{bmatrix} 1 & -1 \\ -1 & 1 \end{bmatrix} \quad (14.9)$$

Finally, the ind 0D finite element of L henrys contributes the following terms to the reluctance $[K_E]$ matrix:

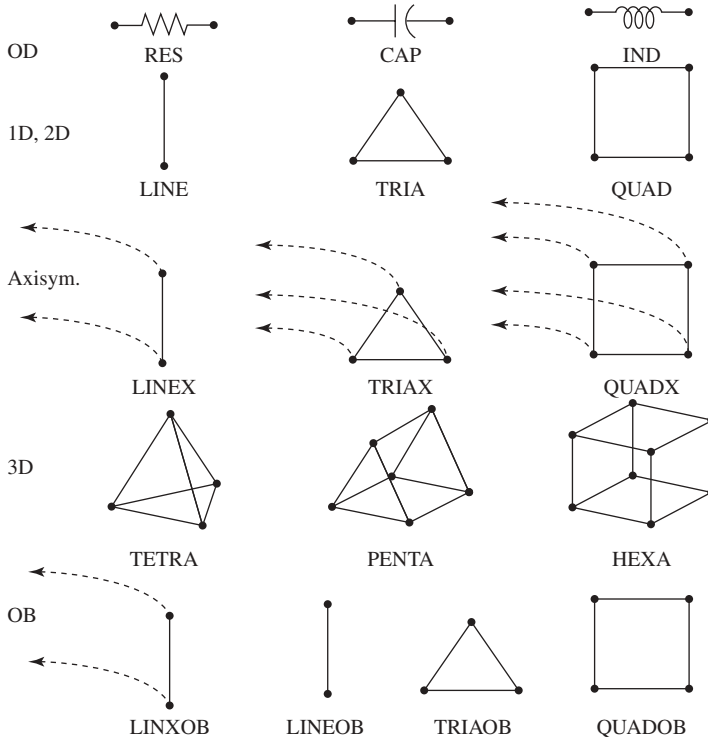


Figure 14.1 Finite elements of various dimensions used in the general formulation (14.1).

$$[K_L] = \frac{1}{L} \begin{bmatrix} 1 & -1 \\ -1 & 1 \end{bmatrix} \quad (14.10)$$

Inserting these above three terms in (14.1) yields the equation

$$C \frac{\partial V}{\partial t} + \frac{V}{R} + \frac{1}{L} \int V dt = I \quad (14.11)$$

where V is the voltage difference between the two nodes and I is their current. Because (14.11) agrees exactly with Kirchhoff's current law of conventional electric circuit theory for a parallel RLC circuit, the 0D finite-element method of analyzing circuits is validated.

To couple the preceding 0D circuit finite elements into a 3D or 2D finite-element model, one-dimensional (1D) finite elements can be used. As shown in Fig. 14.1, there are two types of 1D elements: the line and the linex. The linex is used only for axisymmetric problems, while the line is more general.

The line element usually is made highly conductive in order to represent wires and/or coils. The 1D line element can then connect 0D circuit elements into 2D or

3D finite-element models of magnetic devices. All the available 2D and 3D finite elements are shown in Fig. 14.1, including *open-boundary* finite elements. The balloon boundary finite elements used in previous examples, such as Example 13.1, are one type of open-boundary finite element. The types of open boundary elements shown in Fig. 14.1 are called ABC elements, which stands for *asymptotic boundary condition* or (for high-frequency problems) *absorbing boundary condition*. The ABC elements have the features of producing essentially no increase in computer times and serving well for static [4], transient, and AC problems [5].

Example 14.1 Constant-Permeability Transformer with Impedance Loading its Secondary The transformer shown in Fig. E14.1.1 is made of constant-permeability laminated (zero-conductivity) steel. As discussed for linear variable-differential transformers (LVDTs) in Chapter 11, placing a load impedance on a transformer secondary affects transformer currents and voltages. The transformer in Fig. E14.1.1 has a one ohm resistive load impedance on its four-turn secondary winding. Its one turn primary winding is excited by 120 V at 60 Hz AC and has a resistance of 0.1 Ω . The rectangular primary and secondary windings are separated from the core by 0.25 m. The core has dimensions shown in Fig. E14.1.1. Use the formulation described in the preceding sections to find both transformer currents for the following cases:

- The core permeability is 1.E5 times that of air.
- The core permeability is 500 times that of air.
- Same as (b), but the secondary winding is made nonrectangular by reducing its separation from the primary from 0.5 to 0.25 m over one-half of its depth in the z direction.

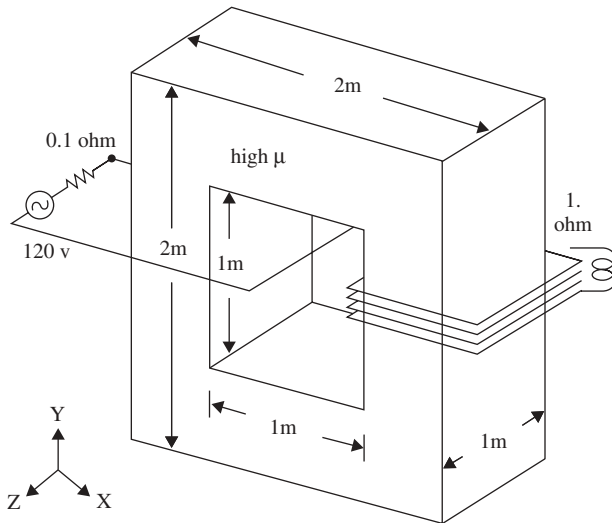


Figure E14.1.1 Transformer of Example 14.1.

Solution: The AC methods of this chapter have been used [6] to obtain the results listed in Table E14.1.1. For case (a), the currents in the row with relative permeability 1.E5 were computed, along with the flux line plot shown in Fig. E14.1.2 with the visible 3D, 1D, and 0D finite elements. Note that the computed primary current I_1 and secondary current I_2 agree closely with those of an ideal transformer listed in the top row of Table E14.1.1, which have a ratio exactly equal to their turns ratio.

For cases (b) and (c), the computed currents are listed in the bottom two rows of Table E14.1.1. As expected, lowering the permeability causes the primary current to rise and the secondary current to fall. However, note that the closer coupling of the two windings of case (c) causes a slight decrease in primary current and increase in secondary current. The flux line plot of case (c) is shown in Fig. E14.1.3, showing the shift in the secondary flux lines.

Example 14.2 Nonlinear Transformer Waveforms with Impedance Loading Its Secondary The transformer of Example 14.1 is now made of nonlinear steel with conductivity 1 S/m. The secondary and primary impedances remain as in Fig. E14.1.1, but the primary voltage is changed from a sinusoid to the triangular waveform shown in Fig. E14.2.1 of period 16 ms with 1200 V peak. This large voltage produces saturation, and the steel is assumed to have the B - H curve listed elsewhere [2]. The waveforms of steel flux density and secondary current are to be computed during two periods after the primary voltage is applied.

Solution: The nonlinear transient methods of this chapter were used [6] to obtain the waveforms shown in Figs. E14.2.2 and E14.2.3. Note that the flux density waveform is “clipped” at approximately 1.5 T as a result of saturation, as one might expect. Because the secondary voltage and current are proportional to the time derivative of flux density according to Faraday’s law, the current waveform is “peaked.” Thus saturation effects are fully computed, including the losses in the steel [6].

14.3 STRUCTURAL FINITE-ELEMENT MATRIX EQUATION

To allow motion of the armatures of magnetic actuators and sensors, some of the electromagnetic finite elements shown in Fig. 14.1 must be allowed to move. The simplest type of motion is *rigid-body motion*, and it can be modeled by placing

TABLE E14.1.1 Calculated Transformer Current Magnitudes.

Core μ_r	Secondary Coil	I_1 (A)	I_2 (A)
Infinity	Ideal	738.4	184.6
1.E5	Rectangle	738.5	184.6
500	Rectangle	1099.1	93.5
500	3D, closer	1098.9	93.6

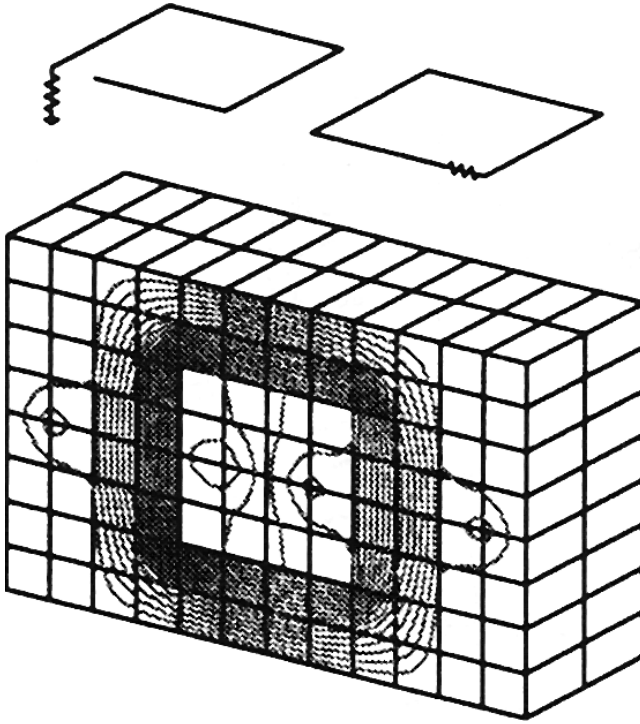


Figure E14.1.2 Computer display of finite-element model and computed flux lines for Example 14.1 case (a).

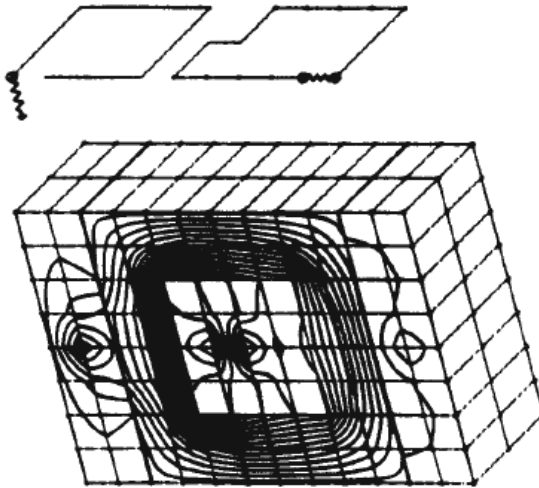


Figure E14.1.3 Computer display of finite-element model and computed flux lines for Example 14.1 case (c).

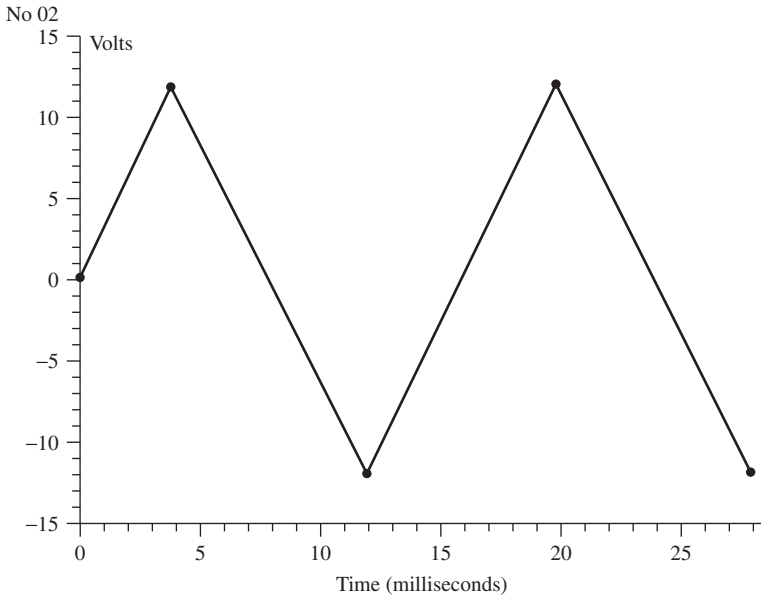


Figure E14.2.1 Applied primary voltage waveform for Example 14.2.

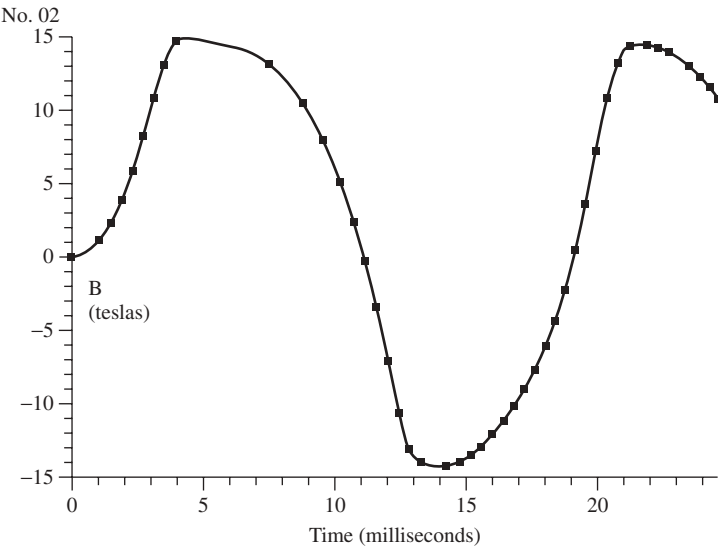


Figure E14.2.2 Computed flux density in transformer steel core of Example 14.2.

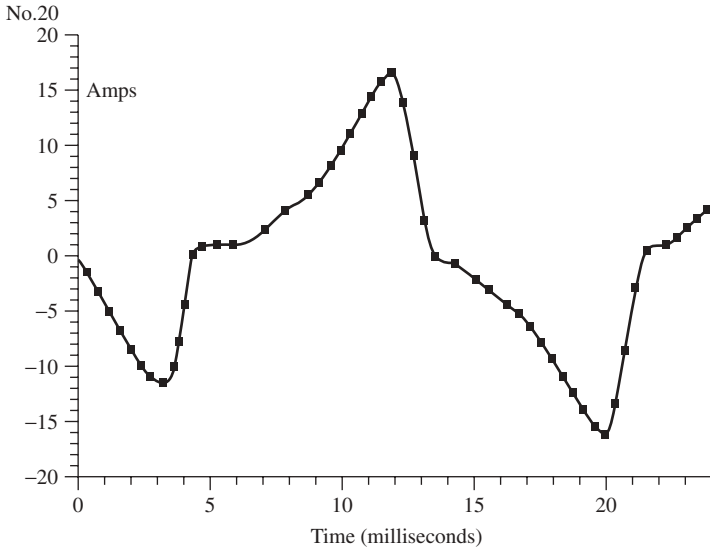


Figure E14.2.3 Computed secondary current waveform for Example 14.2.

moving surfaces around 3D armatures. By including rigid-body motion in finite element eddy current solvers, various types of moving electromechanical devices have been analyzed [8]. Such finite-element software computes the effects of rigid-body motion on eddy currents and transient electromechanical performance.

To allow non-rigid-body motion, that is, deformations and stresses, structural finite elements can be used. Structural finite-element analysis is very commonly used to compute mechanical stresses and other mechanical parameters. The method, available in several commercial software packages, usually solves first for mechanical displacements (deformations), from which the stresses are then obtained.

The 3D structural finite-element formulation described here is based on three matrices: $[K_S]$, $[B_S]$, and $[M_S]$. They appear in the structural finite-element equation [2]

$$[M_S]\{\ddot{u}_S\} + [B_S]\{\dot{u}_S\} + [K_S]\{u_S\} = \{F_S(t)\} \quad (14.12)$$

where $[K_S]$ is the mechanical stiffness matrix mentioned in Chapter 4 and is produced by springs and other elastic structures. Also, $[B_S]$ is the damping matrix due to friction and other power losses, and $[M_S]$ is the mass matrix. All three matrices are common to magnetic actuators and sensors. The matrices are assembled element by element, where various structural elements are available [2,7]. The Appendix includes symbols, dimensions, and units of mechanics.

The unknown structural vector $\{u_S\}$ in (14.12) contains components at each finite element node

$$\{u_S\} = \begin{bmatrix} u_1 \\ u_2 \\ u_3 \end{bmatrix} \quad (14.13)$$

where the three components of translation \mathbf{u} in many cases are x , y , and z components, but may also be in other coordinate systems.

The right-hand side of (14.12) is the structural excitation vector, consisting of the applied forces at nodes. The forces may be produced by electromagnetic fields as described in Chapter 5.

Note that the structural equation (14.12) is directly analogous to the electromagnetic equation (14.1). Both include an $[M]$ matrix times the second time derivative (indicated by the double dot) of $\{u\}$ and a $[B]$ matrix times the first time derivative (indicated by the single dot) of $\{u\}$. They both also include a $[K]$ matrix times $\{u\}$. Because of their time derivatives, (14.1) and (14.12) can solve both static and dynamic (time-varying) problems.

14.4 FORCE AND MOTION COMPUTATION BY TIMESTEPPING

Coupled electromechanical problems can be solved in the time domain by solving both (14.1) and (14.12) at each timestep [9]. The two equations are coupled at each timestep through their right-hand-side excitation vectors. The electromagnetic excitation vector has additional terms due to motion. All finite elements can have both electromagnetic and structural material properties.

The Maxwell stress tensor is used to compute the distributed structural force produced by electromagnetic fields at surface nodes. Chapter 5 presented the component of Maxwell stress normal to a surface; the complete nonlinear stress tensor $[\tau]$ for all pressure components relates pressure and direction \mathbf{n} according to [10]

$$\{P\} = [\tau]\{n\} \quad (14.14)$$

$$\begin{bmatrix} P_x \\ P_y \\ P_z \end{bmatrix} = \begin{pmatrix} B_x H_x - w_m & B_x H_y & B_x H_z \\ B_y H_x & B_y H_y - w_m & B_y H_z \\ B_z H_x & B_z H_y & B_z H_z - w_m \end{pmatrix} \begin{bmatrix} n_x \\ n_y \\ n_z \end{bmatrix} \quad (14.15)$$

where w_m is linear or nonlinear magnetic energy density as in Chapter 5 and n_x , n_y , and n_z are components of the unit vector \mathbf{n} normal to the surface. Integrating the pressure in (14.14) and (14.15) over a closed surface s gives the force component F_{Si} in the direction i [10]:

$$F_{Si} = \oint (\tau_{ij} n_j) ds \quad (14.16)$$

Thus

$$\frac{F_{Si}}{s} = P_i \tau_{ij} n_j \quad (14.17)$$

Substituting (14.15) gives the pressure in terms of normal N and tangent T components of the magnetic fields [10]:

$$P_N = B_N H_N - w_m; \quad P_T = B_T |H_N| \quad (14.18)$$

As shown in Fig. 14.2 [10], there are two ways of computing magnetic force on an object. The first method is to completely surround the object with the surface, such as the armature of a magnetic actuator. This one-sided integration method provides the total force on the armature, but not its distribution. The second method is to place multiple integration surfaces encompassing both steel and air sides of all finite elements on the armature surface. As these integration regions are collapsed to the armature surface, they perform two-sided integrations along the armature face. Because of the higher \mathbf{H} field and magnetic energy density in air, the force on steel and other high-permeability materials is outward. Also, if steel has regions of varying saturation, the two-sided integrations can be carried out at finite-element interfaces within the steel. Thus the two-sided method computes the *distribution* of force, which is helpful in understanding actuator behavior and is essential in obtaining mechanical stresses.

As the motion proceeds, nodes can move. In the examples given below, air is modeled with a very low modulus of elasticity of 1 Pa, which produces very small

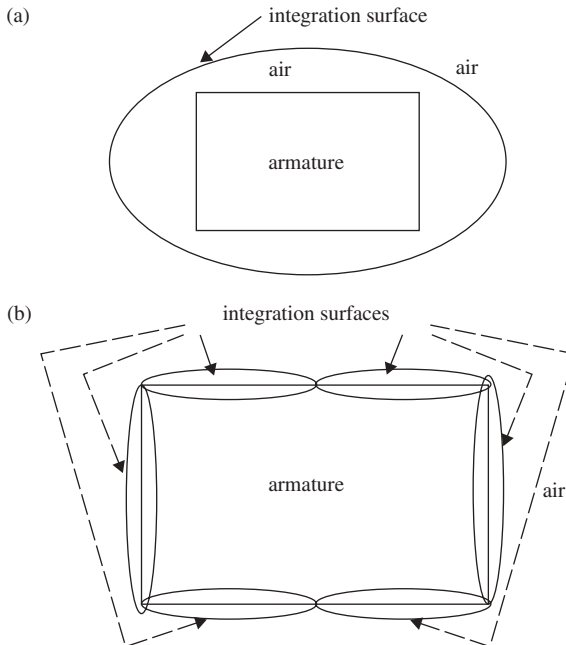


Figure 14.2 Integration surfaces for Maxwell stress tensor computation. (a) one-sided integration; (b) two-sided integration.

contributions to the $[K_s]$ matrix. Thus the air elements easily collapse or expand as motion occurs. If the motion is very large, then some air elements may become very distorted, which reduces their accuracy. For large motion, it may be necessary to not only move nodes but also reconnect the nodes through new finite elements.

14.5 TYPICAL ELECTROMECHANICAL APPLICATIONS

In the examples below the motion is small enough that no element reconnection is required. All results are obtained by timestepping using both nonlinear electromagnetic and structural finite elements. All eddy current effects, including motional EMFs, are included in the solutions. While air is rarely modeled in structural finite-element analysis, air finite elements are required here for electromagnetic fields and also appear in the structural finite-element model. The key parameter usually needed for magnetic actuators and sensors is response time, which is computed as follows by electromagnetic and structural finite elements.

14.5.1 DC Solenoid with Slowly Rising Input Current

The Bessho DC axisymmetric plunger solenoid actuator of Fig. 5.2 has been studied in Chapters 5, 7, 9, and 12. As mentioned in Chapter 12, its time constant is 20 ms according to the original paper by Bessho et al. [11]. The current waveform applied in the Bessho experimental tests obeys

$$I(t) = I_{DC}(1 - e^{-t/0.020}) \quad (14.19)$$

where the final current I_{DC} is 0.5 A during the experimental tests.

To compute the motion of this actuator, the finite-element model shown in Fig. 14.3 is made with all elements having both electromagnetic and structural properties [9]. The steel finite elements are given a modulus of elasticity of 200.E9 Pa and Poisson's ratio of 0.265, as typical for many steels [2]. As mentioned previously, the electromagnetic steel elements have nonlinear B - H curves and electrical conductivity of 1.7E6 S/m. The air finite elements are given a structural modulus of elasticity of 1 pascal. Initial airgaps are set to match the experimental tests at 10, 15, and 20 mm. As set in the experiments, the total moveable mass is 6 kg.

The computed position of the armature versus time is shown in Fig. 14.4 for all three initial airgaps [9]. Also shown in Fig. 14.4 are the corresponding measured position curves. Note that computations and measurements agree quite well. The largest disagreement is for the 20-mm airgap, which produces the greatest node motion and element distortion. Note that the time to close, often the most important parameter for magnetic actuators, is accurately predicted by the coupled finite-element analysis.

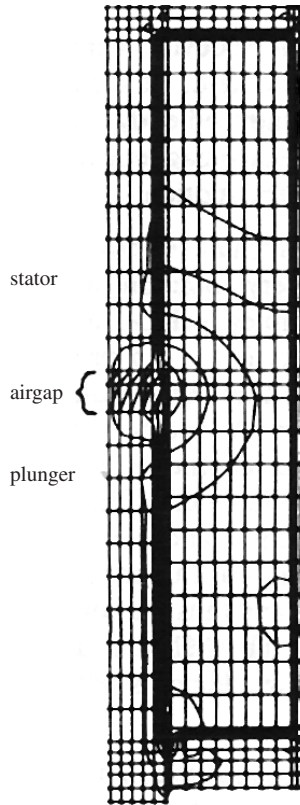


Figure 14.3 Computer display of coupled electromagnetic and structural finite-element model of Bessho magnetic actuator with applied current. The computed flux lines are shown at 5 ms for the 15-mm airgap.

14.5.2 DC Solenoid with Step Input Voltage

Like most DC actuators, the Bessho solenoid is most likely to be excited by a DC voltage step. As mentioned in Chapter 12, the time constant of the Bessho solenoid of 20 ms is unchanged even if its number of turns is changed. However, it is important to note that the current waveform of (14.19) is based on conventional LR circuit theory and does not include the effects of motional EMF. As we shall see, when a voltage is applied, *motion effects can change the current waveform and thus change the actuator response time.*

To apply a voltage, 0D and 1D finite elements are added to Fig. 14.3, producing the finite-element model shown in Fig. 14.5 [12]. The 0D element is a resistor of value $200\ \Omega$, and it is driven by a step voltage source of 100 V. The final DC current is $100\ \text{V}/200\ \Omega = 0.5$ ampere, the desired value. The initial airgap is assumed to be 10 mm.

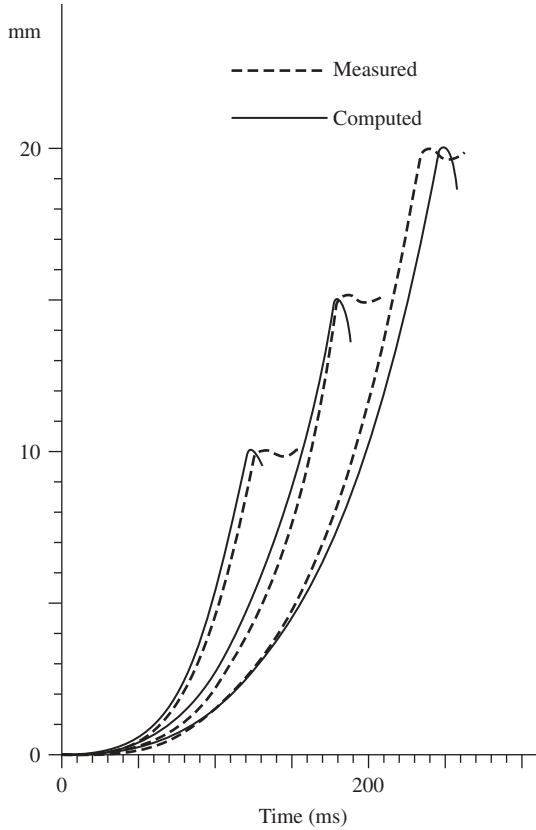


Figure 14.4 Displacement of armature versus time for initial airgaps of 10, 15, and 20 mm. All curves are for the applied current waveform of (14.19) with 0.5 A DC and total moving mass of 6 kg.

The computed current versus time is shown in Fig. 14.6 [12]. Note that for times less than 40 ms, the current increases exponentially with a time constant of approximately 20 ms as in (17). However, from approximately 40 to 120 ms, the current *decreases* as a result of the motional voltage produced by the moving armature. The computed armature position versus time is approximately the same as the 10 mm curve in Fig. 14.4, which shows substantial motion beginning at approximately 40 ms. At approximately 117 ms, the armature reaches closure, and thus at that time the current of Fig. 14.6 dips to a minimum. Beyond that time, the current rises again, but with a different slope than before, because L has changed with armature position. The current dip at closure is sometimes used to sense closure.

The above computations are for measured steel conductivity of $1.7\text{E}6$ S/m. To examine the effects of conductivity on actuator speed, conductivity σ was varied as listed in Table 14.1. Besides varying σ from 0 to $10.\text{E}6$ S/m, four different cases are

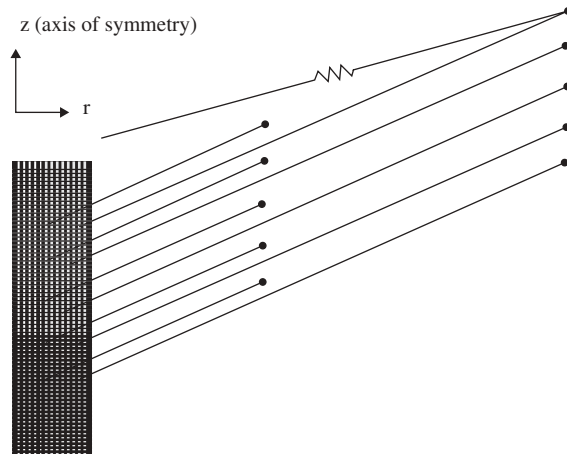


Figure 14.5 Coupled electromagnetic and structural finite-element model of Bessho magnetic actuator with applied voltage. Note that the circuit is distributed over 10 points within the coil area.

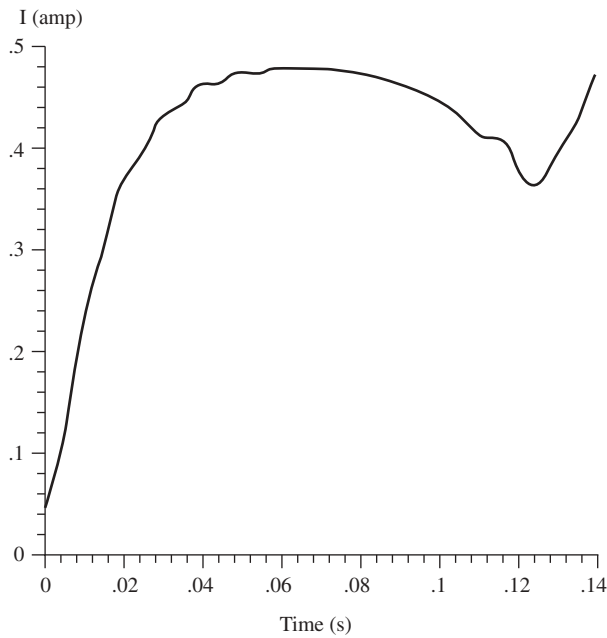


Figure 14.6 Computed current versus time for Bessho actuator with applied step voltage.

TABLE 14.1 Closing Times (ms)^a Computed Using Electromechanical Finite Elements for Various Step Excitations of V or I , Conductivities σ , and Mechanical Parameters

Case	$\sigma = 0$	%	$\sigma = 1.7\text{E}6$	%	$\sigma = 5\text{E}6$	%	$\sigma = 10\text{E}6$	%
1. V , 6 kg	115	0	<u>117</u>	<u>1.7</u>	121	5.2	126	9.6
2. V , 1.4 kg	67	0	<u>72</u>	<u>7.5</u>	75	11.9	80	19.4
3. I , 1.4 kg	46	0	<u>51</u>	<u>10.9</u>	56	21.7	62	34.8
4. I , 1.4 kg, spring	49	0	<u>54</u>	<u>10.2</u>	61	24.5	67	36.7

^aThe percentage changes in closing times due to eddy currents are computed, with Bessho's baseline case underlined.

examined in the table. Case 1 is the voltage step examined in Fig. 14.6; it shows that varying conductivity varies closing time by only ~ 11 ms. In case 2, the moving mass is lowered to the armature mass only, which is 1.4 kg. In case 3, the 0.5-A current is input as a step at time zero, producing the fastest closing times, especially for zero conductivity. Finally, in case 4 a small opposing spring of 1500 N/m is added, typical of relay spring forces [13].

14.5.3 AC Clapper Solenoid Motion and Stress

The Eaton 60-Hz AC clapper solenoid actuator of Figs. 4.3 and 8.4 can be analyzed using coupled nonlinear electromagnetic and structural finite elements. The spring in Fig. 4.3 is made up of multiple steel coils and relay leaves, which interact to produce the nonlinear spring force–position curve shown in Fig. 14.7. When the armature is in the open position with the 5.97 mm airgap of Fig. 4.3, the spring is partially compressed to produce a preload of 2.55 N. The slope of Fig. 14.7, called K_{snl} ,

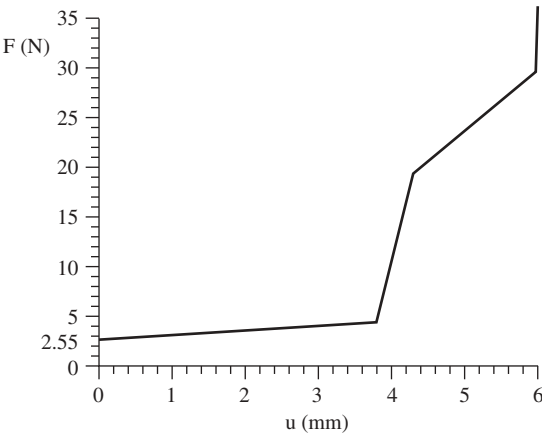


Figure 14.7 Measured nonlinear spring curve of actuator spring and relay of Eaton AC actuator.

varies from as low as 443 N/m to as high as 3.E4 N/m. When the airgap is closed at 5.97 mm, the slope in Fig. 14.7 becomes very high to prevent further motion. Springs are very commonly employed in magnetic actuators to provide return force. Examples (other than the Eaton clapper actuator) include *reciprocating magnetic actuators*. They produce repeated back-and-forth motion by alternately supplying coil current to provide magnetic force and motion in one direction, and removing the coil current to allow the spring to move the armature back. Doorbells are a common example.

The nonlinear spring K_{snl} is included in the coupled finite-element model shown in Fig. 14.8. Just as for the Bessho actuator, the total moving mass M_T is somewhat greater than simply the mass of the magnetic armature. Thus the mass density ρ of the armature structural finite elements is set to M_T divided by the armature volume. The steel 2D finite elements have the same structural properties as in the Bessho actuator, with modulus of elasticity 2.E11 Pa, and Poisson's ratio of 0.265.

The electromagnetic finite-element model is also shown in Fig. 14.8, and consists of 0D, 1D, and 2D finite elements. The 2D finite elements model the nonlinear steel, the air, the coil area, and the aluminum shading ring. To account for 3D end resistance of the shading ring, the aluminum conductivity is reduced somewhat [14]. Figure 14.8 also contains six 1D line finite elements modeling the coil, which are attached to 0D finite elements modeling the coil R and end turn inductance L_{end} .

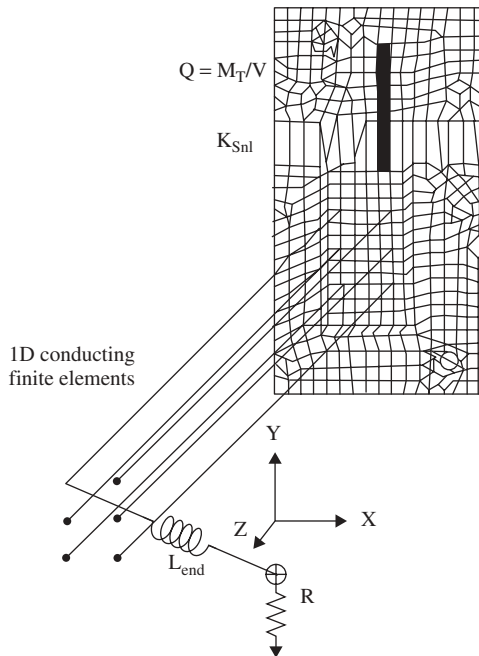


Figure 14.8 Coupled finite-element model of right half of Eaton AC actuator.

The end turn inductance computed using 3D finite elements is 23 mH [14]; adding it to the 2D model of Fig. 14.8 ensures accurate results with minimal computer time. The model of Fig. 14.8 ignores AC hysteresis losses in the steel, but if they are significant, they can be included [15].

The time required for closure of AC actuators depends on the instant within the AC cycle that the voltage is applied. Here the voltage applied at time zero is assumed to be zero and to rise thereafter as a sine wave. The resulting computed current versus time is shown in Fig. 14.9. The measured current is also shown and agrees reasonably well.

The computed armature displacement versus time is shown in Fig. 14.10. The leftmost curve represents an armature density ρ equal to 0.22 kg divided by the model armature volume v . However, it was realized later that the potentiometer used to trace the measured curve in Fig. 14.10 added to the moving mass and produces $M_T = 0.267$ kg. Increasing the armature density accordingly yields the rightmost curve in Fig. 14.10, which agrees very closely with the measured curve. It should be noted that the force of gravity is also included in Fig. 14.10 because the actuator is mounted vertically. Both the computed and measured closure times in Fig. 14.10 are 16.0 ms. In certain AC applications, closure times can be reduced using mechanical resonance [16].

Besides computing the electrical and mechanical responses of Figs. 14.9 and 14.10, the coupled finite-element analysis also obtains mechanical stresses. A common parameter for stress is Von Mises equivalent stress [2], which is plotted for the armature in Fig. 14.11. The stress varies with time and with assumed spring position. The maximum stress in Fig. 14.11 is 943 kPa, which is too low to cause yield or other mechanical failure of most steels. However, improper placement of bolt holes might increase the stresses and produce mechanical failure. Hence computed stress distributions can be very valuable to design engineers [17].

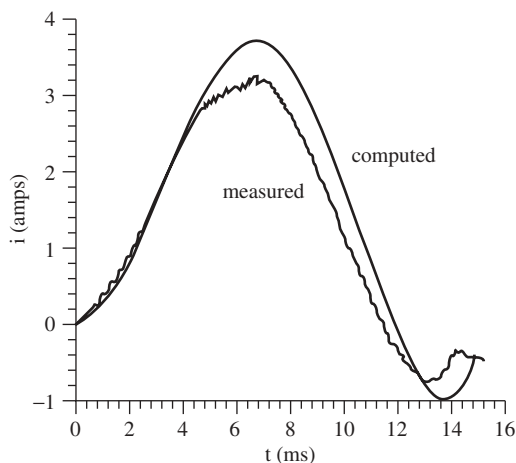


Figure 14.9 Coil current waveform of Eaton AC actuator.

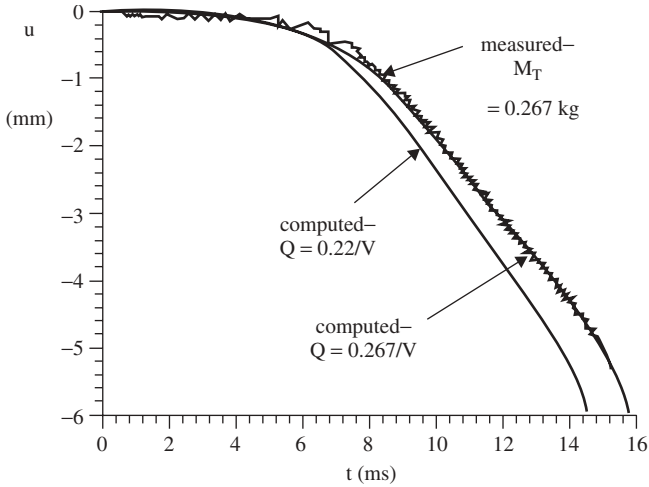


Figure 14.10 Position versus time for Eaton AC actuator mounted vertically.

Since the stresses and strains of the steel armature are quite small, its deformations are also small, only a few micrometers at most. However, armatures of magnetic actuators are sometimes purposely made of flexible material that deforms greatly during actuation. Examples of flexible armatures are common in *magnetic switches*, including flexible reeds in *reed switches* used as relays and sensors

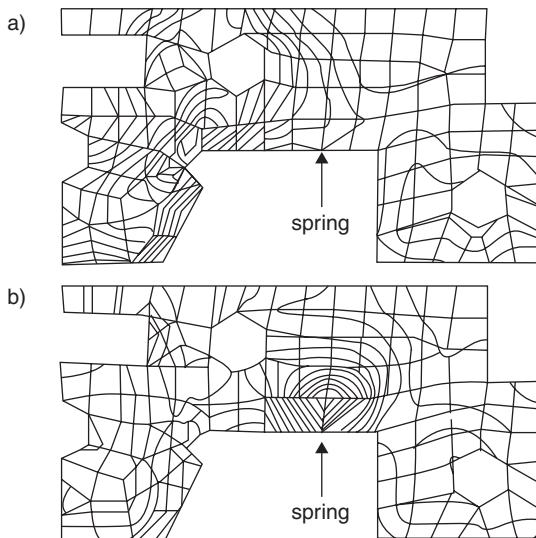


Figure 14.11 Eaton armature finite elements and stress contours (also available in color): (a) at $t = 15.6$ ms, maximum = 943 kPa; (b) at $t = 12$ ms, maximum = 26 kPa.

[18,19], and flexible ferrite rubber permanent magnets used to latch pushbutton switches [20].

14.5.4 Transformers with Switches or Sensors

Magnetic actuators and sensors are often driven by electronic circuits, which usually require nonlinear modeling. The simplest type of nonlinear behavior is a switch. An ideal open switch has zero current, but its voltage drop is unknown. An ideal closed switch has zero voltage, but its current is unknown.

A switch is thus a time-varying resistor, which can be modeled using 1D coupled electromagnetic and structural finite elements [21,22]. The 1D finite element in Fig. 14.12 is a typical variable resistor. It behaves as a line electromagnetic finite element of Fig. 14.1 and also as a 1D structural rod element. To vary the resistance, the line is stretched by applying a mechanical force that varies with time. For example, if the line has a conductivity of 1 siemen per meter and initial length of 1 cm, then its resistance is only $0.01\ \Omega$ initially. Applying a large force to stretch the line length to 1 km, its resistance increases to $1\ \text{k}\Omega$.

Such a switch is attached to the transformer secondary shown in Fig. 14.13. Its primary is excited by a 50 Hz triangular wave. If the switch is always closed, the $86\text{-m}\Omega$ secondary resistor has the computed voltage shown in Fig. 14.14 over time ranging from 0 to 25 ms. If the switch is opened, however, from time 15 to 20 ms, the secondary current is zero during that period but shows an inductive “kick” when reclosed in Fig. 14.15.

Such variable-resistance models can be useful for modeling electronically controlled actuators and sensors. For example, the LVDTs of Chapter 11 can have varying load impedances, and the magnetoresistive sensors of Chapter 10 typically behave as time-varying resistors.

PROBLEMS

- 14.1** The transformer of Example 14.1 can also be analyzed using its equivalent electric circuit. As discussed in Chapter 8, a coil with losses is equivalent to a resistor in parallel with an inductor. From Chapter 5, the parallel magnetizing

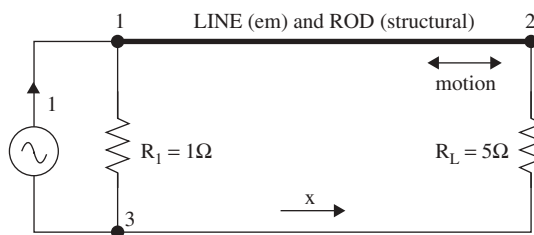


Figure 14.12 Time-varying resistor.

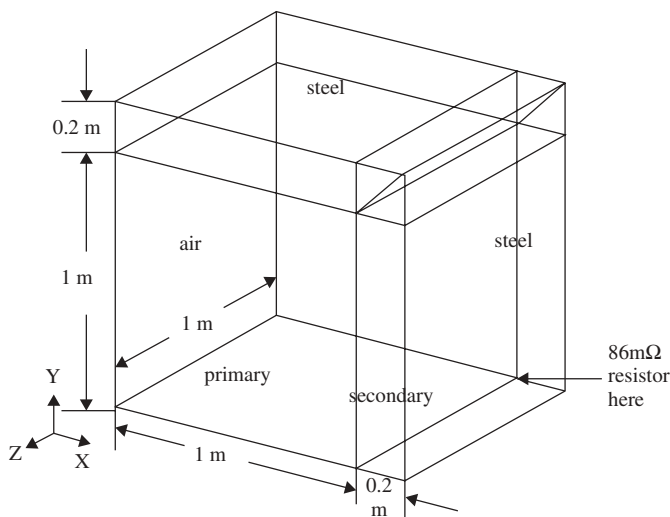


Figure 14.13 Transformer with secondary 86-mΩ resistor that may be switched in or out. One-quarter of the transformer is shown, with its primary and secondary coils modeled by 1D line finite elements.

inductor equals the square of the primary turns divided by the reluctance. The secondary resistor must be referred to the primary according to ideal transformer theory. Calculate the reluctance for relative steel permeability of 1.E5 and the resulting magnetizing inductor. Then use the inductor to calculate the currents and compare them with the finite-element computations of case (a).

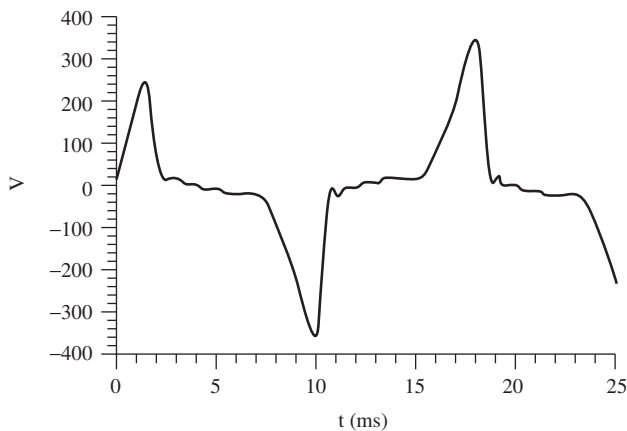


Figure 14.14 Computed secondary resistor voltage for transformer of Fig. 14.13 when secondary switch is always closed.

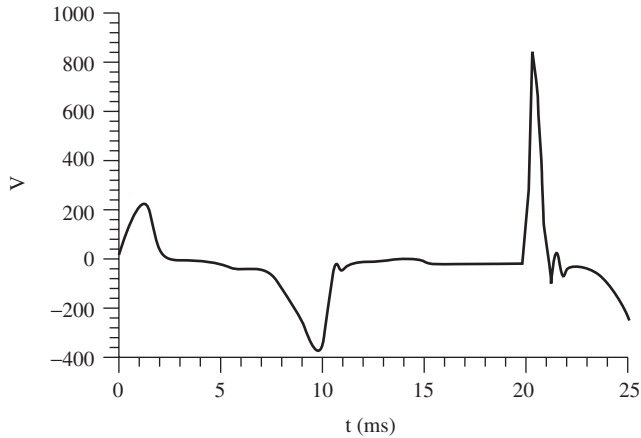


Figure 14.15 Computed secondary voltage for transformer of Fig. 14.13 when secondary switch is closed except during time from 15 to 20 ms.

14.2 Extend Problem 14.1 for case (b) of Example 14.1; that is, let the steel relative permeability be 500 and compare your calculated currents with the finite-element computations of case (b).

REFERENCES

1. B. E. MacNeal, J. R. Brauer, and R. N. Coppolino, A general finite element vector potential formulation of electromagnetics using a time-integrated electric scalar potential, *IEEE Trans. Magn.* **26**: 1768–1770 (Sept. 1990).
2. J. R. Brauer, ed., *What Every Engineer Should Know about Finite Element Analysis*, 2nd ed., Marcel Dekker, New York, 1993, Chapter 5, Electromagnetic analysis, by J. R. Brauer; Chapter 3, Structural analysis, by V. D. Overbye.
3. P. Zhou, W. N. Fu, D. Lin, S. Stanton, and Z. J. Cendes, Numerical modeling of magnetic devices, *IEEE Trans. Magn.* **40**: 1803–1809 (July 2004).
4. J. R. Brauer, S. M. Schaeffer, J.-F. Lee, and R. Mittra, Asymptotic boundary condition for three dimensional magnetostatic finite elements, *IEEE Trans. Magn.* **27**: 5013–5015 (Nov. 1991).
5. J. R. Brauer, R. Mittra, and J.-F. Lee, Absorbing boundary condition for vector and scalar potentials arising in electromagnetic finite element analysis in frequency and time domains, *Proc. IEEE Antenna and Propagation Society Symp.*, July 1992, pp. 1224–1227.
6. J. R. Brauer, B. E. MacNeal, and F. Hirtenfelder, New constraint technique for 3D finite element analysis of multiturn windings with attached circuits, *IEEE Trans. Magn.* **29**: 2446–2448 (Nov. 1993).
7. R. H. MacNeal, *Finite Elements: Their Design and Performance*, Marcel Dekker, New York, 1994.

8. P. Zhou, S. Stanton, and Z. J. Cendes, Dynamic modeling of electric machines, *Proc. Naval Symp. Electrical Machines*, Annapolis, MD, Oct. 26–29, 1998, pp. 43–49.
9. J. R. Brauer and J. J. Ruehl, 3D coupled nonlinear electromagnetic and structural finite element analysis of motional eddy current problems, *IEEE Trans. Magn.* **30**: 3288–3291 (Sept. 1994).
10. J. R. Brauer, J. J. Ruehl, M. A. Juds, M. J. VanderHeiden, and A. A. Arkadan, Dynamic stress in magnetic actuator computed by coupled structural and electromagnetic finite elements, *IEEE Trans. Magn.* **32**: 1046–1049 (May 1996).
11. K. Bessho, S. Yamada, and Y. Kanamura, Analysis of transient characteristics of plunger type electromagnets, *Electric. Eng. Japan* **98**: 56–62 (July 1978).
12. J. R. Brauer, J. J. Ruehl, and F. Hirtenfelder, Coupled nonlinear electromagnetic and structural finite element analysis of an actuator excited by an electric circuit, *IEEE Trans. Magn.* **31**: 1861–1864 (May 1995).
13. J. R. Brauer and Q. M. Chen, Alternative dynamic electromechanical models of magnetic actuators containing eddy currents, *IEEE Trans. Magn.* **36**: 1333–1336 (July 2000).
14. M. A. Juds and J. R. Brauer, AC contactor motion computed with coupled electromagnetic and structural finite elements, *IEEE Trans. Magn.* **31**: 3575–3577 (Nov. 1995).
15. O. Bottauscio, M. Chiampi, and A. Manzin, Advanced model for dynamic analysis of electromechanical devices, *IEEE Trans. Magn.* **41**: 36–46 (Jan. 2005).
16. M.-T. Peng and T. J. Flack, Numerical analysis of the coupled circuit and cooling holes for an electromagnetic shaker, *IEEE Trans. Magn.* **41**: 47–54 (Jan. 2005).
17. V. Overbye, J. Brauer, and P. Bodine, *Blazing Trails—Finite Element Pioneers in Milwaukee*, Writers Club Press of iUniverse, Inc., Lincoln, NE, 2002.
18. Reed switch basics, *Machine Design* 48 (May 6, 2004).
19. T. Ota et al., Dynamic response analysis of opening and closing sensor for windows, *IEEE Trans. Magn.* **41**: 1604–1607 (May 2005).
20. T. Van Zeeland, Magnets in switch design, *Magn. Bus. Technol.* 22–23 (Fall 2004).
21. J. R. Brauer and J. J. Ruehl, Finite element modeling of power electronic circuits containing switches attached to saturable magnetic components, *IEEE Trans. Energy Convers.* **14**: 589–594 (Sept. 1999).
22. J. R. Brauer, Time-varying resistors, capacitors, and inductors in nonlinear transient finite element models, *IEEE Trans. Magn.* **34**: 3086–3089 (Sept. 1998).

Electromechanical Analysis Using Systems Models

While the finite-element techniques of the preceding chapter accurately predict electromechanical behavior of magnetic devices, many engineers need *systems models* instead. Magnetic actuators and sensors are often components in large electromechanical systems such as automobiles, airplanes, power systems, and computers. Design of such systems is carried out nowadays using systems software such as SPICE, MATLAB, and Simplorer. Hence this chapter discusses how magnetic actuators and sensors can be modeled with such systems software.

15.1 ELECTRIC CIRCUIT MODELS OF MAGNETIC DEVICES

15.1.1 Electric Circuit Software Including SPICE

Since most magnetic devices are connected to electric circuits, electric circuit simulation software is appropriate. If an equivalent electric circuit can be found for the magnetic device, then it can be inserted in the circuit software. Popular software for modeling electric and electronic circuits includes SPICE, Simplorer, and Multisim. Electric circuits can be used via analogies to also model the magnetic circuits of Chapter 3, heat transfer of Chapter 12, and mechanical motion as described below.

SPICE is one of the most commonly used electric and electronic circuit simulators. It was originally developed in the early 1970s [1] at the University of California—Berkeley, which has published several SPICE versions in the public domain. Commercial versions include PSPICE, HSPICE, and Maxwell SPICE. SPICE models have been developed over the years for many electronic circuits and magnetic devices.

15.1.2 Simple LR Circuits

As discussed in earlier chapters such as Chapter 9, magnetic devices have an equivalent electric circuit that contains at least one inductance L . Any coil has a resistance R , usually placed in series with L . However, the inductance may be nonlinear, and thus represented as flux linkage versus current. In addition, as the armature moves, the inductance and flux linkage may vary significantly with position.

Example 15.1 SPICE LR Model of Axisymmetric Clapper Actuator The DC axisymmetric clapper armature actuator of Fig. E7.2.1 is to be modeled in very simple fashion as an LR circuit at the modeled airgap of 2 mm. The coil resistance is 10 Ω . Eddy current losses are to be ignored. The number of turns is 2000. Prepare a SPICE circuit model and use it to find the current as a function of time for 1 s after a 12-V step is applied.

Solution: The total energy stored W in Example 7.2 is 0.8604 J for 2000 ampere-turns. Since the number of turns is 2000, the current $I = 1$ A. The inductance is then

$$L = 2W/I^2 = 1.7208 \text{ H} \quad (\text{E15.1.1})$$

The SPICE circuit model consists of the 1.7208-H inductor in series with the 10 Ω coil resistance, along with a 12-V source turned on at time zero. The circuit developed in Maxwell SPICE is shown in Fig. E15.1.1. The computed current versus time is shown in Fig. E15.1.2, and shows the expected exponential rise with time constant $L/R = 0.17208$ s.

Example 15.2 Including a Speed Voltage in Example 15.1 The LR circuit described above is to be modified by including a speed “back” voltage for $t = 0$ –0.8 s:

$$V_{\text{speed}} = 10t^2 \quad (\text{E15.2.1})$$

After $t = 0.8$ s the armature stops moving, and thus the voltage becomes zero. The inductance is assumed to be unchanged from Example 15.1 even though the armature position is changing.

Solution: A voltage source is added to the SPICE circuit of Example 15.1, obtaining the circuit shown in Fig. E15.2.1. The new voltage source varies with time according to (E15.2.1). The computed current waveform is shown in Fig. E15.2.2.

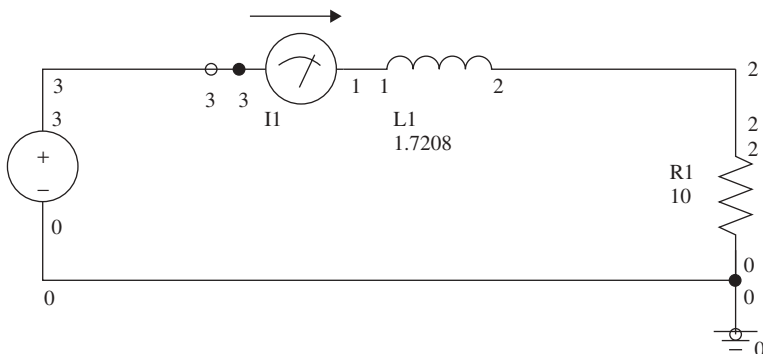


Figure E15.1.1 SPICE circuit series LR circuit for Example 7.2 at a given position.

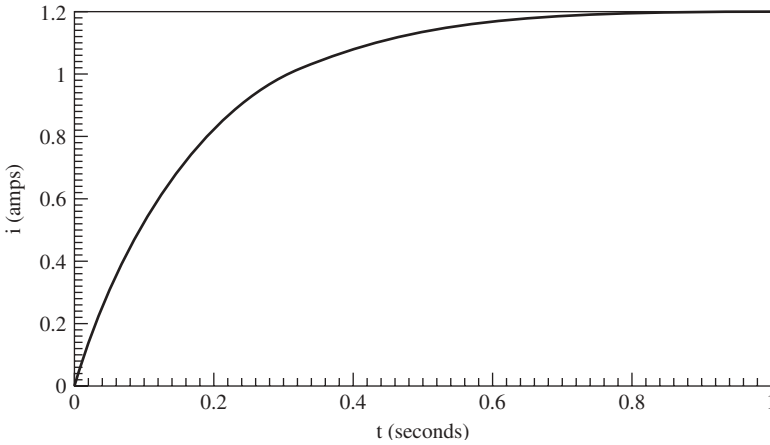


Figure E15.1.2 Current waveform computed by SPICE model of Fig. E15.1.1.

Note that the speed voltage has produced a dip in the current at closure ($t = 0.8$ s), agreeing with the preceding chapter.

15.1.3 Tables of Nonlinear Flux Linkage and Force

In many magnetic actuators and sensors, armature motion causes large changes in flux linkage and inductance. Besides varying with armature position, flux linkage and magnetic force often vary nonlinearly with current because of nonlinear B - H curves. Thus current and position are typically two independent parameters that produce variation in flux linkage and force.

To account for such parametric variations, parametric finite-element analysis can be performed. A table of perhaps 20–100 different rows, each with a different

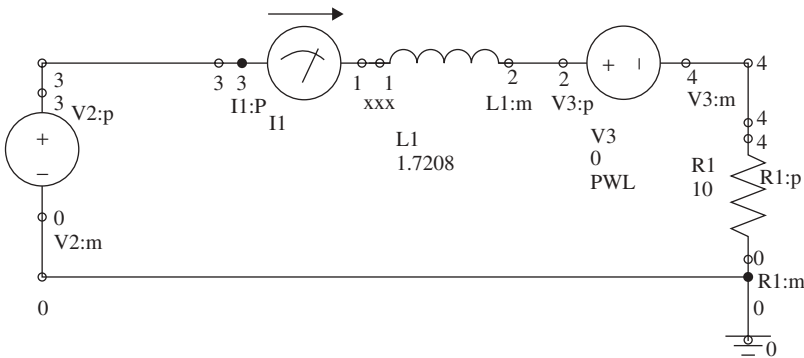


Figure E15.2.1 SPICE circuit series LR circuit of Example 15.1 with added speed voltage.

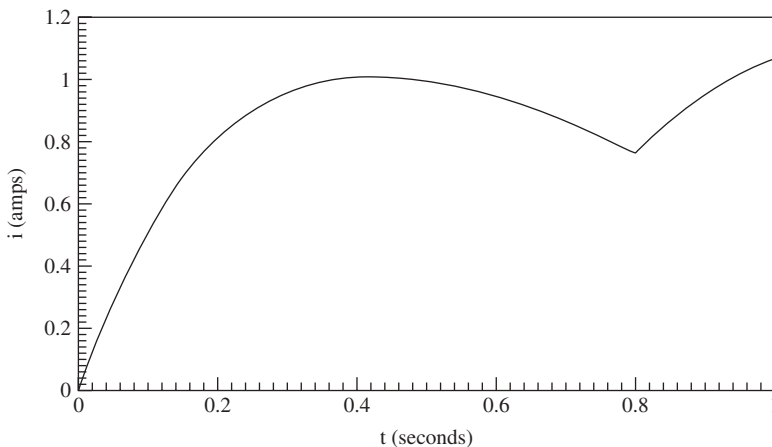


Figure E15.2.2 Current waveform computed by SPICE model of Fig. E15.2.1.

current or position, can be prepared. Magnetostatic finite-element solutions for flux linkage and force can then be obtained for all table rows. Then for any values of current and position within the table range, interpolation can be done to find the related flux linkage and force.

The electrical performance of the magnetic device is directly affected by flux linkage λ according to Faraday's law. Using the standard voltage sign convention for inductors; we obtain

$$V = d\lambda/dt \quad (15.1)$$

Substituting the definition (6.11) for inductance L gives

$$V = \frac{d}{dt}(LI) = L \frac{dI}{dt} + I \frac{dL}{dt} \quad (15.2)$$

The first term can be considered to correspond with Example 15.1, and the second term is the speed voltage included in Example 15.2. Thus the time variation of flux linkage determines the voltage and/or current waveforms versus time.

15.1.4 Analogies for Rigid Armature Motion

The speed and other mechanical performance parameters of the magnetic device are directly affected by the magnetic forces in the parametric table. However, as discussed in Chapter 12, mass and other mechanical parameters also affect the mechanical performance.

The same electric circuit software used to model the electromagnetic behavior of magnetic devices can also be used by analogy to model the mechanical behavior of

rigid armatures. Several analogies are possible. One analogy is based on the mechanical equation (14.10) simplified for a rigid body with one degree of translational freedom x :

$$M_S \frac{d^2x}{dt^2} + B_S \frac{dx}{dt} + K_S x = F_S \quad (15.3)$$

The analogous equation is for an RLC circuit of (14.9) with an additional time derivative taken on both sides:

$$C \frac{d^2V}{dt^2} + \frac{1}{R} \frac{dV}{dt} + \frac{1}{L} V = \frac{dI}{dt} \quad (15.4)$$

Comparing the two analogous equations, the analogy for mass M_S is capacitance C , and other parameters have analogies [2]. Thus SPICE and other electric circuit programs can be used to model rigid-body motion of armatures of magnetic actuators and sensors [2]. Since the armature, stator, and other parts are all assumed to be rigid bodies, their deformations, strains, and stresses are all assumed to be zero.

15.1.5 Maxwell SPICE Model of Bessho Actuator

The Bessho actuator of Chapter 14 and previous chapters is modeled in Maxwell SPICE as shown in Fig. 15.1. The SPICE model was made by exporting parametric tables of flux linkage and force from Maxwell magnetostatic finite-element analyses, represented by the small center icon of the Bessho actuator. The icon produces a speed voltage and a magnetic force. A graph of force versus position for various currents, called pull curves in Chapter 7, is shown in Fig. 15.2. Maxwell SPICE au-

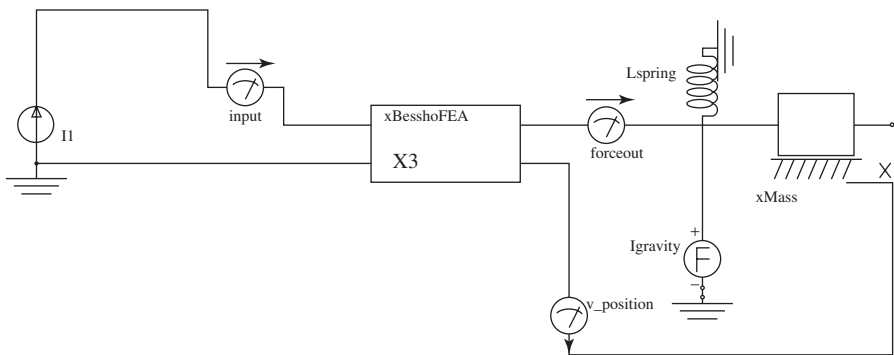


Figure 15.1 SPICE model of Bessho actuator. The electrical drive circuit is at the left (the actuator icon represents nonlinear magnetic flux linkage and force tables); the mechanical circuit is at the right.

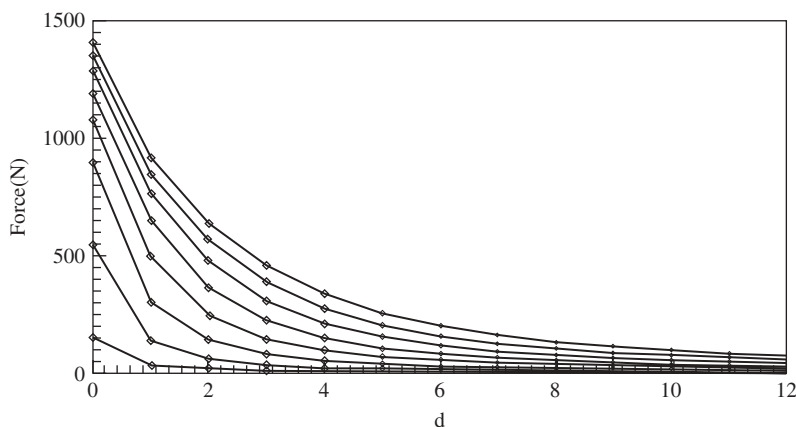


Figure 15.2 Pull curves computed by Maxwell parametric finite-element analysis for air-gap d ranging from 0 to 12 mm and current I ranging from 0 (the bottom zero pull curve along the horizontal axis) to 1.212 A (the top pull curve).

tomatically interpolates to obtain the force for any airgaps from 0 to 12 mm and for any currents from 0 to 1.21 A.

To the left of the Bessho icon is the electric drive circuit, in this case a 0.5-A current source rising with time constant 20 ms as discussed in previous chapters. To the right of the Bessho icon is the SPICE analog of the mechanical system, including a mass and optional spring [3].

The circuit of Fig. 15.1 does not include any eddy current effects in the conducting steel. Thus its results should be comparable to those of Table 14.1 with zero conductivity. The results of Fig. 15.1 computed by SPICE are shown in Fig. 15.3. There are four curves, numbered to correspond with cases 1–4 of Table 14.1. The computed closing times of Fig. 15.3 differ somewhat from those listed in Table 14.1. They agree most closely with the Table 14.1 results for zero conductivity, as they should. The closing times of Fig. 15.3 are reduced by 10–15% from those of Table 14.1, possibly due to different meshes and force computation methods. Also, the SPICE model of Fig. 15.1 does not include any damping B_s or other frictional forces, whereas friction can perceptibly slow down actuator motion.

15.1.6 Simplorer Model of Bessho Actuator

Simplorer[®] is a software package used to design and analyze complex technical systems. Its models can include electric circuit models, models of other physical domains, block diagrams, and state machine structures. One of its languages is SML, the Simplorer Modeling Language. SML is often used to model electro-mechanical systems, and is here used for the Bessho actuator. Simplorer is a much newer program than SPICE, and its timestepping algorithms are more likely to con-

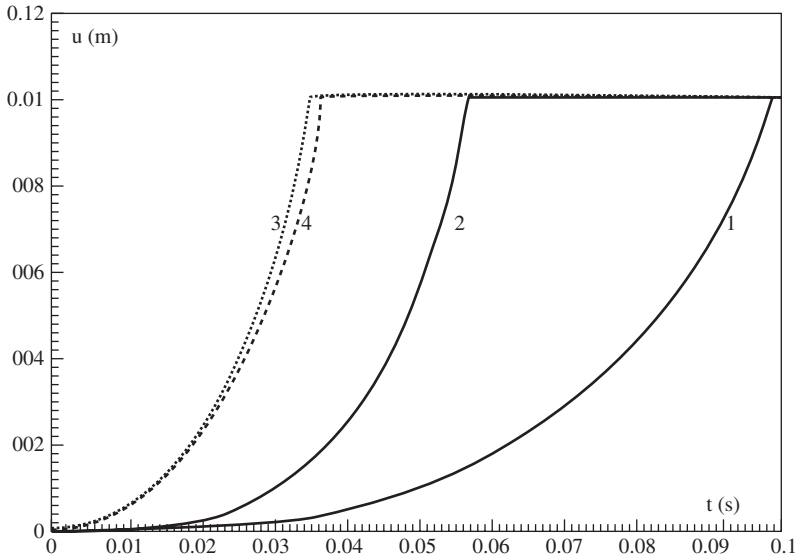


Figure 15.3 Computed SPICE results for Bessho armature position versus time. The four cases are those of Table 14.1 with zero conductivity.

verge properly. Also, Simplorer includes a large number of model libraries, including a sensor library. A free student version is available from Ansoft.

The Simplorer SML model of the Bessho actuator is shown in Fig. 15.4. Similar to the Maxwell SPICE model of Fig. 15.1, it includes an icon of the actuator that represents the Maxwell finite-element model and its flux linkages and forces. To the left of the icon is the electric drive circuit, and to the right is the Simplorer mechanical model.

The Simplorer model was used to predict performance with the 6 kg mass and the 0.5 A input current with 20 ms risetime. The graphs in Fig. 15.5 show that the closure time is 97 ms, almost identical to the SPICE results.

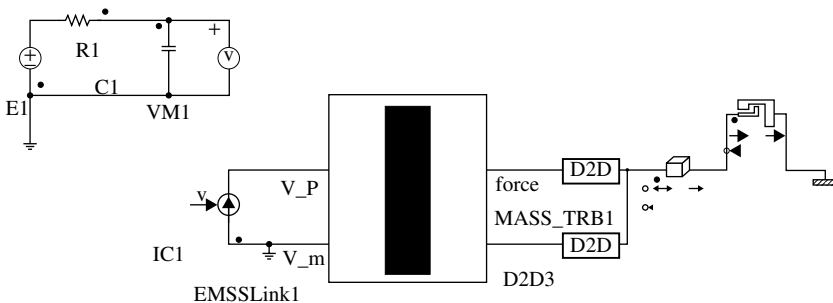


Figure 15.4 Simplorer model of Bessho actuator.

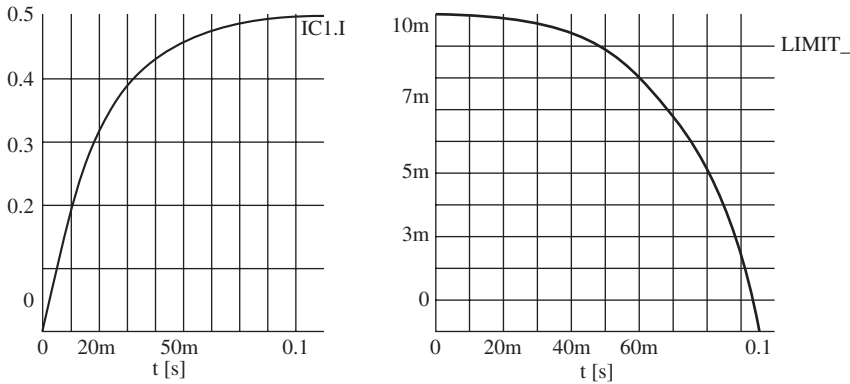


Figure 15.5 Computed Simplorer input and output for Bessho actuator with 6 kg moving mass. The input on the left is the current (in amperes) waveform, and the output on the right is the airgap (in meters) as a function of time (in seconds).

15.2 VHDL-AMS/SIMPLORER MODELS

15.2.1 VHDL-AMS Standard IEEE Language

VHDL-AMS stands for Very high-speed integrated circuit Hardware Description Language–Analog Mixed Signal. It is a standard language used for describing digital, analog, and mixed-signal systems. It is especially popular for automotive electronic system design.

The IEEE standardized the VHDL-1076 language as a Hardware Description Language for digital models. The VHDL standard from 1993 was extended in 1999 for the description of analog and mixed-signal models in the form of the IEEE 1076.1 standard for VHDL-AMS.

A VHDL-AMS model consists of five basic elements: *entity*, *architecture*, *package*, *package body*, and *configuration*. Multidomain systems, such as the electrical and mechanical domains of magnetic actuators and sensors, are specified with the appropriate package entries.

The development and simulation of VHDL-AMS models is supported by Simplorer. It contains wizards, importers, exporters, schematics, netlists, digital stimuli, and other VHDL-AMS modeling capabilities. The Simplorer graphical interface contains common basic VHDL-AMS circuit components and blocks. The Simplorer VHDL-AMS solver contains an analog solver, a digital solver, and a controller that controls their interaction [4].

15.2.2 Model of Solenoid Actuator

The standard VHDL-AMS solenoid model is based on the assumed inductance versus position relation [5]

$$L(x) = \frac{N^2 L_0}{1 + kx} \quad (15.5)$$

where L_0 is the inductance for one turn when airgap $x = 0$, N is number of turns, and k is a dimensionless coefficient. The voltage across this inductance is

$$V = \frac{d\lambda}{dt} = \frac{d}{dt}(LI) = N^2 L_0 \frac{d}{dt} \left(\frac{I}{1 + kx} \right) \quad (15.6)$$

Since both x and I may vary with time, the derivative above gives

$$V = N^2 L_0 \left[\frac{I}{1 + kx} \frac{dI}{dt} - \frac{Ik}{(1 + kx)^2} \frac{dx}{dt} \right] \quad (15.7)$$

where the second term is the speed voltage.

The magnetic force is given by (5.13) and (6.9) as

$$F = \frac{\partial W_{co}}{\partial x}, \text{ where coenergy } W_{co} = \int \lambda dI \quad (15.8)$$

Since the inductance $L(x)$ of (15.5) is independent of current, the flux linkage $\lambda = LI$ becomes

$$\lambda(I, x) = \frac{N^2 L_0 I}{1 + kx} \quad (15.9)$$

and the force of (15.8) becomes

$$F = \frac{N^2 L_0 I^2}{2} \frac{\partial}{\partial x} \left(\frac{1}{1 + kx} \right) = -\frac{N^2 L_0 k I^2}{2(1 + kx)^2} \quad (15.10)$$

The minus sign indicates that the magnetic force tends to close the airgap x . In terms of the flux linkage λ , the force becomes

$$F = -\frac{k\lambda^2}{2L_0 N^2} \quad (15.11)$$

Defining a new variable, the maximum inductance

$$L_{\max} = N^2 L_0 \quad (15.12)$$

results in the following VHDL-AMS model equations:

$$\lambda = \frac{L_{\max} I}{1 + kx}, \quad F_k = \frac{k}{2L_{\max}}, \quad F = -\lambda^2 F_k, \quad V = \frac{d\lambda}{dt} \quad (15.13)$$

The VHDL-AMS model includes two external electrical pins (nodes) and two mechanical pins. Given a current I and armature position x , the model equations compute λ and F . The value of F is passed to the mechanical pins as a variable. The voltage, the time derivative of λ , appears across the electrical pins.

Similar methods can be used to derive VHDL-AMS models for other magnetic components. First, the equations for stored energy, in terms of “across” and “through” variables, must be obtained. Then the forces, voltages, and losses in lossy cases, can be computed.

The VHDL-AMS solenoid model accepts a current value from electrical pins p and m , and a position value from mechanical pins $pos1$ and $pos2$. The model entity parameters are listed in Table 15.1, and the VHDL-AMS entity description is presented in Table 15.2. The VHDL-AMS architecture code is listed in Table 15.3.

Example 15.3 Simplorer VHDL-AMS Voltage Step Response of Solenoid

The VHDL-AMS solenoid model described above is to be used to find the response to a step application of a 12-V automobile battery for one second. As shown in Fig. E15.3.1, the total moving mass is 0.545 kg, and the force of gravity is included over the 0.0127 m stroke.

The solenoid has 12,500 turns, a coil resistance of 103 Ω , and a diode connected as shown in Fig. E15.3.1 to eliminate arcing at its switch on turnoff. The solenoid constant k is not really a constant, and can be calculated in several ways. It can be found using the reluctance method of Chapter 3, the finite-element method of Chapter 4, and/or from measurements if the solenoid is available. In this example, finite-element solutions at two values of x are used. For $I = 0.084$ A and $x = 0$, $L = 1.251\text{E-}7$ H and $F = -27$ N. At the same current and $x = 0.0127$ m, $L = 3.56\text{E-}8$ H and $F = -0.84$ N. Find the current and force versus time from 0 to 2 s.

Solution: The first approach to find k is to choose it to match L at both values of x . This should model the electrical side accurately at all times. Substituting the two L values in (15.5) gives $k = 197.735$.

Another approach is to match both L and F at time zero. Using (15.12) and (15.13) gives $L_{\max} = 19.547$ and then $\lambda = 1.642$. Substituting λ in (15.13) gives $F_k = 10$ and then $k = 391.52$.

TABLE 15.1 VHDL-AMS Solenoid Model Entity Parameters

Interface	Name	Type	Default Value	Description
GENERIC	10	Inductance	1.25E-7	Maximum L for 1 turn
"	k	Real	197.735	L coefficient
"	N	Real	1.0	Number of coil turns
TERMINAL	p, m	Electrical	—	Electrical pins
"	pos1	Translational	—	Mechanical pin
"	pos2	Translational	—	Mechanical pin

TABLE 15.2 VHDL-AMS Solenoid Entity Description for Table 15.1

```

LIBRARY IEEE;
USE IEEE.ELECTRICAL_SYSTEMS.ALL;
USE IEEE.MECHANICAL_SYSTEMS.ALL;
ENTITY solenoid IS
  GENERIC (
    L0 : INDUCTANCE := 1.25e-7;
    K : REAL :=197.735;
    N : REAL :=1.0;
  PORT (
    TERMINAL p,m : ELECTRICAL;
    TERMINAL pos1, pos2 : TRANSLATIONAL);
    QUANTITY force_out : OUT REAL := 0.0);
END ENTITY solenoid;

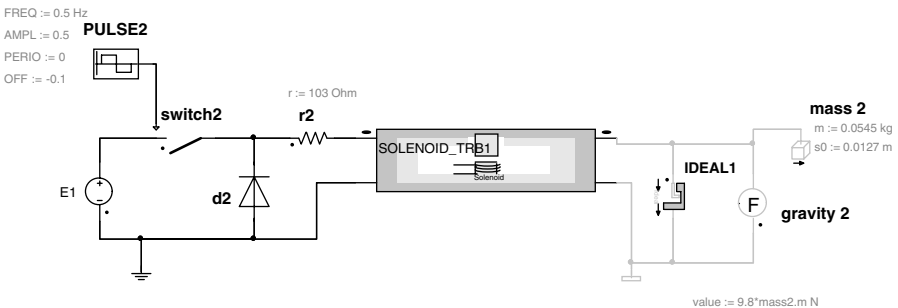
```

TABLE 15.3 VHDL-AMS Solenoid Model Architecture Description

```

ARCHITECTURE behav OF solenoid IS
  CONSTANT Lmax : INDUCTANCE :=L0 * N * N;
  CONSTANT Fk : FORCE :=K / (2.0 * Lmax;
  QUANTITY v ACROSS i THROUGH p TO m;
  QUANTITY position ACROSS force THROUGH pos1 TO pos2;
  QUANTITY L : INDUCTANCE;
  QUANTITY flux : FLUX;
BEGIN
  IF (position > 0.0) USE
    L == Lmax / (1.0 + K * position);
  ELSE
    L == Lmax;
  END USE;
  flux == L * i;
  v == flux'DOT;
  force == flux * flux * Fk;
  force_out == -force;
END ARCHITECTURE behav;

```

**Figure E15.3.1** VHDL-AMS solenoid model in Simplorer with DC voltage switch.

The two values of k are quite different. It is not possible to match both L and F over the whole solenoid operating range because of its nonlinear B - H steel, flux fringing, and other factors. The VHDL-AMS solenoid model thus is not as accurate as the preceding models using tables from finite-element analyses at far more than two positions. Thus the Simplorer SML modeling method of Section 15.1.6 can be more accurate than Simplorer VHDL-AMS models.

To choose k , one might pick a compromise value of perhaps 300. If the mechanical behavior were more important, the 391.52 value might be chosen. Here the electrical behavior must be accurately modeled, so the value 197.735 is chosen.

The resulting current waveform computed by the VHDL-AMS capability of Simplorer is shown in Fig. E15.3.2, along with the computed position versus time. The computed force versus time is shown in Fig. E15.3.3. Note that the force takes time to build up after the voltage is applied at time zero, and takes time to decay after the voltage is switched off at time equal to 1 s.

15.3 MATLAB/SIMULINK MODELS

15.3.1 Software

MATLAB stands for matrix laboratory and was developed by Mathworks, Inc. A related software simulation package called *Simulink* is also popular.

MATLAB performs engineering calculations both with and without matrices [6]. It is especially well suited for analyzing linear systems [15.7]. It offers a number of *toolboxes*, which are extensions for certain application areas. Its *control system toolbox* is commonly used by control systems engineers, and includes models in the Laplace transform s domain [8].

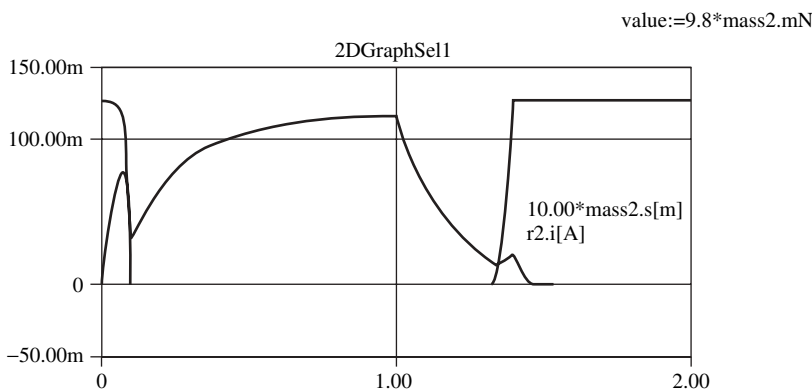


Figure E15.3.2 Current (slowly rising) and position versus time computed by VHDL-AMS model.

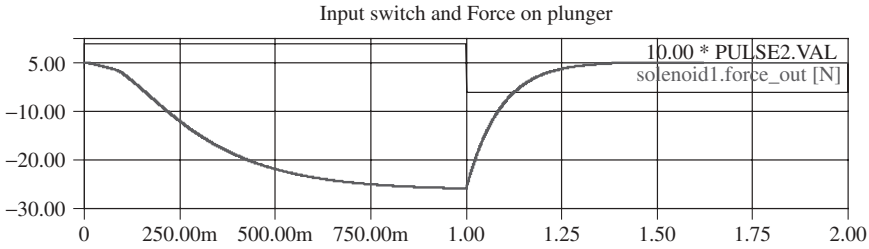


Figure E15.3.3 Force versus time computed by VHDL-AMS model.

Simulink provides an efficient graphical way for MATLAB users to model and simulate control systems in block diagram form. It includes many linear blocks and also some simple nonlinear blocks.

15.3.2 MATLAB Model of Voice Coil Actuator

The voice coil actuator of Chapter 7 has a force linearly proportional to current and thus is easily modeled using MATLAB as follows [9]. The model includes mechanical parameters such as M_s , B_s , and K_s of (15.4), which may be properties of a loud-speaker voice coil actuator.

Example 15.4 Step Response Times and Overshoot of Linear Voice Coil A voice coil actuator has the proportionality constant between voice coil current and magnetic force K_a :

$$F(t) = K_a I(t) \quad (\text{E15.4.1})$$

The actuator is shown schematically in Fig. E15.4.1, and has $K_a = 0.8 \text{ N/A}$. The inductance of the coil is $L = 0.02 \text{ H}$, and its resistance shown externally is $R = 0.5 \Omega$.

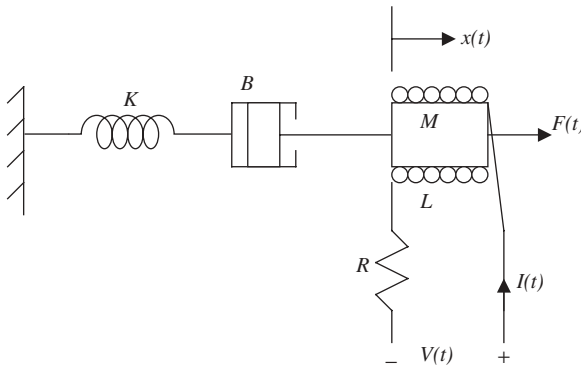


Figure E15.4.1 Voice coil actuator schematic diagram.

Note that $x(t)$ is the displacement and $u(t)$ is the velocity. The mass $M = 0.08$ kg, the damping friction is $B = 0.32$ N-s/m, and the elasticity spring constant is $K = 1.6$ N/m.

To determine performance of the voice coil system using the approach commonly used by control systems engineers, the following tasks are to be performed:

- (a) Write the equation for the electric circuit. Draw the force–voltage electric circuit analogy for the mechanical system, and write the equation describing the mechanical system. Draw the s -domain (Laplace transform) block diagram for the electromagnetic actuator with $V(s)$ as the reference input and the displacement $X(s)$ as the output. Mark all the s -domain variables $V(s)$, $I(s)$, $F(s)$, velocity $U(s)$, and position $X(s)$ on the block diagram and determine the transfer function $X(s)/V(s)$.
- (b) Use the MATLAB `roots` function to find the roots of the system transfer function and determine the time constants. If one time constant is small relative to the other time constants, suggest a reduced-order model. Obtain the step response for the actual model and the reduced-order model on the same graph. After you have defined the numerators and denominators for both systems, you can use `sys3rd = tf(num1, den1)`, and `sys2nd = tf(num2, den2)` to define the transfer function models. Then you can use

```
ltiview('step', sys3rd, 'b', sys2nd, 'r')
```

to obtain the step response for both systems on the same LTI (linear time-invariant) viewer. Right-click on the plot area and determine the time-domain characteristics, risetime t_r , peak time t_p , percent overshoot P.O., and settling time t_s .

- (c) The step response peak time and the percent overshoot of a second-order system is given by

$$t_p = \frac{\pi}{\omega\sqrt{1-\zeta^2}}, \text{ and P.O.} = e^{-\zeta\pi/\sqrt{1-\zeta^2}} \times 100 \quad (\text{E15.4.2})$$

Using these relations, compute t_p , P.O., and the settling time $t_s = 4\tau$ for the reduced-order model and compare it to the value for the actual response found in (b).

Solution

- (a) The time-domain and the s -domain equivalent circuits for the electric circuit of the actuator and the force–voltage electric circuit analogy for the mechanical system are shown in Fig. E15.4.2. Note that the motional voltage is assumed negligible. From the s -domain equivalent circuit we have

$$I(s) = \frac{1}{0.02s + 0.5} V(s) \quad \text{and} \quad U(s) = \frac{1}{0.08s + 0.32 + \frac{1.6}{s}} F(s) \quad (\text{E15.4.3})$$

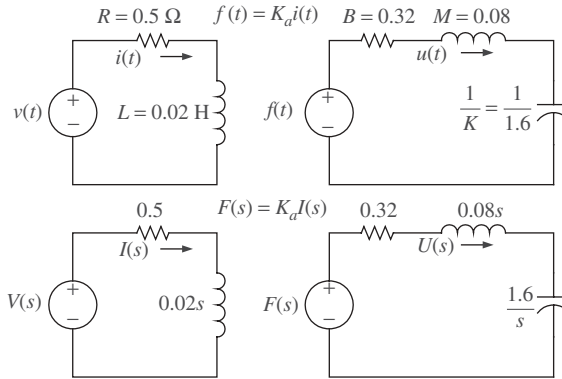


Figure E15.4.2 Time-domain and s -domain equivalent circuits for voice coil actuator.

Also the given transducer equation is

$$F(s) = 0.8I(s) \quad (\text{E15.4.4})$$

and the displacement in terms of velocity is

$$X(s) = \frac{1}{s} U(s) \quad (\text{E15.4.5})$$

The block diagram representing these four equations is shown in Fig. E15.4.3. Thus the transfer function relating the s -domain displacement to the s -domain voltage is

$$G(s) = \frac{X(s)}{V(s)} = \frac{0.8}{(0.02s + 0.5) \left(0.08s + 0.32 + \frac{1.6}{s} \right) s} \quad (\text{E15.4.6})$$

or

$$G(s) = \frac{50}{(s + 25)(s^2 + 4s + 20)} = \frac{500}{s^3 + 29s^2 + 120s + 500} \quad (\text{E15.4.7})$$

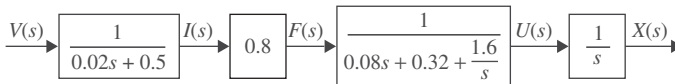


Figure E15.4.3 Block diagram of voice coil actuator.

(b) The roots of the characteristic equation are

$$\begin{aligned}
 r &= \text{roots}([1 \quad 29 \quad 120 \quad 500]) \\
 r &= -25.0000 \\
 &\quad -2.0000 + 4.0000i \\
 &\quad -2.0000 - 4.0000i
 \end{aligned} \tag{E15.4.8}$$

The time constants are

$$\tau_1 = \frac{1}{25} = 0.04 \quad \text{and} \quad \tau_2 = \frac{1}{2} = 0.5 \tag{E15.4.9}$$

$$G(s) = \frac{500}{25(0.04s + 1)(s^2 + 4s + 20)} = \frac{20}{(0.04s + 1)(s^2 + 4s + 20)} \tag{E15.4.10}$$

Note that $\tau_1 \ll \tau_2$. Neglecting the smaller time constant, the approximate second-order model becomes

$$G(s) = \frac{20}{s^2 + 4s + 20} \tag{E15.4.11}$$

To obtain the step response of the third-order and second-order systems, we use the following MATLAB commands:

```

num1 = 500; % third-order system num
den1 = [1 29 120 500]; % third-order system den
num2 = 20; % reduced-order system num
den2 = [1 4 20]; % reduced-order system den
sys3rd = tf(num1, den1) % third-order system
sys2nd = tf(num2, den2) % reduced-order system
ltiview('step', sys3rd, 'b', sys2nd, 'r')

```

The results are plotted in Fig. E15.4.4.

(c) The second-order system characteristic equation is

$$s^2 + 4s + 20 = 0 \tag{E15.4.12}$$

$$\omega_n^2 = 20 \Rightarrow \omega_n = 4.472 \tag{E15.4.13}$$

$$2\zeta\omega_n = 4 \Rightarrow \zeta = \frac{4}{2(4.472)} = 0.4472 \tag{E15.4.14}$$

$$t_p = \frac{\pi}{4.472\sqrt{1 - 0.4472^2}} = 0.785 \tag{E15.4.15}$$

$$\text{P.O.} = \exp\left(\frac{-0.4472\pi}{\sqrt{1-0.4472^2}}\right) = 20.7 \quad (\text{E15.4.16})$$

$$\tau = \frac{1}{s\omega_n} = 0.5 \text{ s} \quad (\text{E15.4.17})$$

$$t_s = 4\tau = 2.0 \text{ s} \quad (\text{E15.4.18})$$

The results are summarized in Table E15.3.1, which shows that the reduced-order model is a good approximation. The frequency response of the two systems can also be compared to again confirm the validity of the approximation.

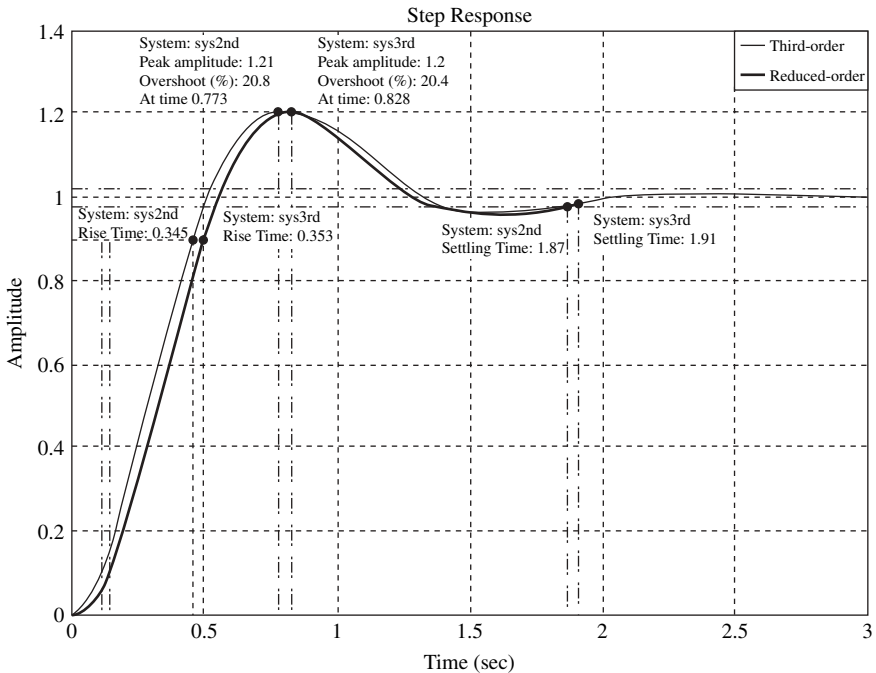


Figure E15.4.4 Plots of response of voice coil actuator.

TABLE E15.3.1 Comparison of Responses of Systems Models of Actuator

Time-Domain Specification	Third-Order System Simulation Results	Reduced-Order Simulation Results	Reduced Order Using Eq. (E15.3.1)
P.O. ^a	20.4	20.8	20.7
t_p (s)	0.828	0.773	0.785
t_s (s)	1.91	1.87	2.0

^aPercent overshoot.

15.4 INCLUDING EDDY CURRENT DIFFUSION USING A RESISTOR

As discussed in Chapters 8 and 9, actuators and sensors made of solid steel can have significant eddy currents and associated diffusion time delays. One example is the Bessho DC axisymmetric plunger actuator, which is made of solid steel. Example 9.2 has shown that planar devices also exhibit transient eddy currents. To include transient eddy current diffusion effects in systems models, one method is to solve the eddy current finite-element model at each timestep along with the systems solution, called *cosimulation* [10].

A simpler way to include eddy current effects in systems models is to add a resistor as described below. The resistor will first be derived for planar problems and then for axisymmetric problems.

15.4.1 Resistor for Planar Devices

The equivalent resistor for eddy current diffusion in a planar slab has been derived for linear B – H material of conductivity σ and a one-turn coil as [5]:

$$R_{EL1} = \pi^2 h_z / (\sigma h_y w) \quad (15.14)$$

where the material depth into the plane is h_z , its width in direction of diffusion is w , and its height in the remaining direction is h_y .

For a coil of N turns, the equation for linear eddy resistance in one slab is

$$R_{EL} = (\pi N)^2 h_z / (\sigma h_y w) \quad (15.15)$$

Chapter 9 has shown that nonlinear B – H curves cause the diffusion time to change. To include nonlinear B – H effects, the eddy resistor is multiplied by the ratio of time constants:

$$R_E = (\tau_{mL} / \tau_{mN}) (\pi N)^2 h_z / (\sigma h_y w) \quad (15.16)$$

where τ_{mL} is the diffusion time of Chapter 9 for linear B – H and τ_{mN} is the diffusion time of Chapter 9 for nonlinear B – H .

Example 15.5 R_E for Inductor of Example 9.2 The eddy current resistor is to be found for the inductor of Example 9.2, shown in Fig. E9.2.1, at a current of 0.5 A.

Solution: The width $w = 0.02$ m, and the diffusion time ratio is $(\tau_{mL} / \tau_{mN}) = (54.6/18.9)$. Also, the total number of turns $N = (26.4)(2)(0.05/0.002) = 1320$. Also, the height $h_y = 0.05$ m and the depth $h_z = 0.1$ m. In addition, since the inductor has two legs (slabs), its power loss is doubled, and thus the eddy resistor of (15.14) must be divided by 2, giving $R_E = 1462 \Omega$.

Example 15.6 Simplorer Model of Inductor of Example 9.2 with Input Step Current and R_E The inductor of Example 9.2, shown in Fig. E9.2.1, is to be modeled in Simplorer with an eddy current resistor added to account for linear mag-

netic diffusion. Its transient performance is to be computed when a step current of 0.5 A is input.

Solution: From Example 15.5, the eddy current resistor is 1462 Ω . The magnetostatic flux linkage versus inductance is found by multiple Maxwell finite-element solutions of the model of Example 9.2 over a wide range of currents. The resulting Simplorer model is shown in Fig. E15.6.1.

The input step current and computed output flux versus time are shown in Fig. E15.6.2. Note that the flux is delayed somewhat less than the nonlinear diffusion time of 18.9 ms of Example 9.2. Since the diffusion time is the time for the center flux to rise, and most of the flux is outside the center of the leg, the Simplorer results are reasonable.

15.4.2 Resistor for Axisymmetric Devices

To derive the equivalent resistor for axisymmetric devices, begin with the constant-permeability case. The classical formula for the resistance seen by current flowing peripherally on an arc around an axis is [3]

$$R_{EL1} = \frac{4\pi}{2\sigma h \ln(b/a)} \quad (15.17)$$

where h is the axial length, b is outer radius, and a is inner radius. For a cylindrical armature and/or stator bore, the effective inner radius a varies with time according to the magnetic diffusion concept of Chapter 9:

$$a = be^{-t/\tau_m} \quad (15.18)$$

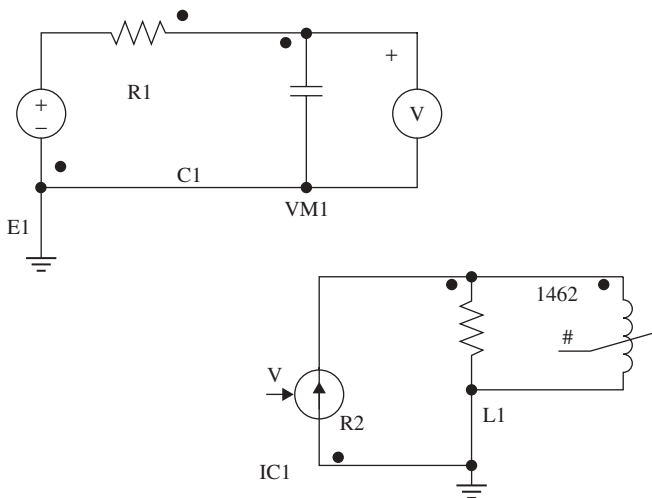


Figure E15.6.1 Simplorer model of inductor made of rectangular solid steel.

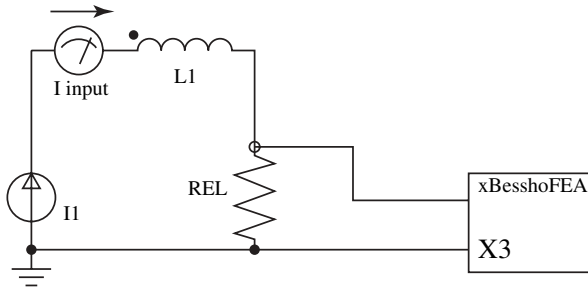


Figure 15.6 Adding leakage inductor L_l and parallel resistor to SPICE model to account for eddy current diffusion.

where the nonlinear diffusion time τ_{mN} varies with applied field intensity H_0 as described in Chapter 9. One must keep in mind, however, that the diffusion time calculations of Chapter 9 were for one-dimensional problems, whereas airgaps and other 2D geometric features of real magnetic devices will cause changes in diffusion. Thus (15.21) is approximate, even when actuators are closed with “zero” airgap. No gap is exactly zero, but instead equals approximately $36\ \mu\text{m}$ for polished steel surfaces [12].

For the Bessho actuator, Example 9.3 has shown that $H_0 = 6600\ \text{A/m}$ for the nominal current of $0.5\ \text{A}$. Using the actual Bessho steel B – H curves (not the step B – H curve of Example 9.3), the nonlinear diffusion time τ_{mN} computed by Maxwell finite-element analysis is $42\ \text{ms}$. Then the corresponding eddy resistor using (15.21) with $(\tau_{mL}/\tau_{mN}) = (93\ \text{ms}/42\ \text{ms})$ is $R_{EN} = 1320\ \Omega$ [11]. The resulting Simplorer output position for the same input current as Fig. 15.5 is shown in Fig. 15.8. The closing time is now $101\ \text{ms}$, increased by 4% from Fig. 15.5, as expected from Table 14.1. Hence in this case the eddy currents cause only a 4% increase in operation time, but larger increases occur in other cases.

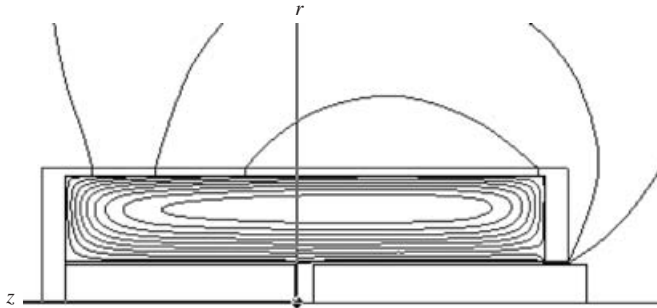


Figure 15.7 Computer display of flux line plot for Bessho actuator with flux excluded from steel, used to obtain value of leakage inductance L_l .

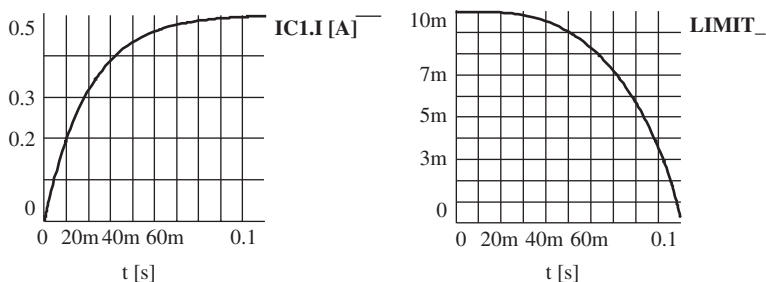


Figure 15.8 Computed Simplorer input and output for Bessho actuator including nonlinear $1320\ \Omega$ eddy resistor and 6 kg moving mass. The input on the left is the current (in amperes) waveform, and the output on the right is the airgap (in meters) as a function of time (in seconds).

PROBLEMS

- 15.1** Redo Example 15.1 for the coil resistance increased (using smaller-diameter wire) by 50%. Use the electric circuit software of your choice.
- 15.2** Redo Example 15.1 for the coil resistance increased (using smaller-diameter wire) by 100%. Use the electric circuit software of your choice.
- 15.3** Redo Example 15.2 with $V_{\text{speed}} = 11t^2$.
- 15.4** Redo Example 15.2 with $V_{\text{speed}} = 9t^2$.
- 15.5** Redo VHDL-AMS Example 15.3 with the solenoid constant $k = 391.5$.
- 15.6** Redo VHDL-AMS Example 15.3 with the solenoid constant $k = 300$.
- 15.7** Redo MATLAB Example 15.4 with mass reduced to 0.06 kg.
- 15.8** Redo MATLAB Example 15.4 with damping reduced to 0.25 N-s/m.
- 15.9** Use the MATLAB bode function to plot the frequency responses of the second-order and third-order models of Example 15.4.

REFERENCES

1. R. Kielkowski, *Inside SPICE*, McGraw-Hill, 1994.
2. T. E. McDermott, P. Zhou, J. Gilmore, and Z. J. Cendes, Electromechanical system simulation with models generated from finite element solutions, *IEEE Trans. Magn.* **33**: 1682–1685 (March 1997).
3. J. R. Brauer and Q. M. Chen, Alternative dynamic electromechanical models of magnetic actuators containing eddy currents, *IEEE Trans. Magn.* **36**: 1333–1336 (July 2000).
4. *Simplorer V7 VHDL-AMS Tutorial*, Ansoft Corp., Pittsburgh, PA, 2004.

5. H. H. Woodson and J. R. Melcher, *Electromechanical Dynamics*, Wiley, New York, 1968, Part II.
6. D. Hanselman and B. Littlefield, *Mastering MATLAB® 6*, Prentice-Hall, Upper Saddle River, NJ, 2001.
7. R. D. Strum and D. E. Kirk, *Contemporary Linear Systems Using MATLAB®*, Brooks/Cole, Pacific Grove, CA, 2000.
8. R. C. Dorf and R. H. Bishop, *Modern Control Systems*, 9th ed., Prentice-Hall, Upper Saddle River, NJ, 2001.
9. H. Saadat, *Control Systems Laboratory Manual*, Milwaukee School of Engineering, Milwaukee, WI, 2003.
10. P. Zhou et al., A general co-simulation approach for coupled field-circuit problems, *Digests of COMPUMAG Conf.*, Shenyang, China, June 2005.
11. J. R. Brauer and I. D. Mayergoyz, Finite element computation of nonlinear magnetic diffusion and its effects when coupled to electrical, mechanical, and hydraulic systems, *IEEE Trans. Magn.* **40**: 537–540 (March 2004).
12. H. C. Roters, *Electromagnetic Devices*, Wiley, New York, 1941.

Coupled Electrohydraulic Analysis Using Systems Models

Airplanes, automobiles, tractors, ships, robots, and other vehicles commonly contain hydraulic actuation systems such as brakes. Besides such *mobile hydraulic* systems, hydraulics are also common in stationary applications such as factories and elevators. In many cases, especially with computer control, the input to the hydraulic system is electrical. Such coupled systems are called *electrohydraulic systems*. The usual coupling devices are magnetic actuators and sensors.

16.1 COMPARING HYDRAULICS AND MAGNETICS

Hydraulic actuation systems have certain advantages over magnetic actuators [1]. As discussed in Chapter 5, magnetic pressures on steel surfaces are given by

$$P_{\text{mag}} = B^2 / (2\mu_0) - w_{co} \quad (16.1)$$

where coenergy w_{co} appears as in (5.17) and (5.13). The magnetic pressure P_{mag} of a typical steel was graphed in Fig. 5.7 and shown to be less than 20 bar, even for magnetic flux densities B as large as 2.4 T. Recall that one bar is $1.E5$ Pa, the standard atmospheric pressure at sea level.

In comparison, hydraulic pressures of hundreds of bar are commonly used. Since force is pressure times area, the higher hydraulic pressures can yield smaller, lighter, and less expensive actuators than can magnetic actuators. High hydraulic pressures produce high forces.

Another big advantage of hydraulic actuators is that magnetic actuator armatures often must be made of steel, a heavy material that reduces acceleration. Since acceleration must be high for fast actuation, armatures made of lighter material such as aluminum are advantageous. Hydraulic armatures do not carry any magnetic flux and need not be made of steel, and thus for a given force can produce faster acceleration.

Pure hydraulic systems, however, have the disadvantage of requiring a mechanical input, as shown in Fig. 16.1. A typical example of Fig. 16.1 is the automobile brake. The required large braking force can be produced by hydraulic cylinders, but

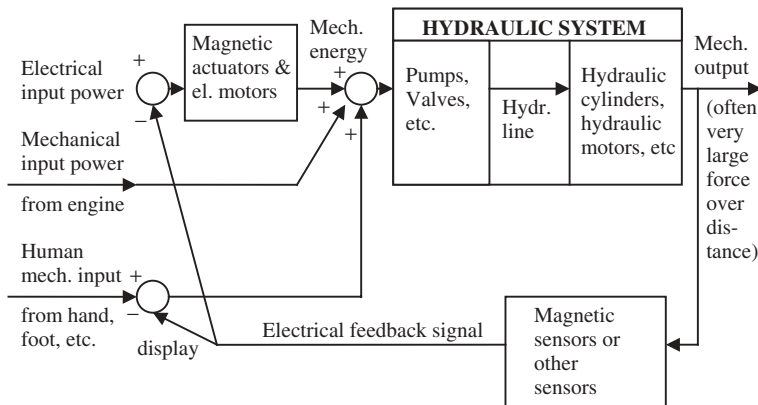


Figure 16.1 Block diagram showing energy conversions in a general system that includes a hydraulic system. The circles represent summing junctions. As shown, magnetic actuators require input electrical energy, which is not necessarily required by magnetic sensors with permanent magnets. The sensors may illuminate a display, such as vehicle speed, which is read by the human operator and thus used as one form of feedback control.

in early days the only input was the human foot for so-called manual brakes. Later, power brakes used the mechanical power of the gasoline engine to power a pump to provide additional hydraulic braking power. Nowadays, electric motors are often used to provide the power, and as discussed in Chapter 10, magnetic actuators and sensors are used for braking feedback control.

The most common way of utilizing electric power as well as optional computer control is through the magnetically operated hydraulic valve, which will be discussed later in this chapter. Thus coupled electrohydraulic systems are becoming increasingly popular.

In converting energy from mechanical to hydraulic and back again, some energy is inevitably lost. Yet if the force output of Fig. 16.1 is not large enough, a second hydraulic system can be added as a second hydraulic *stage*. While such multistage systems have been common in the past to produce large forces in large aircraft and tractors, to increase efficiency the trend nowadays is toward one stage that uses electrohydraulics.

16.2 HYDRAULIC BASICS AND ELECTRICAL ANALOGIES

As discussed in the preceding chapter, analogies are helpful in modeling various types of physical systems. Table 16.1 compares various physical system relationships, with its last column containing hydraulic relationships [2].

Just as standard symbols are used worldwide for electric circuit elements such as resistors, inductors, and capacitors, hydraulic circuits have standard symbols. Like wires in electric circuits, hydraulics lines and hoses are represented by lines.

TABLE 16.1 Physical System Relationships

Parameter	Electrical	Mechanical (Linear)	Mechanical (Rotary)	Hydraulic
Inductance	L	M (mass)	J (inertia)	I (fluid inertia)
Units	henrys	kg	N-m-s ²	N-s ² /m ⁵
Equation	$V = L di/dt$	$F = M dv/dt$	$T = J d\omega/dt$	$p = I dQ/dt$
Energy	$W = Li^2/2$	$W = Mv^2/2$	$W = J\omega^2/2$	$W = IQ^2/2$
Capacitance	C	K (spring)	K (spring)	C (capacitance)
Units	farads	N/m	N-m/rad	m ³ /Pa
Equation	$V = (1/C) \int i dt$	$F = Kx$	$T = K\theta$	$p = (1/C) \int q dt$
Energy	$W = CV^2/2$	$W = Kx^2/2$	$W = K\theta^2/2$	$W = Cp^2/2$
Resistance ^a	R	B (damper)	B (damper)	Orifice
Units	Ω (ohms)	N/m/s	N-m/s	(m ³ /s)/N/m ²) ^{1/2}
Equation	$V = IR$	$F = Bv$	$T = B\omega$	$Q = Kv p^{1/2}$
Power	$P = V^2/R$	$P = Bv^2$	$P = B\omega^2$	$P = pQ$
Effort	V (voltage)	F (force)	T (torque)	p (pressure)
Units	volts	N	N-m	Pa (= N/m ²)
Equation	$\int V dt = LI$	$\int F dt = mv$	$\int T dt = J\omega$	$\int p dt = QI$
Flow	I (current)	v (velocity)	ω (angular velocity)	Q (flow rate)
Units	amperes	m/s	rad/s	m ³ /s
Equation	$\int I dt = q$	$\int v dt = x$	$\int \omega dt = \theta$	$\int Q dt = q$
Power	$P = VI$	$P = Fv$	$P = T\omega$	$P = pQ$

^aTurbulent resistance.

Figure 16.2 shows several common hydraulic ISO standard symbols. The tank shown in Fig. 16.2 is generally at zero pressure, similar to ground in electric circuits. As indicated in Table 16.1, pressure P in hydraulic circuits is analogous to voltage, and fluid flow rate Q is analogous to current. The pressure source is usually a pump. Some types of pumps (such as in artificial hearts) require reciprocating motion and are thus operated by reciprocating magnetic actuators. More often, however, pumps are powered by rotary machines such as internal-combustion engines or electric motors.

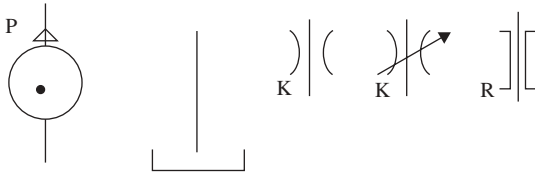


Figure 16.2 Symbols shown for several hydraulic components are, from left to right: pressure source (e.g., a pressure-compensated pump), hydraulic line and tank, common orifice (turbulent flow with square-law relation in Table 16.1), control valve (variable-turbulence orifice), and linear (laminar) orifice.

Analogous to electrical capacitance is hydraulic capacitance, obtained by storage devices such as accumulators. While hydraulic capacitance is common, hydraulic inductance is usually negligible.

Analogous to the electrical resistor is the hydraulic orifice, a narrowing of a hydraulic line. For a linear orifice

$$P = QR \quad (16.2)$$

The more common nonlinear orifice obeys the relation in Table 16.1:

$$P = (Q/K)^2 \quad (16.3)$$

The nonlinear orifice contains turbulent flow, while linear orifices contain laminar flow [3–5]. As shown in Fig. 16.2, the two orifice types have differing symbols. Also as shown in Fig. 16.2, an orifice with variable R or K acts as a *control valve*. The relation between P and Q is often found by measurement, but also can be computed using fluid finite-element software [6] or other computational fluid dynamics (CFD) software. As will be examined later in this chapter, the P – Q relation for hydraulic valves is important, because valves commonly serve in hydraulic actuators. Hydraulic units are listed in the Appendix.

The most common hydraulic fluid is oil, but other fluids such as water are sometimes used. Air is another popular fluid, but systems using it are called pneumatic systems. Because air is much more compressible than hydraulic liquids, thermodynamic effects can no longer be ignored. Thus pneumatic systems are usually more difficult to analyze than are hydraulic systems. Also, pneumatic pressures are seldom as high as common hydraulic pressures, and thus pneumatics are not covered in this book. Both hydraulics and pneumatics are examples of *fluid power systems*.

16.3 MODELING HYDRAULIC CIRCUITS IN SPICE

The varieties of systems software examined in the preceding chapter can be applied to hydraulic and electrohydraulic systems. As that chapter discussed, systems software is often preferred to pure finite-element software. While the coupled finite elements in Chapter 14 solved electric circuits coupled to magnetics and then coupled to structural mechanics, adding coupling to hydraulic finite elements is very difficult. In fact, no papers can be found that attempt coupled electrohydraulic finite-element analysis, although a few couple electromagnetic finite elements with those for acoustics [7] or fluid flow [8].

Because one of the most common systems programs used by electrical engineers is SPICE, it is used here to model hydraulic circuits. The electric circuits in SPICE can be used to model hydraulic circuits by the analogies of Table 16.1. For linear orifices, the ordinary constant resistor suffices. However, for the nonlinear P – Q relation (16.3) of turbulent orifices, the electric circuit requires a resistor with a nonlinear V – I relation. Several versions of SPICE feature such a nonlinear resistor.

Example 16.1 SPICE Model of Hydraulic Circuit with Linear (Laminar) Orifices A hydraulic circuit containing two laminar orifices in parallel hydraulic lines is shown in Fig. E16.1.1. The orifice hydraulic resistances are $R_1 = 1 \text{ MPa-s/m}^3$ and $R_2 = 2 \text{ MPa-s/m}^3$. They are both supplied by a pump of constant pressure $P_S = 5 \text{ kPa}$. Find the flow rates in both orifices.

Solution: The analogous SPICE electric circuit is shown in Fig. E16.1.2. Since there are no capacitances and no inductances (neither hydraulic nor electric), the flows are DC. The computed values agree exactly with Ohm's law, specifically, 5 mA in R_1 and 2.5 mA in R_2 . Thus the flow rates are $5\text{E-}3$ and $2.5\text{E-}3 \text{ m}^3/\text{s}$, respectively.

Example 16.2 SPICE Model of Hydraulic Circuit with Linear and Nonlinear (Turbulent) Orifices A hydraulic circuit containing a linear laminar orifice in series with a turbulent orifice is shown in Fig. E16.2.1 [9,10]. The turbulent orifice has the constant K in its square-law P - Q relation of Table 16.1. The laminar orifice has hydraulic resistance R . The given values are $K = 1$, $R = 1$, and source pressure $P_S = 1 \text{ Pa}$. Find the DC flow rate Q .

Solution: Maxwell SPICE includes nonlinear resistors, indicated by the crooked line superimposed on the upper resistor in the model of Fig. E16.2.2. The computed current is 0.618 A, which means that the computed flow rate $Q = 0.618 \text{ m}^3/\text{s}$.

To verify the computed Q , the following method is used [11]. Applying Kirchhoff's voltage law to Figs. E16.2.1 and E16.2.2, we obtain

$$P_S = P_1 + P_2 \quad (\text{E16.2.1})$$

in which, from (16.2) and (16.3), we further obtain

$$P_1 = \frac{Q^2}{K^2}, \quad P_2 = RQ \quad (\text{E16.2.2})$$

Substituting (E16.2.2) into (E16.2.1) gives

$$P_S = \frac{Q^2}{K^2} + RQ \quad (\text{E16.2.3})$$

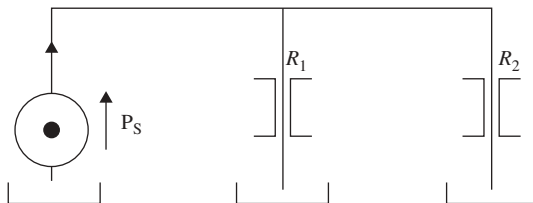


Figure E16.1.1 Hydraulic circuit with two parallel laminar orifices.

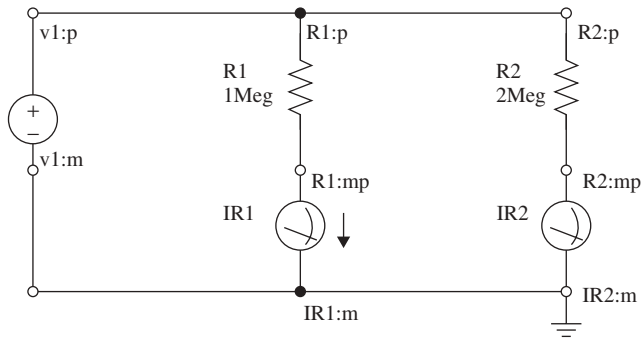


Figure E16.1.2 SPICE electric circuit model of Fig. E16.1.1.

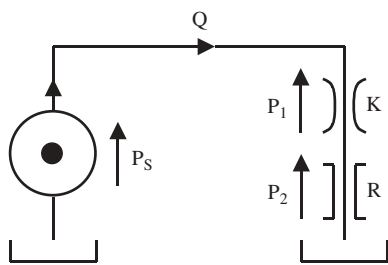


Figure E16.2.1 Hydraulic circuit with a turbulent orifice in series with a laminar orifice. (Reprinted with permission from SAE Paper 2000-01-2633 © 2000 SAE International.)

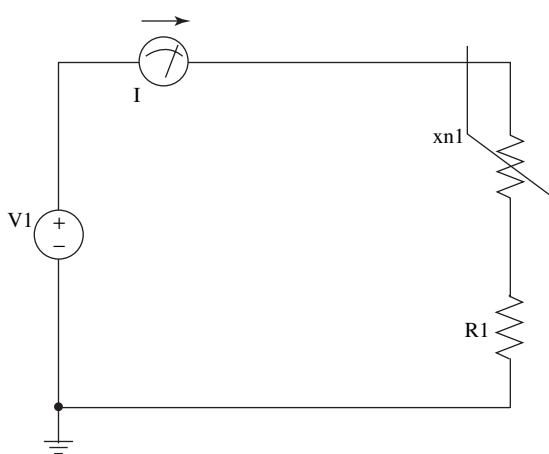


Figure E16.2.2 SPICE electric circuit model of Fig. E16.2.1.

where Q is the unknown. Putting (E16.2.3) in quadratic form, we obtain

$$Q^2 + RK^2Q - K^2P_s = 0 \quad (\text{E16.2.4})$$

Solving using the quadratic formula gives two roots [12]:

$$Q = \frac{RK^2}{2} \pm \frac{1}{2} \sqrt{R^2K^4 + 4K^2P_s} \quad (\text{E16.2.5})$$

Substituting the given unity values of R , K , and P_s gives $Q = +0.618$ and $Q = -1.618$. The negative value is impossible, and thus $Q = +0.618 \text{ m}^3/\text{s}$, agreeing exactly with the SPICE computation.

Example 16.3 SPICE Model of Switched Hydraulic Circuit with Hydraulic Capacitance The hydraulic circuit shown in Fig. E16.3.1 contains a manual valve “switch” that is thrown at time zero. Before time zero, all of the flow from the constant flow source Q is shunted through the valve to the tank “ground.” At time zero, the valve sends the flow through the hydraulic components to the right, consisting of a laminar orifice with hydraulic capacitance. The values are $Q = 10 \text{ m}^3/\text{s}$, $R = 100 \text{ Pa}\cdot\text{s}/\text{m}^3$, and $C = 100\text{E-}6 \text{ m}^3/\text{Pa}$. To be found is the hydraulic pressure as a function of time.

Solution: The analogous SPICE electric circuit model is shown in Fig. E16.3.2. It consists of a current source of 10 A that is switched on at time zero, and a parallel 100- Ω resistor and 100- μF capacitor. Since the RC time constant is 0.01 s, the rise-time of the pressure should be 0.01 s. The SPICE output voltage versus time is shown in Fig. E16.3.3. As expected, its time constant is 0.01 second. It approaches the final value of 1000 V, which equals the expected 10 A times 100 Ω . Thus the final steady-state pressure of the hydraulic circuit is 1000 Pa.

16.4 ELECTROHYDRAULIC MODELS IN SPICE AND SIMPLORER

SPICE hydraulic models can be combined with the SPICE electrical, magnetic, and mechanical models of the preceding chapter to make electrohydraulic models. If de-

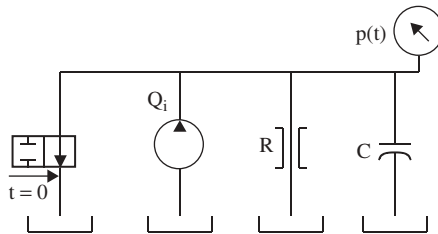


Figure E16.3.1 Hydraulic circuit with capacitance C , laminar resistance R , and constant flow source Q_1 that is switched from tank at time zero. (Reprinted with permission from SAE Paper 2000-01-2633 © 2000 SAE International.)

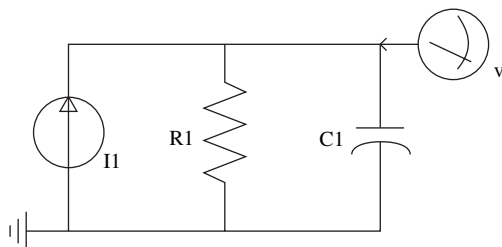


Figure E16.3.2 SPICE electric circuit model of Fig. E16.3.1.

sired, other electric circuit software such as Simplorer can be used instead of SPICE.

The simplest electrohydraulic models assume ideal proportional hydraulic *control valves*. Such valves produce fluid flow proportional to valve position regardless of pressure. An example familiar to everyone is a faucet that has flow rate directly proportional to its position x . If its position is zero, there is no flow, and the flow rate is always approximately proportional to position. In magnetic actuators, often the flow is directly through the “air” gap, and thus such actuators are often called *wet solenoids*. A dry alternative is to have the magnetic actuator armature push a rod through a physically separate proportional valve.

Such proportionality between position and flow rate is readily modeled using the *dependent sources* available in SPICE and Simplorer. SPICE includes four types of dependent sources identified by four letters:

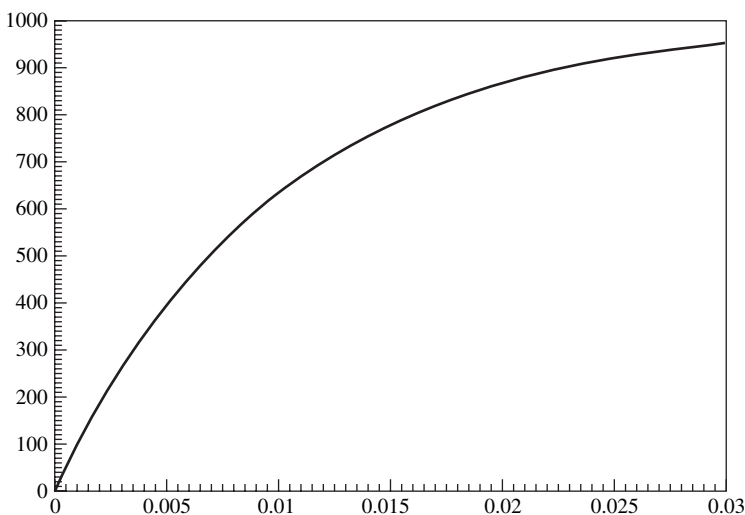


Figure E16.3.3 Voltage versus time (in seconds) computed by model of Fig. E16.3.2.

- E , voltage-controlled voltage source with proportionality constant = (source voltage)/(controlling voltage at any node)
- F , current-controlled current source with proportionality constant = (source current)/(controlling current in any branch)
- G , voltage-controlled current source with proportionality constant = (source current)/(controlling voltage at any node)
- H , current-controlled voltage source with proportionality constant = (source voltage)/(controlling current in any branch)

Use of these dependent sources is shown in the SPICE electrohydraulic model of Fig. 16.3 [10]. It is based on the Bessho magnetic actuator Maxwell SPICE model of Fig. 15.1. Added to it are two dependent sources and other elements to model hydraulics. The hydraulic circuit is in the lower left corner of Fig. 16.3, and consists of a linear orifice with $R = 1$ and the dependent source $G1$. The flow source $G1$ is set to $1000 \text{ m}^3/(\text{s}\cdot\text{m})$ and is dependent on the magnetic actuator airgap x . The second dependent source is $G2$ added to the mechanical circuit on the right. $G2$ is set to 1 N/Pa and is a flow force proportional to the flow in the hydraulic valve. The assumed proportionality of sources $G1$ and $G2$ is usually obeyed only approximately in actual hydraulic valves; in the next section we will discuss more realistic valve and hydraulic system models.

The computed Bessho actuator armature position versus time for Fig. 16.3 is plotted [10] in Fig. 16.4. Compared to the plot of Fig. 15.3 (curve 1), the closure time has increased from 99 ms to 150 ms. The hydraulic force has caused the armature to move more slowly.

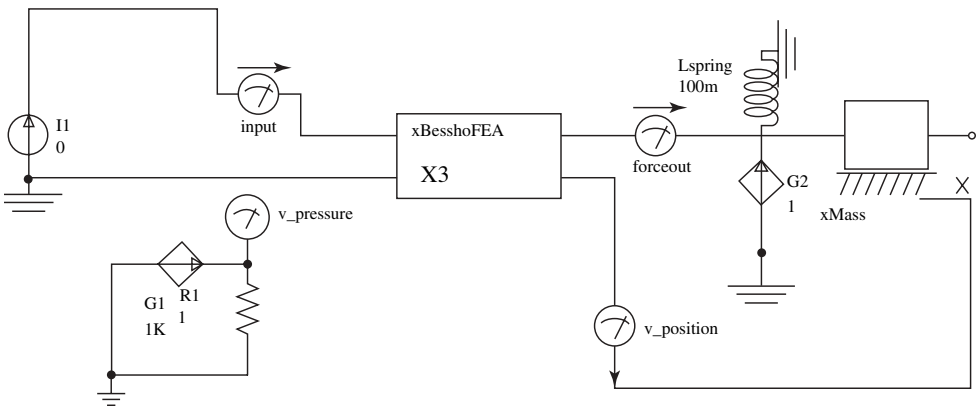


Figure 16.3 Maxwell SPICE model of simple electrohydraulic system with Bessho actuator driving a proportional control valve. (Reprinted with permission from SAE Paper 2000-01-2633 © 2000 SAE International.)

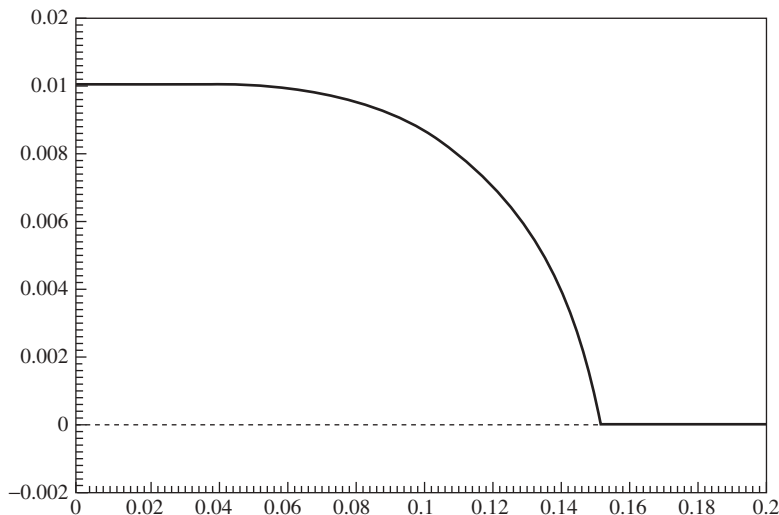


Figure 16.4 Computed magnetic actuator armature position versus time for electrohydraulic system of Fig. 16.3. (Reprinted with permission from SAE Paper 2000-01-2633 © 2000 SAE International.)

The next SPICE model has the linear orifice of Fig. 16.3 replaced by a nonlinear orifice with $K = 3$. The computed armature closure time increases to 160 ms. Next, a hydraulic capacitance $C = 0.1$ is added in parallel with the nonlinear orifice, and the computed closure time changes to 106 ms. The capacitance reduces the hydraulic force acting on the valve, thereby increasing the speed of armature motion.

Another SPICE model was made of the Bessho magnetic actuator driven by a pulsewidth-modulated (PWM) voltage of the type presented in Chapter 7. The electronic chopper circuit creating the PWM voltage is in the upper left of Fig. 16.5, which also contains the electrohydraulic SPICE model of Fig. 16.3. Note that the chopper circuit contains a dependent switch that is governed by the V3 voltage source that has a frequency of 100 Hz. The chopper circuit also contains a “fly-back” diode so that when the 50-V DC source is switched off, the inductive current of the magnetic actuator can flow to ground rather than cause arcing in the switch. The electronic switch is typically a semiconductor chip such as an SCR or IGBT. The resulting PWM voltage computed by SPICE is shown in Fig. 16.6 for a duty cycle of 50%. Thus the DC chopper voltage is 50% of the input 50 V, or 25 V.

The computed input current shown in Fig. 16.7 consists of the previous rising exponential with a dip caused by the moving armature, but it also has a ripple superimposed. The ripple is at the 100 Hz chopper frequency. The resulting magnetic force is shown in Fig. 16.8 and also contains a ripple. The computed magnetic actuator armature air gap versus time is shown in Fig. 16.9; note that closure takes about 140 ms, similar to Fig. 16.4. The computed hydraulic pressure and flow rate are shown in Figs. 16.10 and 16.11, respectively. Since the flow rate is assumed pro-

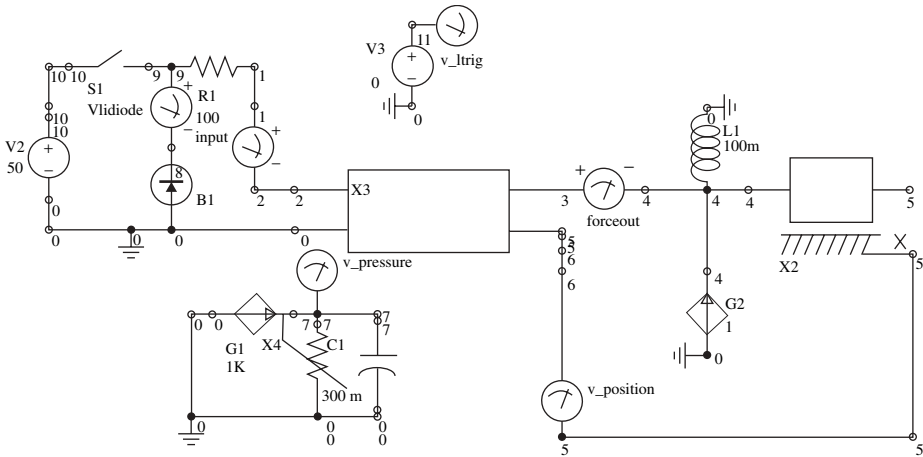


Figure 16.5 Chopper-driven PWM magnetic actuator in an electrohydraulic system modeled in SPICE. The chopper circuit is in the upper left, driving the Bessho actuator represented by the block labeled X3.

portional to armature position (which is 10 mm minus the airgap), the flow rate increases with time [12].

A hydraulics library is available for Simplorer. One of its hydraulic elements, the variable orifice, is used here to model a control valve operated by the Bessho magnetic actuator. The variable orifice is labeled as *RHYD1* in the Simplorer model in Fig. 16.12, which also contains a Simplorer fixed orifice with $R = 1\text{E}9 \text{ Pa}\cdot\text{s}/\text{m}^3$. To

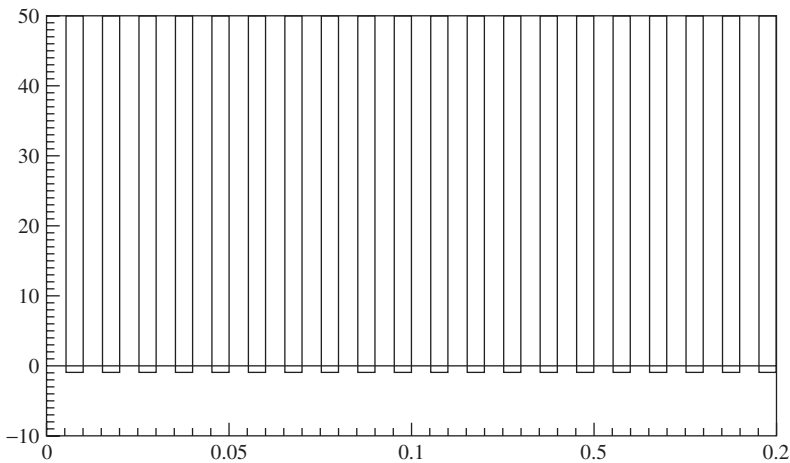


Figure 16.6 Computed PWM voltage (volts) versus time (s) produced by chopper of Fig. 16.5.

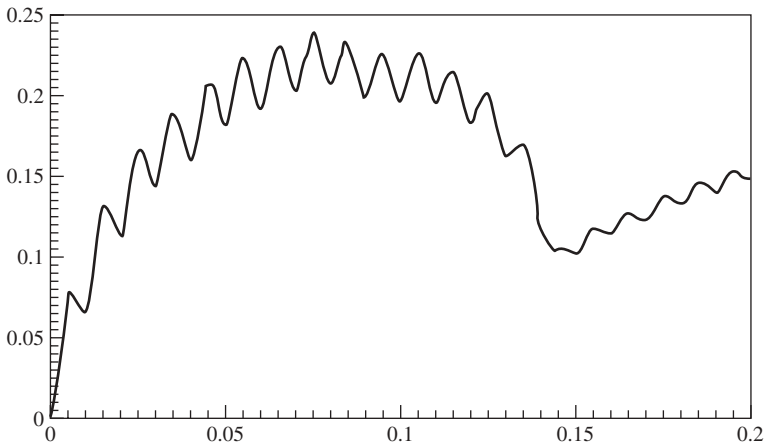


Figure 16.7 Computed magnetic actuator current (amperes) versus time (s) for Fig. 16.5.

achieve faster performance than in the previous electrohydraulic systems shown in Figs. 16.3–16.11, the 0.5 A current is turned on instantly (with 0 rather than 20 ms risetime) and the moving mass is reduced from 6 to 1.4 kg. The resulting armature position versus time computed by Simplorer is shown in Fig. 16.13 assuming no flow forces. As expected, movement is now much faster, closing in only 34 ms. The pressure source of 1 MPa (10 bar) then produces the flow rate also graphed in Fig. 16.13 for wet flow through the airgap that ceases upon its closure.

The Simplorer hydraulic orifice also allows flow forces to be included. For a flow force factor of 10 on the variable orifice, the computed results are graphed in

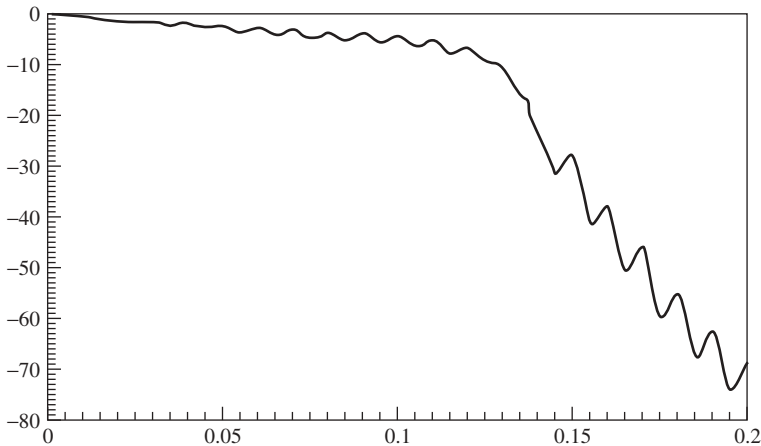


Figure 16.8 Computed magnetic force (N) versus time (s) for Fig. 16.5.

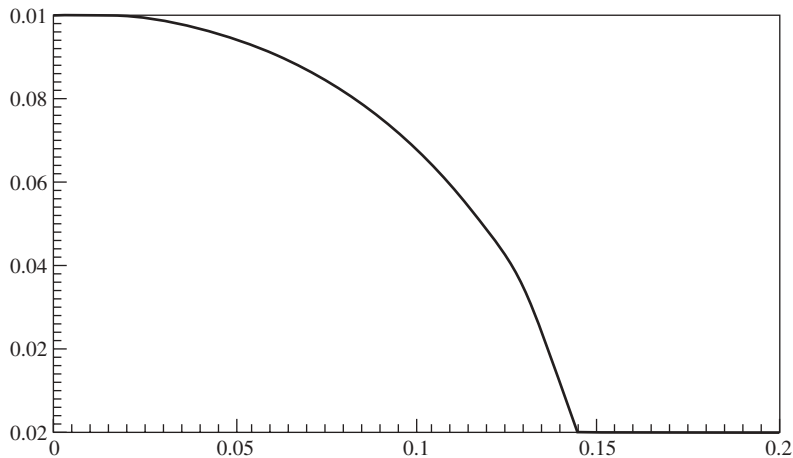


Figure 16.9 Computed magnetic armature position (m) versus time (s) for Fig. 16.5.

Fig. 16.14. Compared with Fig. 16.13, the armature now closes in 31.5 ms, which is 2.5 ms faster.

16.5 HYDRAULIC VALVES AND CYLINDERS IN SYSTEMS MODELS

16.5.1 Valves and Cylinders

The most common hydraulic actuator is the hydraulic cylinder, which contains a piston operated by hydraulic pressure. The cross section of a hydraulic cylinder

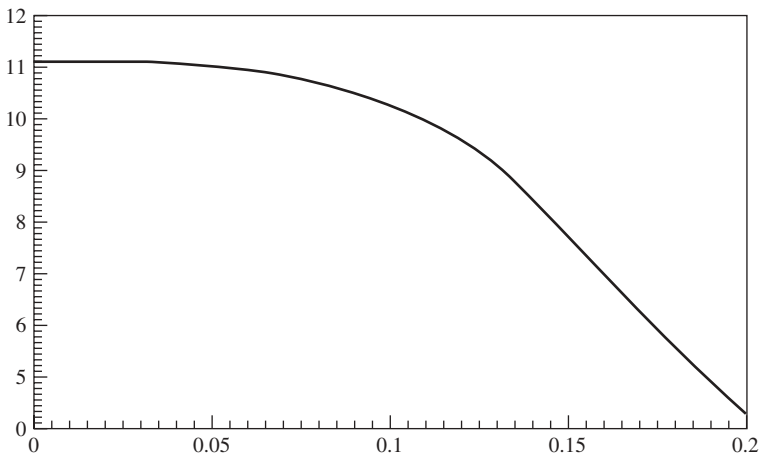


Figure 16.10 Computed hydraulic pressure (Pa) versus time (s) for Fig. 16.5.

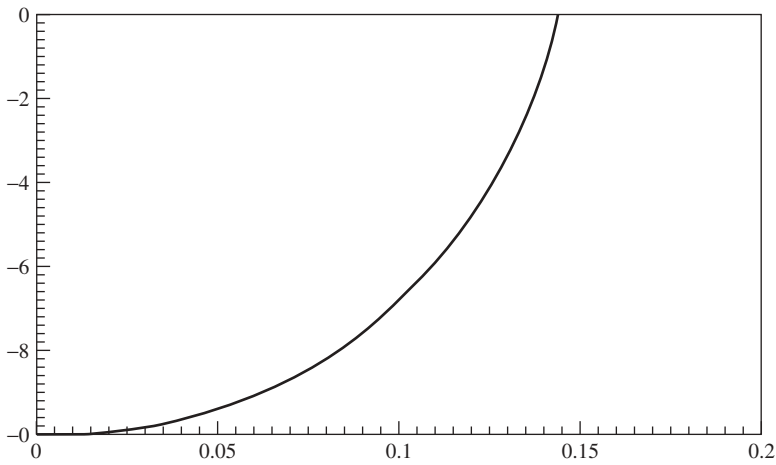


Figure 16.11 Computed hydraulic flow rate (m^3/s) versus time (s) for Fig. 16.5.

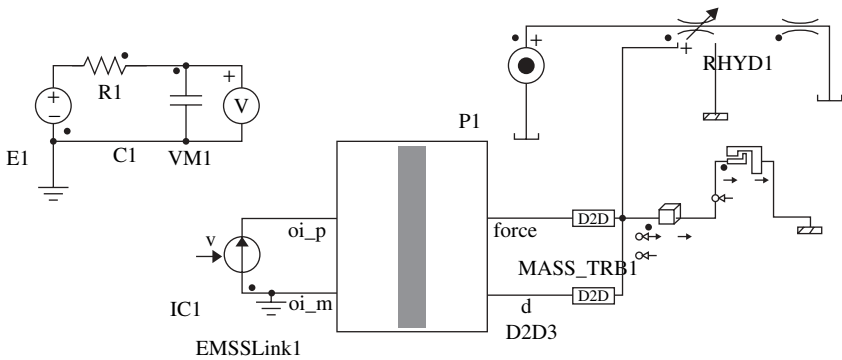


Figure 16.12 Simpler model of Bessho magnetic actuator in an electrohydraulic system containing the variable orifice $RHYD1$. To its right is the fixed orifice with $R = 1\text{E-}9 \text{ m}^3/(\text{s}\cdot\text{Pa})$.

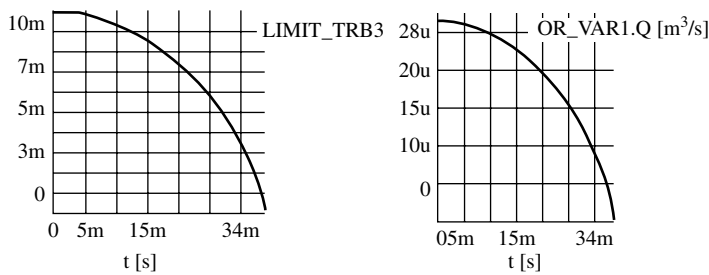


Figure 16.13 Computed results for Fig 16.12 with no flow forces: (a) armature airgap (m) versus time (s); (b) flow rate (m^3/s) versus time (s).

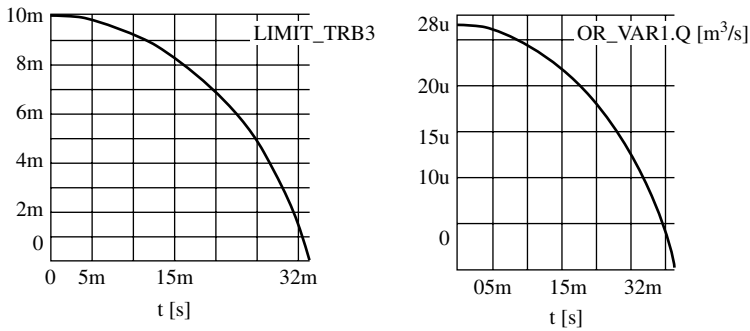


Figure 16.14 Computed results for Fig 16.12 with valve *RHYD1* flow force factor of 10: (a) armature airgap (m) versus time (s); (b) flow rate (m^3/s) versus time (s).

placed in a typical electrohydraulic system is shown in Fig. 16.15. The differential pressure P between the two sides of the piston of area A creates the hydraulic force. Hydraulic cylinders are easily visible on many tractors, dozers, power shovels, dump trucks, garbage trucks, snowplows, vertical lift bridges, and other equipment.

If the cylinder position is y as shown in Fig. 16.15, then the flow rate (in cubic meters per second) must obey the following rule:

$$Q = A \, dy/dt \quad (16.4)$$

The electrohydraulic system of Fig. 16.15 also shows the cross section of a typical control valve [1] driven by a magnetic actuator. The armature of the magnetic

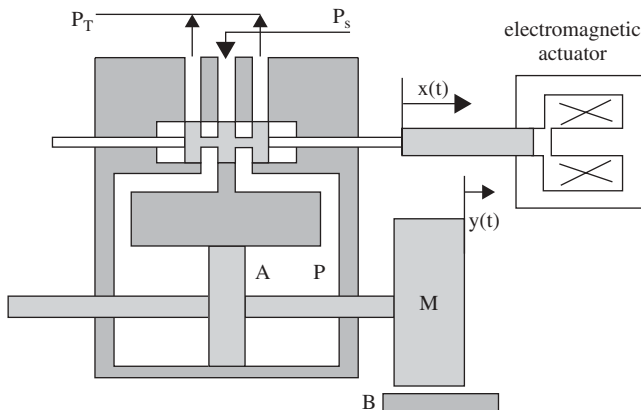


Figure 16.15 Electrohydraulic system containing a magnetic actuator driving a control valve that operates a hydraulic cylinder with moving mass M .

actuator is directly connected to the *valve spool*, the movable part of the valve that is shaped like a spool for thread. The spool in Fig. 16.15 has three *lands*, which are large-diameter cylindrically shaped regions. The valve in Fig. 16.15 is called a *four-way valve* because it has a total of four flow paths [13,14]. Its two hydraulic inputs are tank pressure P_T and supply pressure P_S .

The input–output characteristics of the valve are the shown in the typical family of curves in Fig. 16.16. Each curve is a plot of output (load) pressure P versus flow rate to the load Q . The valve position x is zero when closed and can be moved in either the positive and negative direction in Fig. 16.15. The flow rate curves of Fig. 16.16 are usually approximated by the equation [13]

$$Q = K_v x \sqrt{P_S - P} \quad (16.5)$$

where K_v is the valve coefficient and the tank pressure has been assumed zero.

Since (16.5) is nonlinear with load pressure P , it is often linearized to allow easier analysis. Over a small range, the commonly assumed linear relation is

$$Q = K_x x - K_p P \quad (16.6)$$

Note that if K_p is zero, then the valve is the ideal proportional valve assumed in the preceding section. This section, however, is more realistic in allowing K_p to be nonzero in the following derivations.

16.5.2 Use in SPICE Systems Models

The valve and cylinder described above can be modeled in SPICE based on the linearized valve equation (16.6), the hydraulic cylinder equation (16.4), and Newton's laws. For the cylinder load mass M and damping B shown in Fig. 16.15, the force balance equation is

$$PA = B(dy/dt) + M(d^2y/dt^2) \quad (16.7)$$

To model (16.4), (16.6), and (16.7) in SPICE, they can be written as three simultaneous equations in Q , P , and y , respectively:

$$Q + (K_p)P + (0)y = K_x x \quad (16.8)$$

$$Q + (0)P - A dy/dt = 0 \quad (16.9)$$

$$(-B/A)Q + (A)P - M d^2y/dt^2 = 0 \quad (16.10)$$

These three simultaneous differential equations are simulated here using three circuit meshes in SPICE. The three meshes appear in the bottom of the SPICE schematic of Fig. 16.17. The upper portion of Fig. 16.17 is the same as the previous SPICE electrical–magnetic–mechanical model of the Bessho magnetic actuator of Fig. 15.1. As before, the block labeled X3 contains results of parametric magnetic finite-element analyses of the Bessho magnetic actuator.

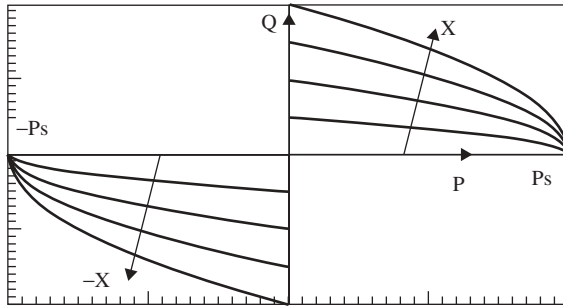


Figure 16.16 Typical pressure–flow rate curves of a control valve: P is the pressure to the load and Q is the flow rate to the load. The valve spool position x is zero when the valve is closed and Q is zero.

The lower left circuit mesh in Fig. 16.17 represents (16.8). P is its mesh current to be computed. Its resistor is K_p . Its two dependent sources are related to the other two terms of (16.8). The left-hand dependent H (current-controlled voltage) source is K_x times the armature position x . Its right-hand dependent H (current-controlled voltage) source is equal to flow rate Q . Thus, according to Kirchhoff's voltage law, this circuit mesh simulates (16.8).

The middle circuit mesh in the bottom of Fig. 16.17 represents (16.9). Its mesh current is the cylinder position y to be computed. The inductor is of value A , and thus its voltage is $A(dy/dt)$. This voltage equals that of the dependent H (current-

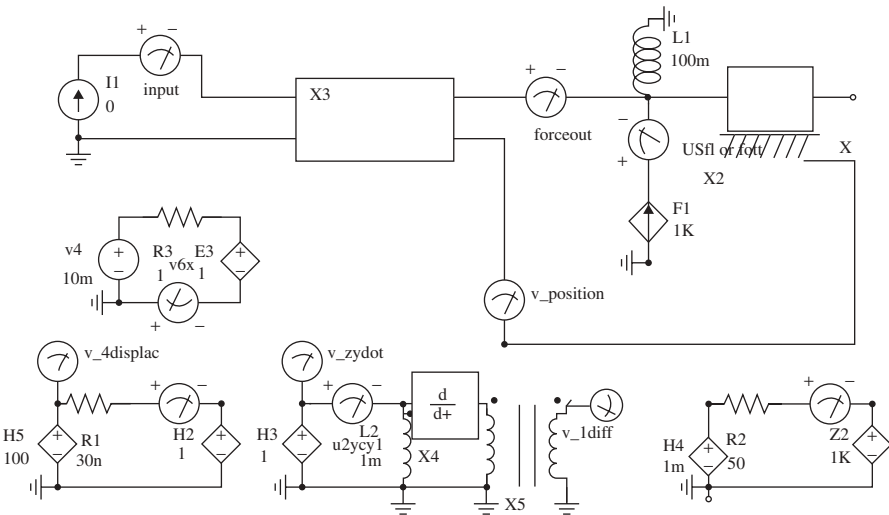


Figure 16.17 SPICE schematic of electrohydraulic system of Fig. 16.15. The upper right armature mass is 6 kg. The upper left current source rises to 0.5 A with a time constant of 20 ms.

controlled voltage) source equal to Q according to Kirchhoff's voltage law. A differentiator is added to produce an additional voltage $A(d^2y/dt^2)$, which is transformed by an added ideal transformer to (d^2y/dt^2) for use elsewhere.

The lower right circuit mesh in Fig. 16.17 represents (16.10). Its mesh current is the flow rate Q to be computed. The resistor is of value B/A . The left-hand dependent H (current-controlled voltage) source is set to A times the pressure P . Its right-hand dependent E (voltage-controlled voltage) source is set to $M(d^2y/dt^2)$, where (d^2y/dt^2) is found from the lower middle mesh.

To model the flow forces, the dependent F (current-controlled current) source is placed in the mechanical circuit in the upper right-hand corner of Fig. 16.17. The flow force acting on the magnetic armature and valve spool is generally a nonlinear function of flow rate Q and position x , but is modeled (as is commonly done [14]) here as a force proportional to Q directed to oppose the valve opening.

Thus the SPICE model of Fig. 16.17 couples the solutions of electric currents, magnetic forces, flux linkages, hydraulic pressures and flow rates, and mechanical armature and cylinder motions, altogether into one simultaneous solution [1].

The performance of the system model of Fig. 16.17 was computed for a typical set of electrical, magnetic, hydraulic, and mechanical parameters. The electrical and magnetic parameters are those of the previously analyzed Bessho solenoid, and the hydraulic and mechanical parameters are labeled in Fig. 16.17, including $A = 1.E-3$ m², $B = 50$ A, $K_x = 100$, and $K_p = 30E-9$. The input current is assumed to rise to its rated 0.5 ampere with a 20 ms risetime, and the armature mass is 6 kg. For a load mass M (of Fig. 16.16) set to 10 kg and then to 1000 kg, some computed results are presented in Figs. 16.18–16.21.

Figure 16.18 shows that the flow rate Q is much higher for the light load M than for the heavy load. This dependence agrees with the governing equations

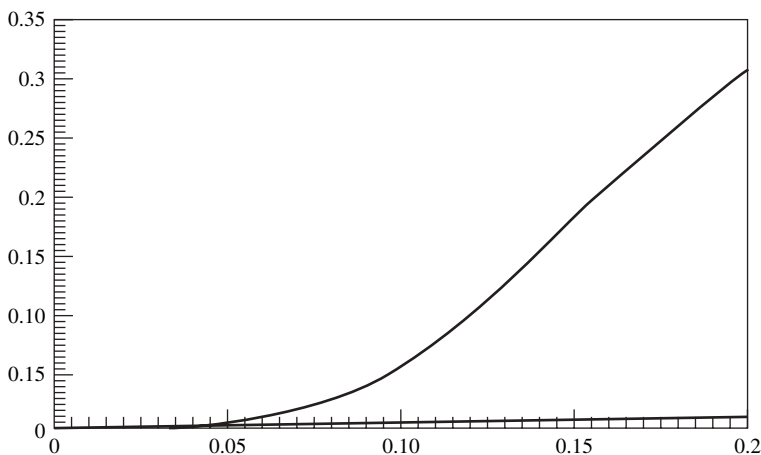


Figure 16.18 Computed Q (m³/s) versus time (s) for electrohydraulic model of Fig. 16.17. The upper curve represents $M = 10$ kg and the lower curve near axis, $M = 1000$ kg.

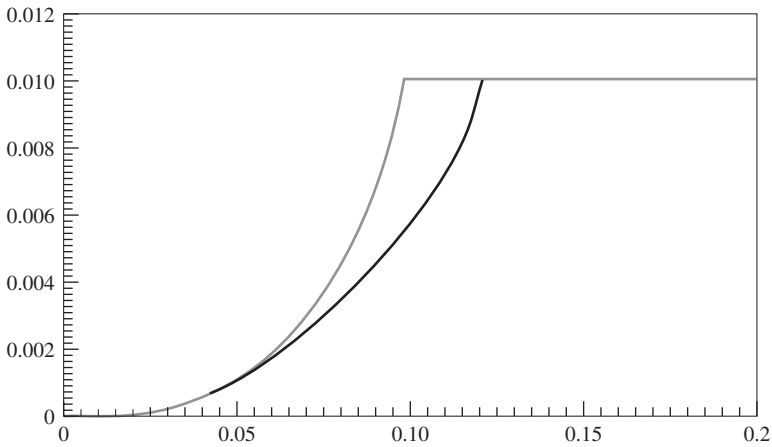


Figure 16.19 Computed magnetic armature position x (m) versus time (s) for electrohydraulic model of Fig. 16.17. The right curve represents $M = 10$ kg and the left curve, $M = 1000$ kg.

(16.8)–(16.10).

Figure 16.19 shows that the armature position x of the magnetic actuator changes more slowly with the light load M . This slowdown is caused by the high flow rate of Fig. 16.18 and the associated high flow force acting on the armature. When the flow rate is low, the flow force is also low. The low flow force is much smaller than magnetic force and thus the time to stroke is approximately 100 ms, the same as computed in Chapter 15 without any hydraulic force.

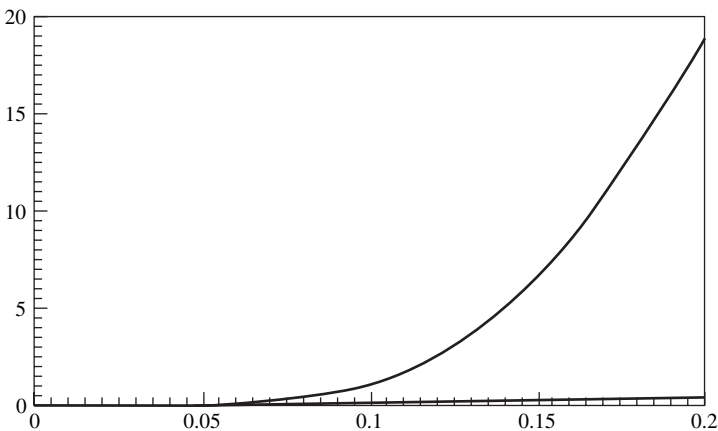


Figure 16.20 Computed cylinder position y (m) versus time (s) for electrohydraulic model of Fig. 16.17. The upper curve represents $M = 10$ kg and the lower curve near axis, $M = 1000$ kg.

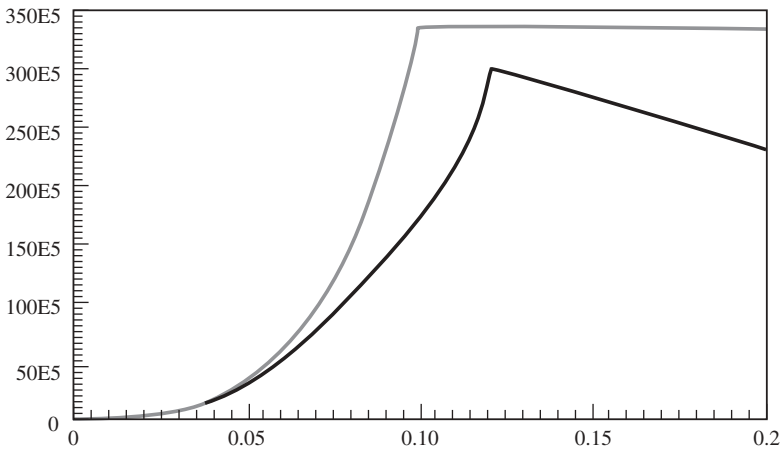


Figure 16.21 Computed differential pressure P (Pa) versus time (s) for electrohydraulic model of Fig. 16.17. The lower curve represents $M = 10$ kg and the upper curve, $M = 1000$ kg.

Figure 16.20 shows that the position y of the mass M changes much more slowly with the heavy mass than with the light mass, as expected from Newton’s law of (16.7).

Finally, Fig. 16.21 shows that the differential pressure P for both light and heavy values of M peaks at about $330.E5 \text{ Pa} = 330 \text{ bar}$, a much higher pressure than mag-

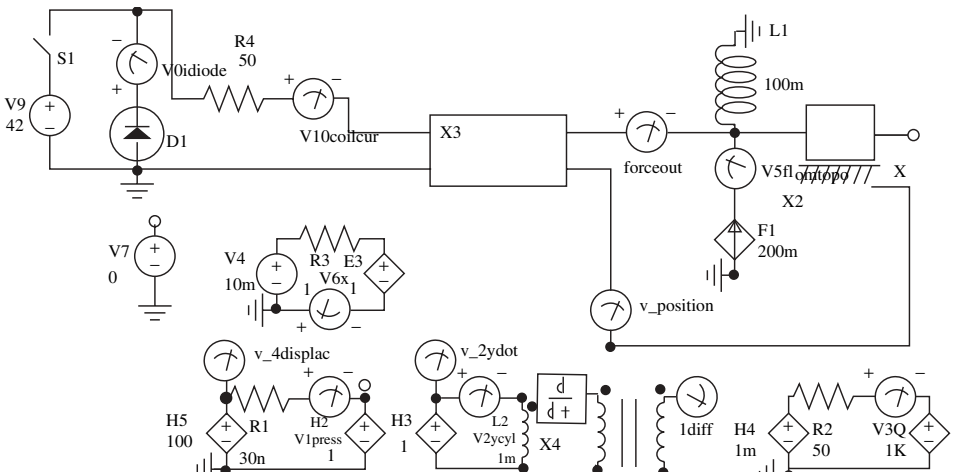


Figure 16.22 SPICE schematic of Fig. 16.17 with added chopper drive in upper left corner. (Reprinted with permission from SAE Paper OH 2002-01-1346 © 2002 SAE International and NFPA.)

netic pressures of less than 20 bar. Multiplying by $A = 1\text{E-}3\text{ m}^2$, the peak hydraulic force is a respectable 33 kN.

The electrohydraulic system can next be modeled when chopper-driven. The chopper is shown in the upper left corner of the SPICE model of Fig. 16.22, and is similar to that of Fig. 16.5. Note that the DC supply voltage is now 42 V, a standard voltage proposed for automobiles. The duty cycle is again 50%, and thus the output of the chopper has 21 V DC. Figure 16.22 shows the computed current waveforms in the coil of the magnetic actuator. For both load mass values, the currents of Fig. 16.23 show the 100 Hz chop rate superimposed on an LR circuit risetime, as expected. The currents of Fig. 16.23 also exhibit the expected dip due to back voltage induced by motion that stops when the armature reaches its full 10-mm stroke. Figure 16.24 shows the computed armature position x . The armature moves its full 10 mm in 0.16 s for $M = 1000\text{ kg}$, but takes 0.19 s for $M = 10\text{ kg}$. The slowdown is caused by the high flow rate for the light mass, similar to the case without the chopper drive. Curves of pressure and flow have also been obtained [15] that are qualitatively similar to those shown for the system without chopper drive.

While no magnetic sensor is shown in the electrohydraulic systems of Figs. 16.15 and 16.22, often magnetic sensors are used. To determine cylinder position, the magnetostrictive and LVDT sensors of Chapter 11 are commonly employed, especially in feedback control systems. Also, to measure hydraulic flow rates, steel paddle wheels are occasionally placed in hydraulic lines; the passing steel paddles behave similarly to the gear teeth of the Hall sensors of Chapter 10. Such *flowmeters* can also use the inductive pickup coils discussed in Chapter 11.

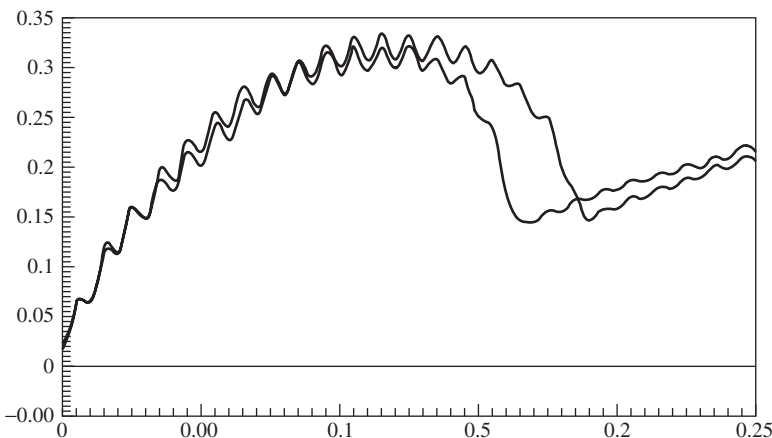


Figure 16.23 Computed coil current (amperes) versus time (s) for model of Fig. 16.22. For $M = 10\text{ kg}$ the current dips at 0.19 s, while for $M = 1000\text{ kg}$ the current dips at 0.16 s. (Reprinted with permission from SAE Paper OH 2002-01-1346 © 2002 SAE International and NFPA.)

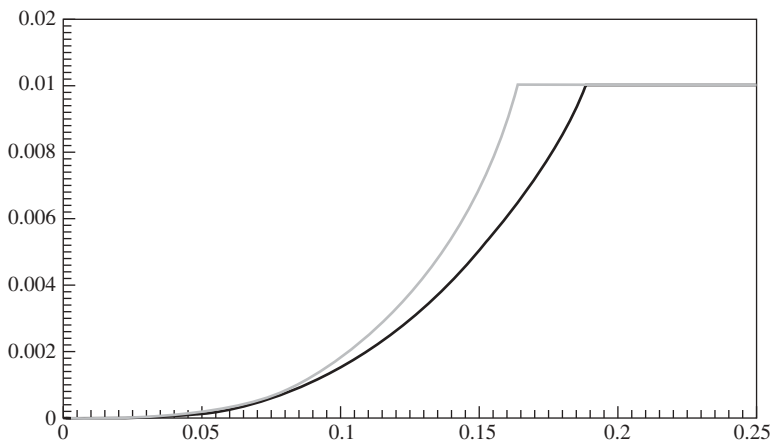


Figure 16.24 Computed armature position x (m) versus time (s) for model of Fig. 16.22. The left curve represents $M = 1000$ kg and the right curve, $M = 10$ kg. (Reprinted with permission from SAE Paper OH 2002-01-1346 © 2002 SAE International and NFPA.)

16.6 MAGNETIC DIFFUSION RESISTOR IN ELECTROHYDRAULIC MODELS

To include the effects of eddy currents in electrohydraulic systems models, one can use the eddy current diffusion resistor introduced in Chapter 15 [16]. As described in Section 15.4, this parallel resistor varies in value with magnetic saturation. Its values were calculated for the Bessho magnetic actuator and will be used here. For the nominal 0.5 A current in the Bessho actuator, the nonlinear eddy current diffusion resistor was computed to be $R_{EN} = 1320 \Omega$.

Adding this parallel resistor to the Simplorer electrohydraulic model of Fig. 16.12, the new output is shown in Fig. 16.25. With no flow force, both the armature position and the flow rate graphs show that the armature now closes in 40 ms, which is 18% longer than the 34 ms of Fig. 16.13. This time delay due to eddy current diffusion can be a problem in automotive fuel injectors and other electrohydraulic systems with models similar to that shown in Fig. 16.12. At high engine speeds, fuel injectors often must open or close in less than 1 millisecond.

The same eddy current diffusion resistor $R_{EN} = 1320 \Omega$ is added to the electrohydraulic system with Bessho magnetic actuator and the hydraulic cylinder of Fig. 16.15. The new SPICE model is shown in Fig. 16.26, which has a step input current of 0.5 A and cylinder load mass of 1000 kg [17]. It has a lighter armature mass of 1.4 kg than does the previous model shown in Fig. 16.17, as well as a higher $K_x = 3000$.

Computed results are shown with and without the 1320- Ω eddy resistor in Figs. 16.27–16.31. Figure 16.27 plots armature position, and Fig. 16.28 shows armature magnetic force. Note that the step current and lighter armature mass cause the air-

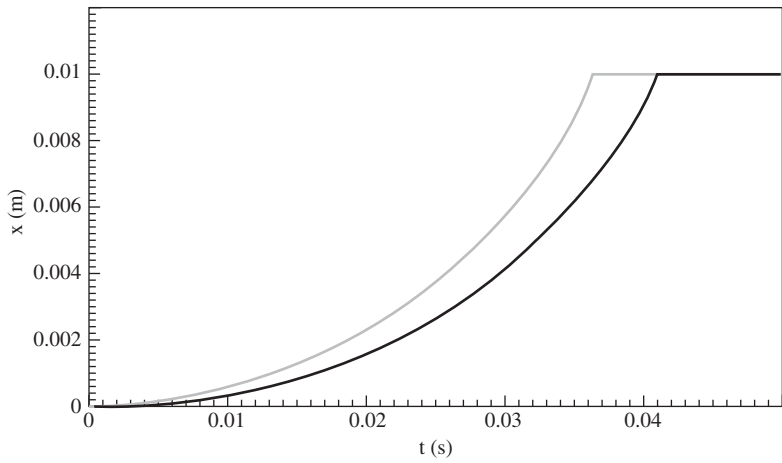


Figure 16.27 Computed armature position x (m) versus time for Fig. 16.26: left curve—without a nonlinear diffusion resistor; right curve—with a parallel 1320- Ω resistor.

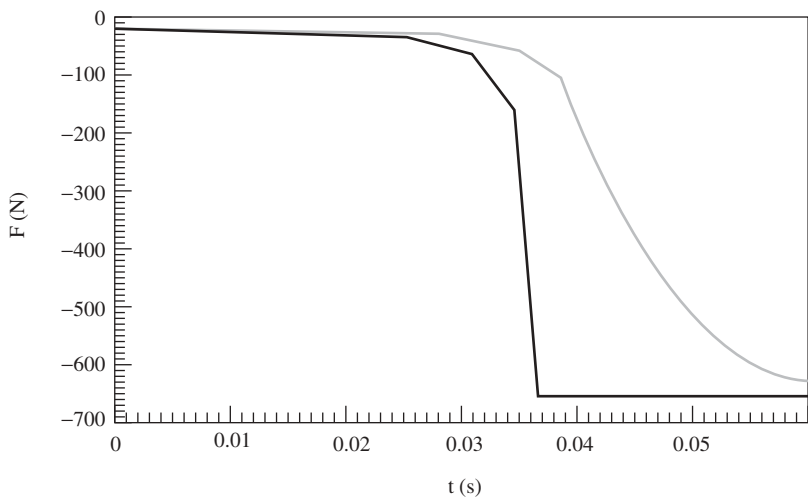


Figure 16.28 Computed magnetic force (N) versus time for Fig. 16.26: left curve—without a nonlinear diffusion resistor; right curve—with a parallel 1320- Ω resistor.

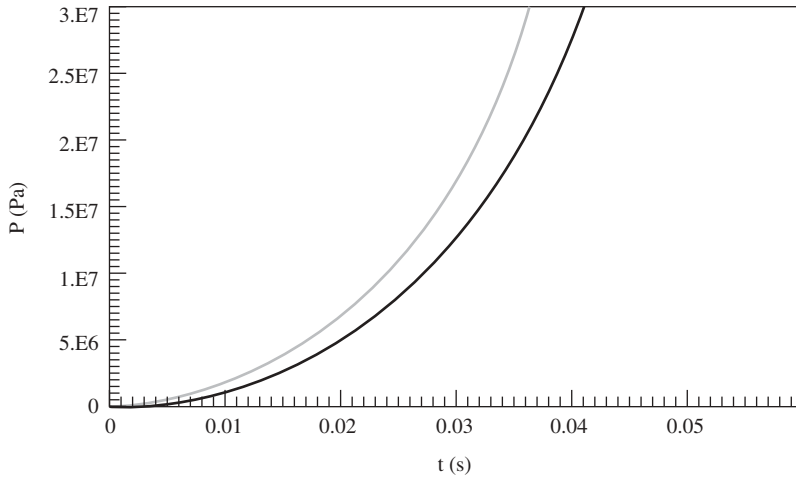


Figure 16.29 Computed hydraulic pressure (Pa) versus time for Fig. 16.26: left curve—without a nonlinear diffusion resistor; right curve—with a parallel 1320- Ω resistor.

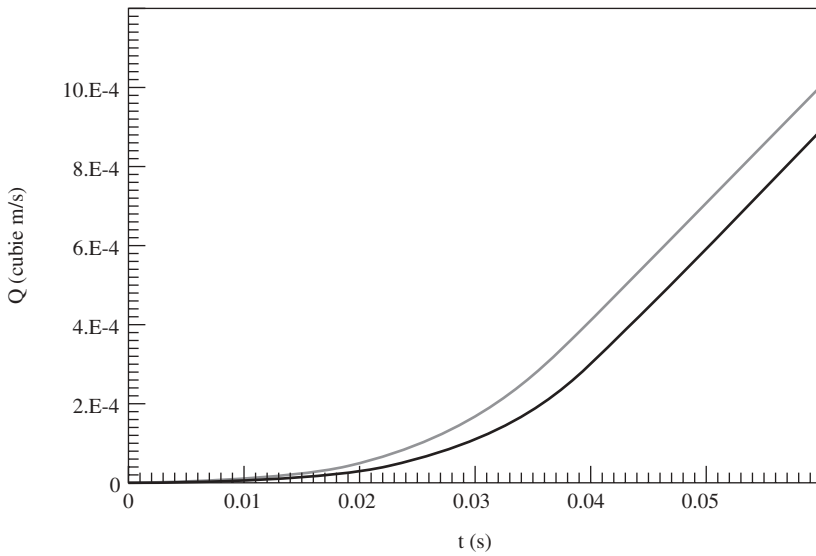


Figure 16.30 Computed flow rate (m^3/s) versus time for Fig. 16.26: left curve—without a nonlinear diffusion resistor; right curve—with a parallel 1320- Ω resistor.

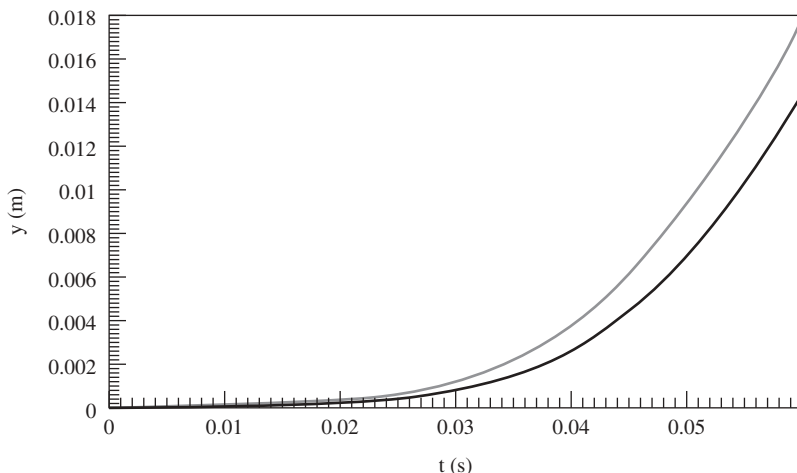


Figure 16.31 Computed cylinder position y versus time for Fig. 16.26: left curve—without a nonlinear diffusion resistor; right curve—with a parallel 1320- Ω resistor.

PROBLEMS

- 16.1** Use SPICE to solve Example 16.1 with $R_1 = 2$ MPa-s/m³ and $R_2 = 4$ MPa-s/m³. Compare your results with those obtained by simple electric circuit theory.
- 16.2** Use SPICE to solve Example 16.1 with $R_1 = 3$ MPa-s/m³ and $R_2 = 5$ MPa-s/m³. Compare your results with simple electric circuit theory.
- 16.3** Redo Example 16.2 using both SPICE and the quadratic formula for $K = 1$, $R = 1$, and source pressure $P_S = 10$ Pa.
- 16.4** Redo Example 16.2 using both SPICE and the quadratic formula for $K = 2$, $R = 1$, and source pressure $P_S = 10$ Pa.
- 16.5** Redo Example 16.2 using both SPICE and the quadratic formula for $K = 1$, $R = 2$, and source pressure $P_S = 10$ Pa.
- 16.6** Redo Example 16.2 using both SPICE and the quadratic formula for $K = 2$, $R = 2$, and source pressure $P_S = 10$ Pa.
- 16.7** Use SPICE to solve Example 16.3 with $Q = 10$ m³/s, $R = 50$ Pa -s/m³, and $C = 100\text{E-}6$ m³/Pa. Find the time constant of your results and compare it with RC .
- 16.8** Use SPICE to solve Example 16.3 with $Q = 10$ m³/s, $R = 50$ Pa -s/m³, and $C = 50\text{E-}6$ m³/Pa. Find the time constant of your results and compare it with RC .

REFERENCES

1. J. R. Brauer and J. H. Lumkes, Jr., Coupled model of a magnetically-actuated valve controlling a hydraulic cylinder and load, *IEEE Trans. Magn.* **38**: 917–920 (March 2002).
2. J. R. Brauer, Electromagnetic analogies for modeling hydraulics, *Int. Compumag Soc. Newsl.* **7**: 3–5 (March 2000).
3. F. M. White, *Fluid Mechanics*, 2nd ed., McGraw-Hill, New York, 1986.
4. J. G. Slater, T. Wanke, and J. Bitant, *Introduction to Hydraulics Seminar Manual*, Milwaukee School of Engineering Fluid Power Institute, Milwaukee, WI, 2005.
5. R. V. Giles, J. B. Evett, and C. Liu, *Fluid Mechanics and Hydraulics*, 3rd ed., McGraw-Hill, New York, 1994.
6. John R. Brauer, ed., *What Every Engineer Should Know about Finite Element Analysis*, 2nd ed., Marcel Dekker, New York, 1993, Chapter 6, Fluid analysis, by N. J. Lambert.
7. M. Rausch, M. Gebhardt, M. Kaltenbacher, and H. Landes, Computer-aided design of clinical magnetic resonance imaging scanners by coupled magnetomechanical-acoustic modeling, *IEEE Trans. Magn.* **41**: 72–81 (Jan. 2005).
8. G. R. Tallbaeck, J. D. Lavers, A. Erraki, and L. S. Beitelman, Influence of model parameters on 3-D turbulent flow in an electromagnetic stirring system for continuous billet casting, *IEEE Trans. Magn.* **40**: 597–600 (March 2004).
9. J. R. Brauer, J. H. Lumkes, Jr., and J. G. Slater, Coupled electromagnetic and hydraulic devices modeled by finite elements and circuits, *Digests of IEEE Conf. Electromagnetic Field Computation*, Milwaukee, WI, June 2000.
10. J. R. Brauer and J. H. Lumkes, Jr., Electrohydraulic systems simulations containing electromagnetic finite element models of magnetic actuators, *SAE Off-Highway & Powerplant Congress*, Milwaukee, WI, Sept. 2000, paper 2000-01-2633.
11. J. L. Johnson, *Design of Electrohydraulic Systems for Industrial Motion Control*, Parker Corp., Cleveland, OH, 1991.
12. J. R. Brauer, Model of a chopper-driven magnetic actuator in an electrohydraulic system, *Proc. IEEE Int. Electric Machines and Drives Conf.*, Cambridge, MA, June 2001.
13. J. H. Lumkes, Jr., *Control Strategies for Dynamic Systems*, Marcel Dekker, New York, 2002.
14. H. E. Merritt, *Hydraulic Control Systems*, Wiley, New York, 1967, pp. 303ff.
15. J. R. Brauer, J. H. Lumkes, Jr., and D. Lin, Modeling an electronically-controlled magnetic actuator operating a hydraulic valve and cylinder, *Proc. Int. Fluid Power Expo/SAE/National Fluid Power Conf.*, Las Vegas, NV, March 2002, SAE paper OH 2002-01-1346.
16. J. R. Brauer, Magnetic actuator models including prediction of nonlinear eddy current effects and coupling to hydraulics and mechanics, *Proc. Congresso Brasileiro de Eletromagnetismo*, Gramado, Brazil, Nov. 2002.
17. J. R. Brauer and I. D. Mayergoyz, Finite element computation of nonlinear magnetic diffusion and its effects when coupled to electrical, mechanical, and hydraulic systems, *IEEE Trans. Magn.* **40**: 537–540 (March 2004).

APPENDIX: SYMBOLS, DIMENSIONS, AND UNITS

Base Dimensions and Their SI Unit Symbols^a

Parameter and Its Symbol	Dimensions	Unit Name	Unit Symbol
<i>Electromagnetics</i>			
Charge <i>Q</i>	<i>Q</i>	coulombs	C
Electric field intensity E	<i>MLT⁻²Q⁻¹</i>	volts per meter	V/m
Electric flux density D	<i>QL⁻²</i>	coulombs per square meter	C/m ²
Electric scalar potential <i>ϕ_v</i>	<i>ML²T⁻²Q⁻¹</i>	volts	V
Current <i>I</i>	<i>QT⁻¹</i>	amperes	A
Current density J	<i>QL⁻²T⁻¹</i>	amperes per square meter	A/m ²
Conductivity <i>σ</i>	<i>M⁻¹L⁻²TQ²</i>	siemens per meter	S/m
Resistance <i>R</i>	<i>ML²T⁻¹Q⁻²</i>	ohms	Ω
Permittivity <i>ε</i>	<i>M⁻¹L⁻³T²Q⁻²</i>	farads per meter	F/m
Capacitance <i>C</i>	<i>M⁻¹L⁻²T²Q⁻²</i>	farads	F
Magnetic field intensity H	<i>L⁻¹T⁻¹Q</i>	amperes per meter	A/m
Magnetic flux density B	<i>MT⁻¹Q⁻¹</i>	webers per square meter = teslas	Wb/m ² = T
Permeability <i>μ</i>	<i>MLQ⁻²</i>	henrys per meter	H/m
Inductance <i>L</i>	<i>ML²Q⁻²</i>	henrys	H
Flux <i>ϕ</i>	<i>ML²T⁻¹Q⁻¹</i>	webers	Wb
Reluctance <i>ℜ</i>	<i>M⁻¹L⁻²Q²</i>	amperes per weber	A/Wb
<i>Mechanics</i>			
Mass <i>M</i>	<i>M</i>	kilograms	kg
Length <i>l</i>	<i>L</i>	meters	m
Time <i>t</i>	<i>T</i>	seconds	s
Velocity V	<i>LT⁻¹</i>	meters per second	m/s
Force F	<i>MLT⁻²</i>	newtons	N
Pressure <i>p</i>	<i>ML⁻¹T⁻²</i>	newtons per square meter = pascals	N/m ² = Pa
Density <i>ρ</i>	<i>ML⁻³</i>	kilograms per cubic meter	kg/m ³
Energy or work <i>W</i>	<i>ML²T⁻²</i>	newton-meters = joules	N-m = J

Parameter and Its Symbol	Dimensions	Unit Name	Unit Symbol
<i>Mechanics (cont.)</i>			
Power P	ML^2T^{-3}	watts	W
Compressibility k	$M^{-1}LT^2$	meters-square seconds per kilogram	m-s ² /kg
Modulus of elasticity Y	$ML^{-1}T^{-2}$	newtons per square meter = pascals	N/m ² = Pa
<i>Hydraulics</i>			
Pressure p	$ML^{-1}T^{-2}$	newtons per square meter = pascals = 1E-5 bar	N/m ² = Pa = 1E-5 bar
Flow rate Q	L^3T^{-1}	cubic meters per second = 1000 liters per second	m ³ /s = 1000 L/s
Laminar orifice resistance R	$M^{-2}L^{-1}T^{-1}$	pascals-seconds per cubic meter	Pa-s/m ³
Turbulent orifice coefficient K	$M^{-2}L^9T^3$	meters to seventh power per (squared newtons-second)	m ⁷ /(N ² s)
Hydraulic capacitance C	$M^{-1}L^4T^2$	cubic meters per pascal	m ³ /Pa
<i>Heat</i>			
Temperature T	τ	kelvin = 273 + degrees Celsius	K = 273 + °C
Quantity of heat q	ML^2T^{-2}	newton-meters = joules	N-m = J
Heat flow Q	MT^{-2}	watts per square meter	W/m ²
Thermal conductivity k	$MLT^{-3}\tau^{-2}$	watts per (meter-degree Celsius)	W/(m-°C)
Film coefficient h	$MT^{-3}\tau^{-2}$	watts per (degree Celsius-square meter)	W/(°C-m ²)

^aKey: M = mass (kg), L = length (m), T = time (s), Q = charge (C), τ = temperature (K or °C).

Index

- ABC finite elements, 225–227
- AC currents, 107, 169, 179–181
- Accumulators, 274
- Acoustics, 274
- Actuator(s), magnetic, *see also* Magnetic actuators
 - acceleration of, 125–127
 - definition of, 3, 85
 - finite element analysis of, 45, *see also* Maxwell SV
 - force of, *see* Magnetic force
 - high speed, 195
 - reciprocating, 239
 - size of, 125–127
- Airgap, 29, 32–35, 267
- Alternator load dump, 210
- Ampere’s Law, 12–14, 29–32
- Analogy(ies), 247, 250–251, 273–277
- Apertures, 210–215
- Architecture of VHDL-AMS models, 254–257
- Armature, 34, 85
- Autocad DXF file, 203
- Automotive brakes and control, 157–158, 271–272
- Automotive sensors, 157–159, 165, 186
- Axisymmetric geometry, 52–53

- Bessel function(s), 118, 131
- Bessho DC solenoid
 - flux plot of, 235
 - geometry, 52–54
 - transient operation, 127, 131–139, 195, 234–238, 251–254, 266–268, 279–296
- Bit, 168
- Block diagram, 4–6, 252, 258–263
- Boundary conditions, 45
- Brake(s), 103, 271–272

- Cable, coaxial, 216
- CAN bus, 186
- Can, 212–215
- Capacitance, 75–77, 109–111
- Capacitor, 23–26, 109–111
- Chambers, absorption, 215
- Chambers, test, 215–220
- Chopper circuit, 280–283, *see also* Pulse-width modulated
- Circuit breakers, 4
- Circulation, 10, 13
- Clapper armature actuator, 196–198, 248, *see also* Eaton AC solenoid
- Closure time, 236–238, 240–241, 248–249, 253, 277–297
- Clutches, 103
- CMOS, 146
- Coenergy, 56–57
- Coil(s)
 - ampere-turns, 13
 - design, 191–206
 - resistance, 172–173, 191–199
 - sensor, 158–159, 165–167, 179–181
 - time constant, 194–195
 - voltage induced, 19
- Common-mode noise, 210
- Complex AC circuit methods, 110–111
- Complex-plane impedance, 169–173
- Composite materials, 21
- Computational fluid dynamics (CFD), 274
- Conductivity
 - electrical, 20
 - temperature effect on, 192
 - tensor electrical, 146–150, 224
 - thermal, 199
- Contactors, 4, *see also* Eaton AC solenoid
- Continuity, 25
- Contours, 51–53, 219–220

- Control system, 6, 258, *see also* Feedback control
- Control System Toolbox for MATLAB, 258
- Controller, 254
- Coordinates, rectangular (Cartesian), 7
- Core loss
 - curves, 109
 - equation, 203
- Corrosion cracks, 174
- Cosimulation, 264
- Coupled electromagnetic
 - analysis, 209–220, 224
 - fields, 25
 - radiation, 209–220
- Coupling electric circuits to finite elements, 225–232
- Coupling, antiferromagnetic, 160
- Cramer's rule, 149
- Curl, 9–12
- Current, 12–14
 - density, 12–14, 193
 - dip, 236–237, 248–249
 - in plane (CIP), 160
 - perpendicular to plane (CPP), 160
 - waveform, 226–231, 236–240
- Cyclotron frequency, 147
- Cylinders, hydraulic, 283–296

- dB, 212–213
- DC coils, 191–193
- Deadbands, 100
- Del operator, 7
- Delay time, 292, *see also* Diffusion time
- Demagnetization curve, 63–64
- Dependent sources, 278–279
- Design optimization methods, 92
- Determinant, 9–10
- Diffusion time, 125, 128–142, 264–268, 202–296
- Digital solver, 254
- Diode, flyback, 280
- Discretization, 39
- Disk drives, 5–6, 97, 160–162, 167–169, *see also* Recording heads and Voice coil actuators
- Displacement current, 25–26
- Displacement (mechanical), 232, 260
- Dither, 101
- Divergence, 9–11

- Eaton AC solenoid
 - flux plot of, 52
 - geometry of, 45
 - shading ring in, 115
 - transient analysis of, 238–341
- Eddy axial formulation, 117–118
- Eddy current(s)
 - braking, 174
 - coefficient, 203
 - effects, 20–22, 195–199, 203, *see also* Diffusion time
 - moving, 173–174
 - resistor, 264–268, 292–296
 - sensors, 169–174
 - stationary, 170–173
- Electric
 - charge density, 23
 - circuit, 225–226
 - field, motional, 20, 235–240, 248–250
 - field intensity, 19
 - flux density, 22–23
 - scalar potential, 22–24, 224
- Electrode(s), 145–148, 150–158
- Electrohydraulic analysis, 271–296
- Electromagnetic compatibility (EMC), 209–220
- Electromagnetic interference (EMI), 209–220
- Electromagnetic problem types, 225
- Electromagnetics, 7–28
- Electromagnets, 64
- Electromechanical analysis, 223–297
- Electronics module, 176, 178
- Electron(s), 146–147
- Electrostatic fields, 200–201, 218–220
- Electrostatic scalar potential, 22, 224
- Emissions, conducted, 209–210
- Emissions, radiated, 209–215
- Energy
 - conservation, 39–40
 - conversion, 3–4, 272
 - density, 56
 - functional, 39–41
 - input, 39–40
 - loss, 195, *see also* Power loss
 - stored, 39–40, 56–57, 218–220
- Entity in VHDL-AMS models, 254, 257
- Equivalent circuits, 109–111

- Excitation vector, 42, 224, 232
- Excitations, 45
- Faraday's Law, 18–22, 165–168, 210, 228, 251
- Feedback control, 6, 158, 168, 272, 291
- Fermi gas theory, 146–149
- Ferrite(s), 21, 36, 63–64, 196–199
- Ferrofluids, 98
- Ferromagnetic layers, 160
- Ferromagnetics, 15–18
- Film coefficient, 201
- Filtering, 209–210
- Finite difference method, 39
- Finite element(s)
 - axisymmetric, 52–53, 226
 - edge, 43
 - model, 44–48
 - nodes, 41
 - first order, 41–42
 - open boundary, 45, 226–227
 - quadratic shape function, 43
 - tangential vector, 43
 - triangular, 41–44
- Finite-element analysis, *see also* Maxwell SV
 - acoustic, 274
 - electric conduction, 149–158, 161–162
 - electromechanical, 223–245
 - fluid(s), 202, 274
 - magnetic, 39–49, 223–229
 - parametric, 89, 92, 249–250, 286
 - structural, 226–241
 - thermal, 199–206
- Flow force, 279–296
- Flow, hydraulic, 273–295
- Flowmeters, 291
- Fluid dynamics, 39, 274
- Fluid power systems, 274–296
- Flux
 - fringing, 33, 36, 55–56
 - leakage, 55–56, 205
 - lines, 218–220
 - linkage, 20, 69–70, 250
 - partial, 55–56
- Flux density plots, 53
- Flux gate sensors, 179–186
- Force(s)
 - bi-directional, 96–98
 - distribution, 226–241
 - integration, 232–234
 - magnetic, *see* Magnetic force
 - on capacitor, 76
 - pulsations, 113–116
 - repulsive, 115
- Frequency, resonant, 110
- Friction, 101, 252, 260
- Fringing factor, 36
- Functional minimization, 40–42
- Galerkin's method, 43
- Gasket, 211–212
- Gradient, 7–9
- Hall effect sensors, 145–159
- Hard-disk drives, *see* Disk drives
- Hardware Description Language (HDL), 254
- Heat, 199–206
- Holes, 146
- Hydraulic(s), 271–296
 - capacitance, 273–274, 277–283
 - cylinders, 283–296
 - inductance, 273–274
 - line(s), 272–273
 - pressure(s), 271–296
 - resistor (orifice), 273–296
 - systems, 271–296
- Hysteresis, 108–109, 168
 - coefficient, 203
 - loss, 108–109
- Impedance, 77–80, 169–174, 194–199
 - characteristic, 216
 - Thevenin, 216
- Inductance, 72–74, 194–199, 202–204, 247–251
 - end turn, 239–240
 - incremental, 73
 - matrix, 72–74
 - mutual, 72
 - secant, 73
 - self, 72
- Inductive kick, 242–244
- Inductor(s), 72, 202–206
 - leakage, 266–267
 - rectangular, 133–135, 140–142
- Injectors, fuel, 3, 292

- Insulation, glastic, 200–201, 204
- Integrated circuits, 146
- Inverse problem, 171–172
- Iron (Fe), 15–17
- Iron filings, 51

- Kirchhoff's Current Law, 9, 226
- Knee, 17

- Laminar orifice(s), 274
- Laminated steel, 108–109
- Laminations, 21
- Laplace transform s domain, 258–263
- Latching switches, 242
- Leakage flux, 55–56, 205
- Levitation, 115
- Light, speed of, 211
- Line segments, 29
- Linear actuators, 85–101
- Linear time invariant (LTI), 260
- Linear variable differential transformers (LVDTs), 174–177, 292
- Lines of force, 51
- Locus, impedance, 171
- Lorentz force, 62, 96–97, 259
- Losses, *see* Power loss
- Loudspeakers, 3, 96

- Machines, rotary, 85, 101–103
- Magnet, lifting, 112–113
- Magnetic
 - AC actuators, 107–123, 238–241, *see also* Eaton AC solenoid
 - bearings, 102–103
 - brakes and clutches, 103, 174
 - constant force actuator, 99–100
 - couplings, 103
 - DC actuators, 85–106, 234–238, 248–268, 271, *see also* Bessho DC solenoid
 - diffusion time, linear, 128–132
 - diffusion time, nonlinear, 132–142
 - domains, 15
 - energy, 40–42, 56–57
 - field, 7
 - field intensity, 12
 - flux, 13, 69–70
 - flux density, 12
 - flux line plots, 51–53
 - force, 3, 51–68, 74–75, 86–101, 113–116, 125–129, 232–234, 251–261
 - materials, 15–18
 - performance parameters, 69–81
 - pole, 32
 - pressure, 60–61, 232–233, 271
 - Resonance Imaging (MRI), 181
 - Reynolds number, 173
 - sensors, 145–186, 272, 291
 - sensors, inductive, 165–177, 210–211
 - separator, 98
 - switches, 241–242
 - torque, 66–67
 - vector potential, 24, 224
- Magnetizing fixtures, 168
- Magnetoimpedance (MI) sensors, 182–186
- Magnetometers, 181
- Magnetomotive force (MMF), 31
- Magneto-resistance (MR), 152–162
 - classical, 152–156, 159–162
 - colossal (CMR), 160
 - extraordinary (EMR), 161
 - giant (GMR), 160
 - tunneling (TMR), 160
- Magneto-resistive heads, 161–162
- Magneto-resistive sensors, 159–162, 242
- Magnetostatics, 39–42
- Magnetostriction, 177–179
- Magnetostrictive materials, 97
- Magnetostrictive sensors, 177–179
- Magnets, permanent, 62–66
- Material
 - anisotropic, 16
 - hard magnetic, 17
 - isotropic, 16
 - soft magnetic, 15
- MATLAB, 258–263
- Matrix
 - conductance, 223–224
 - damping, 231–232
 - equation, 42–44, 223–232
 - mass, 231–232
 - permittance, 223–224
 - reluctance, 42, 223–224
 - solution sparsity, 44
 - stiffness, 42, 231–232
- Maxwell stress tensor, 61, 232–233

- Maxwell® SV (Student Version) finite element software numbered examples
 - chapter 4, 46–49
 - chapter 5, 55–56, 59–60, 65–66
 - chapter 6, 70, 73–74, 76–77, 78–80
 - chapter 7, 88–89, 89–91, 93–94, 94–96
 - chapter 8, 112–113, 115–116, 120–122
 - chapter 9, 129–131, 133–135, 137–142
 - chapter 10, 152–155
 - chapter 11, 168–169, 172–173, 176–177
 - chapter 12, 196, 196–199, 200–201
 - chapter 13, 212–215, 219–220
- Maxwell, James Clerk, 24–26
- Mechanical input, 271–272
- Mechanical stress, 39, 240–241
- Mechatronics, 6
- Metal detectors, 169
- Micro-electromechanical systems (MEMs), 161
- Microphone, 5, 167
- Midnode variables, 43
- Model validation, 53–54
- Modulus of elasticity, 233–234, 239
- MOSFETs, 181
- Motes, 186
- Motion control, 3
- Motional EMF effects, 235–238, 248–250
- Motors, 4, *see also* Step motors
- Moving surfaces, 231
- Multisim software, 247

- Nanoparticles, 182
- Nanotechnology, 15, 161
- Newton's iterative method, 43
- Newton's Law(s), 231–232, 251, 286
- Nodes, 41, 224–226, 231–232, 256
- Noise, 209–210
 - common-mode, 210
 - radiated, 209–220
- Non-destructive evaluation (NDE), 171–172
- Non-destructive testing (NDT), 172
- Nonlinear B - H curve, 17–18, *see also* Saturation
- Nonsinusoidal waveforms, 111
- Normal AC B - H curves, 109
- Nuclear power plants, 174
- Ohm's Law, 20
- Orifice, hydraulic, 274
- Orifice, variable, 273–274, *see also* Valve(s)
- Overshoot, percent (P.O.), 260–263

- Package body, 254
- Packing factor, 192–193
- Parametric finite element analysis, 89–90, 92, 249–250
- Path, closed, 13, 29–31
- Performance parameters, 69–81
- Permanent magnet, moving, 167
- Permanent magnet(s)
 - latch, 242
 - modeling, 224
 - properties, 62–66
 - sensors, 158
- Permeability, 12, 15
 - complex, 212
 - effective, 111
 - incremental, 17
 - relative, 15
 - tensor, 16
- Permeance, 31
- Permittivity, 23, 200–201, 212, 216–218
- Phase angle, 194
- Pickup coils, 291, *see also* Coil(s), sensor
- Pig (traveling sensor), 174
- Pins, 256
- Pipe, 174
- Plastics, 216
- Plug and play, 186
- Plunger armature, 91–96, 126–127, 131–132, 137–138, *see also* Bessho DC solenoid
- Pneumatic systems, 274
- Poisson's differential equation, 199–200
- Poisson's ratio, 234, 239
- Polynomial order p , 43
- Position versus time, *see* Bessho DC solenoid *and* Eaton AC solenoid
- Postprocessing, 51
- Potentials, 22–24
- Power loss(es), 108–113, 195–203, *see also* Eddy current effects
- Preprocessing, 46
- Pressure
 - hydraulic, 271–296

- Pressure (*continued*)
 - magnetic, 60–61, 232–233
 - versus flow curves, 274, 286–287
- Primary winding, 175–176, 227–228, 242–244
- Proportional actuators, 98–101
- Prosthesis, 3
- Proximity effects in coil wires, 195–199
- Proximity sensors, 169–173
- Pull curve, 86–90
- Pulse, interrogation, 178
- Pulse-width modulated (PWM), 100–101, 280–283, 290–292
- Pump(s), 273–296

- Reactance, 78–79
- Reciprocating magnetic actuators, 239, 273
- Recording heads, *see also* Disk drives
 - inductive, 167–169
 - magnetoresistive, 160–162
- Reduced order model, 260–263
- Reed switches, 241
- Reflections, 216
- Relaxation techniques, 39
- Relay(s), 238–241
- Reluctance, 30–37
 - AC complex, 36, 119–123
 - force, 58
 - method, 29–37
 - method, limitations of, 37
- Reluctivity tensor, 224
- Remanent (residual) flux density, 63–64
- Resistance, 148, 191–199
- Resistivity, 149
- Resistor, eddy current (magnetic) diffusion, 264–268, 292–296
- Resonant frequency, natural, 110
- Right hand rule, 16
- Rigid armature motion analogies, 251
- Rigid body motion, 228–231, 250–251
- Ripple, *see* Pulse-width modulated
- Robot(s), 3, 170
- Roots function of MATLAB, 260–262
- Rotary actuators, 101–103

- Saturation, 17, 56–61, 228–231, 242–244
- Scalar(s), 7
- Secondary winding, 175–177, 227–228, 242–244

- Security systems, 169
- Seek time, 97, 168
- Semiconductors, 145–146
- Sensor(s), *see also* Magnetic sensors
 - Hall effect, 5, 145–159
 - LVDT, 291
 - magnetostrictive, 177–179, 291
 - output voltage, 158–159
 - proximity, 5, 169–173
 - toothed armature, 34
 - velocity, 5–6, 165–167, 210
- Shading coil, 114
- Shading ring, 114–115
- Shape functions, 41, 43, 224
- Shields, 210–215
- Signal-to-noise ratio, 209–210
- Signals, 209–210
- Simplorer software, 180–181, 252–256, 278, 281
 - models of electrohydraulics, 283–285, 292–293
 - models of electromechanics, 256–258, 264–268
- Simulink, 258–259
- Skin depth, 107–108
- Skin effect, 112–113, 196–199, 210–214
- Smart dust, 186
- Smart sensors, 186
- Soft adjacent layers (SALs), 160
- Software
 - finite element, 46, 223–245, *see also* Maxwell SV
 - systems, 247–268
- Solenoid actuators, 85–96
 - clapper armature, 85–91, *see also* Eaton AC solenoid
 - plunger armature, 91–96, *see also* Bessho DC solenoid
- Solenoidal coil, 85
- Sources, *see* Excitations
- Speed sensors, 157–159, 165–167
- Speed voltage, 248–250, *see also* Motional EMF effects
- SPICE, 180–181, 247, 274
 - models of electrohydraulics, 278–296
 - models of electromechanics, 248–249, 248–250
 - models of hydraulics, 275, 275–277, 277–278

- Spring, nonlinear, 238–239
- SQUID magnetometers, 181
- Stage, hydraulic, 272
- Stator, 34, 85
- Steel, *see also* Laminated steel
 - B-H* relation, 15–18
 - cuts, 120–123
 - cylinder, 131–132, 135–139
 - slab, 129–131, 132–135
 - solid, 111–113
- Step *B-H* curve, 132–139
- Step motor(s), 101–103
- Stiction, 101
- Stiffness matrix, 42, 231
- Stokes' law, 13
- Strain, mechanical, 177–178, 240–242
- Stress, mechanical, 177–178, 231, 240–242,
 - see also* Maxwell stress tensor
- Stripe, magnetoresistive, 161
- Stroke time, 125–127, 234–238, 240–241,
 - see also* Closure time
- Superconductors, 64
- Surface, closed, 13
- Susceptance, conducted, 209–210
- Susceptance, radiated, 209–210
- Switch, electronic, 280, *see also* Pulse-width modulated
- Switched reluctance motors, 102
- Switches, *see* Magnetic switches *and* Reed switches
- Switchgear, 4
- System(s)
 - models, 247–269
 - second order, 260–263
 - software, *see* MATLAB, Simulink, *and* Simplorer
 - third order, 260–263
- Table, flux linkage, 249–250
- Table, force, 249–250
- Tank, hydraulic, 273
- Target, 170–173
- TEM transmission lines, 215–217
- TEM cells, 217
- Temperature, 191–192, 199–206
- Terfenol, 178
- Tesla, 12
- Tetrahedrons, 43, 226
- Thermal
 - analysis, 39, 199–206
 - conduction, 199–201
 - convection, forced, 201–202
 - convection, free, 201–206
 - radiation, 201–206
- Time constant, 194, *see also* Diffusion time
- Time, *see also* Closure time
 - peak, 260–263
 - rise, 260–263
 - settling, 260–263
- Timeline of actuator operation, 125
- Timestepping, 232–244, 252, 264, *see also* Simplorer *and* SPICE
- Toolboxes for MATLAB, 258
- Tooth pitch, 159
- Toothed wheel sensors, 157–159, 165–167
- Torque sensing, 179
- Torquers, 101
- Transducer(s), 85, 261
- Transfer function, 260–263
- Transformers, 21, 227–231, 242–244
- Transformers, linear variable differential, 5, 174–177
- Transient operation of actuators, 125–142
- Translation, mechanical, 232
- Transmission lines, 215–217
- Tri-plate cells, 217–220
- Turbulent orifices, 273–274
- Turnoff, 128–130
- Turnon, 128–142
- Turns, 13
- Units
 - centimeter-gram-second (CGS), 17
 - SI (meter-kilogram-second), 299–300
- Valve(s)
 - control, 274, 283–291
 - electrohydraulic, 272, 278–296
 - four-way, 283–291
 - hydraulic, 272–274, 278–296
 - lands in, 285
 - spool, 285
- Variable reluctance sensor, 157–159, 165–167
- Variables, across, 256
- Variables, through, 256
- Vector, unknown, 42, 224, 231–232
- Vectors, 7

VHDL-AMS, 254–258

View factors, 202

Virtual work, 57–59

Voice coil actuators, 96–97

 MATLAB model of, 259–263

Voltage

 induced, 19–20

 potential, 22

 read head, 167–169

 step, 194

Wavefront, 132

Waveguide, acoustic, 178–179

Wavelength, 211

Waves, 215–216

Wheel, toothed, 157–160

Wire diameter, 192–193

Wire gauge, 192

Zigbee, 186